COMPOSITIONAL CHARACTERISTICS AND AGES OF PLUTONS IN THE CENTRAL RUBY BATHOLITH, ALASKA: IMPLICATIONS FOR RARE-EARTH-ELEMENT RESOURCES

By

Amy L. Tuzzolino

A Thesis Submitted in Partial Fulfillment of the Requirements

for the Degree of

Masters of Science

in

Geology

University of Alaska Fairbanks

December 2016

APPROVED:

Dr. Rainer Newberry, Committee Co-Chair
Dr. Paul McCarthy, Committee Co-Chair
Dr. Kenneth Severin, Committee Member
Mr. Lawrence Freeman, Committee Member
Dr. Paul McCarthy, Chair
Department of Geosciences
Dr. Paul Layer, Dean
College of Natural Science and Mathematics
Dr. Michael Castellini, Dean
Graduate School

ABSTRACT

The central Ruby batholith, comprising much of the Ray Mountains in central Alaska, consists of at least ten, largely monzogranitic plutons, some of which have been defined as a result of this thesis. The general age of the batholith is estimated at 111 Ma, yet recent $^{40}Ar/^{39}Ar$ muscovite and $^{238}U/^{206}Pb$ zircon data suggests greater variability in ages than previously known, with ages now spanning 90 to 112 Ma. Initial $^{87}Sr/^{86}Sr$ ratios for the area show a general increase from northeast (minimum of 0.706) to southwest (maximum of 0.727).

There are two characteristic mineral assemblages distinguishing the plutons: The northern plutons typically have an oxidized, calcic mineral assemblage featuring allanite + titanite + magnetite ± hornblende ± monazite ± ilmenite. The southern plutons are characterized by the minerals monazite + xenotime + ilmenite ± muscovite ± fluorite. Total alkali-silica classification defines only the No Name Creek pluton as being truly peraluminous, a classification further supported by its unique presence of topaz.

In the north, the rare-earth elements (REE) are primarily hosted in the silicates allanite-(Ce), ($CaCe(Al_2Fe^{2+})(Si_2O_7)(SiO_4)O(OH)$), and to a lesser extent, titanite, ($CaTiSiO_5$), while the phosphate minerals monazite-(Ce), ($CePO_4$), and xenotime, (YPO_4), are REE hosts in the southern plutons. These mineralogical differences are not necessarily due to variable REE concentrations within the melts, but rather are largely functions of peraluminosity and oxidation state, features intrinsic to the primitive source materials.

Chemical analyses of stream gravels draining the batholith highlight geographic trends in trace-element concentrations: The southern gravels are enriched in REE relative to the northern gravels for several reasons. REE in the northern gravels are predominantly hosted in allanite and titanite (both of which contain relatively low REE concentrations), and the REE in the southern gravels are found in monazite and xenotime. Further, magnetite and ilmenite are more abundant in the northern gravels, effectively drowning out the REE carriers. Furthermore, the gravels in the southeast have the highest heavy-rare-earth element to light-rare-earth element ratios. In terms of economics, these ratios are generally the most significant.

TABLE OF CONTENTS

LIST OF FIGURES

Page

LIST OF TABLES

LIST OF APPENDICES

ACKNOWLEDGEMENTS

This thesis would not have been possible without funding from the Cooperative Research Intern Program through the University of Alaska Fairbanks Geosciences Department, the Geophysical Institute at the University of Alaska Fairbanks, and the Alaska Division of Geological & Geophysical Surveys (DGGS). Further funding was provided by the Alaska State Legislature through the Strategic & Critical Minerals Assessment Program, itself a constituent of the Airborne Geophysical/Geological Mineral Inventory, and by the Society of Economic Geologists Graduate Student Fellowship. Portions of this work were performed at the Advanced Instrumentation Laboratory, University of Alaska Fairbanks.

Thanks to all those who have helped me with this thesis, whether directly or merely by remaining in my life throughout the process. It's been a long road, eh. Thanks to my family for putting up with my decision to move from Central New York to Fairbanks; thanks for not questioning me—especially because I never had answers. Thanks for everything—even though you all still have no idea what this thesis is about.

Thanks to the other grad students, particularly the other Rainerites; no one else understands. Thanks to Sarah & Kyle Heinchon for being the most generous folks I know, and for teaching me so many random things!

Thanks to my first Fairbanks roommate, Colin, for pretty much explaining everything to me: cars, credit cards, cooking, etc. You didn't know what you were in for with a 21-year old from New York. Thanks to my 'final' roommate, Katy, and her boyfriend, Andrew. Fort Knox had its ups and (many, many more) downs, but meeting you guys was worth it.

Thanks to my gym friends! This includes Simon Ortega, the first person to show me how to 'use' a barbell. Lifting was certainly my escape from thesis madness.

Thanks to those at DGGS who helped me out. I came to Fairbanks in June of 2012 with a pair of fancy rain boots to trek around the interior—yikes. I've learned a bit since then. Thanks to those in the Mineral Resources section (especially the 2012 field crew, the "rascals"), the Publications ladies, and all of the Administrative ladies, past and present. And of course, a genuine "Thank you" to Larry Freeman, my supervisor and committee member. Thank you for your support and guidance—even after retirement!

Thanks to my other committee members, Paul McCarthy & Ken Severin for the polite encouragement and tough love, respectively. Thanks to Ken and Karen Spaleta in the Advanced Instrumentation Lab. The probe is still my favorite. I wish I got to do more with it!

Lastly, **T H A N K S** to Dr. Rainer Newberry, my advisor, and the greatest educator I've ever had. Life's been weird the past few years, but I wouldn't take back being your student for anything. Thanks for bearing with me all these years; thanks for teaching me; thanks for making me a geologist (because I was just one in name before this). Infinite thanks.

1 INTRODUCTION

1.1 RARE-EARTH ELEMENTS

Rare-earth elements (REE) have been a source of global concern for decades. Though not entirely rare, applications such as use in catalytic converters for automobiles, fluid cracking catalysts in petroleum refining, phosphors for electronic displays, magnets, and rechargeable batteries deem rare-earth production essential (Nieto et al., 2013). The 14 REE, however, are not valued equally. The light-rare-earth elements (LREE), consisting of La to Eu, are more common and typically in less demand. Conversely, the heavy-rare-earth elements (HREE), from Gd to Lu—and also including Y (then referred to as HREE + Y) due to its similar ionic properties—are generally more economic. The significance of REE in modern technology, combined with reliance on foreign imports, has driven numerous exploration endeavors in the United States.

1.2 RARE-EARTH EXPLORATION IN ALASKA

Alaska has several REE occurrences, with the most notable being Bokan Mountain on Prince of Wales Island. REE, Sn, W, U, and base metal exploration in the Ruby batholith (Fig. 1.1), however, has been ongoing since the 1970s (Britton, 2000; Britton, 2003; Szumigala et al., 2004; Freeman et al., 2012). Eventually, beginning in the Livengood quadrangle in 1977, and advancing to the Beaver, Bettles, and Tanana quadrangles in 1978, the now-dissolved U.S. Bureau of Mines (USBM) Alaska Field Operations Center personnel collected stream-sediment samples as part of the National Uranium Resource Evaluation Hydrogeochemical and Stream Sediment Reconnaissance program. During this time, anomalous concentrations of base metals, Sn, W, Cr, REE and U were reported in the Ray Mountains and Kanuti-Hodzana uplands (Smith, 2006). Subsequent resource assessments by the USBM located and detailed bedrock alluvial Sn occurrences (Barker and Foley, 1986), bedrock chromite occurrences (Foley and McDermott, 1983), and alluvial REE occurrences (Barker, 1991a; Barker, 1991b).

Alluvial deposits were investigated to identify locations with elevated REE concentrations. Extensive sheets of alluvial deposits are present in drainages in the area, particularly between the Ray Mountains and Fort Hamlin Hills plutons (Fig. 1.2; Barker, 1991a). Barker (1991a) also noted the heavy-mineral concentrates in the Ray River contained a few percent combined monazite and xenotime, with monazite being more abundant. In contrast, concentrates from the No Name Creek contained greater xenotime than monazite. The drainages

represent major known placer occurrences in the region. Since the lowlands may contain additional placers buried beneath Quaternary cover, and because the known gravel deposits vary considerably in their relative (HREE + Y)/LREE ratios, a better understanding of how REE are associated with them is pertinent.

1.3 REGIONAL GEOLOGY

The general geographic area is known as the Kokrine-Hodzana highlands (Wahrhaftig, 1965). The core of this region is the Ruby terrane, a Proterozoic-Paleozoic assemblage of metasedimentary and metavolcanic rocks, including Devonian orthogneiss, typically metamorphosed to greenschist facies (Patton et al., 2009). Mafic and clastic sedimentary rocks with oceanic affinity of the Angayucham-Tozitna terrane and mafic-ultramafic complex rocks of the Koyukuk terrane are allochthonous with the Ruby terrane as klippe and as bounding units to the northwest and southeast (Fig. 1.1). The Koyukuk and Angayucham-Tozitna terranes are apparently intruded by the plutons of the Ruby batholith (Fig. 1.1; Patton et al., 2009).

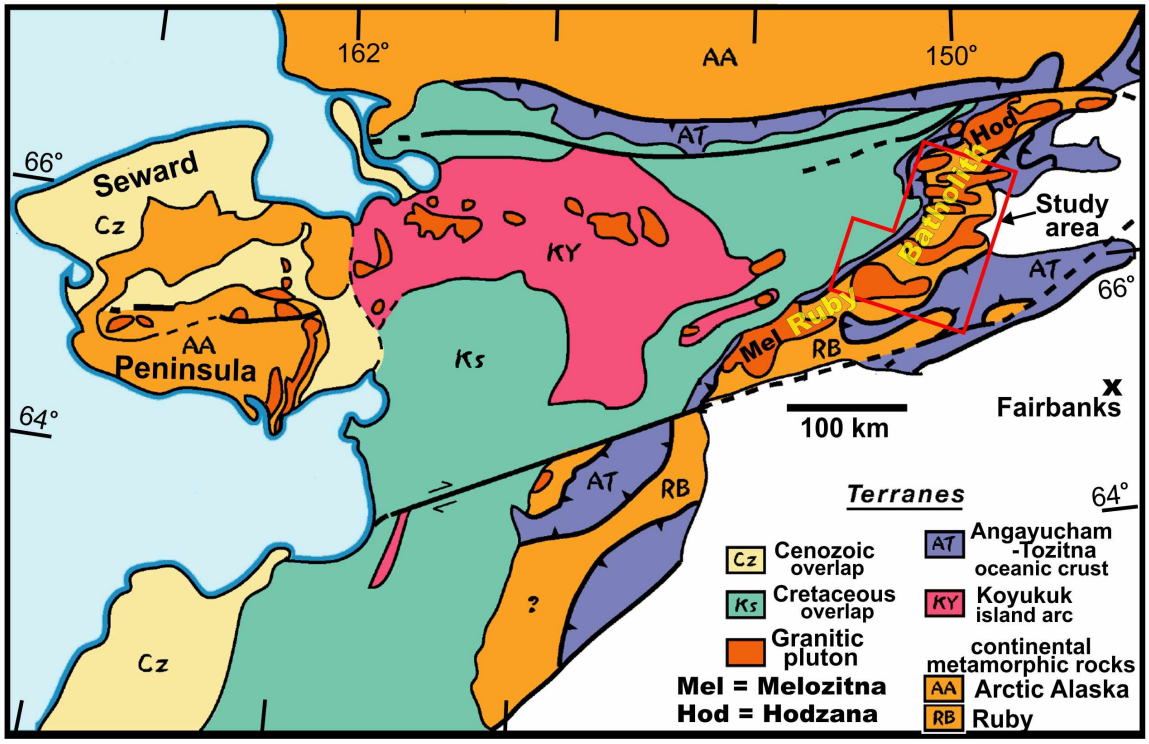

Figure 1.1. Terrane map of central Alaska. Study area is outlined in red. Map modified from DeCarlo (2004).

1.4 THE RUBY BATHOLITH

The rare-earth minerals identified in the gravels are derived from the early Cretaceous granites of the Ruby batholith. The Ruby batholith is a 250-km long belt of ~111 Ma granitic bodies. Variations in initial $^{87}Sr/^{86}Sr$ ratios (0.706 to 0.725, Table 1.1) indicate a heterogeneous source, as could be the case for crustal melting (Puchner, 1984; Blum et al., 1987; Arth et al., 1989). Limited data suggests the individual plutons are characterized by relatively restricted initial $^{87}Sr/^{86}Sr$ ratios (Arth et al., 1989). Only the Sithylemenkat and the western half of the Ray Mountains bodies, however, have sufficiently consistent initial $^{87}Sr/^{86}Sr$ ratios to yield reasonable Rb/Sr isochron ages.

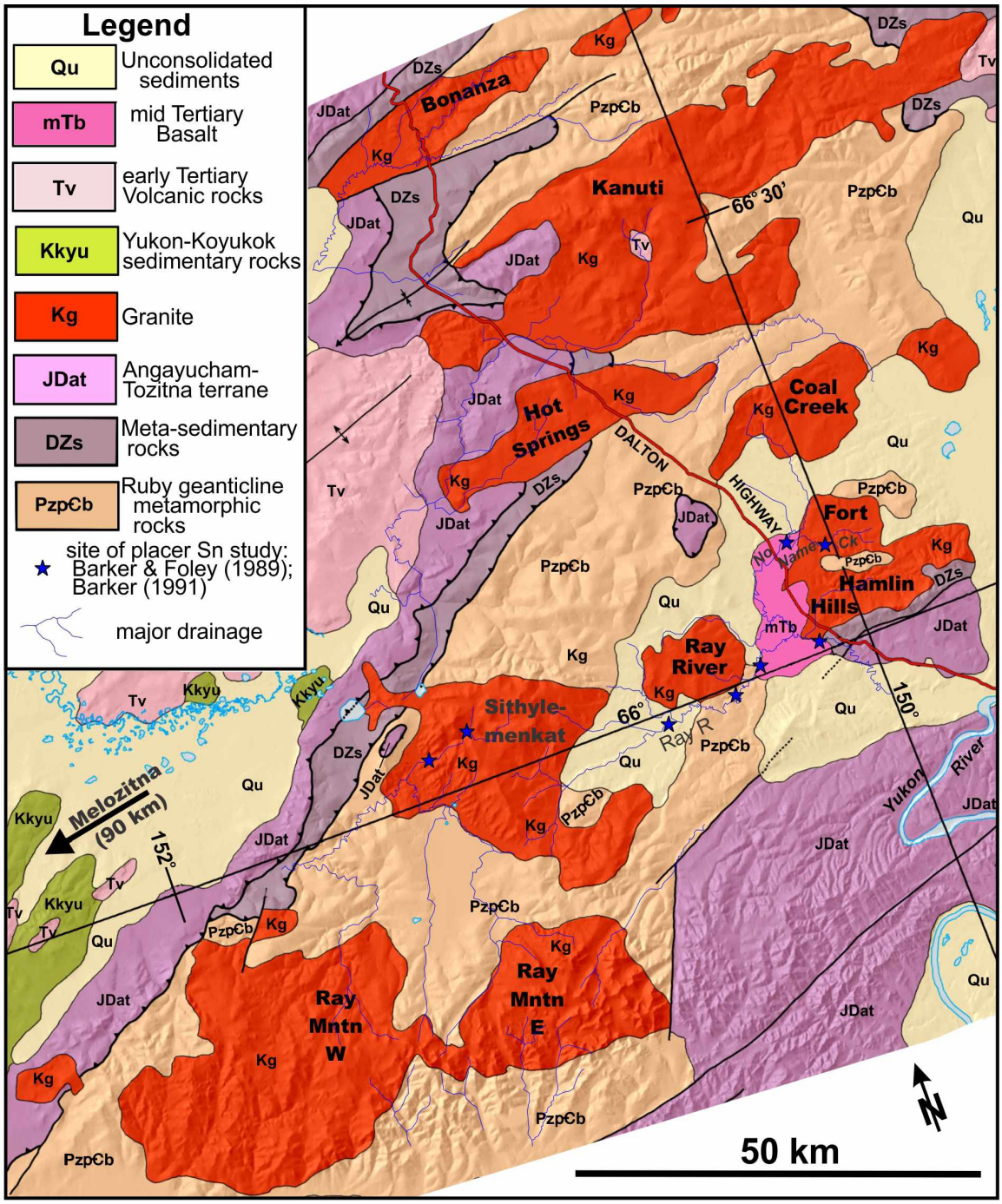

Figure 1.2. Generalized geologic map of the central and southern Ruby geanticline, modified from Till et al. (2006). Pluton names (in bold) are from Brosge et al. (1973), Patton and Miller (1973), and Patton et al. (1987). Blue stars = historical placer studies (Barker and Foley, 1986; Barker, 1991a; Barker, 1991b).

Table 1.1. Calculated[1] initial $^{87}Sr/^{86}Sr$ ratios for Ruby batholith rocks

Pluton	Initial $^{87}Sr/^{86}Sr$	Source
Ray Mountains	0.719 ± 0.0005	Puchner, 1984
Ray Mountains	0.724, 0.719, 0.714, 0.718, 0.714	Arth et al., 1989
Sithylemenkat	0.716, 0.716, 0.716, 0.717	Arth et al., 1989
Hot Springs	0.709, 0.711	Arth et al., 1989
Kanuti	0.707, 0.710, 0.714, 0.706, 0.711, 0.706, 0.709	Arth et al., 1989
Bonanza	0.707	Arth et al., 1989

[1] Puchner (1984) uses an age of 112 Ma; Arth et al. (1989) uses 110 Ma.

Numerous radiometric ages have been generated for the plutons of the Ruby batholith (Table 1.2). K-Ar ages on biotite and hornblende are 96 ± 2 Ma to 113 ± 3 Ma (Puchner, 1984; Miller, 1989). Rb/Sr ages of 111 ± 1 Ma to 112 ± 4 Ma were published by Puchner (1984) and Blum et al. (1987). Patton et al. (1987) reported U-Pb ages of 109 Ma to 112 Ma. The general consensus is that all the various plutons of the Ruby batholith are ~111 Ma (Miller, 1989). The variation in ages is generally interpreted to be the result of different dating techniques with different age-retention temperatures, as well as by possible thermal reheating.

Table 1.2. Radiometric ages for the plutons of the Ruby batholith

Pluton	Dating Technique	Dated Mineral	Preferred Age(s), Ma	Reference
Hot Springs	K/Ar	Biotite	96 ± 2	Miller, 1989
Kanuti	K/Ar	Biotite	98 ± 2, 99 ± 1	Miller, 1989
Sithylemenkat	K/Ar	Biotite	106 ± 3, 106 ± 2	Miller, 1989
Ray Mountains	K/Ar	Biotite	104 ± 3, 107 ± 2, 107 ± 2	Miller, 1989
Ray Mountains	U/Pb	Zircon	109.6 ± ?, 112 ± ?	Patton et al., 1987
Ray Mountains	Rb/Sr	--	110.8 ± 0.1	Puchner, 1984

A mineral can yield a crystallization age or a cooling age. Crystallization age is the time elapsed since the mineral formed, whereas the cooling age marks the time since the mineral passed through its closure (blocking) temperature (Dodson, 1973). The latter is a thermal threshold below which diffusion of parent and daughter isotopes effectively stops. Closure temperatures depend upon the cooling rate, the mineral dated, the mineral's size and, particularly in the case of biotite, its chemical composition. Zircon (U-Pb) has the highest closure temperature (> 900°C; Cherniak and Watson, 2001), and hence generates the oldest age (from a given rock). Hornblende has closure temperatures of 400-600°C (Harrison, 1982; Dahl, 1996),

and muscovite has closure temperatures of 350-425°C (Hodges, 1991; Harrison et al., 2009). Biotite generally has the lowest closure temperatures, 280-345°C (Harrison et al., 1985), and hence generates the youngest ages from a given rock. Such variable—yet systematic—ages are measured in the central Sierra Nevada batholith in eastern California (Fig. 1.3; Stern et al., 1981). Plutonism occurred throughout the mid- to late Cretaceous, and ages from a single body follow the age pattern zircon > hornblende > biotite.

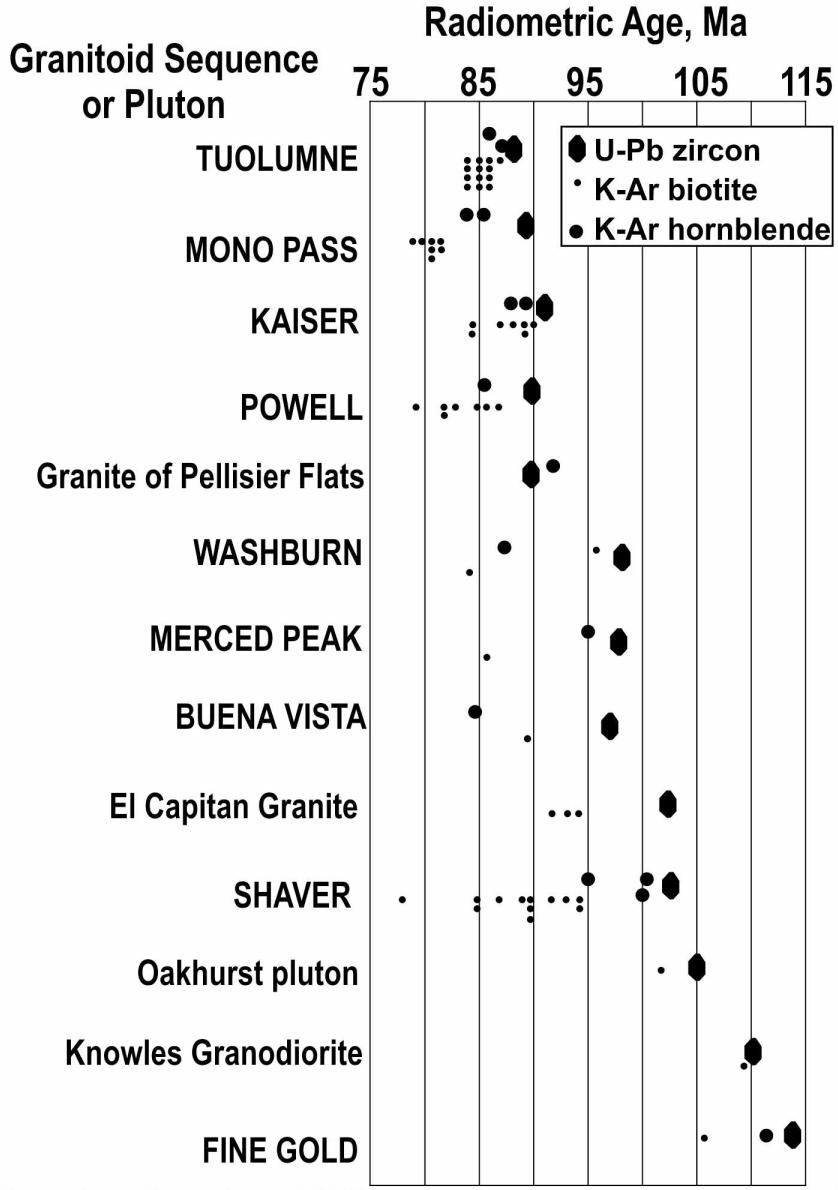

Figure 1.3. Comparison of U-Pb zircon, K-Ar biotite, and K-Ar hornblende ages from plutons of the central Sierra Nevada batholith, California. Modified from Stern et al. (1981).

Zircons may have additional complications. Granites formed by crustal melting typically contain zircons with inherited cores, causing the isotopic ratios to plot off of the concordia curve. The degree of discordance can be interpreted in terms of an inherited, older fraction. Laser ablation of zircons containing inherited cores can yield ages between the older source and the crystallization age.

The Ruby batholith is dominantly coarse-grained, porphyritic biotite-granite with hornblende-biotite granite (and lesser granodiorite) in the northeastern plutons, and biotite-muscovite granite in the southwestern plutons (Miller, 1989). Other rock types are rare in the Ruby batholith; syenite and quartz monzonite occur in the Jim River pluton to the far northeast (outside of the study area).

This study incorporates a large portion of the batholith, ranging from the Bonanza pluton in the northeast, to the Ray Mountains pluton in the southwest (Figure 1.2), and includes limited data for the Melozitna pluton, lying outside of the study area farther southwest. As part of this study, I show that some of the plutons are composite, with distinctly different radiometric ages and compositions within the originally defined pluton.

1.5 TERMINOLOGY

The *Glossary of Geology* defines "batholith" as "A large, generally discordant plutonic body having an aerial extent of 40 mi^2 (100 km^2) or more and no known floor" (Neuendorf et al., 2005). Nothing about this definition specifies the body be contiguous. The archetypical batholith in the United States is the Sierra Nevada batholith, which extends continuously for approximately 600 km and consists predominantly of individual plutons, with small amounts of intervening metamorphic rock. In contrast, perhaps half of the Ruby batholith is plutonic rock (Figs. 1.1, 1.2). Further, by the strict definition, most of the "plutons" of the Ruby batholith are themselves batholiths.

Prior to Arth et al. (1989), workers used terms such as "Ruby Geanticline plutons", "Ruby plutons", and simply "granitic plutons" to describe the collection of plutons. Arth et al., (1989) first used the phrase "Ruby batholith", and (I suspect) for simplicity's sake, subsequent workers adopted the term. In an effort to remain consistent with the literature, I will continue to refer to the group of plutons as the Ruby batholith, though a more appropriate term would be "plutons and batholiths of the Ruby terrane".

1.6 PROJECT BACKGROUND

In 2012, the Alaska Division of Geological & Geophysical Surveys (DGGS) initiated the Ray Mountains project, of which this thesis is a result. The multi-year project, with fieldwork from June to August 2012, and again in August of 2013, is a component of the State's Strategic and Critical Minerals Assessment (SCM) program, a State-funded Capital Improvement Project. The SCM program was established to address the lack of information on the State's SCM resources and to evaluate their potential. Furthermore, the SCM Assessment will assist with the final state-land selection, given the Ray Mountains project lies largely on state-selected lands administered by the U.S. Bureau of Land Management.

1.7 LOCATION, PHYSIOGRAPHY AND ACCESS

The 9000-square km project area (Figure 1.1) begins 200 aerial kilometers northwest of Fairbanks along the Dalton Highway, extending just north of the Yukon River Bridge, and north to Prospect Creek in the foothills of the Brooks Range. The area is east of the Trans-Alaska Pipeline corridor, and continues southwest 120 km into the Ray Mountains. Prior to the construction of the Dalton Highway for the Alyeska Pipeline in 1975, access was achieved either by air or by water via the Yukon River. Since the late 1970s, however, the Ray Mountains area has represented one of the most accessible REE prospects in Alaska.

1.8 RARE-EARTH MINERALOGY

1.8.1 Allanite

Allanite-(Ce) ($CaCe(Al_2Fe^{2+})(Si_2O_7)(SiO_4)O(OH)$) is a member of the epidote group. Allanite features a variety of coupled substitutions, making for a complex crystallographic structure. Notably, Th^{4+} substitutes into the A2 site, which is typically occupied by REE^{3+}, while Ca^{2+} invariably occupies the A1 site (Dollase, 1971). Th^{4+} can enter the structure via several substitutions (Gromet and Silver, 1983; Chesner and Ettlinger, 1989; Gieré et al., 1999; Wood and Ricketts, 2000; Gieré and Sorenson, 2004):

$$Ca^{2+} + Th^{4+} \leftrightarrow 2REE^{3+} \qquad (1)$$

$$Th^{4+} + 2Fe^{2+} \leftrightarrow Ca^{2+} + 2Fe^{3+} \quad (2)$$

$$Th^{4+} + Fe^{2+} \leftrightarrow REE^{3+} + Al^{3+} \quad (3)$$

$$Th^{4+} + Fe^{2+} \leftrightarrow REE^{3+} + Fe^{3+} \quad (4)$$

Further, ferrous iron is commonly substituted into the M1 site, indicating a common ferriallanite component. Fe^{3+} enters allanite with the following coupled substitution (Deere et al., 1986; Hermann, 2002):

$$Ca^{2+} + Fe^{3+} \leftrightarrow REE^{3+} + Fe^{2+} \quad (5)$$

Equation 5 represents the relationship between allanite and epidote.

Mg generally enters the structure via the substitution (Wood and Ricketts, 2000):

$$REE^{3+} + Fe^{2+} + Mg^{2+} \leftrightarrow Ca^{2+} + Al^{3+} + Fe^{2+} \quad (6)$$

Ti^{4+} combines with Fe^{2+} to substitute into the M site via two substitutions (Gieré and Sorensen, 2004):

$$Ti^{4+} + Fe^{2+} \leftrightarrow 2Fe^{3+} \quad (7)$$

$$Ti^{4+} + Fe^{2+} \leftrightarrow 2Al^{3+} \quad (8)$$

1.8.2 Monazite

Monazite-(Ce) ($CePO_4$) is a monoclinic mineral, typically with a squat habit, and often with pleochroic haloes (if found as an inclusion in biotite, as is most common in this study). Monazite preferentially incorporates the LREE (excluding Eu in peraluminous granites), but can also include several wt% ThO_2. Monazite has a solid solution with its isomorphs huttonite ($ThSiO_4$) (Pabst and Hutton, 1951):

$$Th^{4+} + Si^{4+} \leftrightarrow REE^{3+} + P^{5+} \quad (9)$$

and cheralite ($Ca,Th(PO_4)_2$) (Bowie and Horne, 1953):

$$Th^{4+} + Ca^{2+} \leftrightarrow 2REE^{3+} \quad (10)$$

(Cuney and Friedrich, 1987; Burt, 1989; Förster, 1998a; Broska et al., 2000).

1.8.3 Xenotime

Xenotime-(Y) (YPO_4), like monazite, is an orthophosphate, yet xenotime houses the smaller HREE. In thin section, xenotime is very similar to zircon due to its tetragonal symmetry.

Xenotime is common in Ca-poor, peraluminous granites where it incorporates the vast budget of HREE + Y (Förster, 1998b). Xenotime can also host the actinides in a thorite-coffinite (anhydrous) substitution (van Emden et al., 1997; Förster, 1998b):

$$(U,Th)^{4+} + Si^{4+} \leftrightarrow REE^{3+} + P^{5+} \quad (11)$$

Equation 11 is similar to Equation 9, yet thorite ($ThSiO_4$) and coffinite ($USiO_4$) are isomorphs of tetragonal xenotime. U concentrations are generally higher than Th concentrations due to the smaller effective ionic radii of U (Förster, 1998b).

1.9 THESIS OBJECTIVES

This thesis addresses the petrogenesis of the Ruby batholith and the distribution of REE and other trace elements associated with alluvial deposits in the Ray Mountains. My goals are to:

1. Redefine the contacts of the individual plutons.
2. Generate $^{40}Ar/^{39}Ar$ and U-Pb ages for undated plutons, as well as those with anomalous ages.
3. Determine the extent of heterogeneity between the plutons using Sr isotopes.
4. Better define the rock types and mineral assemblages.
5. Chemically define the REE mineralogy using energy dispersive spectroscopy.
6. Decipher the nature and timing of REE mineral formation using trace-element data.
7. Locate gravels with elevated REE.
8. Lastly, tie together characteristics of the Ruby batholith plutons and associated placer deposits.

Providing more thorough constraints on the character of the source materials may lead to the discovery of prospective placer deposits. The ultimate objective of this study is to provide information on the Ruby batholith, and to constrain the extent of anomalous REE and Sn concentrations in the gravels of the Ray Mountains area for further assessment of potential resources.

1.10 METHODOLOGY AND ANALYTICAL TECHNIQUES

1.10.1 Sampling and Sample Preparation

Visibly veined rocks and those with sulfide or weathered sulfide minerals were collected for trace-element analyses and possible thin section examination. Rocks showing little alteration or weathering were collected for whole-rock chemical analyses and possible thin section examination. Fine-grained rock samples were cut into 4-cm disks, polished, and then analyzed directly by X-ray fluorescence (XRF), as described in Bachmann et al. (2013) and Tuzzolino et al. (2014a). All other analyses were performed on crushed and pulverized samples. Eight granite samples (Appendix D), weighing 17 to 21 kg, were crushed to greater than 70% passing 2

mm, and then panned to ~1% of the original mass. The concentrates were then sieved; the less-than-1-mm fraction was processed with a Franz magnetic separator set to 0.3 amps, a side tilt of 18°, and a forward tilt of 25°. All other rock samples were crushed to greater-than-70% passing 2 mm, with a representative 250 g split pulverized to greater-than-85% passing a 0.075 mm screen.

Fine-grained sediments, panned concentrates of sand-rich sediments, and bulk samples (~40L; Appendix G) of sand-gravel material were collected from streams and rivers in the study area. Approximately 2 kg of sand-rich material was panned to approximately 100 g (~5% of the original volume) at collection sites; fine-grained sediment was separately sampled. The fine-grained sediments were sieved to 0.18 mm; the finer fraction was pulverized and then analyzed. The pan-concentrate samples were pulverized to greater-than-0.075 mm and then analyzed.

In Fairbanks, each bulk sand-gravel sample was screened to remove material greater than 1 cm, and then either panned to a concentrate of approximately 150 g, or processed with a Keene Engineering A52 hand sluice and then panned to 150 g of material. The dried concentrates were sieved; the less-than-1-mm fraction was processed with a Franz magnetic separate set to 0.3 amps, a side tilt of 18°, and a forward tilt of 25°. A split of the non-magnetic fraction was pulverized to better-than-85% passing 0.075 mm and was then analyzed.

1.10.2 Commercial Chemical Analyses

ALS Minerals in Vancouver, B.C., performed all analyses described below. Most un- or slightly altered rocks were analyzed for major oxides by fused-disk XRF. (Six samples were analyzed by inductively coupled plasma-atomic emission spectrometry (ICP-AES) with lithium metaborate/lithium tetraborate fusion digestion.) The analysis quality was monitored with standard reference materials. These—and all other materials—were analyzed for major and trace elements by inductively coupled plasma-mass spectrometry (ICP-MS) following four-acid digestion of a pulverized sample split. Pt, Pd, and Au concentrations were determined by 30 g fire assay with an ICP-AES finish. Most samples were also analyzed for trace-element concentrations by ICP-MS following lithium metaborate fusion-acid digestion. Samples with concentrations over detection limits were re-analyzed by pressed-pellet XRF (Sn, Nb, U, W), or four-acid digest followed by ICP-AES (Pb, Zn).

1.10.3 Stream-Sediment Sample Characterization and Elemental Correlations

Elemental concentrations below the detection limit were assigned by ALS a "value" of -1. To eliminate the effects of negative numbers on correlations and to make use of the analyses, I employed a standard procedure. If more than 35 analyses for a given element from either the heavy-mineral concentrates or the stream sediments were below detection limit, then that element was excluded from the correlation coefficient calculations. If fewer than 35 analyses were below detection limit, the -1 was replaced with one-half the value of the lower detection limit. Detection limits are reported in Bachmann et al. (2013). If an element was analyzed employing both four-acid digestion and lithium metaborate fusion digestion, then the latter analysis was used for correlation coefficient calculations. Following these procedures, correlation coefficients were calculated using Microsoft Excel.

1.10.4 Modal Analyses

The official classification for plutonic rocks is the International Union of the Geological Sciences (IUGS) scheme (Le Bas and Streckeisen, 1991) based on modal mineralogy. Accurate identification of modal mineralogy was facilitated by the following procedure. Hand samples were cut and trimmed of weathered surfaces. Each slab was polished to produce a level surface. The slabs were then submerged in concentrated (52%) hydrofluoric acid, followed by immersion within a saturated sodium-cobaltinitrite solution. The resulting reactions caused the surfaces of potassium feldspar to yellow; while the quartz remained grey, and the plagioclase feldspar became either chalky white or altered to a faint yellow-green (Lyons, 1971). The stained slabs were scanned and semi-quantitatively analyzed for percentages of quartz and feldspars (Appendix A) via image processing.

1.10.5 Normative Analyses

Many unofficial classification schemes have been devised for plutonic rocks based on their chemical compositions. I utilized the CIPW normative classification scheme of Streckeisen and Le Maitre (1979), which employs ratios of normative mineral abundances based on the major-oxide analyses (Appendix B).

1.10.6 Electron Probe Microanalysis

Electron probe microanalysis (EPMA) was performed on 22 thin sections and seven grain mounts using the JEOL JXA-8530 Field Emission Electron Probe Microanalyzer at the University of Alaska Fairbanks (UAF) Advanced Instrumentation Laboratory. The voltage was set at 30 keV and the current varied between 100 to 150 nA. Energy dispersive spectroscopy (EDS) was undertaken using the Thermo 7 SDD-EDS System and the analyses were reported in the Thermo Scientific™ NORAN™ System 7 X-Ray Microanalysis System (NSS) software. Count times were 30 to 60 seconds. In most cases, three point-and-shoot analyses were averaged. Check analyses performed on natural, well-characterized, in-house standards generally yielded values within 20% of the accepted values. The results are reported in Chapter 3 and Appendices E and F.

1.10.7 $^{40}Ar/^{39}Ar$ Ages

Four rock samples were submitted to the UAF Geochronology Laboratory. There, the samples were crushed, washed, sieved, and datable muscovite separates were hand-selected. The monitor mineral, MMhb-1 (Samson and Alexander, 1987), with an age of 523.5 Ma (Renne et al., 1994), was used to monitor neutron flux and calculate the irradiation parameter, J. The samples and standards were wrapped in aluminum foil and loaded into aluminum cans of 2.5-cm diameter and 6-cm height. The samples were irradiated in position 8b of the uranium-enriched research reactor at McMaster University in Hamilton, Ontario, Canada, for 150 megawatt-hours.

At the UAF Geochronology Laboratory, the samples were analyzed using the laboratory procedures outlined in Tuzzolino et al. (2014b).

The Ca/K ratio is determined from ^{37}Ar produced from ^{40}Ca and ^{39}Ar produced from ^{39}K, and the Cl/K ratio is determined from ^{38}Ar produced from ^{37}Cl and ^{39}Ar produced from ^{39}K. All ages are reported to the ± 1 sigma level and were calculated using the constants of Renne et al. (2010). The spectrum provides a plateau age if three or more consecutive gas fractions represent at least 50% of the total gas release and are within two standard deviations of each other. All samples show well-defined plateaus (Tuzzolino et al., 2014b).

1.10.8 Zircon U-Pb Ages

Zircons from four rock samples were separated and analyzed by Apatite to Zircon, Inc. Laser ablation-inductively coupled plasma-mass spectrometry (LA-ICP-MS) analyses were performed on a total of 50 zircons per sample with an Agilent 7700x quadrapole mass spectrometer attached to a Resonetics RESOlution M50 Excimer laser. Detailed discussion of the laboratory techniques is provided in Donelick et al. (2005).

The raw data received from A2Z was reviewed and processed, and is available in Tuzzolino et al. (2016). First, the failed and peak-background-corrected analyses were excluded from the age calculations. Next, the analyses for each sample were plotted on concordia plots using Isoplot v. 3.7 (Ludwig, 2008). In two cases, samples 13AT135A and 12RN418A, the datasets yielded poorly defined chords, with mid-Cretaceous lower intercepts and early Paleozoic to late Proterozoic upper intercepts. (The data quality is not sufficient to use the ages so defined, but they do indicate a small amount of contamination from older, inherited zircon.)

To further reduce the data, the relative $^{206}Pb/^{238}U$ age error was calculated using the $^{206}Pb/^{238}U$ age and the quoted error (2σ). All analyses with greater than 10 percent relative error were excluded (Tuzzolino et al., 2016). The excluded data consistently included those samples with anomalously old ages.

Histograms of $^{206}Pb/^{238}U$ ages were constructed to identify age populations well outside the means. For sample 12RN418A, a single, anomalously old age was excluded. The mean error-weighted ages for the remaining $^{206}Pb/^{238}U$ ages were calculated.

Next, the percent deviation from the concordia was calculated. The equation that was used calculates the extent that the measured $^{207}Pb/^{235}U$ deviates from the concordia, assuming the measured $^{206}Pb/^{238}U$ ratio lies on the concordia. In several cases, data that plots increasingly farther from the concordia gives increasingly older ages, again indicating a physical mixing of Pb and U from early Paleozoic to late Proterozoic and from Cretaceous zircon.

Following the elimination of data deviating more than 2 to 3% from the concordia, a mean concordia age was calculated using Isoplot software (Ludwig, 2008). In general, the mean $^{206}Pb/^{238}U$ age and the mean concordia age are indistinguishable (within error), with a smaller error for the concordia age. I prefer the resulting mean concordia age, as it generally has smaller error and fewer inherited components. Detailed tables and figures can be found in Tuzzolino et al. (2016).

1.10.9 Sr Isotopic Ratios

Four samples, consisting of approximately 3 g of pulp remaining from whole-rock analyses, were analyzed at the Pacific Centre for Isotopic and Geochemical Research at the University of British Columbia. The pulps were subjected to standard rock digestion and element concentration procedures outlined in Weis et al. (2006). Following these procedures, $^{87}Sr/^{86}Sr$ ratios were measured using the Thermo Scientific™ Finnigan TRITON Thermal Ionization Mass Spectrometer (TIMS). Replicate and standard analyses indicate analytical uncertainties of $\pm 10^{-5}$, reported to the 2-sigma level. I used these ratios in conjunction with Rb- and Sr-rock concentrations and best age estimates to calculate the initial $^{87}Sr/^{86}Sr$ ratios (Chapter 2).

2 GENERAL GEOLOGY

2.1 INTRODUCTION

The bulk of the Ruby batholith has been traditionally viewed (e.g., Arth et al., 1989; Miller, 1989) as a compositionally and mineralogically uniform set of granitic intrusions. As reviewed in Chapter 1, however, K-Ar age anomalies hint at a more complicated evolution. Further, the tremendous variations in initial $^{87}Sr/^{86}Sr$ isotopes (Table 1.1) seemingly require variable source materials, which ought to be expressed in some manner. Finally, Barker (1991a) showed that heavy-mineral concentrates in the No Name Creek area contrast considerably with those from other locations in the region. Better understanding of the ages, lithologies, and mineralogies of the batholith will further a better understanding of how this enormous volume of magma formed.

Given the poor access to the study area, the physical extent of each major pluton in the central and southern Ruby batholith has been largely inferred based on aerial photographs and limited foot traverses. Pluton outlines given in the most recent geologic maps (e.g., Till et al., 2006; Patton et al., 2009) are essentially unchanged from the original 1:250,000 geologic maps of the 1970s. Aside from reports covering small areas in the batholith (e.g., Barker, 1991a), maps of the batholith at more detailed scales than 1:250,000 are not publically available. As part of the sampling associated with this study, Alaska DGGS personnel made more than 1000 rock stations, collecting rock-type and magnetic susceptibility data (amidst other information). In the winter of 2012-2013, I recognized that the Fort Hamlin Hills pluton (Figure 1.2) contained rocks with very different trace-element characteristics. In particular, samples from the No Name Creek (NNC) area were quite different from the others. Recognizing that the NNC area might actually represent a separate body, in August of 2013, I re-mapped the portion of the NNC body accessible by foot traverse from the Dalton Highway and Alyeska Pipeline Corridor. Similarly, I recognized sub-plutons in the Hot Springs pluton (Figure 1.2). I used the station data from 2012 and 2013 to create revised pluton boundaries (Bachmann et al., 2013; Tuzzolino et al., 2014a).

Based on the revised plutons and pluton boundaries, in this chapter I report on general characteristics of plutons in the batholith: modal compositions, major-element compositions, petrographic characteristics, and magnetic susceptibility. Finally, I employ $^{40}Ar/^{39}Ar$ and U-Pb dating techniques to better constrain ages in the batholith. Based on these various tools, I

recognize (a) several sub-plutons exist and (b) the batholith cannot be described by a single age, but rather contains portions with measurably different ages.

2.2 Revised Pluton Outlines

As an example of the information used in creating revised pluton outlines, Figure 2.1 shows the existing geologic map (Figure 2.1a) and my revised map of the Fort Hamlin Hills (Figure 2.1b). I used the NNC 2013 foot traverse data (Tuzzolino et al., 2014a), in conjunction with the 2012 site data (Bachmann et al., 2013) and appropriate 1:63,360 aeromagnetic maps (U.S. Geological Survey, 1973; Decker and Dillon, 1982). I used the aeromagnetic maps because magnetic resistivity data (see ahead) shows that granitic bodies in the region south of the Coal Creek pluton have very low magnetic susceptibilities; in contrast, the surrounding metamorphic rocks and basalt have generally high magnetic susceptibilities.

The existing geologic map (Figure 2.1a) shows a single pluton with a small septum of metamorphic rocks in the center. My revised map (Figure 2.1b) shows a continuous body of metamorphic rock that separates the now smaller Fort Hamlin Hills pluton from the newly designated No Name Creek (NNC) pluton. The existing map shows an L-shaped pluton; my map shows a small, nearly circular NNC pluton, and a more dike-shaped Fort Hamlin Hills pluton.

2.3 Magnetic Susceptibility

Magnetic susceptibility measurements were made in the field with a minimum of five measurements using a model KT-6 Kappameter. Magnetite and monoclinic pyrrhotite are the two most common minerals with significant magnetism. In pyrrhotite-absent rocks, the magnetism is mostly due to the amount of magnetite present. Magnetic susceptibility (MS) is a measure of a rock's magnetism, and is thus primarily related to the abundance of magnetite within the rock. Chemical alteration of the rock can cause magnetite formation (observed in the chlorite greisen of the Sithylemenkat pluton, see ahead) or magnetite destruction (especially in weathered rocks). Consequently, I have removed MS values from altered rocks from the original set of approximately 1000 measurements made during the summers of 2012 and 2013 (Appendix C).

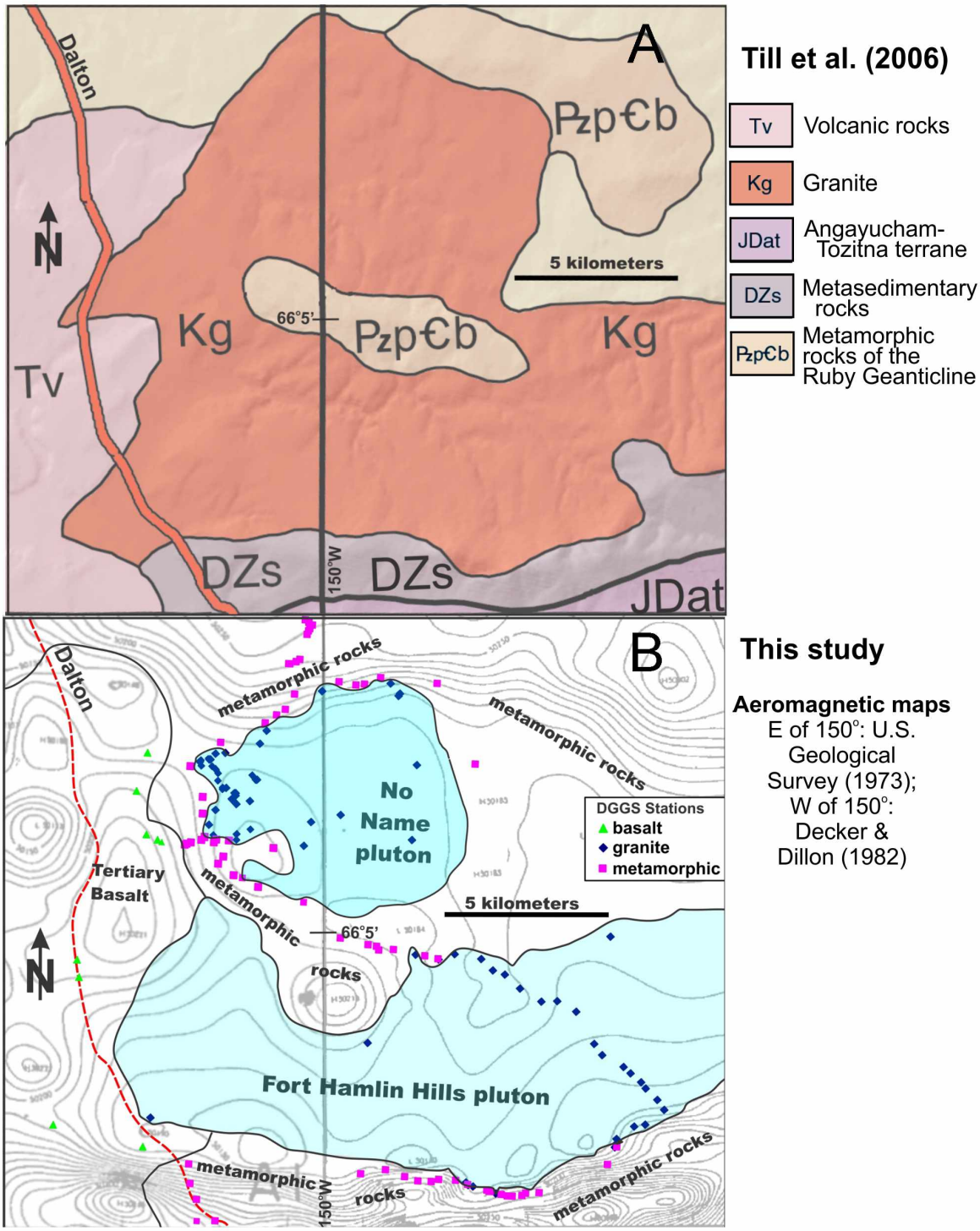

Figure 2.1. Existing (A) and revised (B) bedrock geologic maps of the Fort Hamlin Hills pluton. Triangles, squares, and diamonds on the lower map indicate stations where bedrock was identified and recorded. In general, Tertiary basalt underlies the metamorphic rocks (the more magnetic regions); the less magnetic regions are underlain by granite. Data from Bachmann et al. (2013) and Tuzzolino et al. (2014a).

I have organized MS measurements for unaltered rocks from the Ruby batholith area into three groups: (a) plutons in the southwestern two-thirds of the batholith, (b) plutons in the northeastern one-third of the batholith (including the Hot Springs pluton), and (c) metamorphic rocks surrounding the batholith (Figure 2.2). In addition, a small number of measurements were made on the Tertiary basalt near NNC (Figure 2.1) with values of 0.9×10^{-3} to 2.5×10^{-3} SI. Plutonic rocks from the southern part of the batholith have uniformly low MS (usually $< 0.06 \times 10^{-3}$ SI). Meanwhile, plutonic rocks from the northern part are variable, but generally are more magnetic; the data show three or four different mean values (Figure 2.2b).

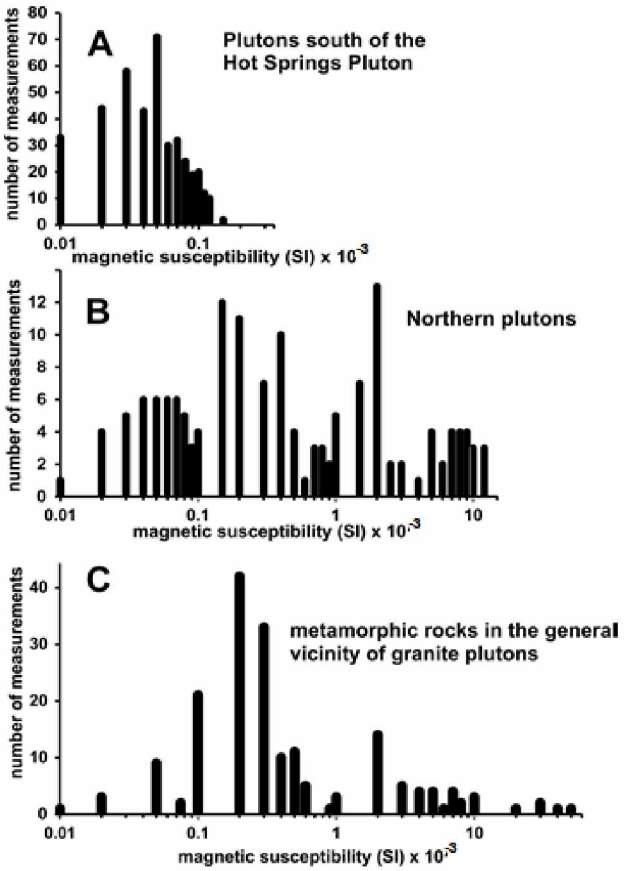

Figure 2.2. Histograms of magnetic susceptibility for unaltered granitic and metamorphic rocks from the central and southern Ruby batholith area. A) Refers to pluton south of the Hot Springs pluton; B) refers to the northern plutons, including the Hot Springs pluton; C) refers to the metamorphic rocks proximal to the plutons.

Metamorphic rocks show the greatest variability, with values ranging from 0.01×10^{-3} to 50×10^{-3} SI (Figure 2.2c). The histogram can be interpreted as two main modes, one at approximately 0.2×10^{-3} SI and the other at 2×10^{-3} SI. The former value largely represents the magnetite-poor metasedimentary rocks of the Ruby metamorphic assemblage (Figure 1.2); the latter represents data from the Angayucham-Tozitna mafic-ultramafic terrane (Figure 1.2).

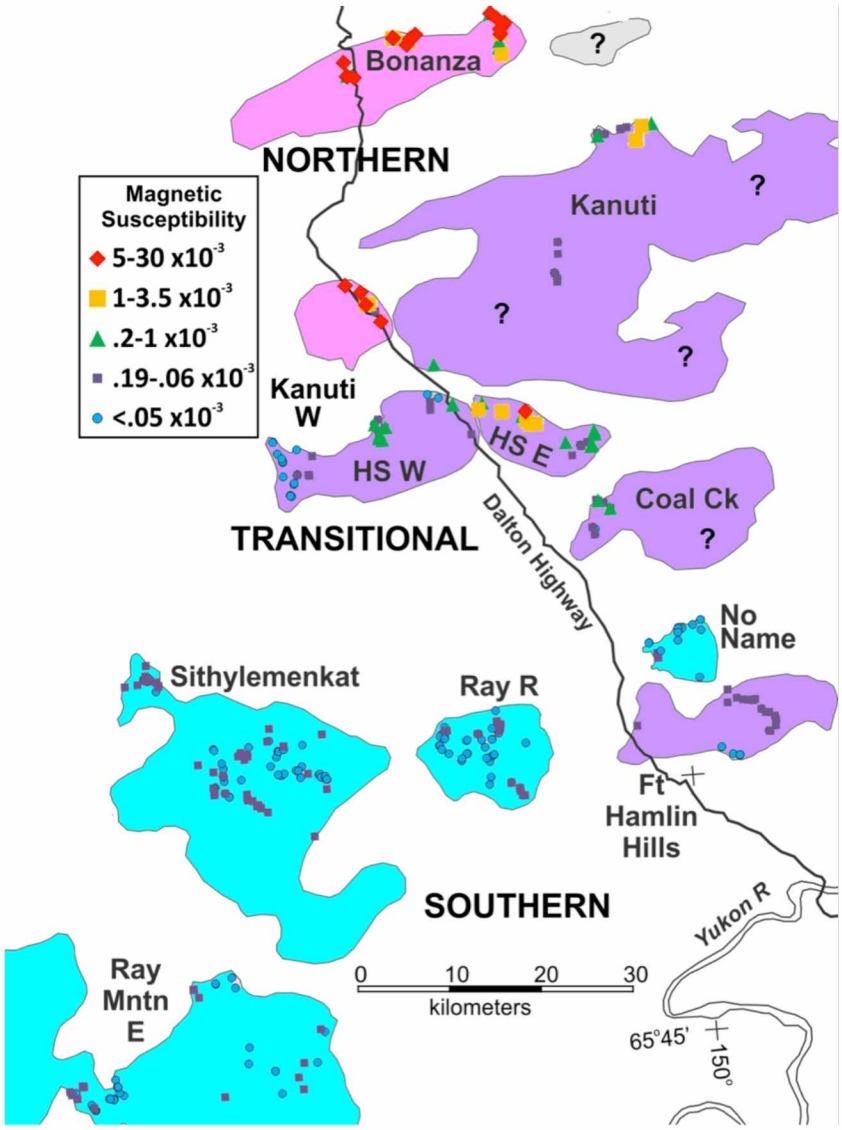

Figure 2.3. Magnetic susceptibility (MS) values from unaltered plutonic rocks from the central and southern Ruby batholith. Each symbol represents the average value measured at a single station. Plutons are color-coded according to MS and geography: pink represents plutons with relatively high MS values and are hereafter characterized as "northern" plutons, purple is for those plutons with moderate MS values and are referred to as "transitional", and blue is for plutons with low MS values and are referred to as "southern".

Individual sample points show generally consistent MS values for the individual plutons but variability among the plutons (Figure 2.3). I have loosely divided the plutons into three groups. The Bonanza pluton and the Kanuti West lobe, hereafter both defined as "northern-group" plutons, have the highest magnetic susceptibilities. The Bonanza pluton is the most consistently magnetic body, with all MS values greater than $0.25x10^{-3}$ SI (Table 2.1, Figure 2.3). On the other hand, the Kanuti pluton is distinctly composite, with a strongly magnetic western portion (hence why it is grouped with the Bonanza pluton), a strongly non-magnetic central portion, and a moderately magnetic northeastern portion (Figure 2.3). The "southern-group" plutons—the NNC, Ray River, Sithylemenkat and Ray Mountains East plutons—have uniformly low MS values of $0.01x10^{-3}$ to $0.19x10^{-3}$ SI (Table 2.1). Of these, the NNC pluton stands out with the lowest average MS and the lowest range in MS values (Table 2.1). The remaining plutons and lobes are considered "transitional-group" plutons. The transitional Hot Springs pluton is best treated as two different bodies. The western half (which also has a younger age, see ahead) is less magnetic, and most MS values are less than $0.2x10^{-3}$ SI. MS values for the eastern portion are all greater than $0.11x10^{-3}$ SI, with a maximum value ($9x10^{-3}$ SI) twenty times as great as the maximum value for the western part (Table 2.1).

Table 2.1. Average magnetic susceptibility values for Ruby batholith samples

Pluton	Average MS	MS Range	*n*
Bonanza	6.7	0.25-9	28
Kanuti West	4.6	1-9	7
Hot Springs E	1.2	0.11-9	29
Kanuti NE	0.3	0.03-2	14
Hot Springs W	0.14	0.02-.55	44
Coal Creek	0.11	0.01-0.4	16
Ft Hamlin Hills	0.07	0.01-0.12	33
Sithylemenkat	0.05	0.01-.19	131
Ray Mntns E	0.05	0.01-.12	86
Ray River	0.05	0.01-.12	66
Kanuti Central	0.05	0.01-.13	21
No Name Creek	0.038	0.01-0.1	35

Note: "MS " = Magnetic susceptibility. All values are x 10^{-3} SI.

2.4 RADIOMETRIC DATING

Previous workers (e.g., Arth et al., 1989) have treated the Ruby batholith as a body of uniform-110 Ma age. Few K-Ar biotite ages from the Kanuti and Hot Springs West plutons, however, are significantly younger (96 to 98 Ma) than 110 Ma. The biotite ages were previously assumed to represent thermal resetting and were ignored (Arth et al., 1989). To further investigate these age anomalies, I undertook radiometric dating of several plutons, employing both $^{40}Ar/^{39}Ar$ on muscovite separates (Table 2.2) and U-Pb on zircons (Table 2.3). The analytical techniques and data are more thoroughly presented and discussed in Tuzzolino et al. (2014b) and Tuzzolino et al. (2016).

Table 2.2. $^{40}Ar/^{39}Ar$ plateau ages for samples from the Ruby batholith

Sample	Pluton	Dated Material	Plateau Age (± 2 sigma)
12LF247A	Kanuti Northeast	Muscovite	90.0 ± 1 Ma
13LF416A	No Name Creek	Muscovite	105.6 ± 1.2 Ma
12LF322A	Hot Springs East	Muscovite	106.8 ± 1.6 Ma
12RN352C	Ray River	Muscovite	108.0 ± 1.2 Ma

Table 2.3. U-Pb ages for samples from the Ruby batholith

Sample	Pluton	Mean Error-Weighted $^{206}Pb/^{238}U$ Age ± 2σ	Mean Concordia Age ± 2σ
12RN364A	Hot Springs West	98.6 ± 1.0 Ma	98.0 ± 0.9 Ma
13AT135A	No Name Creek	107.0 ± 1.2 Ma	106.6 ± 1.3 Ma
12RN418A	Ray River	111.0 ± 1.3 Ma	110.6 ± 1.1 Ma
12CW033A	Kanuti Central	111.7 ± 1.0 Ma	111.6 ± 1.0 Ma

The complete set of radiometric ages for the plutons of the study area, plus an additional pluton, Melozitna (lying immediately southwest), and a pluton to the northeast, Hodzana, is shown geographically in Figure 2.4. I chose to include these two additional plutons to clarify the lack of a systematic NE-SW pattern of ages. The most reliable methods for determining magmatic ages (U-Pb and Rb/Sr) yield an average age of 111 ± 1 Ma for all but two of the plutons. The U-Pb age for the NNC pluton (Table 2.3, Figure 2.4) is close to—but roughly 4-Ma younger than—the majority of the magmatic ages. More strikingly, the U-Pb age for the Hot Springs West pluton (Table 2.3, Figure 2.4) is 12-Ma younger than the majority of the U-Pb ages. Further, this anomalously young U-Pb age is near the site of a similarly K-Ar -aged biotite (Figure 2.5).

K-Ar biotite ages of approximately 100 Ma in the Kanuti pluton—to the east of Hot Springs West (Figure 2.5)—suggest that the Kanuti pluton is a composite of several magmatic ages. Similarly, the yet younger (90 Ma) $^{40}Ar/^{39}Ar$ age for magmatic muscovite from a garnet-muscovite-biotite-bearing granite in the northeastern Kanuti pluton (Figure 2.5) suggests a later magmatic event.

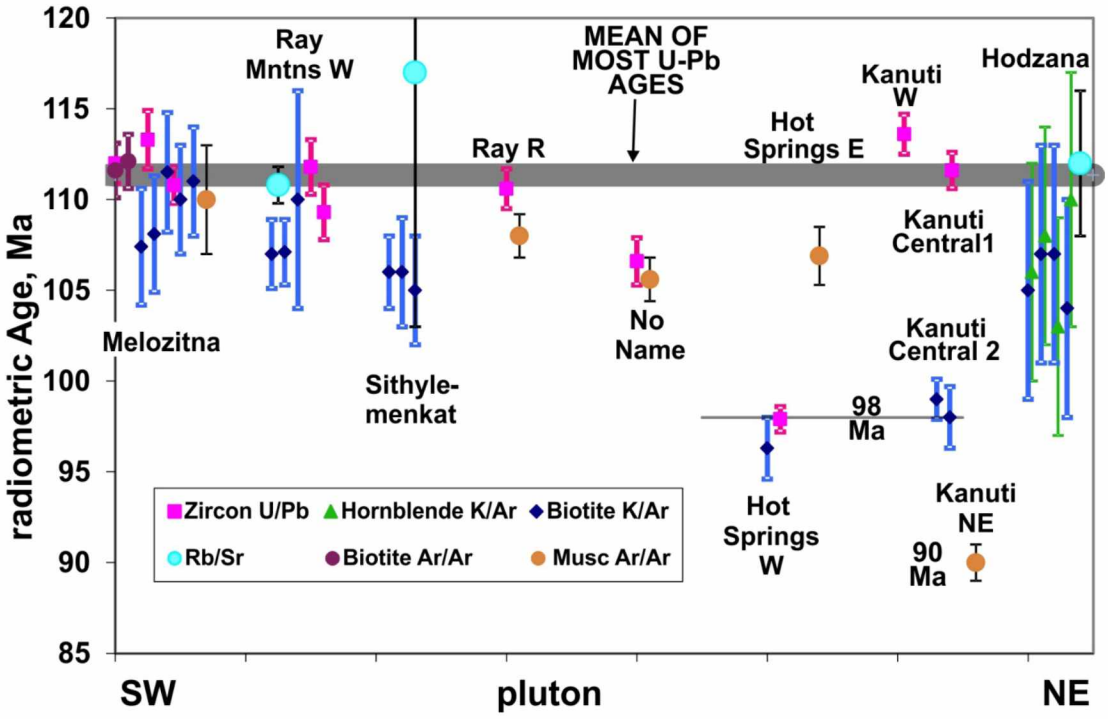

Figure 2.4. Radiometric age summary for plutons of the study area and immediately to the NE (Hodzana) and SW (Melozitna). Two-sigma uncertainties are shown where given in the original data; otherwise, the published uncertainties are depicted. Ages are taken from Brosge and Reiser (1964), Silberman et al. (1979), Dillon et al. (1985), Patton et al. (1987), Blum et al. (1987), Miller (1989), McClellan (writ. comm.), this study, and unpublished DGGS sources.

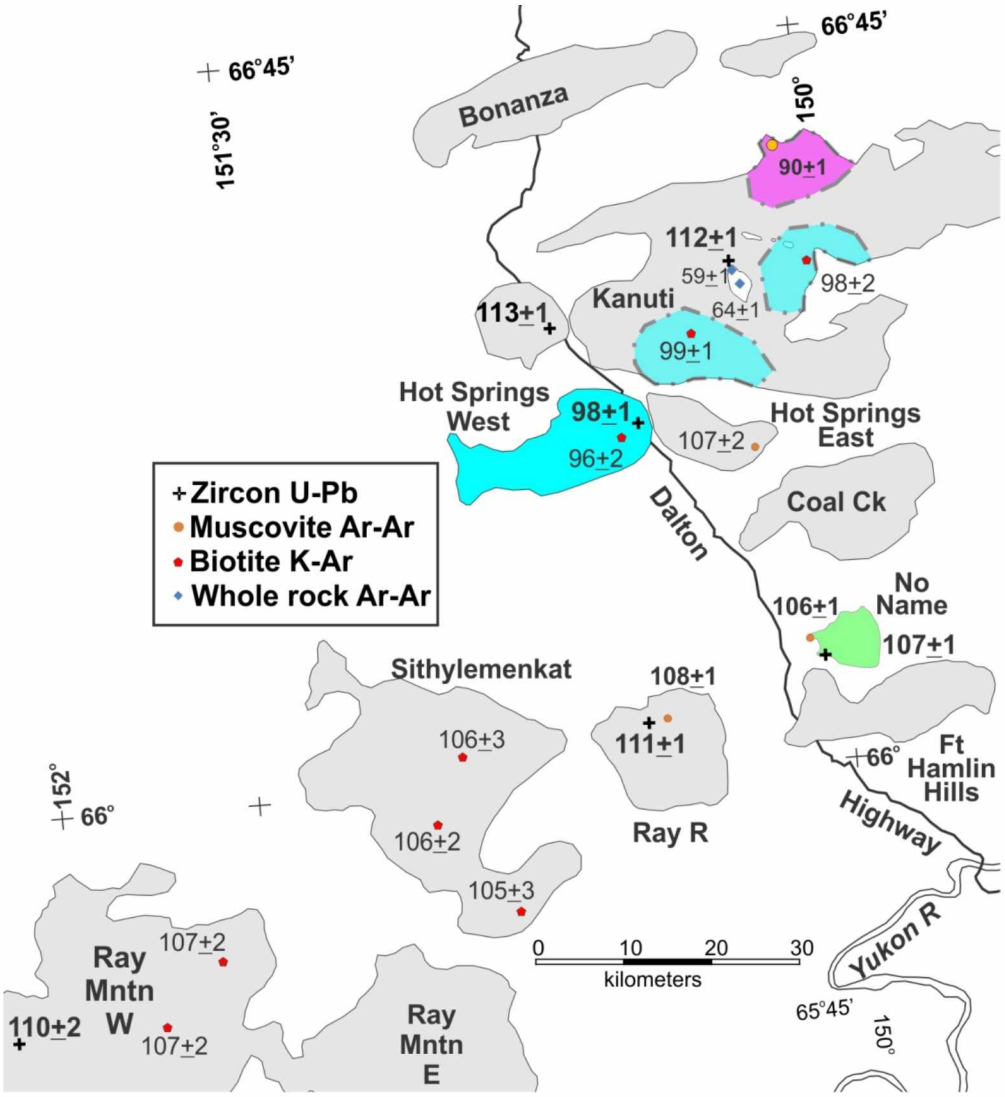

Figure 2.5. Map showing distribution of radiometric ages in the study area, with different symbols for different age techniques. Plutons and areas within plutons with anomalously young ages are shown in color. The 59 to 64 Ma whole-rock ages are for a small, early Tertiary volcanic field either on top of or faulted into the Kanuti pluton. Ages are from sources listed with Figure 2.4.

In sum, it appears that the majority of the Ruby batholith (Figure 2.4, Figure 2.5) was emplaced at 111 ± 1 Ma. Lacking radiometric ages, it cannot be stated with certainty that the Fort Hamlin Hills, Coal Creek and Bonanza plutons are also 111 ± 1 Ma, but the absence of plutons with significantly different ages in the immediate vicinity of the Coal Creek and Fort Hamlin Hills plutons suggests they are of the same age. Given the abundance of evidence for older ages in the Hodzana pluton (just north of the Bonanza pluton, Figure 2.4), a magmatic age of approximately 111 Ma seems likely for the Bonanza pluton as well.

2.5 INITIAL $^{87}Sr/^{86}Sr$ RATIOS

Radiogenic ^{87}Sr is generated as a result of the β-decay of ^{87}Rb. Minerals formed from a single, homogeneous melt contain the same initial $^{87}Sr/^{86}Sr$ ratio (SIR); minerals crystallized from different or inhomogeneous melts will likely have different SIR. Chappell and White (2001) noted that S-type granites invariably have higher SIR than I-type granites, and in the Lachlan fold belt of Australia, S-type granites have SIR of 0.709-0.720, and I-type granites have SIR of 0.704-0.712. I had $^{87}Sr/^{86}Sr$ ratios measured for four granite samples (see Chapter 1) from the Ruby batholith and used these in conjunction with Rb- and Sr-rock concentrations and best-age estimates (Table 2.2, Table 2.3) to calculate SIR values (Table 2.4). In addition, I recalculated the SIR for 17 samples presented by Arth et al. (1989) using my revised age estimates (Figure 2.5) and plotted all the data on Figure 2.6.

Table 2.4. Calculated initial $^{87}Sr/^{86}Sr$ ratios for four samples from the Ruby batholith

Sample	Pluton	Age	Rb (ppm)	Sr (ppm)	$^{87}Rb/^{86}Sr$ (calc)	$^{87}Sr/^{86}Sr$ (measured)	$^{87}Sr/^{86}Sr_i$ (calc)
12RN228A	Coal Creek	111	325	84	11.25	0.73182	0.714
12RN460A	Ft Hamlin Hills	111	296	118	7.25	0.72749	0.716
12RN429A	Ray River	111	407	144	8.22	0.72976	0.717
12LF304A	No Name Creek	107	577	41	41.35	0.78944	0.727

Note: "$^{87}Sr/^{86}Sr_i$" = initial $^{87}Sr/^{86}Sr$ ratio (SIR); "calc" = calculated.

The plutons of the Ruby batholith have SIR of 0.706 to 0.727, with values generally increasing from northeast to southwest (as noted by Arth et al., 1989). I divided the batholith into two groups (Figure 2.6): the northern group has SIR $\leq$ 0.714, and the southern group has SIR $\geq$ 0.714. The line almost perfectly corresponds with breaks in average magnetic susceptibilities for the plutons: plutons below the line have MS $< 0.1 \times 10^{-3}$ SI; while those above (except central Kanuti) have MS $> 0.1 \times 10^{-3}$ SI (Table 2.1).

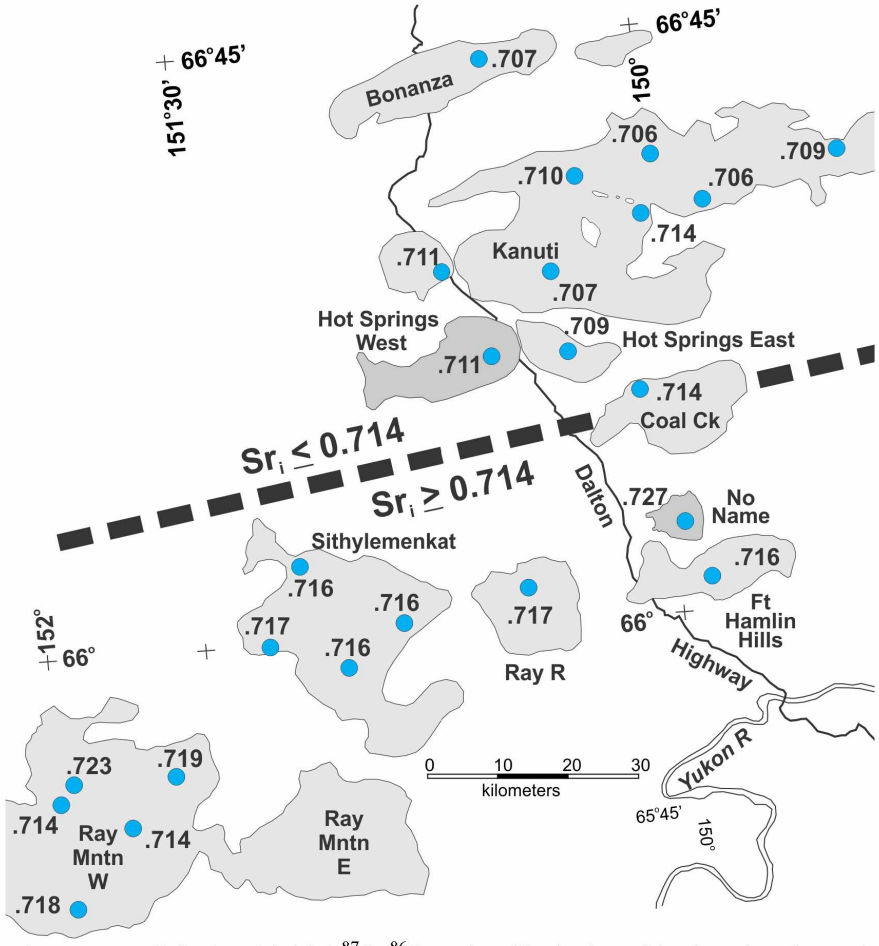

Figure 2.6. Calculated initial $^{87}Sr/^{86}Sr$ ratios (SIR) plotted by location for rocks of the central and southern Ruby batholith. Initial ratios were calculated using present-day $^{87}Sr/^{86}Sr$ ratios and Rb and Sr concentrations for each sample, and the known or suspected magmatic age of each pluton (Table 2.3). Also includes data from Arth et al. (1989) recalculated to current estimated pluton ages. The thick dashed line divides the batholith into regions with high (≥ 0.714) and low (≤ 0.714) $^{87}Sr/^{86}Sr_i$.

The NNC pluton has an anomalously high SIR, marring the trends set by its neighbors. The Sithylemenkat, Kanuti, and Ray Mountains West plutons each contain at least four different sample sites. SIR values for the Sithylemenkat pluton are sufficiently close that a poor Rb/Sr isochron age can be calculated (Figure 2.4); those from the other plutons have widely varying SIR (Figure 2.6). Major differences in SIR for the Kanuti pluton (Figure 2.6) could be related to the several different ages of magmatism (Figure 2.5); hence, potentially different magma sources. The Ray Mountains West pluton, on the other hand, contains SIR from 0.714 to 0.723, yet appears to be of a single age (Figure 2.5). It is either a body with cryptic sub-intrusions or, if a single body of magma, is extremely inhomogeneous with regard to SIR.

As shown in Figure 2.7, the SIR division just north of the NNC pluton is highly asymmetric: north of this partition, SIR decrease considerably—and variably, while to the south, SIR stays at 0.716 ± 0.001 for more than 50 km. The limited variation in SIR between the Fort Hamlin Hills, Ray River and Sithylemenkat plutons is in marked contrast to the highly irregular SIR for the Kanuti (to the north) and Ray Mountains West (to the south) plutons.

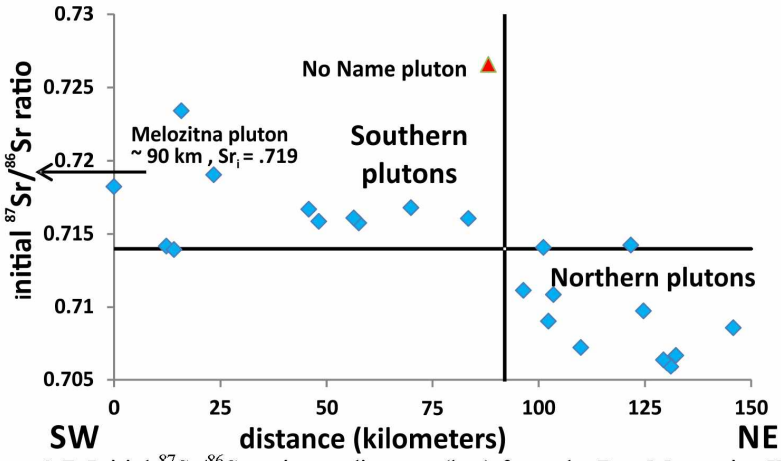

Figure 2.7. Initial $^{87}Sr/^{86}Sr$ ratio vs. distance (km) from the Ray Mountains West pluton for plutonic rocks of the central and southern Ruby batholith. Data are taken from Figure 2.6.

2.6 LITHOLOGY OF THE RUBY BATHOLITH

Apart from variations in grain sizes, rocks of the Ruby batholith are largely indistinguishable to the unaided eye. Modal and normative analyses (Appendices A and B) were executed to improve lithological definitions and to aid in making distinctions among the plutons.

Based on the mineral estimations from potassium feldspar-stained slabs, the bulk of the rocks from the Ruby batholith are monzogranite; that is, they contain sub-equal amounts of quartz, alkali feldspar, and plagioclase feldspar (Figure 2.8). Among the southern plutons, most are monzogranite—unlike the average rock-type for the NNC pluton, which is uniquely syenogranite (Figure 2.8E). The samples from the Hot Springs East pluton plot in a manner similar to those of the southern plutons (i.e., entirely monzogranite), whereas those from Hot Springs West pluton (ca. 98 Ma) plot with a wide range, from tonalite to syenogranite and quartz syenite (Figure 2.8C). The northernmost (Bonanza) pluton is different from the others in that it contains low relative quartz contents and notably, much of the pluton is granodiorite or quartz monzonite (Figure 2.8A). Although the various parts of the Kanuti pluton yield different ages

(Figure 2.5) and magnetic susceptibilities (Figure 2.3), the majority of its rocks are also monzogranite. The spread of samples for the Kanuti pluton, however, is insufficient to adequately characterize the individual lobes of the plutons.

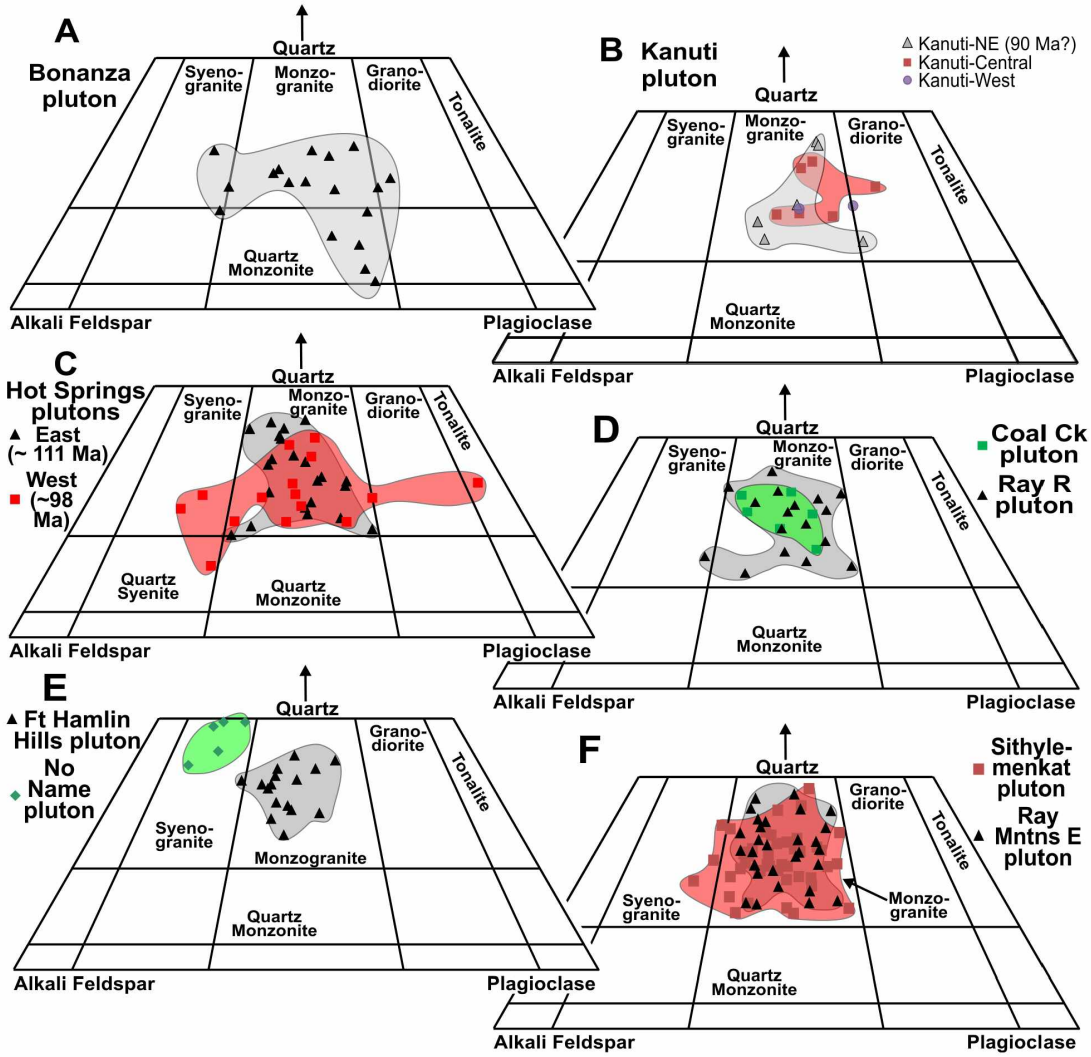

Figure 2.8. Mineral abundance estimations plotted onto standard quartz-alkali feldspar-plagioclase (QAP) diagrams with appropriate rock fields labeled. Portions of plutons have been broken out based on different radiometric ages (Fig. 2.4). The plots are arranged such that the northern plutons are at the top of the figure and the southern plutons are at the bottom. A) Bonanza pluton, B) Kanuti pluton, C) Hot Springs plutons, D) Coal Creek and Ray River plutons, E) Fort Hamlin Hills and No Name plutons, and F) Sithylemenkat and Ray Mountains plutons. Data from this study and is provided in Appendix A. Plots modified from Le Bas and Streckeisen (1991).

As mentioned in Chapter 1, plutonic rocks are officially classified based on their mineral abundances (as in Figure 2.8; Le Bas and Streckeisen, 1991); yet there are several schemes that attempt to classify them based on their chemical composition in a manner similar to the classification of volcanic rocks. One scheme (Figure 2.9) employs the CIPW normative mineral abundances (Appendix B). This scheme (Streckeisen and Le Maitre, 1979) avoids the albitic component considering Na occurs in both plagioclase and alkali feldspar.

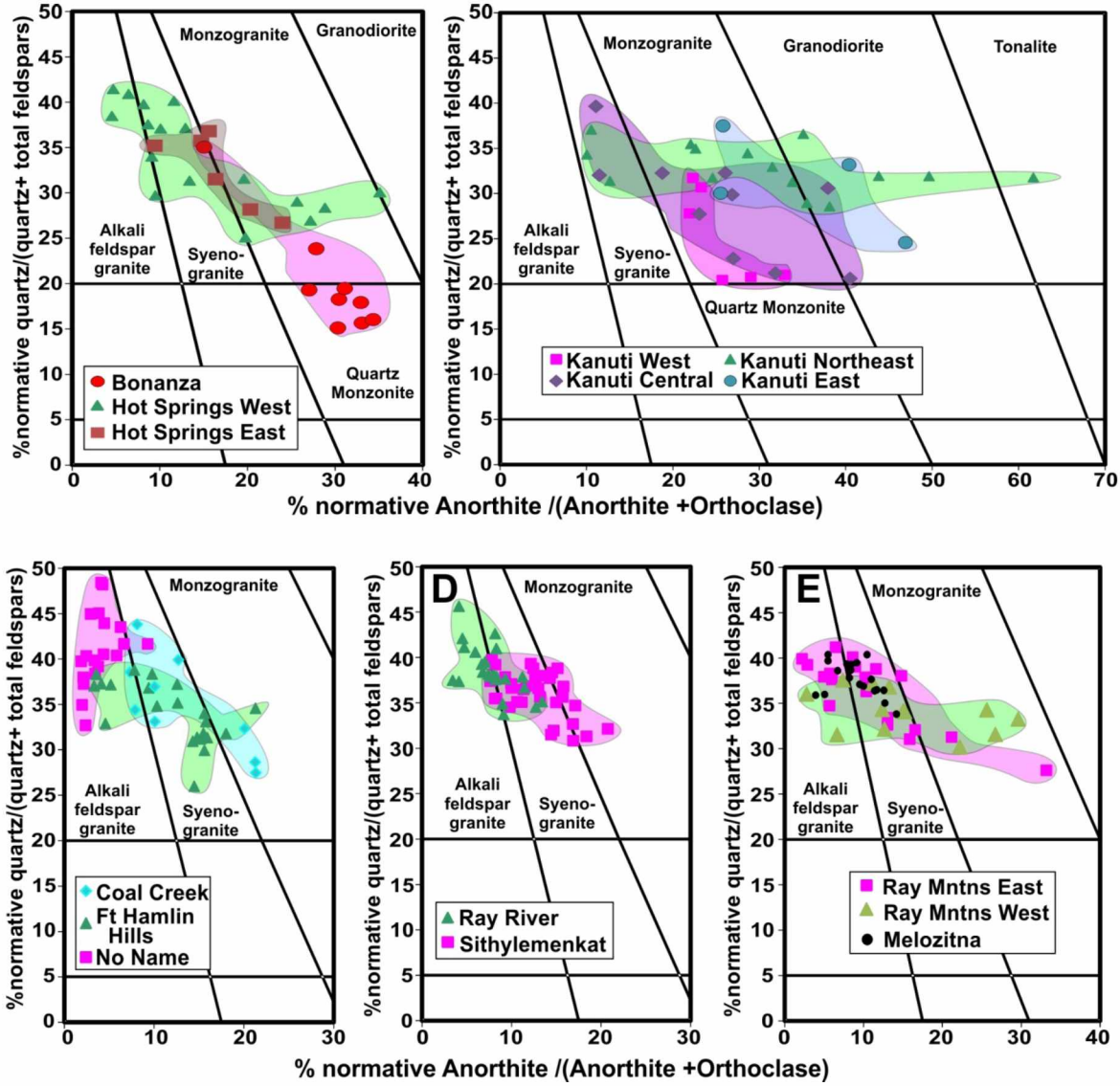

Figure 2.9. CIPW normative mineralogies for rocks of the Ruby batholith plotted on the classification diagram of Streckeisen and Le Maitre (1979). Data is from Clautice (1983), Barker and Foley (1986), Miller (1989), Barker (1991a), Clautice et al. (1993), Solie et al. (1993), and this study (Appendix B).

Normative classification diagrams for the Ruby batholith samples (Figure 2.9) yield somewhat different rock types than the modal analyses of the stained slabs (Table 2.5), but the general patterns are similar. For example, the NNC pluton is exclusively syenogranite based on the stained slab analyses, yet exclusively alkali feldspar granite based on the chemical compositions. Even so, there are important differences to note. Stained slabs yielded monzogranite as the average and typical rock type for all the plutonic rocks (except those from NNC), but the normative scheme identified plutons north of Coal Creek as (on average) monzogranite, but identified the Coal Creek pluton itself and the others farther south as (on average) syenogranite (Figure 2.9, Table 2.5).

Table 2.5. Rock types determined by stained slab mineral estimates compared to CIPW normative classification scheme

Pluton	Avg Name (Stain Slab)	Modal Range[1]	Avg Name[2] (Norm-Based)	Normative Range[1]
Bonanza	Mzgr	Sygr-Qtz Monz	Mzgr	Sygr-Qtz Monz
Kanuti West	Mzgr	Mzgr	Mzgr	Mzgr only
Kanuti Central	Mzgr	Mzgr-Grd	Mzgr	Sygr-Mzgr-Grd
Kanuti NE	Mzgr	Mzgr	Mzgr	Sygr-Grd-Ton
Kanuti East	*No data*	*No data*	Mzgr/Grd	Mzgr-Grd
Hot Springs W	Mzgr	Qtz Sy-Sygr-Grd-Ton	Mzgr	Afgr-Sygr-Grd
Hot Springs E	Mzgr	Mzgr only	Mzgr/Sygr	Sygr-Mzgr
Coal Creek	Mzgr	Mzgr	Sygr	Sygr-Mzgr
No Name Creek	Sygr	Sygr only	Afgr	Afgr only
Ft Hamlin Hills	Mzgr	Mzgr only	Sygr	Afgr-Sygr-Mzgr
Ray River	Mzgr	Mzgr only	Sygr/Afgr	Afgr-Sygr
Sithylemenkat	Mzgr	Sygr-Mzgr	Sygr	Afgr-Sygr-Mzgr
Ray Mntns E	Mzgr	Mzgr	Sygr	Afgr-Sygr-Mzgr
Ray Mntns W	*No data*	*No data*	Sygr	Afgr-Sygr-Mzgr

[1]Range = range of names given (except where very close to boundary); rock type abbreviations: Afgr = Alkali feldspar granite, Sygr = Syenogranite, Mzgr = Monzogranite, Qtz Sy = Quartz syenite, Qtz Monz = Quartz monzonite, Grd = Granodiorite, Ton = Tonalite.
[2]Two names are given where the average falls on the boundary between two rock types.

Finally, significant compositional differences are present for the plutons that I have sub-divided. The NNC pluton is considerably different from the Fort Hamlin Hills pluton (Figs. 2.8, 2.9; Table 2.4), despite being historically mapped as a unified body. Similarly, the Hot Springs West pluton has both a much wider range in compositions than its eastern neighbor (Figs. 2.8, 2.9; Table 2.5), and is also (on average) less felsic. Additionally, based on the chemical compositions, the eastern and northeastern Kanuti plutons similarly both show a greater range in rock types (Fig. 2.9) and are (on average) less felsic than the western and central parts.

2.7 OTHER MAJOR-ELEMENT CHARACTERISTICS OF THE RUBY BATHOLITH

The major-element analyses also allow for other comparisons among the plutonic rocks. Chappell and White (1974, 2001) introduced and extensively developed the concept of (melted) sediment-derived (S-type) and igneous-derived (I-type) granites, and provided compositional criteria for distinguishing between types. Figure 2.10 shows K_2O vs. Na_2O data for Ruby batholith plutonic rocks with the dividing line presented in Chappell and White (2001). The samples show three general types of behavior. The geographically northernmost plutons, including some northern and transitional plutons—Bonanza, Kanuti Central, Kanuti East and Kanuti Northeast—plot largely in the high-Na (I-type) field (Fig. 2.10A). Plutons a bit farther south, including northern and transitional plutons—Kanuti West, Hot Springs West and Coal Creek—more-or-less straddle the I-S-type boundary (Fig. 2.10A). The southern and few remaining transitional plutons—Hot Springs East, NNC, Fort Hamlin Hill, Ray River, Sithylemenkat, Ray Mountains East, and Ray Mountains West—largely plot below the I-S boundary, in the S-type field, though many samples from the Sithylemenkat pluton plot slightly above it (Fig. 2.10B).

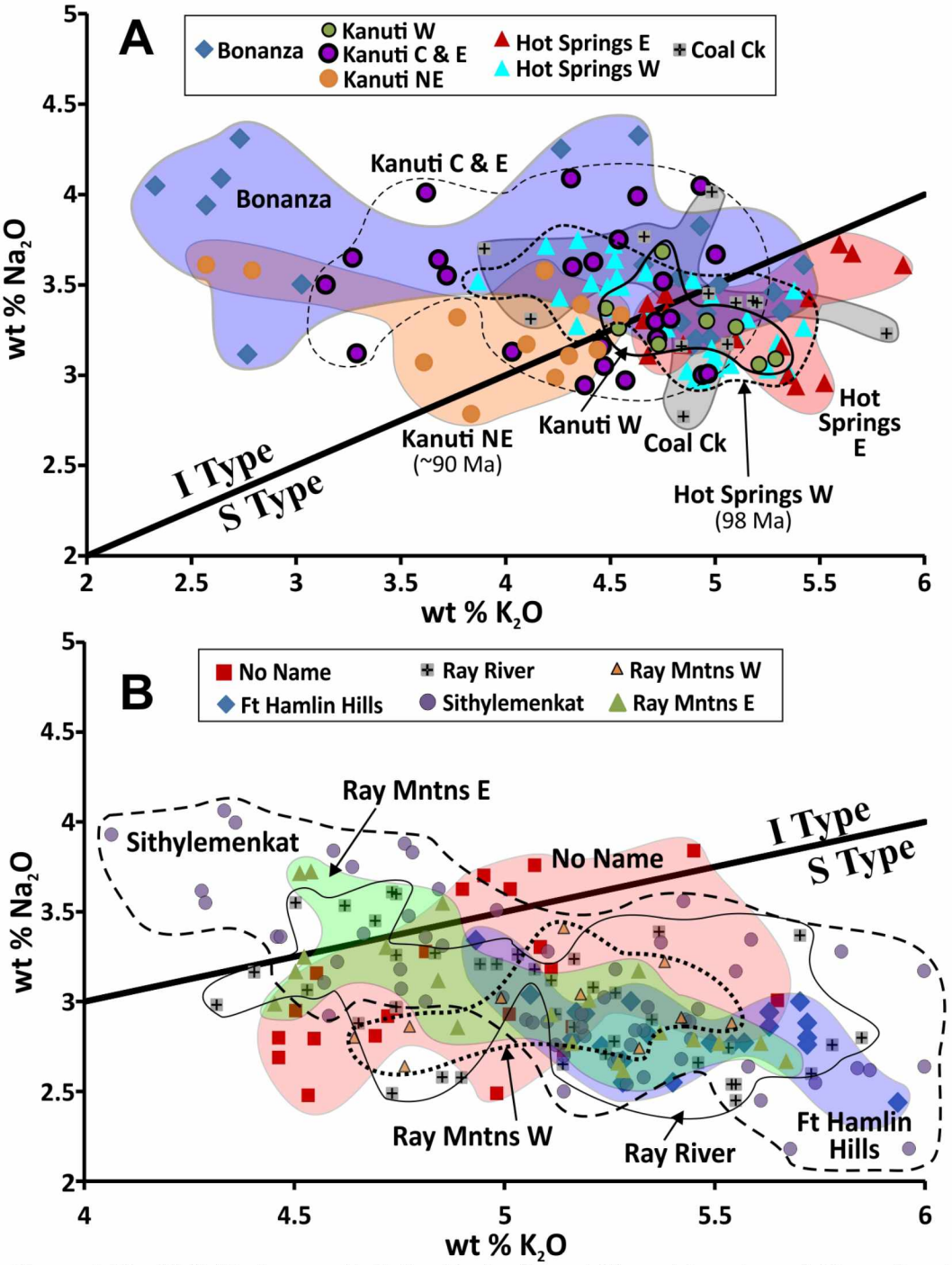

Figure 2.10. Wt% Na_2O vs. wt% K_2O with the 'I-type'-'S-type' boundary of Chappell and White (2001) for samples from the Ruby batholith. A) northern plutons, B) southern plutons. Data is from the same sources as listed with Figure 2.9.

Chappell and White (1974, 2001) similarly use aluminum saturation index (ASI) as a measure of the degree to which a rock contains Al in excess of that needed to crystallize feldspars and apatite. The ASI is defined as:

$$ASI = \frac{Al_2O_3}{CaO - 1.67P + Na_2O + K_2O} \quad (12)$$

with compounds given in molecular weights (Shand, 1943; Zen, 1988). Chappell and White (2001) note that felsic rocks generally increase in ASI with increasing degrees of fractionation—a result of the removal of the low-Al mineral hornblende—suggesting a boundary between I- and S-type granites at ASI = 1.10. I have plotted the ASI for rocks of the Ruby batholith (Fig. 2.11), which shows that the NNC and Melozitna plutons have an average ASI > 1.1, and thus qualifies each for S-type designation. Most of the samples are peraluminous (ASI > 1.0), but not strongly so. Plutons with ASI < 1.05 are restricted to the northern and transitional groups (Bonanza, Kanuti West, Hot Springs West and Coal Creek). Two other transitional plutons, Kanuti Northeast and Hot Springs East, have ASI ≈ 1.1. Plutons of the southern group (excluding NNC and Melozitna) all have ASI of 1.05-1.09 (Fig. 2.11). Of these, the most southern plutons (Ray Mountains East and West) have the highest ASI vales. Meanwhile, the Sithylemenkat pluton has the lowest ASI of the southern group. In short, there is no straightforward correlation between latitude and ASI (Fig. 2.11).

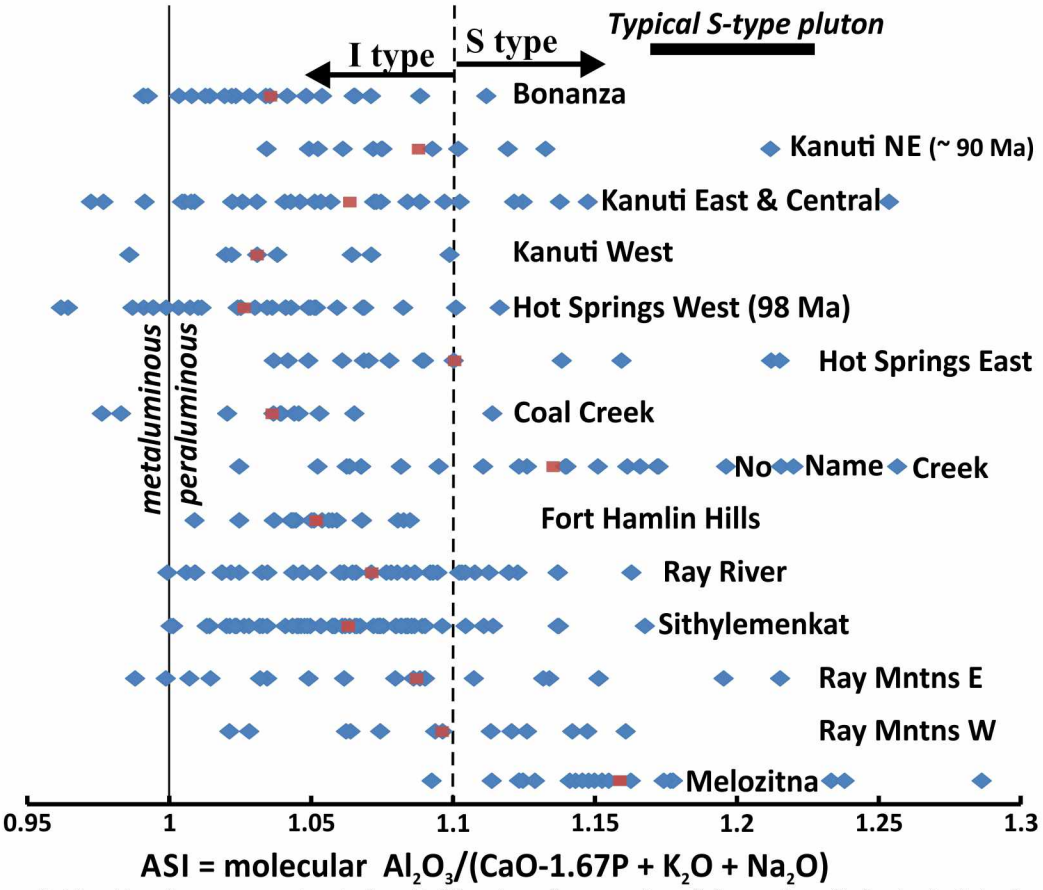

Figure 2.11. Aluminum saturation index (ASI) values for samples of the various Ruby batholith plutons, arranged from N (top) to S (bottom). Blue diamond = single sample, red square = average for the group. I/S type boundary from Chappell and White (1974). Data from sources listed with Figure 2.9.

Another compositional characteristic of importance is the Fe_2O_3/FeO ratio, which is necessary for computing the CIPW normative mineralogy for a rock, and gives insight into the oxidation state of a sample and thus the pluton itself. For my analyses, only total Fe was determined; however, several previous researchers have had both types of Fe measured. Figure 2.12 shows the compiled data for ten different plutons (or lobes of plutons) from the Ruby batholith. With the exceptions of the (younger) Hot Springs West and Kanuti Northeast bodies, the data suggest a gradual increase in Fe_2O_3/FeO from south to north.

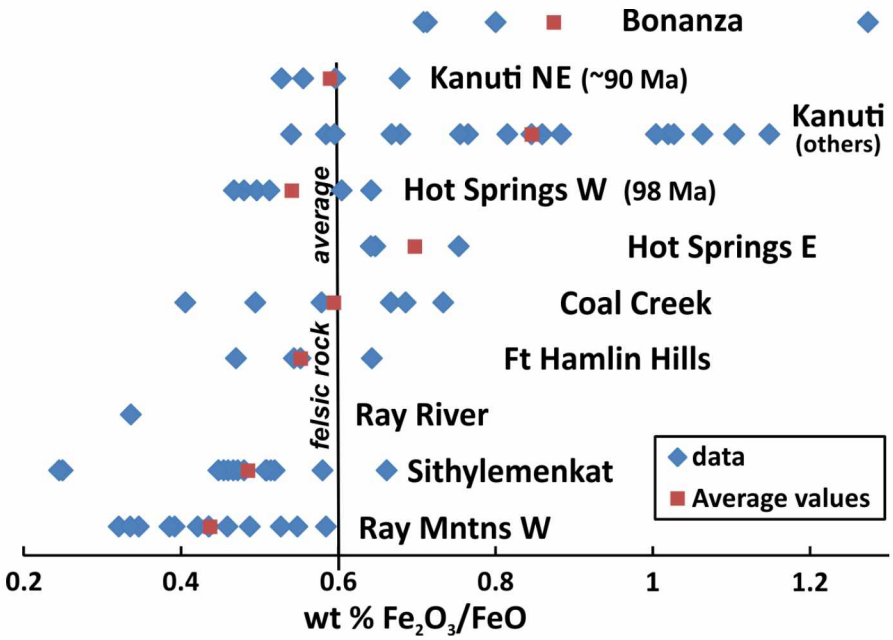

Figure 2.12. Wt% Fe_2O_3/FeO measurements for rocks of the Ruby batholith, arranged from S (bottom) to N (top). The average value for felsic igneous rocks of 0.6 is from El-Hinnawi (2016). Data is from Clautice (1983), Barker and Foley (1986), Miller (1989), Clautice et al. (1993), and Solie et al. (1993).

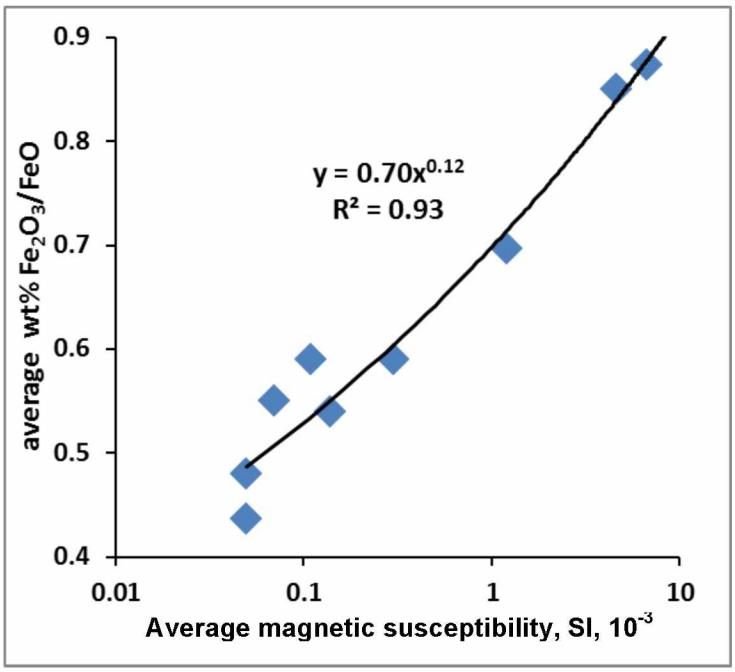

Figure 2.13. Average Fe_2O_3/FeO ratio (from Fig. 2.12) vs. average pluton magnetic susceptibility (Table 2.1).

One measure of the consistency of the Fe_2O_3/FeO ratios (Fig. 2.12) is to plot the average Fe-oxide ratios against the average magnetic susceptibility values (Table 2.1) for each pluton. I have done so (Figure 2.13) and found a strong correlation between the two factors. The results suggest that either factor can be used to depict the relative oxidation state of a given pluton.

One final aspect of the major-element compositions is that TiO_2 can be used as a measure of fractional crystallization of a pluton (e.g., Lehmann, 1982; Swanson et al., 1988). As shown in Figure 2.14, TiO_2 decreases as the differentiation index (the sum of CIPW normative quartz + albite + orthoclase) increases. One result is that several of the plutons exhibit a pattern of inward fractional crystallization, as seen in zoning of TiO_2 concentrations for the Sithylemenkat pluton (Fig. 2.15).

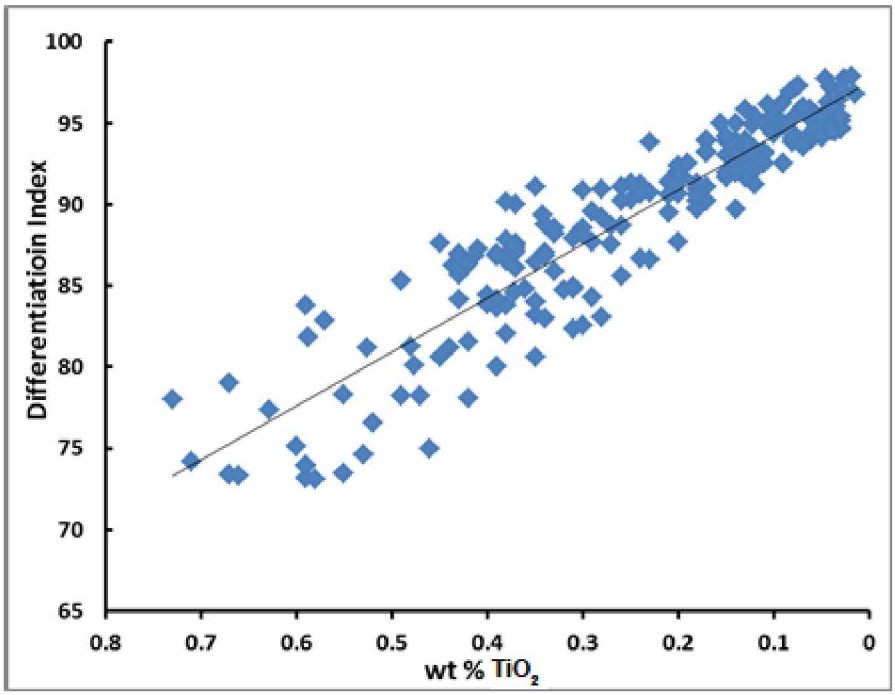

Figure 2.14. Wt% TiO_2 vs. differentiation index (sum of CIPW normative quartz + albite + orthoclase) for plutonic rock samples from the Ruby batholith. Data sources are the same as listed with Figure 2.9.

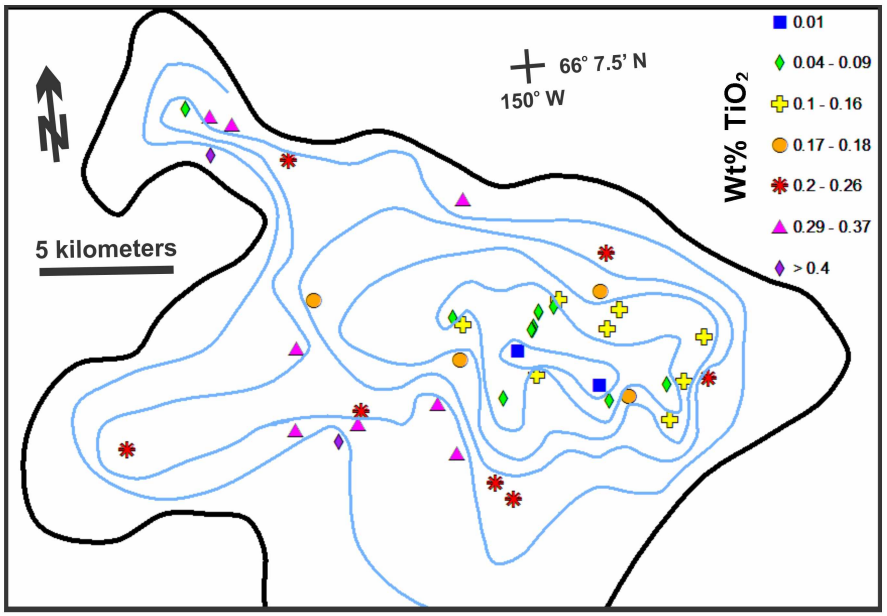

Figure 2.15. Distribution of wt% TiO_2 in samples from the Sithylemenkat pluton (outlined in the heavy black line), southwest Ruby batholith. Data from sources listed with Figure 2.9.

2.8 CHARACTERISTIC MINERAL ASSEMBLAGES

All samples examined contain quartz, alkali feldspar, plagioclase, biotite, apatite and zircon. As indicated by a combination of thin section petrography and microprobe-based identifications, systematic mineralogical differences are present among the various plutons (Table 2.6). In particular, most—but not all—plutons with primary magnetite also contain hornblende and titanite, and almost all of the plutons contain at least one thin section with some allanite. The absence of peraluminous minerals outside of muscovite is surprising. Topaz is restricted to the NNC pluton, and garnet is rarely present in the Kanuti Northeast lobe and the Hot Springs East pluton. Given that only the NNC pluton is significantly peraluminous (Figure 2.11), it is reasonable to assume it is mineralogically unique.

Although all plutons contain apatite, there are major differences in apatite abundance among the plutons (e.g., Figure 2.16, 2.17). Based on chemical analyses and petrographic observations, northern plutons typically contain 0.4 to 0.5% apatite, often observed as abundant inclusions in biotite (Fig. 2.16). In contrast, biotite from southern plutons typically appears nearly apatite-free (Fig. 2.17), and based on a combination of chemical analyses and visual examination, typically contain 0.1 to 0.2% apatite.

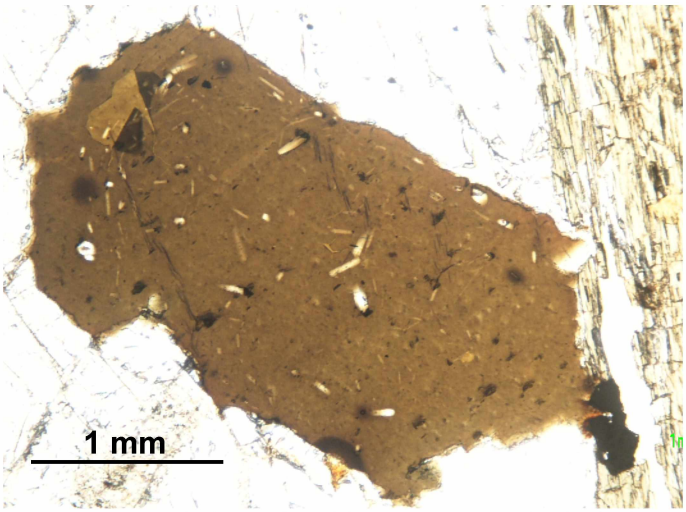

Figure 2.16. Biotite grain with numerous apatite inclusions. Sample 12RN375B from the Bonanza pluton.

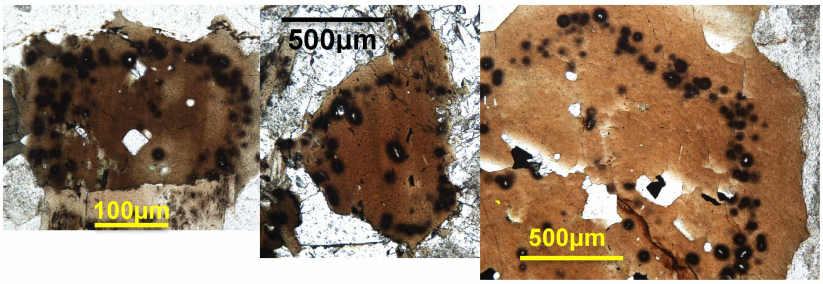

Figure 2.17. Biotites with oriented rings of inclusions. Inclusions consist of zircon, monazite and xenotime, all with pleochroic haloes. All photomicrographs from samples from the NNC pluton.

Three different REE accessory minerals occur: two orthophosphates, monazite-(Ce), ($CePO_4$), and xenotime-(Y), (YPO_4), and the silicate allanite-(Ce), ($CaCe(Al_2Fe^{2+})(Si_2O_7)(SiO_4)O(OH)$), analogous to epidote, but with significant LREE (represented by Ce) substituting for Ca. Differentiating zircon, monazite and xenotime petrographically is problematic, especially given their small (< to << 100 µm) grain sizes. Both monazite and xenotime are typically surrounded by pleochroic haloes in biotite. Monazite and xenotime identifications were confirmed using energy dispersive spectroscopy (EDS) on the electron microprobe. Backscattered electron (BSE) images from the microprobe also indicated oscillatory zoning is common in monazite.

Table 2.6. Additional minerals identified by petrographic microscope and (or) energy-dispersive spectroscopy (electron microprobe)

Pluton	Monazite	Xenotime	Allanite	Tourmaline	Titanite	Hornblende	Magnetite	Ilmenite	Muscovite+	Topaz	Fluorite	Garnet	Cassiterite*	Wolframite*	Scheelite*
Bonanza			x		x	x	x								
Kanuti W	x		x		x	x	x								
Kanuti NE	x		x		$		x	x	x		1	x			
Hot Springs E	x		1	x			x	x	x			1			
Hot Springs W			x	x	x	x	x	x							
Coal Creek			x		x	x	x	x							
No Name	x	x		x				x	x	x	x		x	x	
Ft Hamlin Hills	x	x	x		x	x	x	x				#		x	x
Ray River	x	x	x	x				x	x		x				x
Sithylemenkat	x	x	x	x				x	x		1		x		
Ray Mntns E	x	x	x	x				x	x		1			x	x

Notes: "1" = 1 grain found in 1 thin section; "+" = texturally primary; "$" = Titanite in this sample is intergrown with or near chloritized biotite and is likely secondary; "*" = These minerals are likely secondary.

Allanite is present in all but the NNC pluton (Table 2.6), but the crystals invariably display a complex growth history. Three types of allanite reactions are shown in Figure 2.18: (1) early-formed allanite surrounded by later-stage allanite; (2) embayed allanite edges, suggesting magmatic resorption; (3) mineral intergrowths, suggesting late-magmatic replacement of allanite. Allanite is typically replaced by an Fe-Al mineral (usually biotite, but in at least one case, almandine garnet) ± monazite. Typically, the textures are compatible with late-magmatic reactions, but fine veinlets of monazite within allanite suggest a hydrothermal replacement.

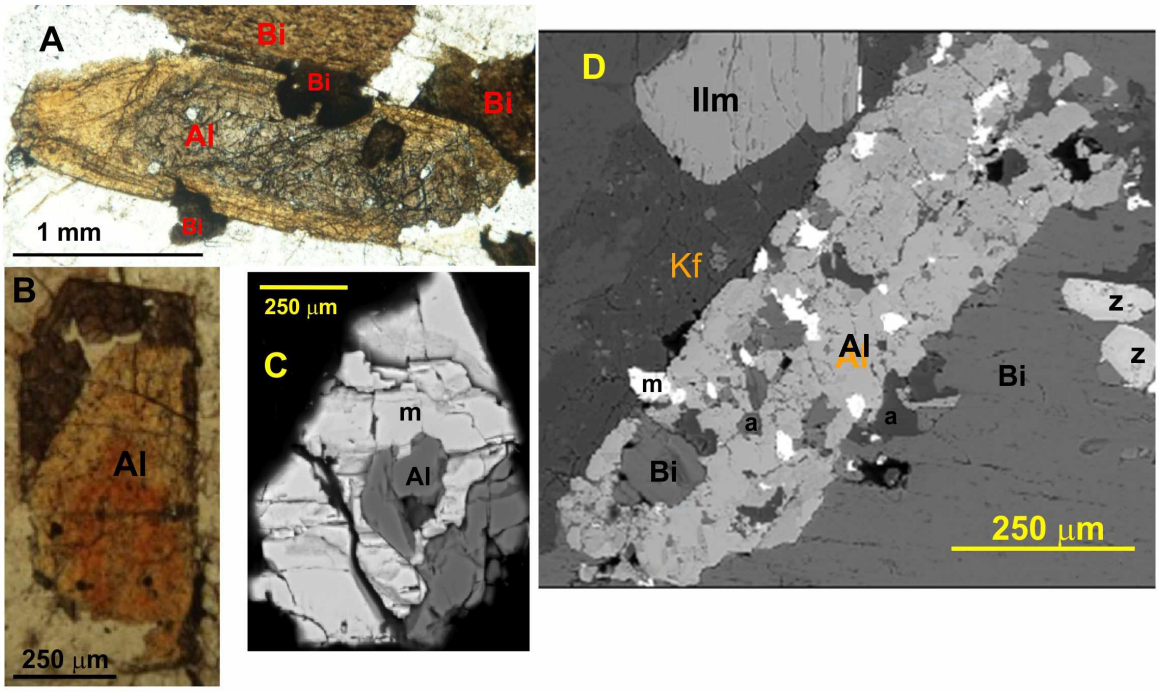

Figure 2.18. Representative allanite (Al) textures from Ruby batholith samples. A) Dark core with apatite (colorless) inclusions and paler rim; both are replaced by biotite (Bi) as a late magmatic reaction. The embayed right margin of the grain suggests magmatic resorption. Sample from the Coal Creek pluton. B) Allanite with pale core surrounded by darker growth; both display scalloped lower margin suggesting magmatic resorption. Sample from the Sithylemenkat pluton. C) Backscattered-electron (BSE) image (brightness increases with mean atomic number) of allanite being replaced by monazite (m). Sample from the Sithylemenkat pluton. D) BSE image of allanite grain with apatite (a) inclusions being replaced by biotite (Bi) + monazite (m). Nearby ilmenite (Ilm) and zircon (z) grains are not affected. Sample from the Ray River pluton.

Two characteristic REE mineral assemblages dominate the plutons. The northern and few transitional plutons—Bonanza, Kanuti West, Hot Springs West, Coal Creek, and Fort Hamlin Hills—contain an oxidized, calcic mineral assemblage including allanite + titanite + magnetite + hornblende ± monazite ± ilmenite (Table 2.6). The transitional Hot Springs East and Kanuti Northeast plutons contain magnetite and rare garnet, but no hornblende or significant allanite. In the southern plutons, the rare-earth mineralogy is dominated by the phosphates monazite and xenotime. The assemblage excludes hornblende, but includes ilmenite + coarse (primary?) muscovite ± fluorite. Topaz is present exclusively in the NNC pluton. In the few cases where allanite is present, it is restricted to the higher-TiO_2 (and thus less fractionated) rocks, and displays textural relations suggesting it crystallized early and was subsequently resorbed or replaced (Fig. 2.18).

Biotite from the southern plutons commonly contains oriented rings of inclusions (Fig. 2.17), including zircon, monazite and xenotime. This phenomenon is especially prominent in samples from the NNC pluton. A vaguely similar texture is present in some biotites from the northern plutons, but the inclusions in these cases are primarily apatite. Disseminated tourmaline is present in the southern plutons, and also in the Hot Springs East and West plutons (Table 2.6). It is arguably of late-magmatic origin. I have identified rare, disseminated cassiterite, wolframite, and (or) scheelite in all of the plutons south of the Coal Creek pluton (Table 2.6). These minerals are typically in the vicinity of biotite altered to chlorite ± muscovite, and hence are possibly hydrothermal in origin.

2.9 GREISENS AND OTHER HYDROTHERMAL ALTERATION

Cassiterite-bearing veins within granite are historically called "greisen". Plutons in the study area contain chlorite-rich (Sithylemenkat pluton), muscovite-tourmaline-rich (Ray River and NNC plutons), and tourmaline-rich (Ray Mountains, Hot Springs West and Hot Springs East) greisen veins. All types are rare, certainly less than 1% of any exposed pluton. In addition, skarns are present adjacent to the Kanuti Northeast and the Fort Hamlin Hills plutons. Table 2.7 gives the maximum concentrations of selected elements in the various types of altered rock. Notably, the highest (or second highest) concentrations in virtually every element listed are from the Sithylemenkat greisens. The maximum Ce in greisen, however, is only twice that of unaltered granite, but the maximum Y (representative of the HREE) is nearly five times as high as the maximum concentration for unaltered granite. In other words, Table 2.7 gives evidence for localized concentration of HREE + Y in select Ruby batholith greisens.

The Sithylemenkat chlorite greisen (Appendix D) consists of veins and veinlets of chlorite ± magnetite, predominantly replacing feldspar. I identified galena, sphalerite, cassiterite, tourmaline, kaolinite, and Pb-Mn oxide coatings in chlorite-rich greisen. The REE were associated with Rb, Ca and Th in fine-grained clay (?) minerals. Phosphorus was not associated with the REE, indicating the original REE phosphate minerals were dissolved during chlorite greisen formation. I was unable to identify an actual REE mineral in the chlorite greisen, despite the relatively high maximum REE concentration (Table 2.7).

My examination of muscovite greisen from the Ray River pluton (Appendix D) yielded different results. I identified allanite, partly replaced by monazite, as well as ilmenite and

scheelite. Tourmaline-muscovite greisen from the NNC pluton yielded wolframite and cassiterite, but little else. I did not examine in detail the samples from the other greisens, but it is clear from Table 2.7 that the higher metal grades are in the two most southern plutons, Sithylemenkat and Ray Mountains East. Two exceptions are the greisen from the 98 Ma-Hot Springs West pluton, which has anomalous Ce, U and As, and the W-rich skarn adjacent to the 90 Ma-Kanuti Northeast pluton. The latter bears a distinctively high W/Sn ratio of nearly 100:1 (Table 2.7), much higher than any other mineralization in the region.

Table 2.7. Maximum concentrations (ppm, unless otherwise indicated) of selected elements in altered granite and adjacent rock, Ruby batholith area

Pluton	Type*	Ce	Y	Sn	W	Nb	U	Be	Rb	Bi	Pb	Cu	As
Bonanza	--	62	29	3	6	10	8	4	235	6	65	34	56
Kanuti West	--	122	52	7	35	17	15	12	415	6	99	5	5
Kanuti Northeast	skarn	84	32	45	**4240**	15	15	23	341	46	400	**570**	35
Hot Springs West	tour + ser	**478**	36	217	12	20	**151**	5	360	23	536	213	**8240**
Hot Springs East	tour	90	35	31	400	39	39	59	335	127	145	15	41
No Name	tour	153	70	268	41	24	12	36	**1020**	24	104	48	187
Fort Hamlin Hills	hfls/ skarn	94	46	128	13	19	5	4	223	15	31	166	66
Ray River	mu-tour	158	112	1725	343	**86**	64	**205**	**1905**	29	87	11	29
Sithylemenkat	chl	276	**572**	**2.57%**	**2720**	68	**668**	**181**	928	**955**	**2.4%**	**1300**	**2590**
Ray Mntns E	tour	**504**	**132**	0.49%	459	67	**198**	59	**1585**	200	**2080**	**451**	266
Max Rock	none	**244**	**109**	**25**	**18**	**35**	**34**		**854**				

Notes: "*" = type is greisen, dominated by the mineral indicated, unless otherwise stated; "--" = unspecified altered granite; "hfls" = hornfels, "tour" = tourmaline, "ser" = sericite, "mu" = muscovite, "chl" = chlorite. "Max Rock" = maximum concentration in apparently unaltered rock from the Ruby batholith. Data from Bachmann et al. (2013), Tuzzolino et al. (2014a), and this study.

2.10 DISCUSSION

2.10.1 Multiple Ages and Origins of the Ruby Batholith

Multiple ages of the Ruby batholith are of two sorts: ages caused by dating different minerals, and those ages apparently reflecting differences in magmatic ages. Despite the complications of variable dating techniques, the Ruby batholith data indicate multiple magmatic ages.

The general zircon U-Pb age for the emplacement of the Ruby batholith is 111 Ma. Incontestably, the Hot Springs West pluton has a zircon U-Pb age (98 Ma) much younger than the other plutons (Fig. 2.4). Although not as dramatic, the NNC pluton zircon U-Pb age (107 Ma) also appears distinctly younger than the majority of the U-Pb ages in the Ruby batholith. A detailed analysis of the zircon populations for this sample (Tuzzolino et al., 2016) failed to conclude that the young age is spurious. The NNC pluton has a unique composition (Figs. 2.6-2.12, Table 2.5), a unique mineralogy (topaz-bearing, allanite absent; Table 2.6), and a unique size (much smaller than the other plutons; Fig. 2.5); hence, the NNC pluton being 4 Ma younger than the average age of the Ruby batholith is not much more of a complication. Nevertheless, the propensity of crustal melting to continue in the NNC area—and only that area—is difficult to explain.

There are five muscovite $^{40}Ar/^{39}Ar$ ages; four are approximately 3 Ma younger than the zircon U-Pb ages. The final muscovite $^{40}Ar/^{39}Ar$ age is much younger than all other ages. The sample is from the garnet-bearing granite of the Kanuti Northeast lobe (Figs. 2.4, 2.5). The relatively coarse-grained muscovite yielded a clean Ar-release spectrum (Tuzzolino et al., 2014b) that argues against this being a thermal reset age. The fact that this part of the Kanuti body is the only extensive area in the Ruby batholith with garnet-bearing granite and high Sn/W skarns nearby suggests a magmatic event distinct from that producing the 111-Ma majority of the Ruby batholith.

The numerous K-Ar ages of hornblende and biotite are typically younger than the zircon U-Pb ages for the same plutons, an expected result due to differences in closure temperatures. The pattern of anomalously young K-Ar ages from the literature now has an explanation; some of the plutons of the Ruby batholith actually are younger than the others. The 5-Ma difference between the biotite K-Ar (106 ± 3 Ma) and the likely magmatic age of the Sithylemenkat pluton (111 ± 1 Ma) can be explained by a combination of slow cooling and the likelihood that the K-Ar

age uncertainty is actually 1 sigma rather than 2 sigma. That is, 106 ± 6 Ma is indistinguishable from 111 ± 1 Ma. On the contrary, the 96 to 98 ± 2 Ma biotite K-Ar ages in—and in the general vicinity of—the Hot Springs West pluton (Fig. 2.5) are significantly younger than the average age of 111 Ma.

Given the U-Pb age of 98 ± 1 Ma for the Hot Springs West pluton, it is probable that more than one magma body in the region is of this younger age. Furthermore, in retrospect, the Hot Springs East and Hot Springs West bodies are considerably different from one another (Figs. 2.8-2.11). It seems more than coincidence that all three anomalously young biotite K-Ar ages (from Kanuti and Hot Springs West) line up (Fig. 2.5), suggesting a structural control on the ca. 98 Ma magmatism. The extent of the Kanuti pluton that actually is younger than 111 Ma, however, cannot be determined.

Among other factors, the internal variability in initial $^{87}Sr/^{86}Sr$ ratios (SIR) may indicate a "pluton" may instead be a composite of several different coalescing magma bodies (potentially with different ages?), or that various source materials melted. There are two cases: the Sithylemenkat pluton, for instance, has a poorly defined magmatic age, yet the SIR data attests that the Sithylemenkat pluton formed as a result of a single melting event of relatively homogeneous material. Ti zoning expresses broadly uniform changes supporting the notion of a magma fractionating from a single body. In contrast, the Kanuti pluton generates multiple ages, and the variable SIR support the notion that individual bodies of this "pluton" were generated at different times using different materials.

2.10.2 Plutonic Rock Types and Their Identification

As previously mentioned (Table 2.5), examination of stained slabs indicate most of the batholith is monzogranite, while chemical analyses indicate syenogranite instead. The discrepancies are likely due to inherent problems with each method. Unfortunately, most of the samples selected for staining were not submitted for chemical analysis, so few direct comparisons can be made.

A coarse grain size is ideal for mineral-abundance determination by feldspar staining, but causes problems for accurate chemical analysis. As coarseness and grain size increase, sample size must also increase to ensure accurate representation. Transporting many kg of rock for a single sample was not generally practicable. By-and-large, slabs of coarser samples were

collected for rock staining, and finer-grained (< 1 cm average) samples were used for chemical analysis.

For the modal analyses, once the slabs were stained to highlight the differences between potassium and plagioclase feldspar, the next step was to estimate the percentage of quartz, feldspars and mafic minerals. Traditionally, investigators at DGGS estimated mineral abundance by comparison with standard abundance charts. The digital image processing procedure (described in Chapter 1) was used for this study with the intention of both saving time and making more quantitative estimations. A range of colors was selected to represent a specific mineral. The distinction, however, between bright-yellow potassium feldspar and faintly yellow plagioclase—while easily visible to the naked eye—has proved problematic with a digital image. The range of hues selected within the digital image processing program likely overlapped mineralogies, selecting portions of both feldspars when generating percentages. Hence, accurate discrimination between the two feldspars was usually met with resistance. Similarly, many of the rocks contained smoky quartz, which is difficult to distinguish from mafic minerals.

A comparison of field-estimated, mafic mineral abundances to those generated using the stained slabs (Fig. 2.19) shows that—for most rocks—the field estimates of mafic mineral abundances were 2 to 10 times that of the stained slab estimates. Over-estimation of dark mineral content in the field could be part of the problem, but the known presence of dark quartz indicates that the problem is in part associated with the image processing software.

Due to a lack of very coarse-grained samples, as well as the paucity of clean, competent samples from the Bonanza pluton, an unusually high proportion of rocks from that pluton had both modal and chemical analyses generated for the same samples. I compared the results for the two and found that the estimated percentages of quartz were invariably higher than those calculated by the CIPW norms of the chemical analyses. Consequently, I retrieved and reviewed the stained slabs from the Bonanza pluton and manually re-estimated the modal mineral abundances. I concluded that the modal abundances of quartz were overestimated, particularly for the finer grained (< 2 mm) samples. It was simply not possible to distinguish between quartz and mafic minerals from the image alone.

On the other hand, I selected and re-examined stained slabs from the Hot Springs East pluton due to anomalously low modal quartz. Contrary to the Bonanza samples, the mafic mineral abundances in these samples were overestimated due to characteristic dark quartz being

mistaken for mafic minerals. In sum, due to a variety of problems, the mineral abundances generated from the stained slabs must be used with caution.

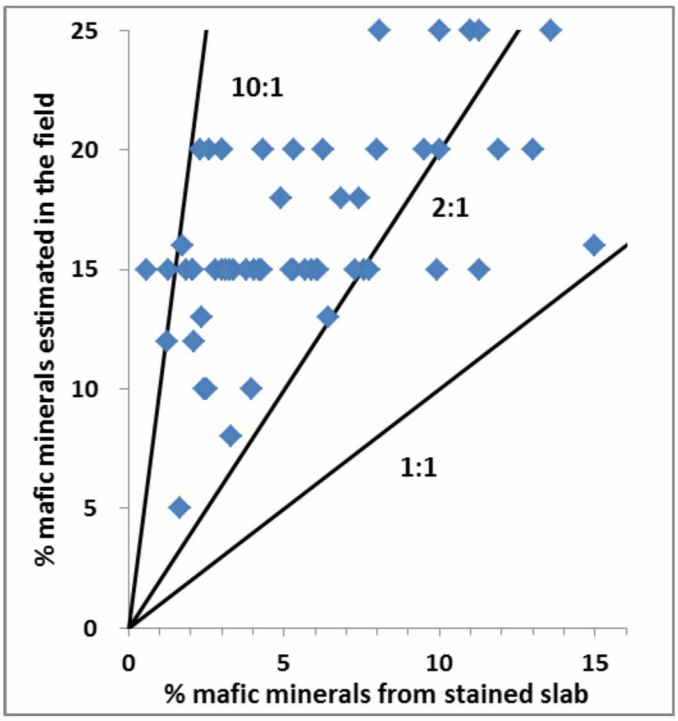

Figure 2.19. Comparison of % mafic minerals estimated in the field compared to those from the stained slab for the same rock. The bulk of the data presented indicate 2 to 10 times as much mafic mineral from field estimate as from the stained slab. Data from this study.

Granitic rock classification based on the CIPW normative analyses (Streckeisen and Le Maitre, 1979) is problematic as well. While the ratio of CIPW quartz to quartz + total feldspar probably approximates the true mineral ratios (vertical axis, Fig. 2.9), the ratio of alkali feldspar to plagioclase is more variable. There are two issues: (1) all K in a normal chemical analysis becomes CIPW normative orthoclase, as biotite is not calculated in a CIPW norm; (2) for granites, the typical plagioclase is Na-rich, with greater than 80% albite component, whereas the alkali feldspar is rarely more than half the albite component. In consequence, using the CIPW normative orthoclase-versus-anorthite ratio as an approximation to the actual alkali feldspar-to-plagioclase ratio overestimates alkali feldspar and underestimates plagioclase. On the other hand, use of the Streckeisen and Le Maitre (1979) diagram better emphasizes the differences between the plutons. For example, data from the Ray River pluton (Fig. 2.9D) are clearly different from those of the Sithylemenkat pluton, even though both plot as primarily monzogranites on the modal diagrams (Figure 2.8).

In sum, the bulk of the rocks from the central part of the Ruby batholith (the study area) should be classified as a monzogranite, with the exception of the NNC pluton, which is distinctly unique. Therefore, the normative classification diagrams better highlight the presence of significant differences among the monzogranites.

2.10.3 Mineralogical Differences Among Plutons

Several distinctive mineral assemblages occur in the central Ruby batholith. These assemblages reflect differences in intrinsic oxidation state (as measured by the Fe_2O_3/FeO ratio, Fig 2.12, or the magnetic susceptibilities, Fig. 2.3) and also in degree of aluminum saturation (as measured by the aluminum saturation index, Fig. 2.11). I have combined the two in Figure 2.20 as a means of expressing that the two are somewhat independent variables. The northern plutons are characterized by the assemblage magnetite + titanite and only slightly peraluminous compositions, supporting hornblende stability. Two of the northern plutons (Kanuti Northeast and Hot Springs East), however, are significantly peraluminous, and although magnetite-bearing, lack hornblende; hence, these plutons are specifically characterized as transitional as opposed to strictly northern.

The key significance of titanite as the typical Ti-bearing mineral of the northern Ruby batholith plutons lies in the equilibrium:

$$FeTiO_3 + CaFeSi_2O_6 + .33O_2 = CaTiSiO_5 + .66Fe_3O_4 + SiO_2 \quad (13)$$

ilmenite hedenbergite titanite magnetite quartz

That is, for sufficiently high abundance of Ca (here symbolized by Ca-Fe-pyroxene), a relatively high oxidation state is necessary to generate the titanite + magnetite assemblage. At a lower oxidation state, the Ti is present as either ilmenite or as titanomagnetite. The necessary Ca could be simply supplied by the magma. However, the northern plutons that contain magnetite yet lack titanite are also strongly peraluminous, and are hence transitional (Fig. 2.20). That is, they contain significantly more Al than that needed to make feldspar from the available Ca, Na, and K. A model reaction like:

$$Fe_3Al_2Si_3O_{12} + CaTiSiO_5 + .167O_2 = CaAl_2Si_2O_8 + 2SiO_2 + .33Fe_3O_4 + Fe_2TiO_4 \quad (14)$$

garnet titanite plagioclase quartz titanomagnetite

could explain the lack of titanite, especially because the titanite-absent granite in Kanuti Northeast *does* contain almandine garnet.

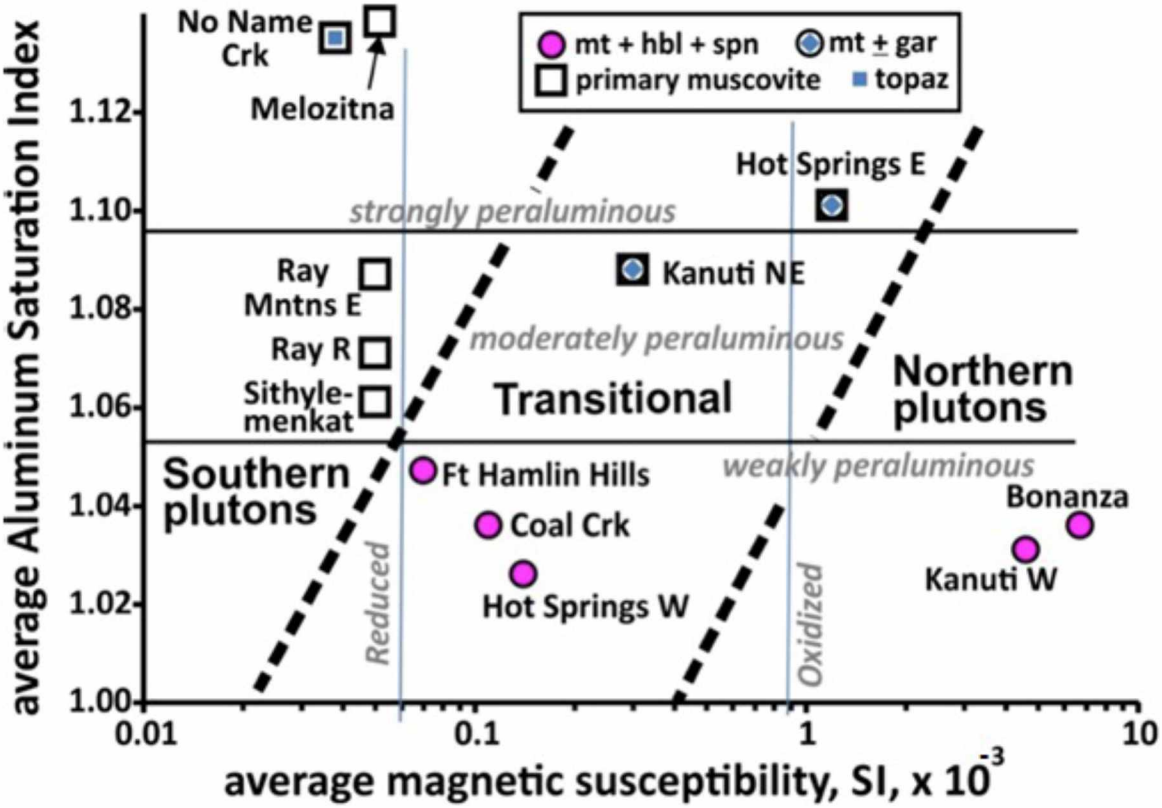

Figure 2.20. Average magnetic susceptibility vs. average aluminum saturation index for plutons of the central and southern Ruby batholith, with symbols indicating characteristic pluton mineralogy. Diagonal dashed lines represent breaks in plutons displaying characteristically northern, transitional, or southern features. Data are from Table 2.1 and Figure 2.9.

A similar explanation may explain the occurrence (and absence) of allanite, the Ca-rich REE silicate mineral. The relative stability of monazite, apatite and allanite are related to the Ca activity and peraluminosity of the melt (Dini et al., 2004). Monazite crystallizes in a low-Ca environment, whereas allanite precipitates at higher Ca activities. The replacement of allanite by monazite as the dominant LREE phase may result from decreased Ca activity as plagioclase crystallizes during the differentiation of a peraluminous magma (Broska et al., 2000). Crystallization of plagioclase lowers the Ca activity in the melt, the composition of which now makes monazite the stable LREE phase (Broska et al., 2000), and causes allanite to resorb into the melt. In the Minto Block of the Superior Province of northern Quebec, Bédard (2003) noted igneous allanites showing embayments—representing magmatic resorption structures—where the allanite contacted the quartzofeldspathic matrix.

The NNC pluton is the *only* pluton completely lacking evidence of allanite (Table 2.6). It is also the most peraluminous pluton (aside from the Melozitna pluton, Figs. 2.11, 2.20). The

northern plutons contain euhedral allanite crystals, showing no signs of magmatic resorption; whereas in the Ray River, Sithylemenkat, and Ray Mountains East plutons, allanites only occur in the most Ca-rich rocks and display abundant evidence for a combination of resorption and replacement (Fig. 2.18). Allanite does not occur in the Ca-poor rocks of these southern plutons.

Most samples of the southern plutons contain the rare-earth phosphates monazite and xenotime as opposed to allanite, and have qualitatively less apatite. Biotites in the northern plutons commonly contain one-half percent apatite as inclusions (Fig. 2.16), while the biotites in the southern plutons contain abundant inclusions of monazite and xenotime (Fig. 2.17).

The key significance of these rare-earth minerals is that they will be responsible for the patterns of REE-abundance changes with fractionation and for the minerals concentrating in the gravels. The nature of the potential placer REE resources in the area will be strongly affected by the REE mineralogy of the eroded plutons, which in turn is related to magma Al saturation and oxidation state (Fig. 2.20).

Based on thin section examination and rock F contents (see Chapter 3), the NNC pluton appears to contain the most fluorite, and is the only pluton where topaz has been identified. Topaz ($Al_2SiO_4(F,OH)_2$) is both Al- and F-rich. High fluorine contents suggest some combination of extensive fractional crystallization and a somewhat different parent melt than the less-peraluminous, slightly older plutons of the Ruby batholith.

2.10.4 Summary

So far I have shown—based on variability in age, major-element composition, and mineralogy—that the seemingly similar monzogranites of the Ruby batholith encompass a wide range of ages, oxidation states, and aluminum saturation indices, leading to a variety of REE and Ti minerals and mineral assemblages. In the following chapter, I pursue trace-element comparisons of the plutons through a combination of rock and mineral compositional studies.

3 TRACE-ELEMENT GEOCHEMISTRY OF THE RUBY BATHOLITH

3.1 INTRODUCTION

Trace-element geochemistry provides information on the origin and evolution of igneous rocks. In this chapter, I provide the compositions of REE minerals to gain insight into REE behavior during fractional crystallization of the plutons. I track REE distribution within the southern plutons to decipher magmatic enrichment and depletion patterns. As well, I employ elemental concentration vs. TiO_2 trends among the individual plutons to explore the relationship between elemental behavior and fractionation for individual plutons.

3.2 CHEMICAL COMPOSITIONS OF RARE-EARTH-BEARING MINERALS

3.2.1 Microprobe Analytical Considerations

I used semi-quantitative energy-dispersive X-ray spectroscopy (EDS) to determine the chemical compositions of allanite (Appendix E), monazite (Appendix F), xenotime and titanite in rocks from the central Ruby batholith. Considering each REE emits L X-rays of several different energies, the complete X-ray spectrum of a mineral containing multiple REE is quite complex and difficult to decipher. EDS is a method that requires minimum set-up time and quick analysis, but energy-dispersive spectrometers have a limited ability to distinguish similar X-ray energies. Further, the P-Kα X-ray emission line is practically indistinguishable (by EDS) from the Y-Lα X-ray emission line. In order to measure Y in P-rich minerals (e.g., monazite and xenotime), I employed the Y-Kα X-ray line, which requires a high (30 keV) voltage. At the time of my analyses, UAF's only REE standards were glasses containing groups of REE + Y that do not yield X-ray interferences (Drake and Weill, 1972). I tested the capabilities of the UAF EDS system by analyzing these glasses at 15 keV (the lower voltage avoids damaging the glass standards) and achieved satisfactory results (Tables 3.1, 3.2, 3.3).

Table 3.1. UAF microprobe EDS analyses of glass standard REE1, along with the published analysis of REE1

	Microprobe EDS Analyses				Published Values	
Voltage (keV)	15		30			
	Avg	StDev	Avg	StDev	X-Ray Line	
Al_2O_3	38.6	0.8	38.1	0.4	Kα	30.521
SiO_2	23.3	0.9	23.2	0.3	Kα	26.96
CaO	19.0	0.7	19.8	0.1	Kα	25.16
Eu_2O_3	4.3	0.6	4.6	0.3	Lα	4.2
Gd_2O_3	4.9	0.7	5.3	0.2	Lα	4.459
Tb_2O_3	5.2	0.9	5.4	0.2	Lα	4.35
Tm_2O_3	4.4	0.8	3.7	0.3	Lα	4.35

Notes: Voltage varied. Analysis of REE1 by Drake and Weill (1972).

Table 3.2. UAF microprobe EDS analyses of glass standard REE2, along with the published analysis of REE2

	Microprobe EDS Analyses				Published Values	
Voltage (keV)	15		30			
	Avg	StDev	Avg	StDev	X-Ray Line	
Al_2O_3	36.0	0.8	35.4	0.2	Kα	30.63
SiO_2	27.5	0.5	27.5	0.4	Kα	27.071
CaO	21.4	0.3	22.9	0.3	Kα	25.26
Nd_2O_3	4.1	0.5	3.3	0.2	Lα	4.26
Sm_2O_3	4.0	0.5	3.4	0.4	Lα	4.26
Yb_2O_3	3.6	0.3	3.5	0.2	Lα	4.26
Lu_2O_3	3.4	0.8	4.1	0.5	Lα	4.26

Notes: Voltage varied. Analysis of REE2 by Drake and Weill (1972).

Table 3.3. UAF microprobe EDS analyses of glass standard REE3, along with the published analysis of REE3

	Microprobe EDS Analyses						Published Values	
Y X-Ray Line	Lα		Lα		Kα			
Voltage (keV)	15		30		30			
	Avg	StDev	Avg	StDev	Avg	StDev	X-Ray Lines	
Al_2O_3	32.5	0.8	32.8	0.3	33.2	0.3	Kα	30.721
SiO_2	21.9	0.8	21.9	0.3	22.3	0.3	Kα	27.151
CaO	23.3	0.8	24.8	0.1	25.0	0.2	Kα	25.331
Y_2O_3	4.5	1.0	4.7	0.2	3.5	0.4	Lα	4.08
La_2O_3	5.4	0.6	5.2	0.4	5.3	0.4	Lα	4.281
Ce_2O_3	7.0	1.1	6.0	0.3	6.0	0.3	Lα	4.00
Pr_2O_3	5.4	1.0	4.6	0.2	4.7	0.2	Lα	4.44

Notes: Voltage and Y X-ray emission lines varied. Analysis of REE3 by Drake and Weill (1972).

To assess the ability of UAF's EDS software to quantify concentrations of REE in minerals, I cut large pieces of allanite, monazite and xenotime from specimens in UAF's mineral collection. I then analyzed the cut and polished surfaces by wavelength-dispersive spectrometry (WDS) X-ray fluorescence (XRF) using UAF's Panalytical XRF analyzer. I analyzed each mineral ten times and averaged the compositions, checking to ensure that each analysis yielded an appropriate stoichiometry. I then analyzed each of these minerals with the UAF microprobe EDS system multiple times with different voltages and X-ray lines (Tables 3.4, 3.5, 3.6). I found that the EDS system yielded better results for Th if the M (rather than the L) X-ray emission line was utilized. Monazite analyses were problematic. The EDS system was typically unable to detect Y if the Y-Lα line was employed. The results for the other REEs, however, were more accurate with the Y-Lα line. I also had better results for Y in allanite using the Y-Lα line. Average EDS results (optimal settings) for the XRF-analyzed REE minerals, along with their XRF and microprobe analyses, are usually within 10% of the actual amount present, unless at the detection limits. Most importantly, I determined that it was important to *consistently* use a particular X-ray line for the analysis of a given mineral.

Table 3.4. Average microprobe EDS analyses of the secondary allanite standard, along with its XRF analysis

	Microprobe EDS Analysis		**WDS XRF Analysis**	
	Avg	StDev	Avg	StDev
Al_2O_3	13.0	0.4	13.8	0.4
SiO_2	30.4	0.7	28.2	0.7
CaO	10.1	0.4	9.7	0.2
TiO_2	1.0	0.2	0.9	0.03
MnO	0.7	0.1	0.7	0.03
Fe_2O_3	16.4	0.5	17.5	0.7
Y_2O_3	--	--	0.2	0.1
La_2O_3	7.8	0.6	8.5	0.5
Ce_2O_3	13.9	0.7	12.7	0.9
Pr_2O_3	1.7	0.5	1.0	0.1
Nd_2O_3	3.6	0.2	3.4	0.1
Sm_2O_3	--	--	0.3	0.05
ThO_2	0.8	0.36	0.8	0.1

Notes: Voltage varied. Th-M and Y-K X-ray lines used. "--" indicates concentration below detection limit.

Table 3.5. Average microprobe EDS analyses of secondary monazite standard, along with its XRF analysis

	Microprobe EDS Analyses						WDS XRF Analysis	
Th X-Ray Line	Mα		Mα		Mα			
Y X-Ray Line	Lα		Lα		Kα			
Voltage (keV)	15		30		30			
	Avg	StDev	Avg	StDev	Avg	StDev	Avg	StDev
SiO_2	2.4	0.1	2.4	0.4	2.4	0.3	3.0	0.4
P_2O_5	30.7	3.4	36.0	0.6	35.5	0.7	24	1
CaO	1.3	0.3	1.4	0.1	1.4	0.1	0.9	0.3
Y_2O_3	0.9	0.8	0.3	0.3	1.5	0.6	1.9	0.3
La_2O_3	8.6	0.8	6.6	0.8	6.5	0.7	14	1
Ce_2O_3	24.3	2.9	23.2	0.9	23.0	1.1	22	1
Pr_2O_3	4.2	2.2	1.5	0.4	1.5	0.4	3.6	0.4
Nd_2O_3	9.6	0.4	7.0	1.1	7.0	1.2	9.0	0.6
Sm_2O_3	3.4	0.1	4.0	0.4	4.0	0.3	3.8	0.4
Gd_2O_3	1.1	0.6	1.9	0.2	1.9	0.2	2.2	0.5
Dy_2O_3	0.5	0.4	0.7	0.2	0.6	0.2	0.9	0.4
ThO_2	13.2	1.41	15.0	0.7	14.9	0.6	13	1

Notes: Voltage, and Th and Y X-ray lines varied.

Table 3.6. Average microprobe EDS analyses of secondary xenotime standard, along with its XRF analysis

	Microprobe EDS Analyses						WDS XRF Analysis	
Y X-Ray Line	Lα		Lα		Kα			
Voltage (keV)	15		30		30			
	Avg	StDev	Avg	StDev	Avg	StDev	Avg	StDev
P_2O_5	31	1	33	1	47	2	36	1
Y_2O_3	53	2	51	1	33	1	44	1
Sm_2O_3	0.4	0.4	0.6	0.2			0.9	0.2
Gd_2O_3	2.8	0.4	2.7	0.2	3.5	0.1	3.4	0.3
Dy_2O_3	5.4	0.5	5.2	0.4	6.9	0.2	5.5	0.4
Ho_2O_3	1.2	0.9	1.7	0.3	2.0	0.2	1.1	0.3
Er_2O_3	3.9	1.1	4.0	0.2	5.0	0.6	4.3	0.4
Yb_2O_3	2.3	1.1	2.5	0.3	2.7	0.1	3.4	0.3

Notes: Voltage, and Th and Y X-ray lines varied.

3.2.2 Allanite

Following the nomenclature of Bayliss and Levinson (1988), all allanite analyzed (Appendix E) is technically allanite-(Ce); that is, the most abundant REE is Ce. This is the usual variety present in most rock types. It also typically contains significant Th and Ti.

Allanite is present as at least one grain in at least one thin section from every pluton I examined—aside from the NNC pluton. The allanite I observed typically possessed magmatic zoning, both normal and oscillatory, as viewed in both transmitted-light microscopy and backscattered electron (BSE) images (Fig. 3.1). In this case (Table 3.7), the oscillations are between high-Th-Ti-Fe and high-Al-Ca-La-Ce zones, with an overall core-to-rim decrease in Ti and Th. The core contains approximately 5% ThO_2 and 4% TiO_2; the rim has approximately 3% of each.

Table 3.7. Microprobe EDS analyses of sample 12LF054A, an oscillatory-zoned allanite (Fig. 3.1) from the Hot Springs West pluton

	Rim	Near Rim		Near Core		Core		Near Core	
Al_2O_3	12.6	12.0	11.8	11.8	12.0	11.6	12.0	11.2	12.1
SiO_2	31.5	31.6	34	31.8	31.9	31.5	31.1	32.4	31.5
CaO	8.1	7.8	7.2	7.7	8.26	7.3	7.6	7.5	8.5
TiO_2	3.21	3.72	3.6	3.7	3.53	3.9	4.0	4.13	3.2
Fe_2O_3	15.9	16.0	16.4	16.7	16.8	16.8	16.7	18.1	16.6
La_2O_3	6.79	7.0	5.9	6.61	6.6	6.0	6.0	6.2	7.3
Ce_2O_3	12.8	13.1	12.0	12.7	12.1	12.0	12.8	10.9	12.6
Pr_2O_3	2.0	1.8	1.9	1.6	1.6	2.0	1.9	1.2	1.5
Nd_2O_3	3.6	3.2	3.46	3.24	3.7	3.7	3.6	3.3	3.5
ThO_2	2.9	3.4	4.0	3.7	3.3	4.9	3.9	5.0	2.7

Notes: Each composition represents the average of three, closely spaced measurements. Analytical error and single-point variability are generally < 10% of the amount present.

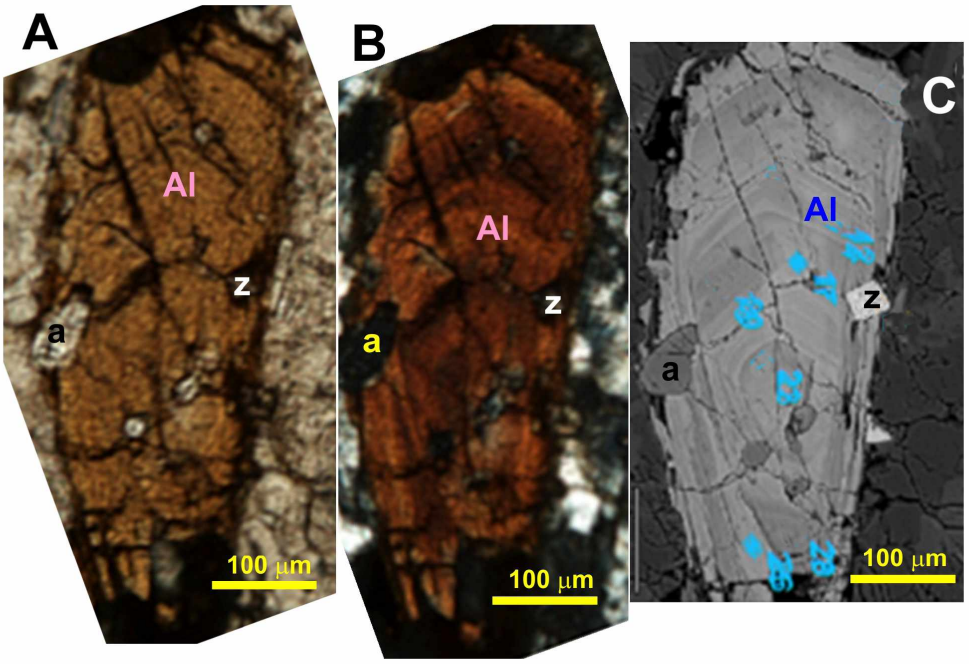

Figure 3.1. Euhedral allanite crystal from Hot Springs West pluton sample 12LF054A showing oscillatory zoning. A) Plane-polarized light; B) crossed polarizers; C) back-scattered electron (BSE) image. The allanite (Al) contains inclusions of zircon (z) and apatite (a) and displays a slightly scalloped edge in BSE, suggesting some magmatic resorption. Analyses are given in Table 3.7.

In other cases, instead of gradual compositional changes, a sharp break separates an earlier, partially resorbed allanite and a later overgrowth (e.g., Fig. 3.2). In the case of allanite from the Sithylemenkat pluton, based on color (transmitted light, Fig. 2.18B) or brightness (BSE, Fig. 3.2) bands, the original core of the allanite is now the lower right edge (points 2-4, Fig. 3.2), and the original large grain is now mostly resorbed. Following resorption, a new allanite completely surrounded (bright area, point 1, Fig. 3.2) the embayed, older allanite. Finally, the newer allanite itself possesses scalloped edges too (bottom of Fig. 3.2), testifying to the final (younger) allanite incompletely redissolving into the melt.

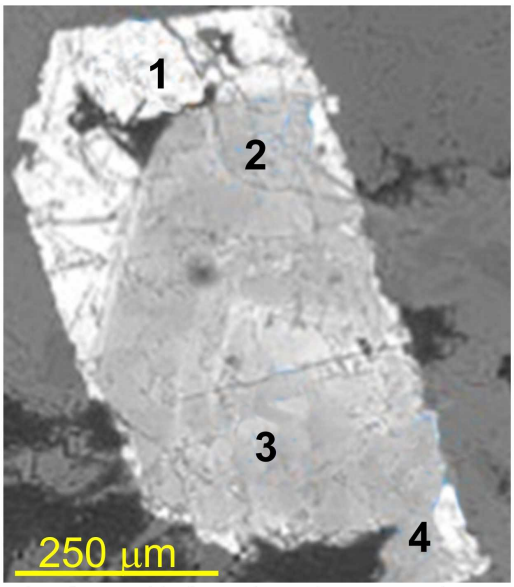

Figure 3.2. BSE image of allanite from Sithylemenkat pluton sample 12RN344A. The brighter rim is a compositionally distinct allanite that grew after the original grain was largely resorbed. Numbers on the image refer to analyses in Table 3.8. This grain is shown in transmitted light as Fig. 2.14B.

The inner, earlier allanite in Figure 3.2 displays oscillatory zoning and a small change in ThO_2 from core (4.8%) to margin (4.2%), accompanied by a slight increase in CaO. The later allanite overgrowth contains significantly higher Ce, Nd, and Ca, and much lower Th, Ti, and Fe.

Table 3.8. Microprobe EDS analyses of multi-stage allanite from Sithylemenkat-pluton sample 12RN344A

	Late-Stage Al		**Rim of Early Al**		**Middle of Early Al**		**Core of Early Al**	
Point	**1**	StDev	**2**	StDev	**3**	StDev	**4**	StDev
Al_2O_3	14.2	0.4	15.9	0.7	14.9	0.2	16.2	0.3
SiO_2	30.14	0.04	30.1	0.4	28.0	0.6	28.8	0.7
CaO	9.6	0.1	7.2	0.4	6.7	0.2	6.03	0.08
TiO_2	1.4	0.1	2.9	0.1	2.81	0.09	3.0	0.1
Fe_2O_3	15.8	0.3	16.9	0.1	21.2	0.9	18.0	0.6
La_2O_3	4.9	0.3	4.8	0.2	4.1	0.4	4.6	0.2
Ce_2O_3	13.6	0.1	12.0	0.9	12.3	0.8	12.6	0.2
Pr_2O_3	2.53	0.05	2.1	0.7	2.54	0.04	2.5	0.3
Nd_2O_3	5.6	0.2	3.4	0.2	3.7	0.1	3.1	0.3
Sm_2O_3	1.2	0.1	0.54	0.07	--	--	--	--
ThO_2	1.1	0.2	4.2	0.5	3.5	0.3	4.8	0.1

Notes: Each analysis is the average of three, closely spaced measurements (points shown on Figure 3.2). "StDev" = standard deviation from three measurements; actual analytical error may be greater. "--" indicates element analyzed, yet concentrations fell below detection limit, approximately 0.3% Sm_2O_3.

A third texture, allanite destruction, was observed; this occurs as a late-magmatic reaction (e.g., Fig. 2.18C, 2.18D), a hydrothermal reaction, or both (Fig. 3.3). In Figure 3.3A, compositionally zoned allanite (Table 3.9) contains microveinlets of monazite (bright areas on BSE image), along with intergrown almandine garnet (Gt 1). If the garnet were simply an inclusion, one would expect to see more grains elsewhere in the slide, outside of the allanite. No such garnets occur. Consequently, I interpret the garnet as part of a (late-magmatic?) breakdown of allanite, simplistically:

$$3CaCeAl_2FeSi_3O_{12}(OH) + Ca_5(PO_4)_3(OH) \leftrightarrow 3CePO_4 + 3Ca_2FeAl_2Si_3O_{12} + 2CaO(melt) \qquad (15)$$

allanite apatite monazite garnet

In Figure 3.3B, early allanite (with moderate Th and Ti concentrations) is partly surrounded by a later, Ti- and Th-poor, Mn-bearing allanite (bright rim in BSE image, Table 3.9). In the center of the grain is another garnet, which is intergrown with a low-Ti, low-Th, high-Mn allanite that I interpret to be a replacement of an earlier, high-Ti, high-Th allanite. Both the unusual presence of the garnet and the composition of the allanite (akin to the late-stage rim of a neighboring allanite) suggest replacement. The specifics of this process appear quite complex.

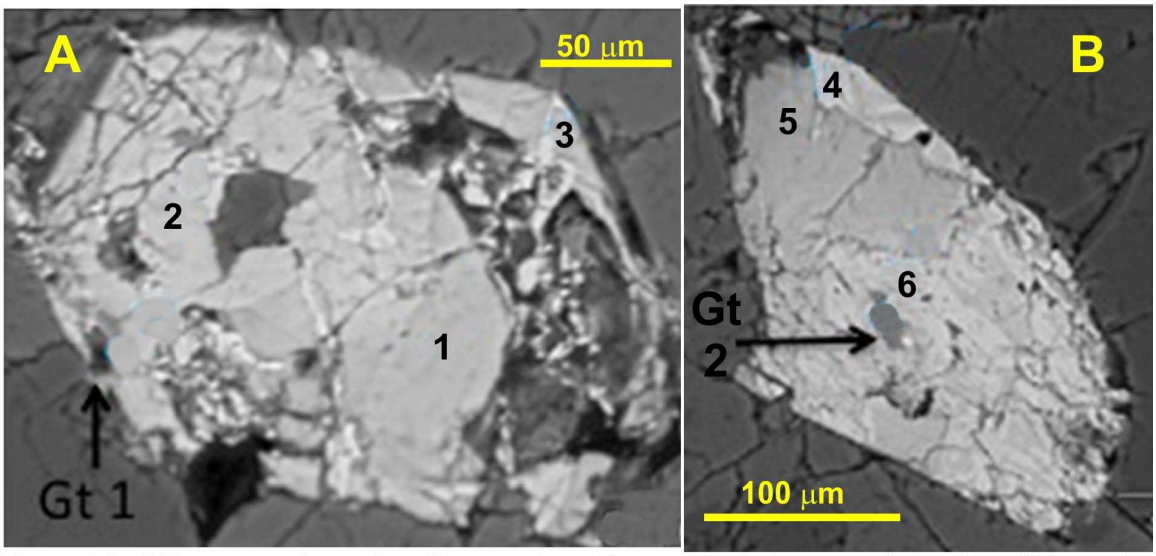

Figure 3.3. BSE images of complex allanite grains with garnet inclusions (reaction products?) from Fort Hamlin Hills-pluton sample 12NR461B. Numbers correspond to analysis locations (Table 3.5).

Table 3.9. Microprobe EDS analyses of complex allanite grains from the Fort Hamlin Hills-pluton sample 12RN461B

	Grain A						Grain B					
	Near Core		Interior		Rim		New Rim		Old Rim		Altered Core	
Point	**1**	SD	**2**	SD	**3**	SD	**4**	SD	**5**	SD	**6**	SD
Al_2O_3	15.0	0.2	13.7	0.2	18.5	0.1	16.2	0.1	16.2	0.1	16.6	0.3
SiO_2	29.6	0.4	31.5	0.6	33.7	0.1	31.0	0.1	29.8	0.1	30.8	0.3
CaO	8.1	0.2	8.79	0.06	9.7	0.1	8.3	0.1	7.8	0.2	8.0	0.1
TiO_2	2.8	0.2	3.10	0.04	<0.2	--	0.44	0.03	2.6	0.1	0.51	0.04
MnO	<0.2	--	<0.2	--	<0.3	--	1.34	0.02	<0.2	--	1.54	0.07
Fe_2O_3	16.8	0.5	16.4	0.2	13.9	0.1	14.2	0.2	15.5	0.2	14.8	0.1
Y_2O_3	3.7	0.4	<0.4	--	<0.4	--	<0.4	--	3.9	0.1	<0.4	--
La_2O_3	5.5	0.4	6.0	0.3	5.8	0.6	5.49	0.06	5.1	0.5	5.4	0.1
Ce_2O_3	11.4	0.5	13.8	0.2	12.6	0.3	15.4	0.1	11.9	0.2	14.8	0.3
Pr_2O_3	1.0	0.4	1.4	0.2	0.85	0.08	1.89	0.03	1.49	0.01	1.6	0.2
Nd_2O_3	2.3	0.7	2.7	0.2	3.1	0.4	4.8	0.1	2.5	0.2	5.0	0.1
Sm_2O_3	<0.3	--	0.56	0.01	1.10	0.02	0.19	0.06	0.54	0.07	0.5	0.2
ThO_2	3.1	0.2	2.0	0.1	0.62	0.06	0.77	0.09	2.7	0.2	0.66	0.08

Notes: Each analysis is the average of three, closely spaced measurements (points shown on Figure 3.3). "StDev" = standard deviation for the three measurements; actual analytical error may be greater. "--" indicates element concentration is below detection limit.

Although most of the central Ruby batholith plutons contain at least traces of allanite, the compositions vary in different fashions among the plutons. Given the highly zoned character of many allanite grains, an "average" composition for a pluton is problematic, but the averages do illustrate important similarities and differences (Table 3.10). In particular, (1) Allanite with detectable MgO is restricted to the northern plutons; (2) allanite with significant P_2O_5 (P substitutes for Si in the T site) is only present in the Bonanza pluton; (3) detectable MnO is restricted to the southern plutons; (4) detectable Y is restricted to transitional plutons (Kanuti Northeast and Hot Springs West are both significantly younger than the others; the Fort Hamlin Hills pluton shares some characteristics of both the northern and southern pluton groupings); and (5) the maximum wt% CaO is much higher for allanite from the two northernmost plutons, Bonanza and Kanuti.

Table 3.10. Average allanite compositions (wt% oxide) for many plutons of the central and southern Ruby batholith

Pluton	Bonanza	Kanuti West	Kanuti Northeast	Hot Springs West	Fort Hamlin Hills	Ray River	Sithyl-emenkat	Ray Mntns East
MgO	1.5	0.9	0.8	0.2	--	--	--	--
Al_2O_3	17	15	15	12	16	16	16	15.8
SiO_2	25	33	34	32	31	32	30	31.5
P_2O_5	5.2	--	--	--	--	--	--	--
CaO	8.2	10.3	11	8.2	8.6	8.8	7.6	9.0
TiO_2	2.3	2.8	1.9	3.4	1.8	0.9	2.4	0.7
MnO	--	--	--	--	0.6	1.3	--	--
Fe_2O_3	19	15	15	17	16	15	17	14
Y_2O_3	--	--	0.9	1.2	2.7	--	--	--
La_2O_3	4.3	5.1	5.0	5.7	5.5	5.8	4.8	6.9
Ce_2O_3	10.5	10.4	11	12	13	14	13	14.5
Pr_2O_3	2.0	1.5	1.3	1.5	1.4	1.5	2.3	2.0
Nd_2O_3	2.5	1.8	2.6	3.0	3.3	3.6	4.1	3.8
Sm_2O_3	0.4	0.5	1.1	0.3	0.5	0.5	0.9	0.2
ThO_2	2.8	2.9	1.4	4.0	1.8	1.7	3.3	0.7
max CaO	14.5	17	11	9.5	9.7	9.7	9.9	9.6
at La/Nd*	2.3	3.2	2.3	2.0	1.8	1.7	1.3	1.9

Notes: "--" all or nearly all analyses from the pluton are below detection limit for that element. "at La/Nd" = atomic ratio of La/Nd. Averages taken from data presented in Appendix E.

A final difference between allanite in the various plutons is illustrated by patterns of Th in allanite (Fig. 3.4). Gieré and Sorensen (2004) list several different coupled substitution mechanisms for incorporating Th^{4+} into allanite (Eqns. 1-4, Chapter 1). All but one equation, Equation 2, involve the substitution of Th^{4+} for REE^{3+}; Equation 2 involves Th^{4+} substituting for Ca^{2+}. Given this, one would expect to see Th and Ce inversely related. In fact, the Th-Ce relations in allanite vary among the plutons (Fig. 3.4A). Allanites from the Sithylemenkat, Ray River, and Ray Mountains East plutons plot together with a steep slope (-1.5), which is approximately the weight ratio of ThO_2/Ce_2O_3 (1.6). This is consistent with a simple Ce-Th exchange. Allanites from the Fort Hamlin Hills and Hot Springs West plutons plot a little less steeply, implying an additional exchange mechanism. Allanites from the Bonanza and Kanuti plutons, however, plot as two different groups, low and high Th, with no apparent relation to wt% Ce_2O_3. Instead (Fig. 3.4B), ThO_2 in allanites from the Bonanza and Kanuti plutons shows a negative correlation with wt% CaO.

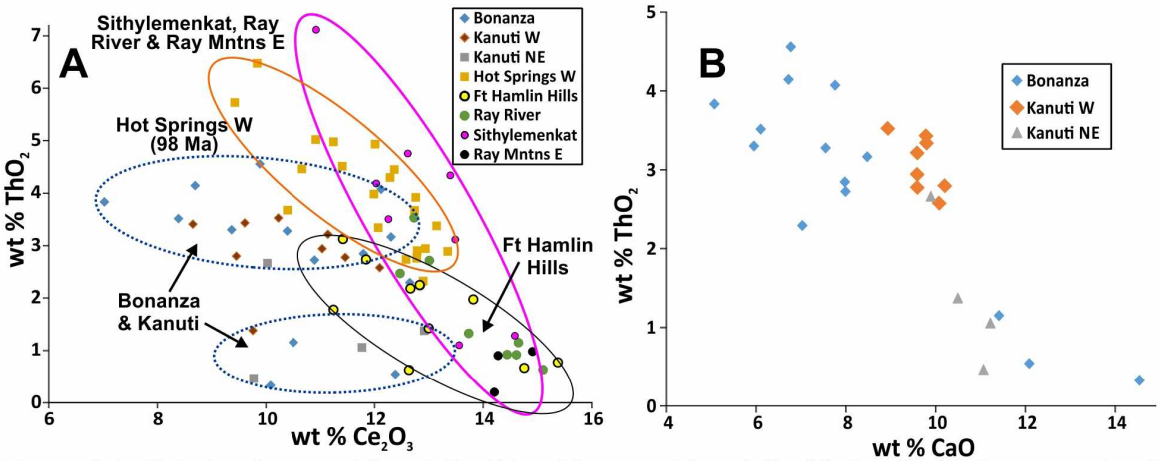

Figure 3.4. Relations between Th and Ce (A) and between Th and Ca (B) for allanite from central and southern Ruby batholith plutons. Each point represents the average of three, closely spaced EDS measurements. Data is given in Appendix E.

The Ti concentrations I measured in allanite are commonly higher than the 1 to 2 wt% TiO_2 given for typical igneous allanites (e.g., Gieré and Sorensen, 2004). Poitrasson (2002), however, reported 1.4 to 4.7 wt% TiO_2 in allanite of Corsican Paleozoic granites, so my values are likely realistic.

Rock TiO_2 can be applied as a robust indicator of magmatic fractionation (Fig. 2.15), so one might expect TiO_2 in allanite to reflect magmatic fractionation as well. Yet the tremendous compositional zoning and multiple allanite generations in some samples complicate this comparison. Nevertheless, a plot of average TiO_2 in allanite vs. TiO_2 in the host granite (Fig. 3.5) shows patterns explainable in terms of different magmatic evolution. First, for a given pluton, lower rock TiO_2 is reflected in lower average allanite TiO_2. Perhaps not too surprisingly—given their similarities in aluminum saturation index (they're all weakly peraluminous, Fig. 2.20)—allanite TiO_2 vs. rock TiO_2 for the Bonanza, Kanuti, and Fort Hamlin Hills plutons plot near a single curve. In contrast, the three moderately peraluminous plutons (Sithylemenkat, Ray River, and Ray Mountains East) for which I have data all plot in very different places on Figure 3.5.

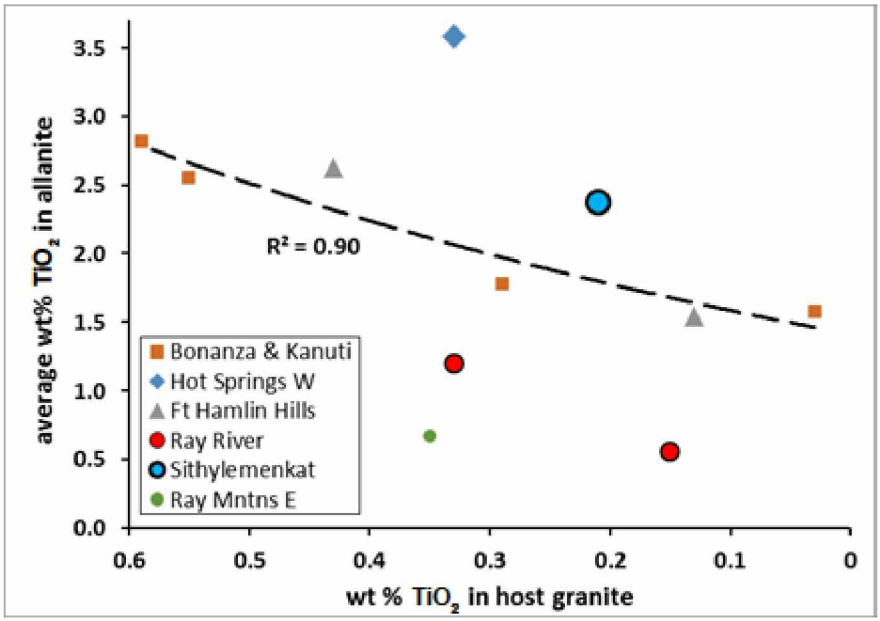

Figure 3.5. Average wt% TiO_2 in allanite vs. wt% TiO_2 in the host granite for plutons of the central and southern Ruby batholith. The dashed line is the best-fit curve through points for the Bonanza, Kanuti, and Fort Hamlin Hills plutons.

3.2.3 Monazite

I confirmed the presence of monazite in plutons of the Ruby batholith using EDS microprobe analyses (Appendix F). I identified monazite in all but the Bonanza, Coal Creek, and Hot Springs West plutons, and the remaining northern and transitional plutons had very little of it when it was identified. The grains in the southern plutons were large enough for microprobe analyses; a summary of the data is presented in Table 3.11. Although the monazites can contain up to 23 wt% ThO_2, they are sufficiently rich in LREE (and Ce) to be officially classified as monazite-(Ce) (Bayliss and Levinson, 1988). Th^{4+} substitutes for REE^{3+} through two different substitution mechanisms (Equations 9, 10, Chapter 1). Consequently, igneous monazite invariably contains sufficient Th to be detected by the microprobe (e.g., Burt, 1989; Förster, 1998a; Broska et al., 2000). The quality of the analyses can be assessed by plotting atomic fraction Th vs. atomic (Si + Ca); they should define a line with slope = 1. Most of my analyses do fall on that line (Fig. 3.6); however, those that fall on the Si + Ca side are essentially monazite-rim compositions measured on grains included in quartz, and thus the excess Si is an artifact of the effective microprobe beam size.

Many of the monazites I analyzed are compositionally zoned; they contain Th-enriched, LREE-depleted cores, gradually zoning outward to Th-depleted, LREE-enriched rims (Figure 3.7).

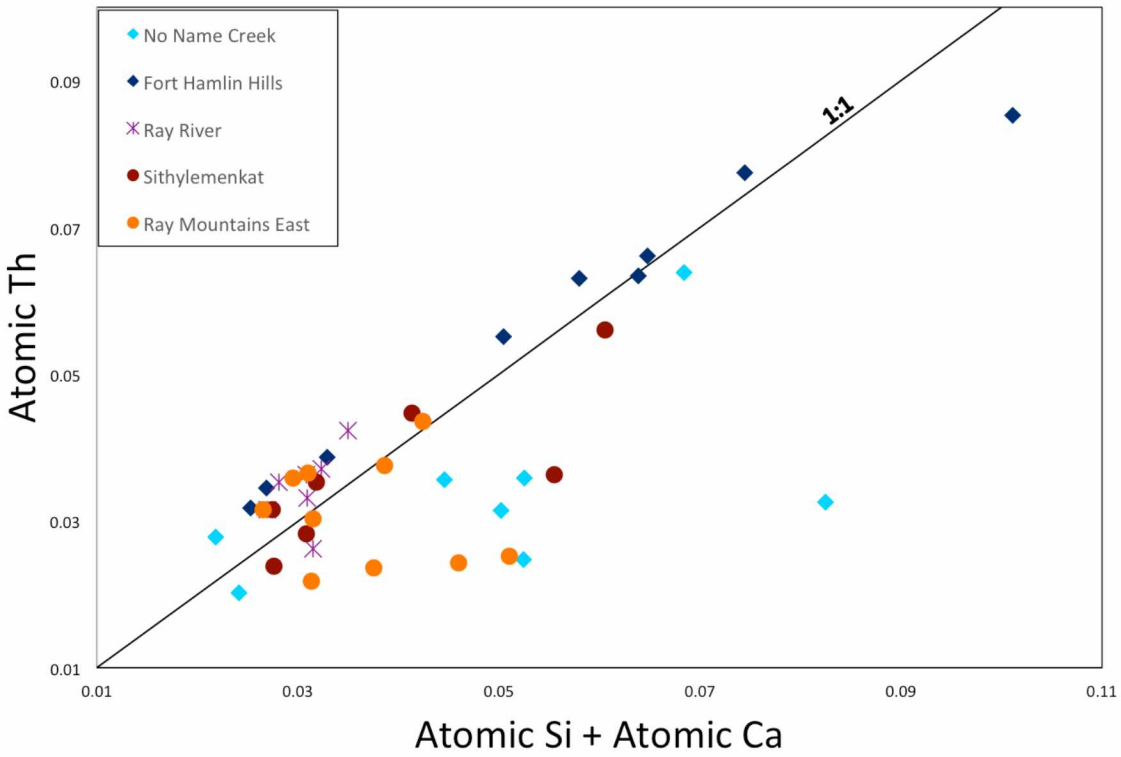

Figure 3.6. Atomic Th vs. atomic (Si + Ca) for monazite analyses (Appendix F) from the central and southern Ruby batholith. Given the substitution mechanisms, the data should fall on the 1:1 line.

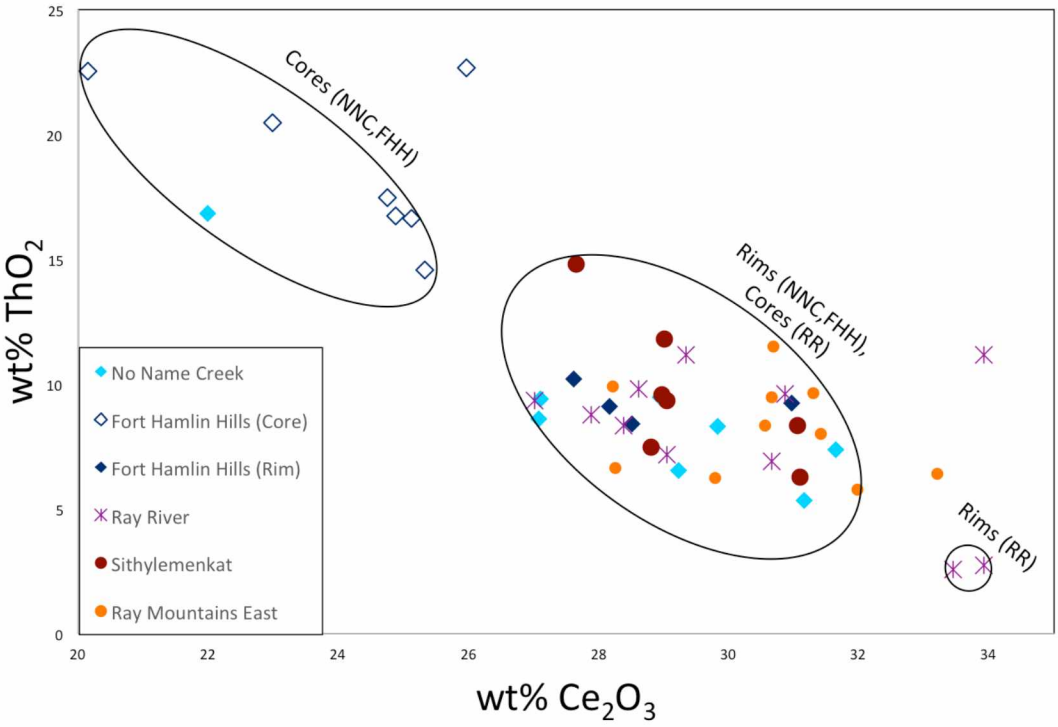

Figure 3.7. Ce and Th concentrations in monazite grains (Appendix F) from plutons of the central and southern Ruby batholith. Typical core and rim populations are identified.

Table 3.11. Microprobe EDS averages and ranges of monazite compositions in the central and southern Ruby batholith plutons

Pluton	No Name Creek $n = 8$				Fort Hamlin Hills $n = 11$			
	Min	Max	Avg	StDev	Min	Max	Avg	StDev
SiO_2	0.7	3.4	1.7	0.8	1.2	4.2	2.5	1.0
P_2O_5	33	36	35	1.2	25	33	30	2.8
CaO	0.3	3.0	1.2	0.8	0.2	2.9	0.7	0.7
Y_2O_3	--	3.9	2.4*	**	--	3.7	2.1*	**
La_2O_3	6.4	12	10	1.7	7.6	13	9.3	1.6
Ce_2O_3	22	32	28	2.9	20	31	26	2.8
Pr_2O_3	2.1	3.8	2.7	0.5	2.5	3.1	2.8	0.2
Nd_2O_3	7.0	8.6	7.8	0.4	6.6	10	8.8	1.0
Sm_2O_3	--	1.7	1.2*	**	--	2.3	1.6*	**
Gd_2O_3	0.6	1.3	1.0	0.3	--	1.9	1.5*	**
ThO_2	5.3	16.8	9.0	3.3	8.4	23	15	5.1

Pluton	Ray River $n = 10$				Sithylemenkat $n = 7$			
	Min	Max	Avg	StDev	Min	Max	Avg	StDev
SiO_2	--	2.0	1.5*	**	1.1	3.2	1.8	0.7
P_2O_5	31	35	33	1.6	28	34	32	1.9
CaO	--	0.64	0.4*	**	0.3	0.8	0.5	0.2
Y_2O_3	--	3.7	2.5*	**	--	3.6	2.4*	**
La_2O_3	10	13	12	0.8	11	13	12	0.9
Ce_2O_3	27	34	30	2.3	28	31	29	1.2
Pr_2O_3	2.1	2.8	2.5	0.2	2.0	2.9	2.3	0.3
Nd_2O_3	7.0	10	9.0	0.9	7.2	8.4	7.8	0.4
Sm_2O_3	1.3	2.1	1.7	0.3	0.8	1.6	1.1	0.3
Gd_2O_3	0.53	1.7	1.0	0.4	0.8	1.3	1.0	0.2
ThO_2	2.6	11	7.7	2.9	6.3	15	9.7	2.6

Pluton	Ray Mountains East $n = 10$			
	Min	Max	Avg	StDev
SiO_2	0.9	2.0	1.4	0.4
P_2O_5	29	35	33	1.9
CaO	0.4	1.1	0.7	0.2
Y_2O_3	--	5.5	3.5*	**
La_2O_3	9.6	15	13	1.5
Ce_2O_3	28	33	31	1.5
Pr_2O_3	2.3	3.4	2.8	0.3
Nd_2O_3	6.6	8.8	7.7	0.7
Sm_2O_3	--	1.5	1.1*	**
Gd_2O_3	--	1.7	1.3*	**
ThO_2	5.8	12	8.2	1.8

Notes: "*n*" = number of analyses. "--" indicates concentration is below detection limit.
* indicates average value calculated using those concentrations above detection limit.
** indicates standard deviation not meaningful due to concentrations below detection limit.
Averages compiled from data presented in Appendix F.

Although allanite and monazite may compete for LREE and Th, they can occur in the same rock. I have microprobed examples from four different specimens, and found that the Th concentration in monazite is 3 to 10 times higher than that of allanite in the same thin section (Fig. 3.8). Considering the zoning present in both minerals, it is unclear if the two minerals are in equilibrium, but the fact that there is a consistent Th-enrichment in monazite is encouraging for some variety of equilibrium.

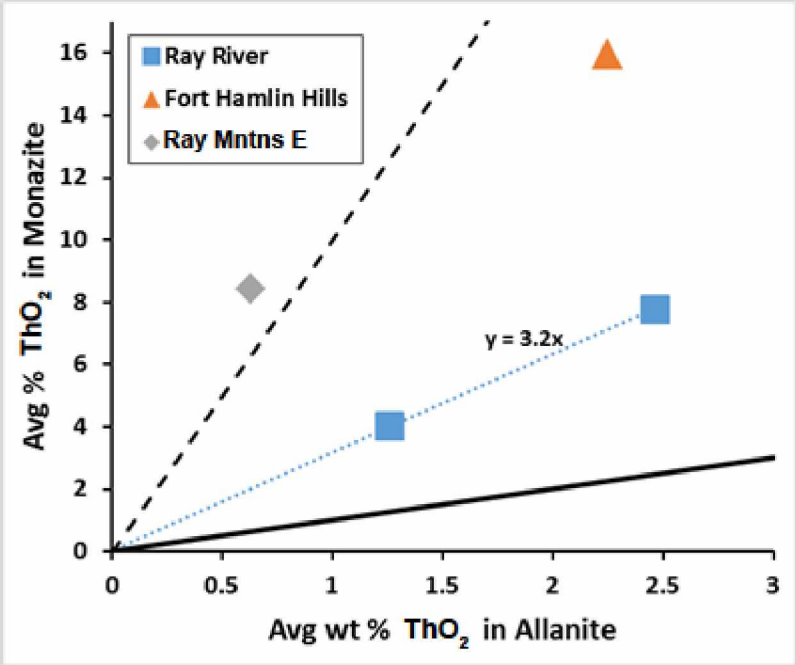

Figure 3.8. Average wt% ThO_2 in monazite vs. average wt% ThO_2 in allanite, with analyses from the same thin section. The solid black line is at 1:1, and the dashed black line is at 1:10. Data is from this study (Appendices E and F).

The most dramatic compositional change in monazite is the zoning in ThO_2; in a single grain, the ThO_2 can decrease from > 20 wt% in the center, to < 10 wt% in the rim. Notably, the monazite from the Fort Hamlin Hills pluton contains higher maximum, minimum, and average wt% ThO_2 than monazite from all other plutons (Table 3.11, Fig. 3.7). Differences in Th content of monazite from the other plutons, however, are not obvious. Less dramatic—but potentially meaningful—is that the crystallizing monazite *should* reflect changes in the REE distribution in the melt. Unfortunately, it is not possible to accurately determine small amounts of Y in a P-rich mineral via EDS on the microprobe. There do appear to be differences in the average Y

concentrations in monazite (Table 3.11), but the data is too scattered to interpret. The relative concentrations of La (the larger of the REE) and Gd (the smallest REE that is sufficiently abundant to be measurable by microprobe EDS) can however be measured readily. Individual mineral grains exhibit mixed patterns. Figure 3.9 shows the changes in average monazite La/Gd for individual thin sections from the various plutons. On that figure, I have noted the wt% TiO_2 in the host granite as a means of assessing trends with fractional crystallization. As TiO_2 decreases with increasing differentiation (Fig 2.15), the decrease in host-rock TiO_2 is a measure of changes in the magma during crystallization.

Plotting wt% La_2O_3 vs. wt% Gd_2O_3 for average monazite from individual rocks indicates two divergent trends: increasing La/Gd with increasing fractionation (decrease in TiO_2), and decreasing La/Gd with increasing fractionation (Fig. 3.9). Samples from the Fort Hamlin Hills pluton display a relative rise in Gd with a decrease in rock TiO_2, an effect I ascribe to allanite-dominated fractionation. (Allanite is much more abundant than monazite in this pluton.) The monazite from the Ray River and NNC plutons display the opposite trend, which I infer to be related to crystallization without much allanite. Samples from the Ray Mountains East pluton mar the simple trend. They—like those samples from the Fort Hamlin Hills pluton—also display increasing Gd with increasing fractionation, though monazite appears to be more abundant than allanite in this pluton based on three thin sections. Further petrographic analysis is needed.

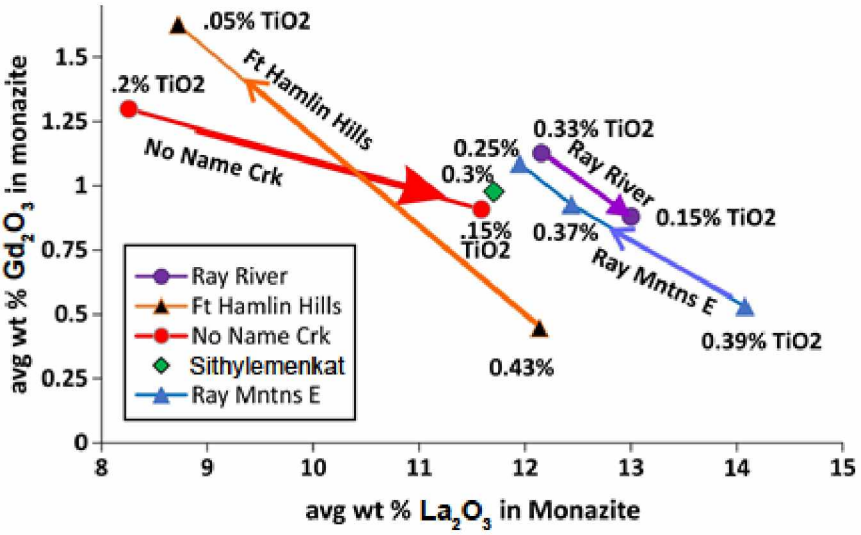

Figure 3.9. Average composition of monazite (wt% La_2O_3 vs. wt% Gd_2O_3) in rocks of the central and southern Ruby batholith. Lines connect samples taken from the same pluton, with arrows pointing in the direction of increasing fractionation (decreasing TiO_2). Data points are labeled with wt% TiO_2 in the host granite as a means of assessing fractionation trends. Data from this study (Appendix F).

3.2.4 Xenotime

Xenotime is common in Ca-poor, peraluminous granites, such as those plutons of the southern Ruby batholith. Xenotime incorporates the majority of the HREE + Y budget in such rocks (Förster, 1998b). I conclusively (via microprobe EDS) identified xenotime-(Y) (YPO_4) in the NNC, Fort Hamlin Hills, Ray River, Sithylemenkat, and Ray Mountains East plutons. Due to the small size of the typical xenotime I analyzed (often less than 10 μm) and the high voltage I used, the excitation bulb (zone excited by the electron beam) was likely, in many cases, larger than the grains I analyzed. That is, the measured "concentration" is a mix of xenotime plus surrounding minerals. Consequently, the analyses need to viewed with caution.

The xenotime analyses from the Ray River pluton (Table 3.12) include considerable Ca, which is likely an artifact caused by the beam overflowing onto surrounding apatites. In contrast, the analysis of a Ray Mountains East xenotime (Table 3.13) contains too much P and insufficient REE. (I excluded the xenotime from the Fort Hamlin Hills pluton, as its measured concentrations were far worse.) In terms of atomic proportions of P and total REE + Y, only the analysis of xenotime from the Sithylemenkat pluton comes close to the ideal ratio (Fig. 3.10A). The negative correlation between atomic (REE + Y) and atomic P results from the energy overlap between Y-Lα and P-Kα X-ray emission lines. For a given intensity peak at that energy, as the software assigns more of the peak to P, it consequently assigns less to Y.

Given the less-than-reliable major-element compositions for most of the xenotime grains, it would not be worthwhile to analyze differences in REE distributions between the various grains. Notably, however, xenotimes from the NNC, Sithylemenkat, and Ray Mountains East plutons do contain significant U and Th. Based on more accurate WDS microprobe analyses of plutonic xenotime, van Emden et al. (1997) and Förster (1998b) suggested the coupled substitution presented in Equation 11 (Chapter 1), in which the actinides substitute for the REE. I plotted atomic Si vs. atomic (U + Th) for plutonic xenotime analyses of Förster (1998b) and obtained a best-fit line with a slope of 1.06 (Fig. 3.10B), reasonably close to the theoretical value of 1. Doing similarly for my data (Fig. 3.10B) yields somewhat encouraging results: for three of the analyses with Si, U and Th above detection, atomic (U + Th) increases with increasing atomic Si. The slope of the best-fit line is wrong, but the trend is correct. Based on that, and the atomic U/Th ratio for my analyses of > 1 (typical of most xenotimes; Förster, 1998b), the U and

Th concentrations are reasonable. Because I only detected U in one of four analyses (Table 3.12), it is likely that the Ray River xenotimes are low in U.

Table 3.12. Microprobe EDS analyses of xenotime for the Ray River-pluton sample 12RN429A

Grain	A	StDev	A	StDev	B	StDev	C	StDev
SiO_2	1.9	0.5	3.2	0.3	3.5	0.5	2.4	0.3
P_2O_5	29.3	0.5	28.9	0.4	29	1	29.3	0.3
CaO*	2.0	0.3	4.7	0.5	1.2	0.2	0.7	0.1
TiO_2	--	--	0.3	0.1	0.5	0.1	--	--
Y_2O_3	47	1	44	1	46	1	45.7	0.4
Sm_2O_3	1.8	0.2	1.4	0.2	1.3	0.1	1.8	0.2
Gd_2O_3	2.9	0.3	2.7	0.1	3.1	0.5	3	0.2
Dy_2O_3	6.2	0.5	6	0.3	6.3	0.6	7.1	0.3
Ho_2O_3	1.8	0.2	1.3	0.3	1.4	0.2	1.8	0.2
Er_2O_3	3.8	0.3	3.5	0.2	3.6	0.3	4.0	0.2
Yb_2O_3	2.3	0.1	2.1	0.2	2.7	0.3	2.7	0.1
UO_2	--	--	0.53	0.04	--	--	--	--

* CaO is almost certainly an analytical artifact and should be ignored.
Notes: Each analysis is the average of three, closely spaced measurements. "StDev" = standard deviation for the three averaged measurements; analytical error is likely greater. "--" indicates concentration below detection limit.

Table 3.13. Microprobe EDS analyses of xenotimes from three plutons of the central and southern Ruby batholith

Pluton	No Name Creek						Sithylemenkat		Ray Mntns E	
Sample	12RN319A				12LF304A		12RN341A		12LF212A	
Grain	1	StDev	2	StDev	3	StDev	4	StDev	5	StDev
SiO_2	3.5	0.4	2.1	0.2	1.2	0.1	--	--	--	--
P_2O_5	28	1	28.8	0.3	29.2	0.5	36	6	43*	3
Y_2O_3	47	1	48.6	0.5	48.5	0.1	44	5	32*	1
Sm_2O_3	0.5	0.2	0.5	0.1	0.6	0.2	0.4	0.1	--	--
Gd_2O_3	1.9	0.1	1.9	0.2	2.4	0.1	2.0	0.1	2.1	0.3
Tb_2O_3	--	--	--	--	1.4	0.3	1.1	0.3	2.0	0.3
Dy_2O_3	4.9	0.5	5.0	0.1	6.5	0.3	5.7	0.3	7.6	0.5
Ho_2O_3	1.4	0.4	1.7	0.3	1.6	0.3	1.8	0.3	1.7	0.3
Er_2O_3	3.2	0.2	3.8	0.1	3.6	0.5	3.9	0.3	4.2	0.7
Yb_2O_3	2.1	0.3	2.3	0.4	2.9	0.3	2.5	0.5	2.9	0.2
ThO_2	2.2	0.1	1.6	0.3	0.7	0.2	1.0	0.1	1.2	0.2
UO_2	3.8	0.2	3.4	0.6	1.3	0.2	1.5	0.2	2.5	0.3

* = unreliable measurement.

Notes: Each analysis is the average of three, closely spaced measurements. "StDev" = standard deviation for the three averaged measurements; analytical error is likely larger in most cases. "--" indicates below detection limit.

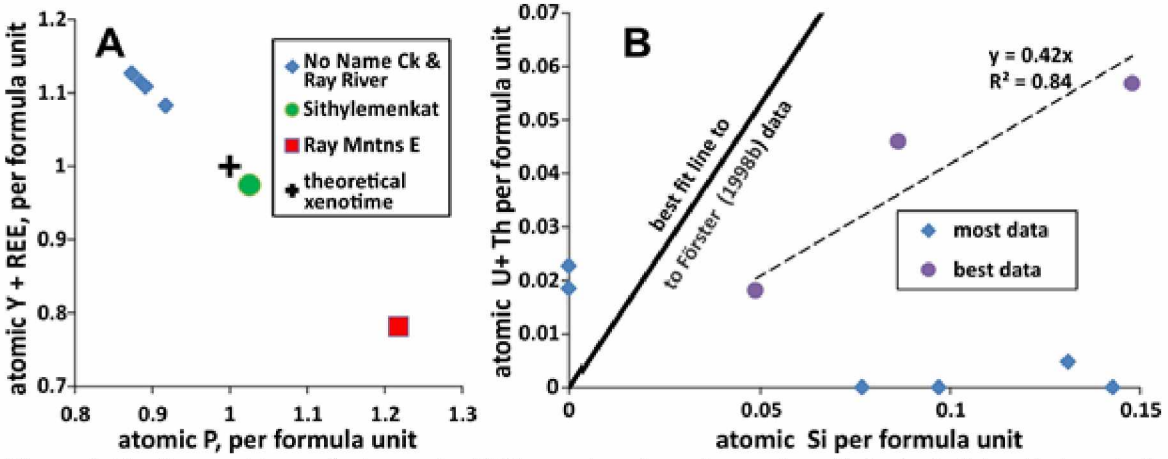

Figure 3.10. Compositions of microprobe EDS xenotime from the southern Ruby batholith. A) Atomic P vs. atomic (Y + REE); B) Atomic Si vs. atomic U + Th. The major element analyses are not very good, but the U + Th is likely real. Data from Förster (1998b) and this study.

3.2.5 Titanite

Although officially $CaTiSiO_5$, the actual composition of titanite is considerably more complex and can include significant amounts of REE (e.g., Ackerson, 2011). I analyzed titanite from the Bonanza, Kanuti, and Hot Springs West plutons (Tables 3.14, 3.15) and found measurable Y in the more Fe-rich grains and portions of grains (Fig. 3.11). Based on my limited data, Y concentration rises with increasing Fe, and is not detectable (by microprobe EDS) for titanite with less than approximately 2 wt% Fe_2O_3. I ascribe the need for Fe to the coupled substitution:

$$Ca^{2+} + Ti^{4+} \leftrightarrow Y^{3+} + Fe^{3+} \qquad (16)$$

I was unable to detect REE in the analyses, which is significant because Ce is typically 4 to 5 times as abundant in rocks as is Y. The variable presence of Y without Ce indicates that the titanite in these rocks is HREE enriched.

Table 3.14. Representative titanite analyses from the Hot Springs West pluton

Sample	12RN364A, Titanite 1			12RN364A, Titanite 2				
Location	Rim	Interior	Core	random points				StDev*
Al_2O_3	2.5	2.6	2.7	2.6	2.6	2.6	2.6	0.2
SiO_2	30.9	31.2	30.6	30.8	30.6	30.9	30.9	0.3
CaO	28.0	28.7	26.3	28.8	28.1	28.4	28.4	0.2
TiO_2	35.3	35.7	33.8	35.4	35.2	35.9	35.9	0.4
Fe_2O_3	2.3	1.9	3.0	2.0	2.5	1.9	1.9	0.2
Y_2O_3	1.0	0.1	3.6	--	1.0	--	--	0.1

Notes: "StDev" = representative 1 sigma standard deviation for the set of analyses. "--" = below detection limit (approximately 0.5 wt% Y_2O_3).

Table 3.15. Representative titanite analyses from northern plutons, Ruby batholith

Pluton	Kanuti Northeast				Kanuti West				Bonanza	
Sample	12LF246A				12LF002A				12RN375B	
Location	Grain 1	Grain 2	Grain 3	StDev	Rim	Core	Rim	StDev	Grain 1	StDev
Al_2O_3	1.6	1.3	2.6	0.1	1.3	1.3	1.3	0.2	2.3	0.3
SiO_2	31.1	31.0	30.9	0.3	31.0	30.8	30.6	0.2	31.0	0.9
CaO	29.0	29.5	29.0	0.1	29.0	29.0	29.1	0.1	28.0	0.5
TiO_2	37.3	37.1	36.4	0.2	36.6	36.5	36.6	0.3	35.8	0.7
Fe_2O_3	1.0	1.1	1.1	0.1	1.8	1.9	2.1	0.1	2.2	0.2
Y_2O_3	--	--	--		--	--	--		0.8	0.2

Notes: Only one titanite analyzed for sample 12LF002A. "StDev" = representative 1 sigma standard deviation for the set of analyses. "--" = below detection limit (approximately 0.5 wt% Y_2O_3).

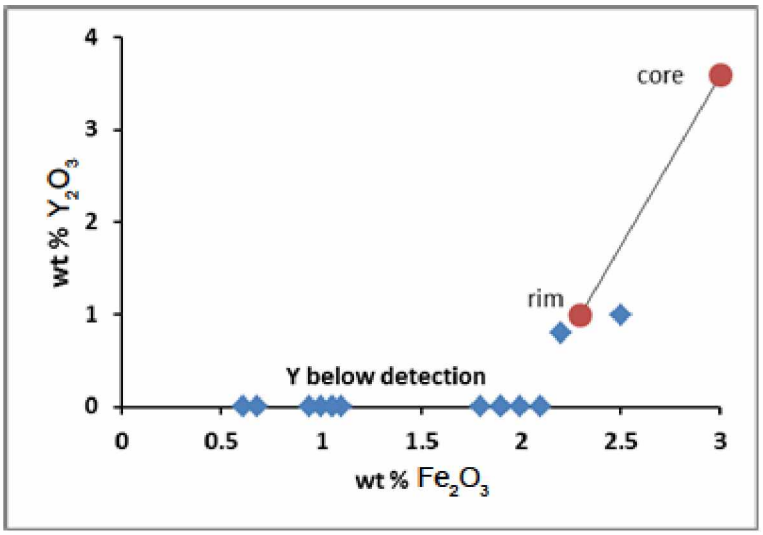

Figure 3.11. Wt% Fe_2O_3 vs. wt% Y_2O_3 for titanite from the Bonanza, Kanuti, and Hot Springs West plutons. Points plotting at zero Y_2O_3 are actually below detection limits with EDS, approximately 0.5 wt%. The two connected points are from the core and rim of a single titanite from sample 12RN364A.

3.2.6 Summary of Mineral Compositions and Relations

By measuring REE, Y, and Th concentrations in a variety of minerals known to occur in the Ruby batholith, I have established that several minerals are likely important in the fate of these elements during fractional crystallization. Titanite contains significant Y and, by inference, HREE. Allanite and monazite predominantly contain LREE and Th, and the occurrence of either one mineral or both within a pluton has significant implications about REE partitioning and melt chemistry during fractionation. Finally, xenotime is both the primary carrier of HREE + Y (at least in the southern plutons of the Ruby batholith) and is also an

important host for U. I anticipate that the mineralogical characteristics of the plutons will be of importance in understanding their trace-element patterns.

3.3 TRACE-ELEMENT FRACTIONATION

Titanium decreases uniformly with progressive crystal fractionation (e.g., Lehmann, 1982; Swanson et al., 1988). Therefore, I employ Ti as a proxy for the degree of fractionation of the granitic melt. Samples collected from the Bonanza, Kanuti, Coal Creek, Fort Hamlin Hills, and Ray Mountains East plutons show an extensive range in Ti concentrations. Samples from the Hot Springs East, Hot Springs West, Ray River and Sithylemenkat plutons show moderate Ti concentrations. Finally, multiple sampling efforts failed to locate NNC pluton samples with greater than 0.25 wt% TiO_2. The Melozitna pluton, located southwest of the Sithylemenkat pluton and hence outside of the study area, is included in this section to offer further comparison and to enhance trends.

3.3.1 Spatial Elemental Patterns Suggesting Inward Crystallization of Plutons

I have previously shown—based on progressive inward decrease in TiO_2—the Sithylemenkat pluton appears to have undergone progressive inward crystallization, with early crystallized minerals concentrated at the margins and later-crystallizing minerals concentrated toward the center (Fig. 2.15). In a similar manner, spatial distribution of LREE/(HREE + Y) in rocks from the Sithylemenkat, Ray River and NNC plutons is similarly compatible with changes related to inward crystallization (Fig. 3.12). In contrast, the transitional Fort Hamlin Hills pluton either lacks systematic patterns, or has not been sufficiently sampled to observe patterns. More notably, only a small portion of the Sithylemenkat pluton contains rocks with low ratios, whereas at least a quarter of the Ray River pluton has such low ratios. Given the evidence for individual granitic bodies of multiple ages and character in the Kanuti "pluton", I would expect complex patterns. Similarly, the Ray Mountains West pluton, with zones characterized by radical changes in initial $^{87}Sr/^{86}Sr$ (Fig. 2.6), must consist of separate magma bodies, even if all are of approximately the same age. The lack of evidence, however, for multiple age events in most of the plutons suggests that a simple fractional crystallization model may be appropriate.

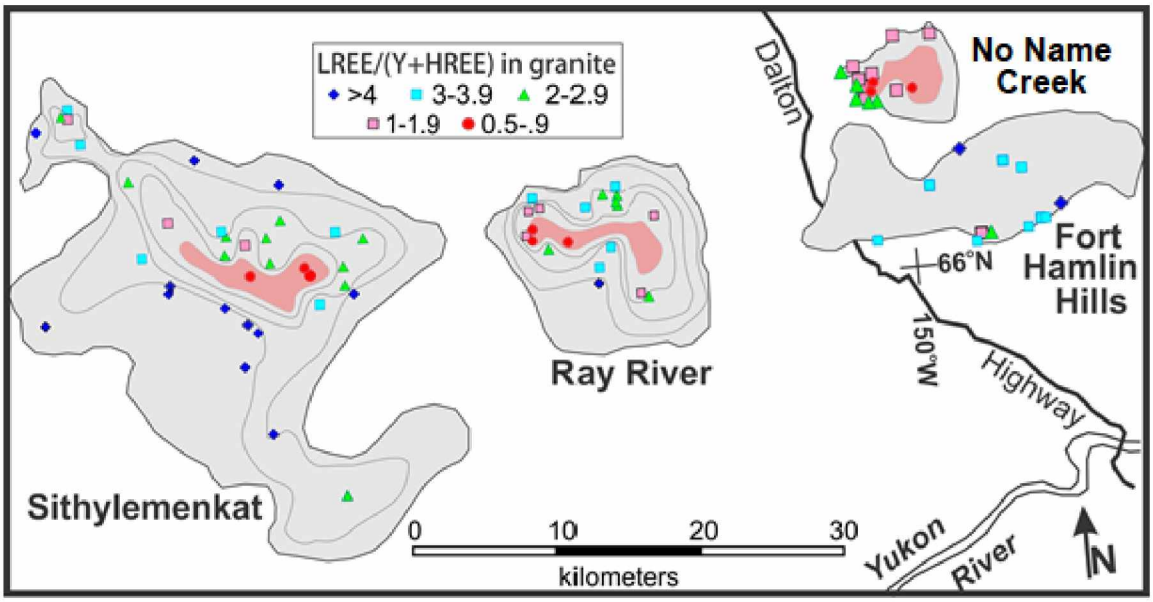

Figure 3.12. Spatial distribution of LREE/(HREE + Y) ratios for granitic rocks from the NNC, Fort Hamlin Hills, Ray River and Sithylemenkat plutons. Data from Arth et al. (1989) and this study.

3.3.2 Pluton Elemental Trends as Functions of TiO_2

Rubidium is well characterized as a +1 ion that is too large to be easily accommodated into most silicate minerals. Consequently, the concentration is well documented as rising with increasing fractionation (Taylor, 1965; Imeokparia, 1981). For plutonic rocks of the Ruby batholith, Rb displays a clear increase in concentration with decreasing TiO_2 (Fig. 3.13), especially at very low wt% TiO_2. Such behavior is consistent with a fractional crystallization model, and suggests that one of the major differences between the northern, transitional, and southern plutons is the degree to which the pluton has undergone fractional crystallization. If a melt is truly rejected from all crystallizing minerals, then as the amount of melt drops from 100% melt (no crystallization) to 10% melt (90% crystallized), the "rejected" element will increase in concentration by a factor of 10. For an element that is only partly rejected, the increase will be less, but still significant. Viewing Rb vs. TiO_2 (Figure 3.13) in this manner, the southern plutons appear to have undergone a greater degree of fractional crystallization, and perhaps more efficient fractional crystallization. Forecasting to pre-fractionation magmas, for instance, with 0.7 wt% TiO_2, the original Rb contents of the southern-pluton melts were approximately 300 ppm, compared to approximately 130-180 ppm for the northern and transitional plutons. On this and future diagrams, there is no data available for Hot Springs East rocks with less than 0.15

wt% TiO_2. The magenta line representing the best fit for the Hot Springs East pluton *could* trend steeply upward at a low TiO_2 concentrations, but there is no way to know with the present data set. Similarly, data for the Coal Creek pluton appear to fit with the southern trend, but lacking rocks with less than 0.1 wt% TiO_2, the method of fractionation is unclear. Finally, the NNC data plots in an anomalous manner relative to all others; it contains far more Rb for its TiO_2 concentrations than does any other pluton.

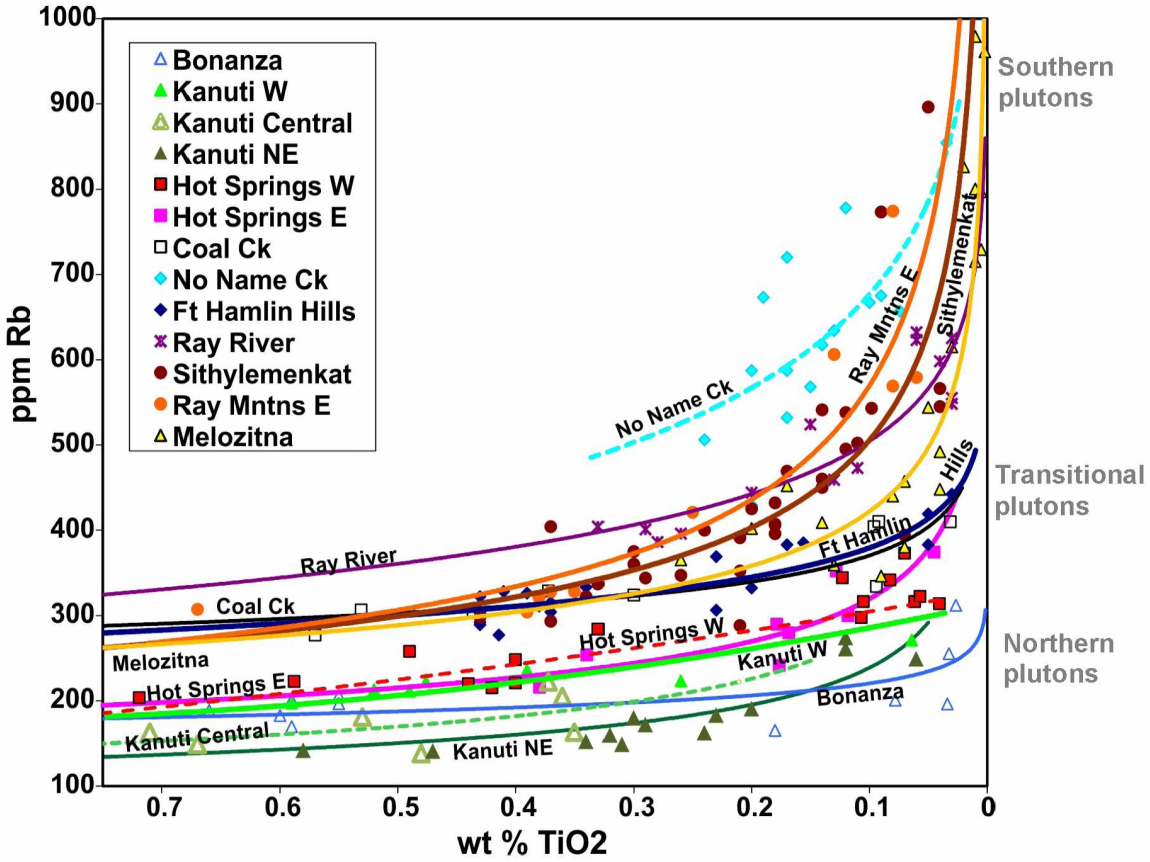

Figure 3.13. Rb vs. TiO_2 for rocks of the central and southern Ruby batholith plutons. Each point represents one sample; trend lines are best-fit curves. Note variably projected initial Rb concentrations. Data is from Clautice (1983), Barker and Foley (1986), Miller (1989), Barker (1991a), Clautice et al. (1993), Solie et al. (1993), Lough et al. (2012), and this study.

A major control on element behavior during fractional crystallization is the oxidation state of the magma, as this controls the relative abundances of Fe-Ti-bearing minerals (ilmenite, titanomagnetite, titanite), and the tendency for an element to be incorporated into a mineral depends on its oxidation state. Sn^{2+}, for example, is too large to substitute into magnetite (or any other common mineral), and thus concentrates into a melt with a low oxidation state (Chappell

and White, 2001). Under oxidizing conditions, Sn^{4+} becomes the predominant form, and this ion is readily incorporated into magnetite, and is hence lost from the magma during fractionation.

I have previously shown (Chapter 2) that significant differences in oxidation states of the plutons are recorded by their magnetic susceptibilities and Fe_2O_3/FeO ratios (Table 2.1, Figs. 2.12, 2.13). Another test for variable oxidation state involves Eu and immediately adjacent REE. The REE are generally trivalent cations; however, Eu is divalent in reduced environments and trivalent under oxidizing conditions. Eu^{2+} readily substitutes for Ca^{2+} (e.g., in plagioclase) if the oxidation state is low enough. At higher oxidation states, Eu^{3+} behaves like other REE. As Eu^{2+} leaves the melt for crystallizing feldspar, the melt becomes depleted in Eu relative to the other REE. The Eu anomaly, symbolized by Eu*/Eu, is the concentration of Eu the melt *would* have if Eu behaved like its neighboring REE, divided by its actual concentration (de Baar et al., 1985). Thus,

$$Eu/_{Eu^*} = \frac{2Eu}{Sm + Gd} \qquad (17)$$

where each element is a concentration (ppm). Negative Eu anomalies are typical of low-oxidation state granites, and large negative Eu anomalies are characteristic of highly fractionated granites. The Ruby batholith is no exception. All plutons have negative Eu anomalies, the degree of which varies (Fig. 3.14). The northernmost Bonanza and Kanuti plutons, along with the transitional Hot Springs East pluton, have moderate Eu anomalies (Eu/Eu* ≈ 0.2) that do not become larger with increasing fractionation (decreasing TiO_2). The other plutons develop Eu/Eu* values as low as 0.01. A straightforward explanation is the northern plutons experienced a relatively high oxidation state, while the others are not as oxidized. Note the tremendous contrast in behavior between the Hot Springs East and Hot Springs West plutons.

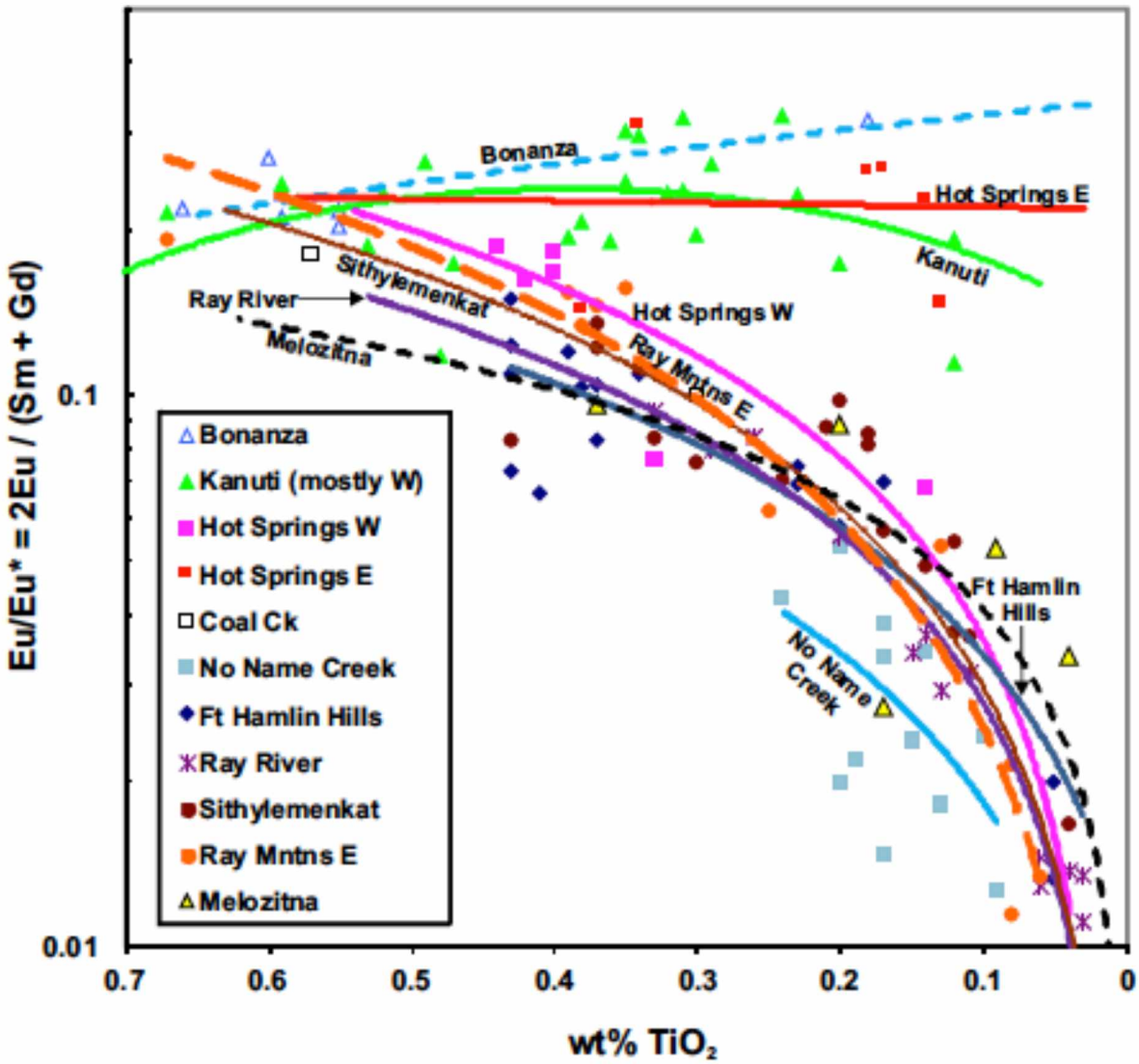

Figure 3.14. Eu/Eu* vs. TiO_2 for rocks of the central and southern Ruby batholith. Best-fit trend lines indicate extreme Eu anomalies for all of the southern plutons. Data sources given with Fig. 3.13.

The likely effect of magmatic oxidation state is seen in the patterns of ppm Sn vs. wt% TiO_2 (Fig. 3.15). Plutons with evidence of a high-to-moderately high oxidation state (from Fe_2O_3/FeO ratios and magnetic susceptibility) show no tendency to concentrate Sn; rather, their patterns are ones of moderate decreases in Sn with decreasing TiO_2 (increasing fractionation). Only the plutons with low oxidation states—those that lack magnetite (Table 2.6)—show Sn enrichment with fractionation. A poorly defined trend involving the NNC pluton samples is consistent with an increase in Sn as Ti decreases to about 0.15 wt% TiO_2; further fractionation causes a major drop in Sn concentration. Alternatively, the rocks have been altered and their Sn contents do not accurately reflect the magmatic concentrations.

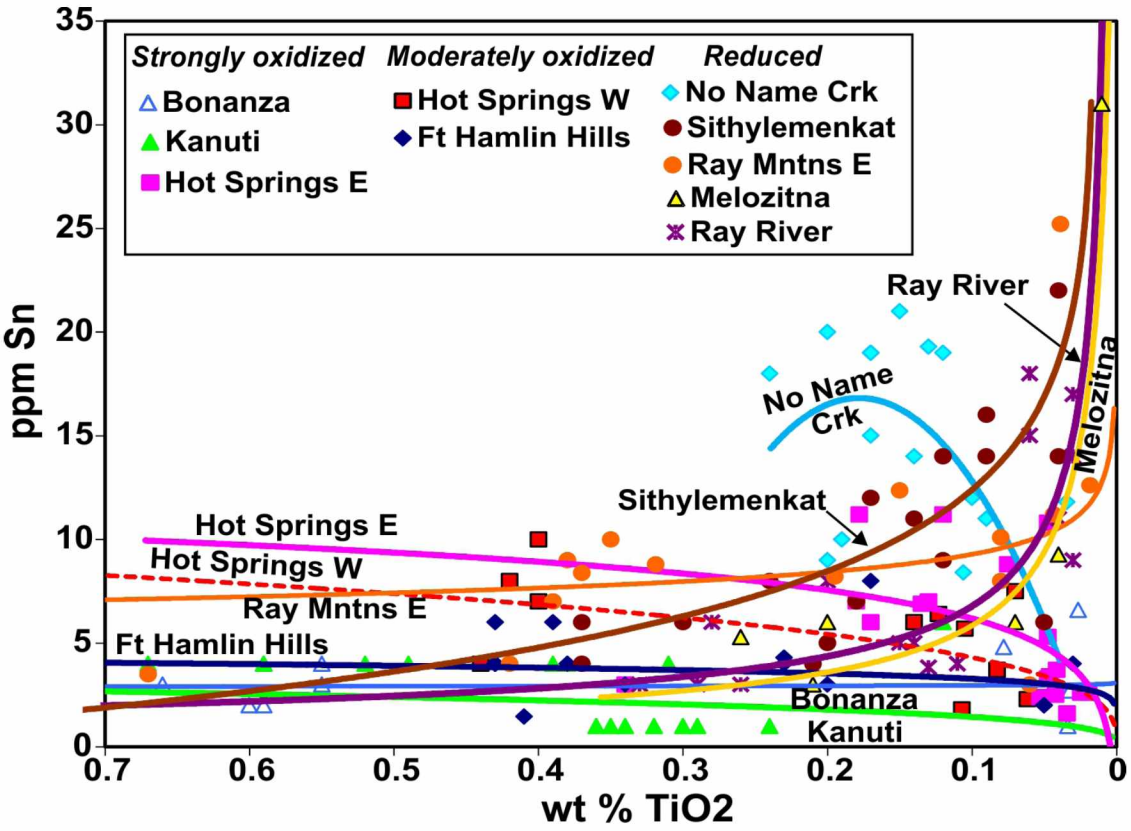

Figure 3.15. Sn vs. TiO_2 concentrations for rocks of the central and southern Ruby batholith. Grouping by oxidation state is based on rock magnetic susceptibility and Fe_2O_3/FeO ratios (Fig. 2.16). Data from sources listed with Fig. 3.13.

Although they are technically major elements, Ca and P play important roles in the precipitation of REE-carrying phases and need to be considered. Figure 3.16 shows the variations in changes of wt% CaO and wt% P_2O_5 as functions of rock TiO_2. The northern and few transitional plutons show similar behavior, with a moderately steep increase in Ca while TiO_2 increases (Fig. 3.16A). The northernmost plutons (Bonanza, Kanuti, Hot Springs East and Hot Springs West) project back to 3 to 3.5 wt% CaO with 0.75 wt% TiO_2, which is nearly twice as great as the projected CaO for the southern plutons. That is, the northernmost plutons started as granitic melts with significantly higher CaO and lower Rb than the southern melts. These higher CaO magmas would necessarily tend to precipitate high-Ca phases, such as hornblende, titanite, allanite, and apatite. In contrast, the southern plutons show only a modest increase in Ca with increasing TiO_2, indicating that even the most primitive precursors were relatively Ca-poor.

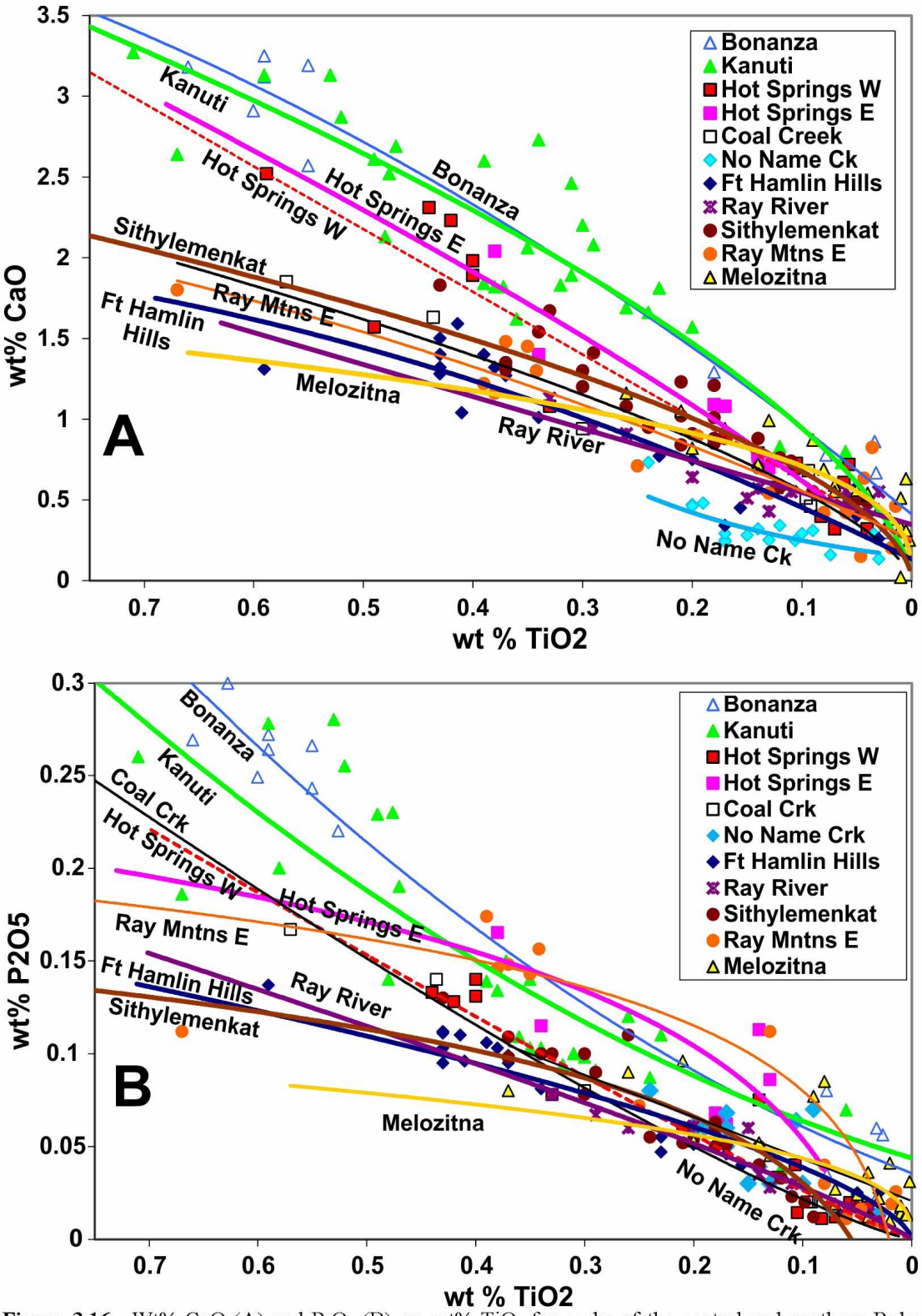

Figure 3.16. Wt% CaO (A) and P_2O_5 (B) vs. wt% TiO_2 for rocks of the central and southern Ruby batholith. Data from sources listed with Fig. 3.13.

The Ruby batholith plutons exhibit P_2O_5 vs. TiO_2 trends (Fig. 3.16B) broadly similar to their CaO trends; namely, the northern plutons show relatively steep increases with increasing TiO_2, and southern plutons express less exaggerated changes. The likely cause (and effect!) was crystallization of abundant apatite in the northern plutons, seen very commonly as apatite needles as inclusions in biotite and plagioclase (and locally, allanite). Although initially lower in P_2O_5 than the northern plutons, limited apatite crystallized from these melts and an abrupt decrease in P_2O_5 is only seen at a TiO_2 of about 0.1 wt%. Note that in this aspect, the Hot Springs East pluton displays a P_2O_5-TiO_2 trend much more like the southern than the northern plutons.

Behavior of the HREE is best modeled by examination of trends for Y, as Y is much more abundant than any of the HREE and is easily measured in rocks by X-ray fluorescence analysis. I have found significant Y concentrations in titanite, monazite, allanite and, of course, xenotime (Tables 3.7-3.15) in the Ruby batholith plutons by microprobe EDS studies. Consequently, the magmatic fractionation of Y should be affected by the abundant variations of Ca and P. In fact, ppm Y vs. wt% TiO_2 (Figure 3.17A) shows that Y behavior can be viewed largely in terms of crystallization of magmatic titanite vs. xenotime. All the plutons—aside from NNC—have trends that project back to an initial Y concentration of about 30 ppm for a magma containing 0.7 wt% TiO_2. Within the accuracy limits of such projections, there are no significant differences in initial Y content between northern and southern Ruby batholith plutons. As fractionation progresses, the trends deviate. All of the northern (titanite-bearing) plutons display slowly decreasing Y with increasing fractionation. If the zoned titanite from the Hot Springs West pluton (Fig. 3.11) is representative, then a fall in the Y content of the titanite as it crystallizes reflects a decrease in the Y content of the magma. Crystallization of allanite, which also contains Y, further partitions Y, removing it from the melt and preventing concentration. The formation of titanite is favored both by the higher oxidation state and the higher Ca content of the northern plutons. Allanite is similarly favored by these conditions, particularly high Ca.

In contrast, most of the southern plutons show patterns of Y enrichment with increasing fractionation (Fig. 3.17A). Based on my exhaustive hunt for the elusive xenotime in the southern plutons, my explanation for the continued enrichment of Y in the melt—despite xenotime formation—is that the volume fraction of xenotime is minute, likely less than 0.01%. Though the Y contents of titanite (and allanite) are relatively small, their combined modal abundance is

commonly 1% of the thin section. Hence, in the southern plutons, continued Y fractionation causes the Y content, and thus xenotime abundance, to continue rising.

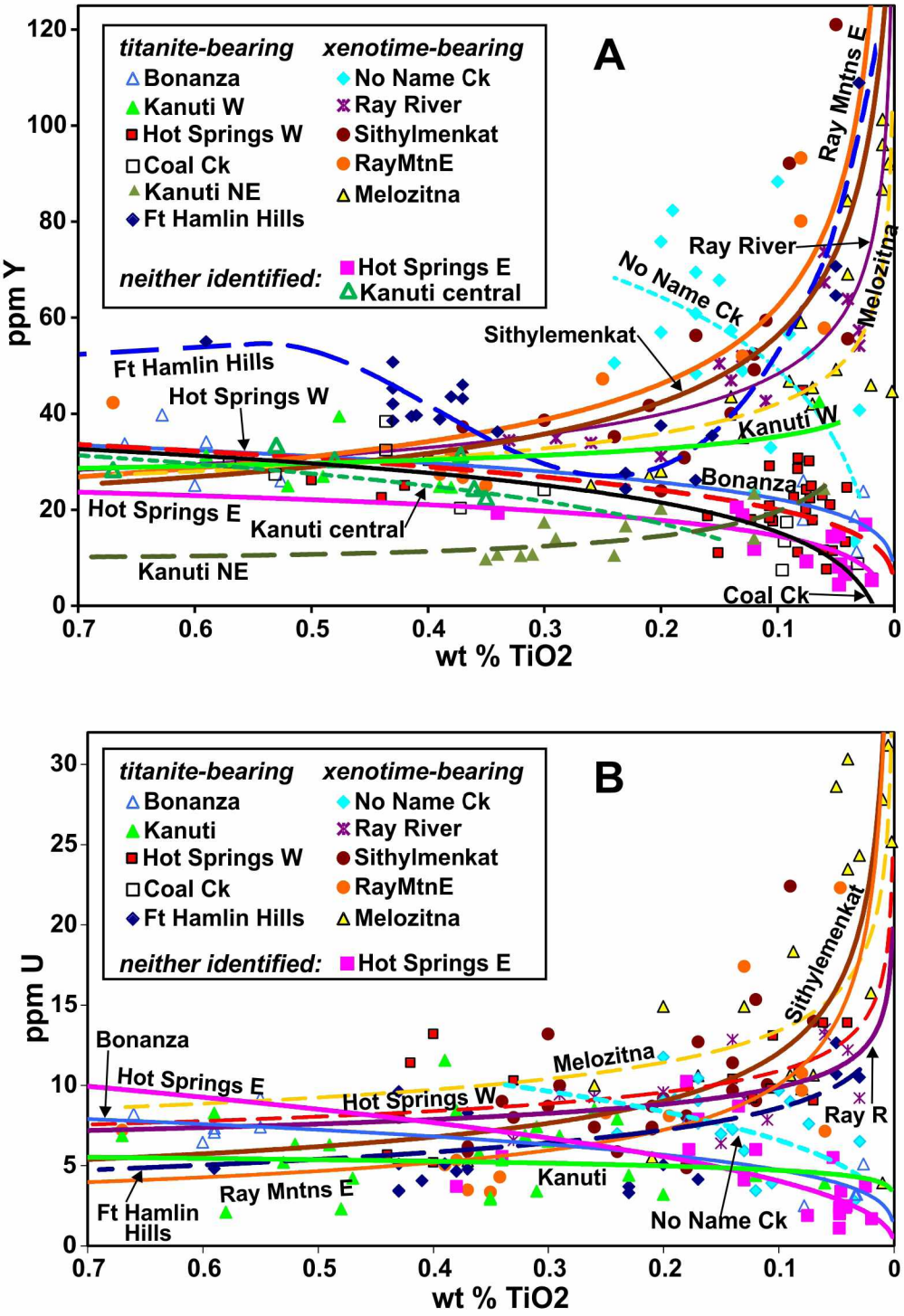

Figure 3.17. Y (A) and U (B) vs. TiO_2 for rocks of the central and southern Ruby batholith. Curves are best fit to the data for a given pluton. Mineral data from Table 2.6. Data from sources given with Figure 3.13.

The two exceptions to these generalizations are the NNC and Fort Hamlin Hills plutons. The NNC pluton contains abundant xenotime (seen as Y concentrations 2 to 5 times as high in panned concentrates than as for the others; see Chapter 4); its abrupt crystallization causes Y concentrations to decrease rapidly with a minor decrease in TiO_2. (Of course, the mystery is how the NNC pluton acquired such a high Y concentration for a given TiO_2 in the first place.) The Fort Hamlin Hills pluton is in several ways transitional between the northern and southern plutons. It does contain both titanite and allanite, but less than the other northern-type plutons, as is supported by the lower CaO concentrations (Fig. 3.16A). The Fort Hamlin Hills pluton also contains multiple populations of allanite and the younger (overgrowth) allanite is Y-poor (Fig. 3.3, Table 3.9). I hypothesize that the amount of Y removal from the Fort Hamlin Hills melt was insufficient to cause Y depletion, but large enough to prevent much Y enrichment (Fig. 3.17A).

The only mineral in which I have found significant, consistent U concentrations is xenotime. Given the similarities in size between U^{4+} and $HREE^{3+}$, the fate of U during fractional crystallization (Fig. 3.17B) of the Ruby batholith plutons would potentially parallel that of Y. The two major differences between Figures 3.17A and 3.17B involve the Hot Springs West and NNC plutons. The latter seems more straightforward. Considering xenotime contains far less U than Y, even abundant xenotime crystallization will cause a less drastic U depletion than Y depletion (Fig. 3.17B). In contrast, I am at a loss to explain the enrichment in U with decreasing TiO_2 observed for the Hot Springs West pluton. The enrichment in U with increasing fractionation in the Hot Springs West pluton does however explain the presence of local U prospects (e.g., Barker and Foley, 1986).

Cerium is both the most common LREE and is also representative in chemical behavior of the other LREE. The plot of Ce vs. TiO_2 (Fig. 3.18A) shows two major trends that cut across the southern/northern pluton distinction. Most of the plutons, including Ray Mountains East, Fort Hamlin Hills, and most of the northern plutons, display slowly decreasing Ce with decreasing TiO_2 that projects back to an initial magma composition of about 120 to 150 ppm Ce. Most of the plutons with this slowly decreasing trend contain allanite >> monazite; therefore, I attribute this trend to allanite crystallization.

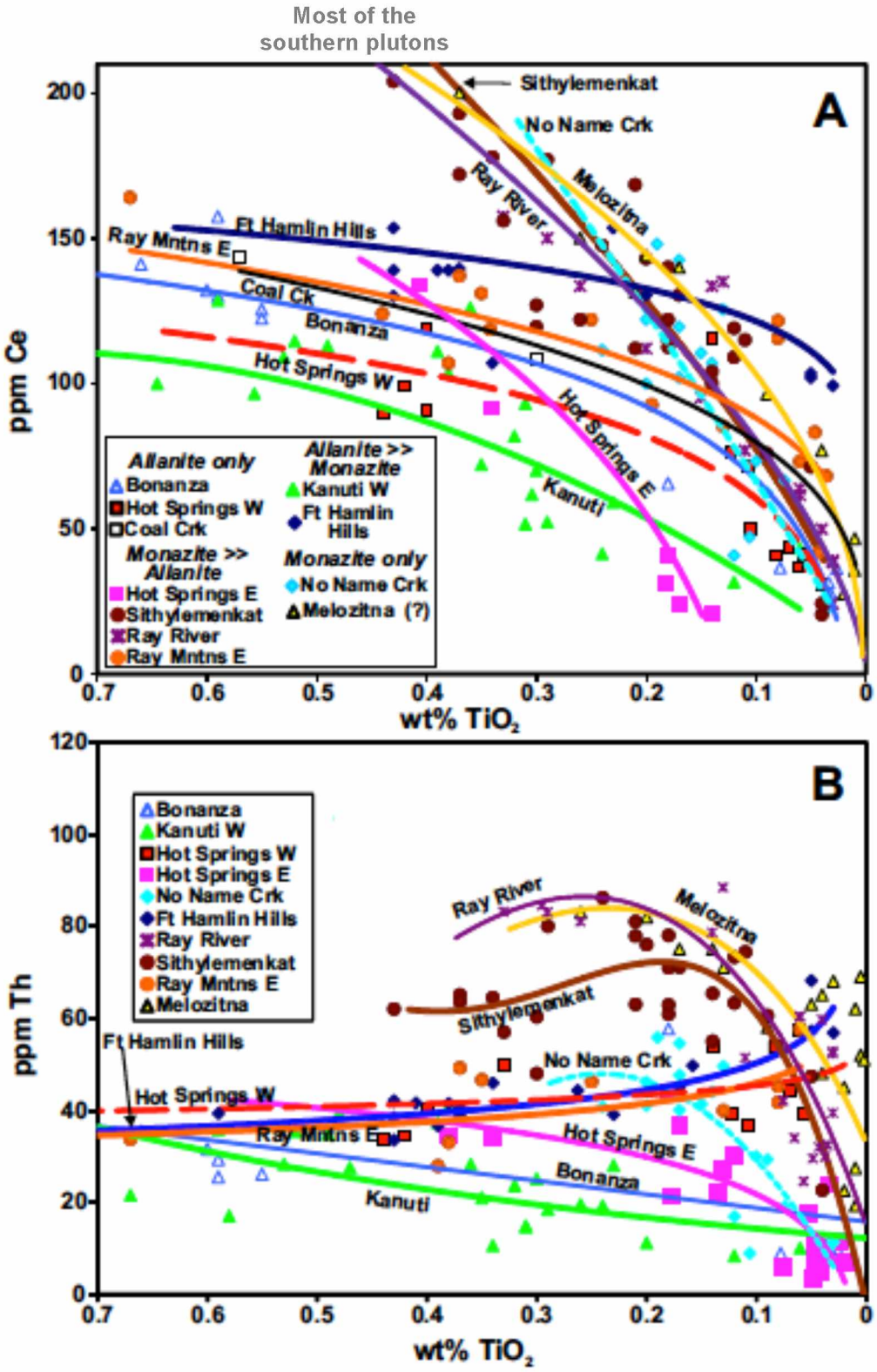

Figure 3.18. Ce (A) and Th (B) vs. TiO_2 for rocks of the central and southern Ruby batholith. Allanite-monazite abundance is taken from Table 2.6. Data is from sources listed with Fig. 3.13.

Crystallization of allanite (typically 10 wt% Ce_2O_3) instead of monazite (typically 20 wt% Ce_2O_3) would cause less of the Ce to migrate from magma to crystals, and thus a less drastic fall in Ce concentration with ongoing fractionation. The Ce concentration vs. TiO_2 curves (Fig. 3.18A) for the NNC, Ray River, Sithylemenkat, and Melozitna plutons, however, are much steeper and project back to "impossibly" high concentrations of Ce for a magma with 0.7 wt% TiO_2. Rather than postulating a Ce- (and LREE-) enriched magmatic source, I postulate that the high-Ce rocks were produced by fractionation with little or no allanite (or other Ce-bearing mineral) crystallization. Notably, these southern-pluton trends fall on the NNC-pluton trend—which, for practically every other element—requires pre-concentration to give the observed concentrations for its TiO_2 content (e.g., Figs. 3.13, 3.15, 3.17A). Crystallization of significant monazite then caused rapid loss of LREE from melt to yield the steep slopes on Figure 3.18A.

The Ray Mountains East pluton contains much more monazite than allanite, yet displays the "allanite" trend. Frustrating searches for monazite in samples from this pluton make me suspect that although there's much more monazite than allanite, there really is not much of either mineral. Notably, the monazite from the Ray Mountains East pluton shares the "reverse" trend on the monazite La vs. Gd diagram with the monazite from the Fort Hamlin Hills pluton (Fig. 3.9), a possible link between the two. The Hot Springs East pluton, in contrast, has the steep Ce-TiO_2 slope of the monazite > allanite plutons, but much smaller Ce concentrations (Fig. 3.18A). With little data from this pluton, I can offer little explanation.

Thorium is readily incorporated into both allanite and monazite, as shown by my microprobe EDS analyses (Tables 3.7-3.11); therefore, there should be some relation between Ce and Th fractionation trends, and to a certain extent, there is (Fig. 3.18B). Th in both the Bonanza and Kanuti West plutons decreases gradually with decreasing TiO_2. Allanite from these two plutons has moderately high ThO_2 contents, nearly 2 to 3 wt% (Table 3.10), and these high-Th allanites apparently caused Th to be preferentially extracted from the melt. Allanites from the Hot Springs West and Fort Hamlin Hills plutons are not as Th-rich (1.8 to 2 wt% ThO_2), and Th was not as efficiently extracted from the melt. Th-concentration trends for the four plutons with monazite-dominated patterns are not as simple. Unlike many other elements, the abundance variation cannot be modeled by a simple curve; rather, Th concentrations appear to peak at about 0.2 to 0.3 wt% TiO_2, and drop rapidly from there to near-zero at near-zero TiO_2. This may

reflect a lag between initiation of monazite crystallization and reduction in Th content of the melt by extensive incorporation into monazite.

A final diagram is for Ce/Y vs. TiO_2. Ce/Y is analogous to LREE/(HREE + Y), but I have much more Ce and Y data than I have for the other REE. This ratio (Fig. 3.19) is a combination of the trends in Y (increases with fractionation for some southern plutons, mostly decreases with fractionation for the others) and Ce (strongly decreases with fractionation for some southern plutons, gradually decreases for most others). As with many other diagrams, three trends are apparent. Most of the plutons show a slowly decreasing Ce/Y ratio with decreasing TiO_2.

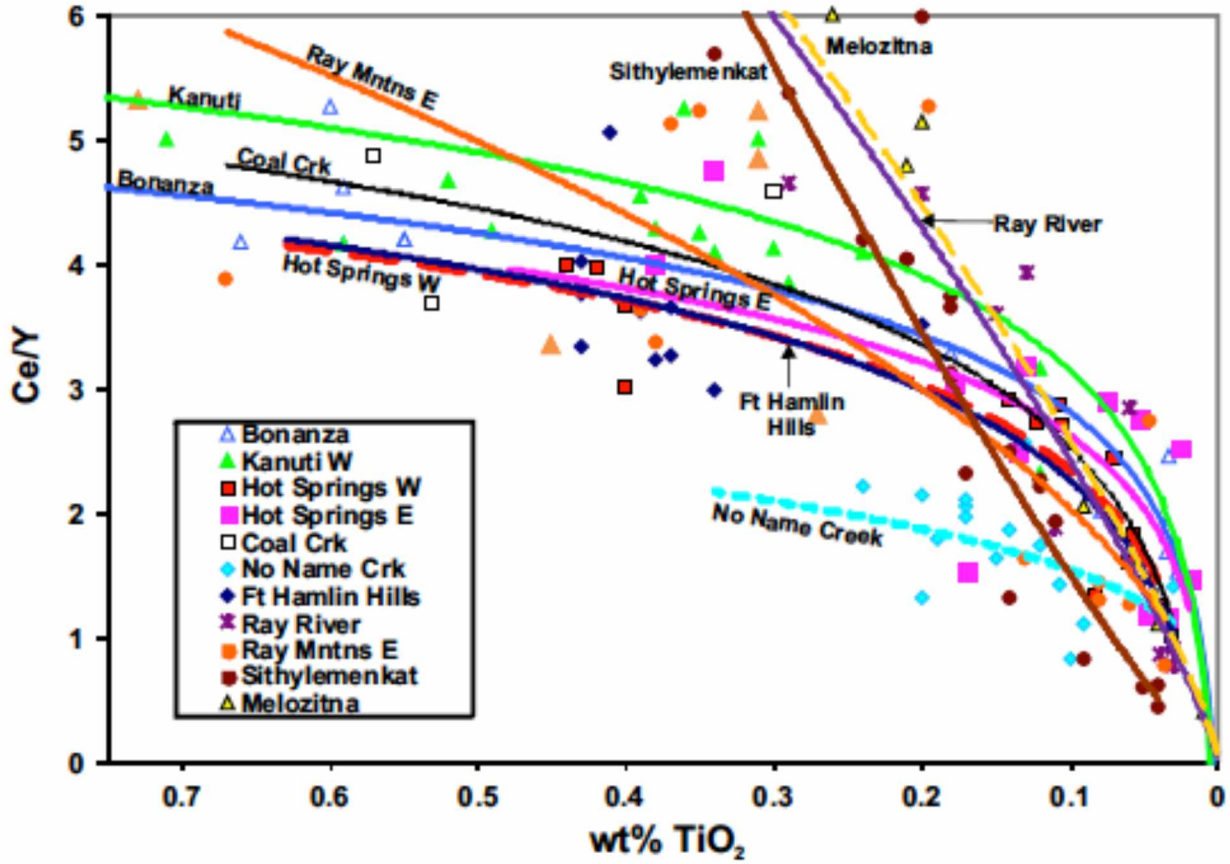

Figure 3.19. Ce/Y (weight ratio) vs. TiO_2 for rocks of the central and southern Ruby batholith. Rocks from most plutons exhibit modest changes in Ce/Y over the bulk of fractionation. The plutons with abundant monazite show steep slopes instead.

In contrast, the plutons that crystallized major amounts of monazite yield the steepest slopes. That is, for rocks with less than about 0.3 wt% TiO_2, rapid changes in Ce/Y accompany modest changes in TiO_2. These are the plutons—Sithylemenkat and Ray River—that exhibit significant spatial zoning in LREE/(HREE + Y) (Fig. 3.12).

The NNC pluton is anomalous in two ways: a) its Ce/Y ratio is much lower than the other plutons (for comparable TiO_2), and b) its Ce/Y ratio really does not change significantly with a decrease in TiO_2. The lack of exchange in Ce/Y is suspected to be caused by the crystallization of a sufficiently high ratio of monazite to xenotime so that both are sub-equally depleted from the crystallizing melt.

3.3.3 Summary of Elemental Trends

For most cases, two types of trends are seen in the element vs. TiO_2 diagrams: a trend exhibited by rocks of the Bonanza pluton, and a trend typified by rocks of the Sithylemenkat pluton. In many cases, the NNC pluton behaves uniquely. In a few cases, some plutons behave with intermediate behavior, and in the case of Th, a fourth group appears. These observations are summarized in Table 3.16. It is clear that the two northernmost plutons—or at least the Bonanza pluton and the western part of the Kanuti pluton—display the same elemental trends.

Table 3.16. Summary of elemental trends vs. TiO_2 for plutons of the Ruby batholith

Pluton	Rb	Eu/Eu*	Ca	P	Sn	Ce	Y	U	Th
Bonanza	1	1	1	1	1	1	1	1	1
Kanuti West	1	1	1	1	1	1	1	1	1
Hot Springs E	1	1	1	**2**	1	1.5	1	1	1
Hot Springs W	1	**2**	1	1	1	1	1	**2**	**4**
Coal Creek	2	2	2	**1**	**1**	2	**1**	--	**4**
No Name Creek	3	3	3	1	3	2	3	3	2
Ft Hamlin Hills	2	2	2	2	**1**	**1**	**1.5**	2	**4**
Ray River	2	2	2	2	2	2	2	2	2
Sithylemenkat	2	2	2	2	2	2	2	2	2
Ray Mntns East	2	2	2	2	2	**1**	2	2	**4**
Melozitna	2	2	2	2	2	2	2	2	2

Notes: Type 1 behaves like the Bonanza pluton; type 2 behaves like the Sithylemenkat pluton; type 3 behaves uniquely (NNC pluton); type 4 = none of the above. Type 1.5 displays characteristics of both type 1 and 2. "--" = insufficient data to classify.

At the south end of the Ruby Batholith, the Ray River, Sithylemenkat, and Melozitna plutons also always show the same compositional trends. The Ray Mountains East pluton shows contrasting behavior for LREE (and Th), but is otherwise like the other southern plutons. In between these two groups, the plutons display transitional characteristics. The Hot Springs East and West plutons commonly behave like the Bonanza and Kanuti West plutons. The Fort Hamlin Hills and Coal Creek plutons appear split between the two extremes.

3.4 DISCUSSION

3.4.1 Trace-Element Fractionation

The groupings expressed in the Rb vs. TiO_2 plot broadly correspond to the initial $^{87}Sr/^{86}Sr$ groupings: the group with lower projected primary magma Rb content (~130 to 180 ppm, Fig. 3.13) has lower initial $^{87}Sr/^{86}Sr$ ratio ($\leq$ 0.714, Figure 2.6); the group with higher projected primary magma Rb (~250 to 300 ppm) has higher initial $^{87}Sr/^{86}Sr$ ratio ($\geq$ 0.714). The Coal Creek pluton has an intermediate initial $^{87}Sr/^{86}Sr$ ratio (0.714), though its projected primary Rb concentration is in the higher group (Fig 3.13). There is no correlation, however, between projected Rb concentration and initial $^{87}Sr/^{86}Sr$ ratio, in part because a single pluton (e.g., Ray Mountains West) can have multiple initial $^{87}Sr/^{86}Sr$ ratios, and in part because the projection lacks accuracy. It is true that the pluton with the highest initial $^{87}Sr/^{86}Sr$ ratio (0.727) also has the highest projected primary Rb content (~450 ppm). This is a problem in itself. How did the No Name pluton acquire so much Rb? And how did it acquire its extremely high initial $^{87}Sr/^{86}Sr$ ratio? And why is it just a little bit younger (ca. 107 ± 1 Ma) than most of the other plutons (ca. 111 ±1 Ma)?

The degree to which a pluton expresses a Eu anomaly is related to the pluton's oxidation state. The fact that the Eu anomaly for the Bonanza, Kanuti West, and Hot Springs East plutons suggests that their magmas were more oxidized than the other plutons implies that most of the Eu is Eu^{3+}, and is therefore not partitioning into plagioclase. These trends are reflected in the magnetic susceptibility data as well. The Bonanza, Kanuti West, and Hot Springs East plutons have the highest magnetic susceptibilities (Table 2.1). Despite significant differences in magnetic susceptibilities among these three plutons, however, there is no clear difference in the Eu anomaly expressed (Fig. 3.14). Further, although there is an observable gradation in average magnetic susceptibilities (Table 2.1), there does not appear to be a gradation effect on the Eu

anomaly; either a sizeable anomaly is produced by continued fractionation (measured by decreasing TiO_2) or it is not.

The Y depletion observed in the northern plutons indicates its incorporation into Y-bearing phases early in the crystallization process. Those phases include titanite and allanite, but also apatite and magnetite (Ewart and Griffin, 1994). In contrast, the residual melts of the southern plutons—lacking magnetite and titanite, and with little allanite and lesser apatite (lower P_2O_5) —become enriched in Y. This is true even after xenotime starts to crystallize in the southern plutons, suggesting that the total amount of Y incorporated into xenotime is small relative to the overall Y concentration in the melt, and possibly small relative to that incorporated into the rock. Suggested K_d values (concentration in mineral/concentration in melt for Y relative to a granitic melt) are 0.8 for plagioclase and 2.4 for biotite (Bea et al., 1994). For a rock that consists of approximately 35% plagioclase and 10% biotite, along with the aforementioned K_d values, the overall concentration in the rock relative to the concentration in the melt (ignoring xenotime and apatite) is approximately 0.5. That is, crystallization of those two minerals would result in about ⅓ of the Y in the melt being sequestered into silicates. With the addition of several percent titanite, allanite, and apatite, the amount of Y being incorporated into crystallizing minerals would increase and the melt would lose Y with crystallization; such appears to be the case for the northern intrusions (Fig. 3.17A).

Finally, there is again the problem of the NNC pluton. The average Y concentration of the highest Ti rock from that pluton (65 ppm Y at about 0.2 wt% TiO_2) is approximately 50% higher than that of rocks from other southern plutons with the same TiO_2 concentrations (40 ppm Y; Fig. 3.17A). How did this body of magma form? I will discuss the problem more in Chapter 5, but the least implausible suggestion is that the magma represents the product of concentration (of some sort) from a larger, unexposed body. The decrease in the Y content of the NNC pluton rocks with fractionation seems reasonable. The highest concentrations of Y in drainage sediments occur in the NNC valley (see ahead, Chapter 4).

The considerable differences in the changes in the Ce/Y ratio in rocks of the Ruby batholith underscore major differences in REE distribution between the Ray River, Sithylemenkat, and Melozitna plutons, and the rest. Something different happened in the Ray Mountains East pluton such that it does not show the same strong decrease in Ce/Y with decreasing TiO_2. This is not part of a N-S trend, as evidenced from the fact that data from the

Melozitna pluton (90 km SW of the Ray Mountains pluton) is quite similar to that of the Sithylemenkat body. The differences between the northern (and Fort Hamlin Hills) plutons and the southern plutons are more fundamental than the differences between the Ray Mountains East and most other southern plutons. There is something fundamentally different about how LREE and HREE + Y fractionated in the northern and southern plutons. The NNC pluton is (again!) unique in that all samples from this body possess much lower Ce/Y than is typical of the other plutons, and that ratio does not change with fractionation. Again, the evidence points to the NNC pluton as a hyper-fractionated melt that evolved from a more typical melt.

The trends of Th concentration with continuing fractionation vary considerably; I have identified three major trends (Fig. 3.18B). The Bonanza and Kanuti plutons—both containing just allanite as a major LREE carrier, with no monazite observed—show decreasing Th concentrations with increasing fractionation. This suggests that allanite incorporated much of the Th from the magma. The middle group, the Hot Springs West, Ray Mountains East and Fort Hamlin Hills plutons, show a slight enrichment in Th with fractionation. Two of these plutons, Fort Hamlin Hills and Ray Mountains East, contain both monazite and allanite. Finally, the Ray River, Sithylemenkat, and Melozitna plutons contain abundant monazite, and replaced and resorbed allanite. (My examination of a placer concentrate from the Melozitna pluton revealed mostly monazite with little cassiterite and ilmenite, but no allanite). These plutons yielded least fractionated (highest wt% TiO_2) rocks with much higher Th concentrations than *any* of rocks from *any* of the other plutons. There is a weak sense of approximately constant Th as TiO_2 drops from 0.4 to 0.35 % TiO_2 to about 0.2% TiO_2, then a steep drop in Th concentration with a further drop in TiO_2 (Fig. 3.18B). The NNC pluton contains only monazite (that is, no allanite), and it possibly shows the same patterns of initially constant Th with decreasing TiO_2 and then sharp drop for $TiO_2 < 0.2\%$. That is, it might represent a variant on the Ray River-Sithylemenkat-Melozitna pattern, but starting from a lower Th concentration.

U substitutes into xenotime, so U enrichment with decreasing TiO_2 (Fig. 3.17B) for most of the plutons indicates something additional is controlling U in melt and solids. Ironically, the three plutons that show U decreasing with increasing fractionation (Bonanza, Hot Springs East, and Kanuti West) are those in which xenotime has not been identified. As with Y, it appears that the total U budget well exceeds what was observed in the xenotime. Another possible U hosting-mineral is titanite (e.g., Hurley and Fairbairn, 1957). U definitely drops with increasing

fractionation in the NNC pluton, but that body contains the highest concentration of xenotime, possibly high enough to account for U depletion from melt.

The P concentrations are significant in that the two northernmost plutons contain the least-fractionated (highest TiO_2) rocks with higher P_2O_5 (ca. 0.25 to 0.3 wt%) than *any* rocks from *any* of the other plutons. Projected primitive melt (0.7 wt% TiO_2) P_2O_5 contents for the southern plutons are commonly 0.1 to 0.2 wt% P_2O_5 (Fig. 3.16B), as little as half as much as in the northern plutons. Nevertheless, the high-P plutons contain no identified monazite or xenotime, while the lower-P plutons do. Clearly, P content alone does not control the crystallization of monazite and xenotime; rather, the higher CaO content of the P-rich plutons (Fig. 3.16A) caused apatite to be the principal phosphate mineral.

3.4.2 Rare-Earth-Bearing Minerals

In the northern plutons, the LREE and Th partition into allanite, and Y (and likely undetectable amounts of HREE) partitions into titanite. In the southern plutons, the LREE and Th are primarily incorporated into monazite, and the HREE + Y go into xenotime. The high-P concentrations measured in allanite from the Bonanza pluton are exceedingly unusual; such high-P concentrations in an allanite-like specimen have only previously been noted by Iimori et al. (1931), yet the crystallographic data was never published to confirm the mineral species.

The Th depletion observed in monazite rims likely records Th depletion in the melt caused by preferential incorporation into monazite (Fig. 3.18B). Similarly, the common (but not ubiquitous) decrease in Th in allanite with decreasing TiO_2 reflects a Th-concentration decrease in the melt due to its incorporation into minerals.

Microprobe EDS confirmed the identification of monazite as a replacement of allanite, in some cases as a complex reaction involving minerals such as garnet (Fig. 3.3). Most likely, a decrease in Ca content of the melt by plagioclase removal (with attendant development of extreme Eu anomalies) triggered the change in crystallization from apatite + allanite (both Ca-rich minerals) to Ca-poor monazite + an Fe-Al mineral (such as biotite).

3.4.3 Spatial Distribution of REE within Plutons

The spatial variations of relative REE abundances within individual plutons (inward increase in (HREE + Y)/LREE, Fig. 3.12) parallels the observed changes in Ce/Y with decreasing TiO_2 seen in individual rock samples (Fig. 3.19). These variations imply crystal fractionation occurred from the margins toward the interior for both the Ray River and Sithylemenkat plutons, and also shows that the bulk of the Sithylemenkat pluton contains rocks with much higher LREE/(HREE + Y) than those of the Ray River pluton. In particular, the bulk of the NNC pluton consists of rocks with LREE/(HREE + Y) < 2.0. Rocks with LREE/(HREE + Y) ratios of 2 to 3 are confined to the immediate contact zone (Fig. 3.12). It is probable that the bulk of the interior of the pluton has LREE/(HREE + Y) of < 1. In contrast, at least ¾ of the Sithylemenkat pluton consists of rocks with LREE/(HREE + Y) > 2 (Fig. 3.12).

The Fort Hamlin Hills pluton shows no obvious spatial patterns in relative REE concentrations. In part this is due to lower sampling density, but it is largely due to the limited range in (HREE + Y)/LREE seen in rocks of the pluton (Fig. 3.19), a characteristic of the monazite-poor granites. The fact that the NNC pluton is fundamentally different from the Fort Hamlin Hills pluton (despite being historically mapped as the same body), as well as its differences among the southern plutons, have important implications for the sediments found draining these plutons. I discuss those differences and their implications in the next chapter.

3.4.4 Summary

In this chapter, I have provided elemental compositions of rare-earth-bearing minerals in the central and southern Ruby batholith. Many of the compositions and compositional changes measured in the minerals reflect changes in the residual melts. I have also grouped plutons based on their elemental trends with ongoing fractionation, and few plutons show transitional characteristics between the northern and southern groups. Additionally, these groupings are largely based on the notion of fractional crystallization, which I provide support for given the inward crystallization of REE.

4 TRACE-ELEMENT DISTRIBUTION IN STREAM GRAVELS OF THE RAY MOUNTAINS AREA

4.1 INTRODUCTION

Heavy-mineral (including Sn, W, Nb, Ta, and REE) resources in the region are largely concentrated in stream gravels. In this chapter, I will present data compiled following various sampling techniques, including stream-sediment sampling and heavy-mineral panned concentrate sampling. Stream sediments and field-panned concentrates were collected throughout the study area, while laboratory panned, bulk heavy-mineral concentrates were confined to gravels in the southern half of the field area, encompassing the NNC, Fort Hamlin Hills, Ray River, Sithylemenkat and Ray Mountains East plutons. Field-panned concentrates were collected at approximately 200 sites in the area; an additional twenty-three 40 L sand samples (Appendix G) were collected for heavy-mineral extraction at the laboratory in Fairbanks (Bachmann et al., 2013).

Stream-sediment samples are ideally composed of "fines", that is, fine sand, silt, and clay. The best places to find such sediments are cobble- and gravel-armored riffles, point bars, eddies, flood deposits, and moss mats (Fletcher, 1997). Large samples are collected to ensure adequate abundance of sediments. Clay-sized grains are ideal because certain metals suspended within the streams readily adsorb onto their surfaces; thus, fines act as metal transporters (Bachmann et al., 2013).

Heavy-mineral samples, taken from similar sources as the stream sediments, are concentrated in a gold pan. Using alternating shaking and washing motions, the sediment in the pan is reduced to visible heavy minerals (a volume of approximately 30 mL), a relatively time-consuming process compared to collecting a stream-sediment sample. Whereas stream sediments tend to collect metal ions and metal hydroxides, panned concentrates capture mechanically and chemically resistant detrital grains. These grains have larger densities than most rock-forming minerals.

Where possible, samples are collected over a distance of ~ 10 m to ensure a representative sample of the stream is analyzed.

4.2 ANALYTICAL CONSIDERATIONS

Several analytical issues arose throughout the course of data collection and interpretation; these include variations in panning technique, sample contamination, sample dissolution (and lack thereof), and the reliability of the chemical analyses.

4.2.1 Contamination

Five of the laboratory-concentrated, heavy-mineral samples (from here, simply referred to as lab concentrates, Appendix G) contained Pb concentrations far in excess of the others (Figure 4.1). Pb is most commonly concentrated by gravity techniques if the mineral is galena (PbS). Galena, however, does not withstand stream transport; its excellent cleavage planes cause the crystal to decompose into nano-cubes, which themselves are extremely susceptible to oxidation. Such considerations make the high-Pb concentrations suspicious. Furthermore, in nature, Pb and Zn are commonly associated (e.g., as the minerals galena and sphalerite). Plotting Pb vs. Zn, however, shows no correlation (Fig. 4.1).

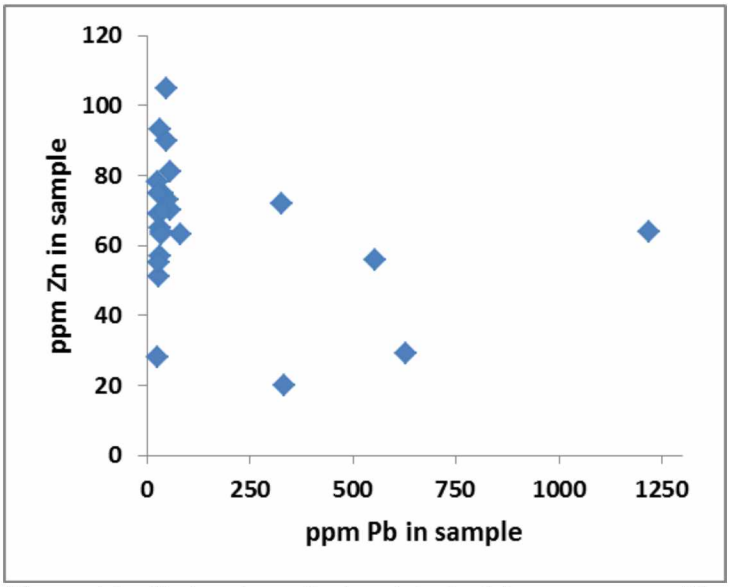

Figure 4.1. Pb (ppm) vs. Zn (ppm) in the lab concentrates. The Pb concentrations are bimodal: one group has 25-80 ppm Pb, while the other has 326-1250 ppm Pb. No correlation exists between Pb and Zn. Data presented in Appendix G.

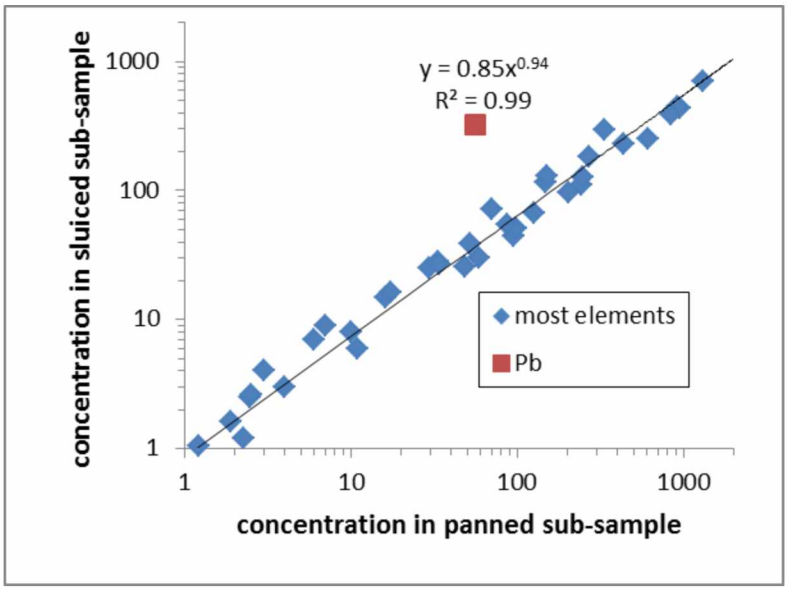

Figure 4.2. Concentrations of 34 elements in the sluiced sample 12LF301BA vs. the concentrations of 34 elements in the corresponding panned sample 12LF301BB. Only the Pb concentrations deviate significantly from the 1:1 line (shown).

To determine if sample preparation techniques caused the high-Pb concentrations, sample 12LF301B was split into two sub-samples: 12LF301BA was sluiced, and 12LF301BB was strictly panned. A plot of elemental concentrations in the sluiced vs. panned samples (Fig. 4.2) shows a near-perfect correlation for every element except Pb. Sluiced sample 12LF301BA contained 326 ppm Pb, whereas the strictly panned sample, 12LF301BB, contains 56 ppm Pb. For most elements, the panned sample concentrations are 1.5 to 2 times as high as the sluiced concentrations. In contrast, the Pb concentration in the panned sample is six times lower than the sluiced sample. Visual searching of the five sluiced, contaminated, non-magnetic separates with a dissecting microscope confirmed the presence of metallic spheres, 0.1 to 0.5 mm in diameter. Semi-quantitative portable XRF analysis of a dozen spheres indicated they were mostly composed of Pb and Sn, i.e., Pb-Sn solder. I conclude that the sluiced samples were contaminated with beads of solder.

Table 4.1. Correlation coefficients between Pb and selected elements in the five Pb-rich lab concentrates

Element	Hf	La	Th	P	As	Sr	Zr	U	W	Tb	Y	Lu
R^2	0.99	0.98	0.96	0.95	0.94	0.94	0.93	0.89	0.80	0.60	0.19	0.03

The problem is potentially more complicated, because (a) not all of the sluiced samples were contaminated with solder and (b) some of the non-sluiced (strictly panned) samples were also contaminated. Other possible sources of solder beads are sieves, shovels, and other equipment and laboratory facilities.

Further, among the five Pb-rich samples, several elements exhibit a strong-to-extremely strong elemental correlation with Pb (Table 4.1). Based on the elemental signature (Table 4.1), as the abundance of Pb-Sn solder increases, so too does the abundance of zircon, monazite, and either wolframite ($FeWO_4$) or scheelite ($CaWO_4$). The elements that correlate strongly with Pb in the Pb-rich samples do not correlate in the Pb-poor samples.

4.2.2 Partial Dissolution of Elements Prior to Analysis

Elemental analysis by ICP-MS and ISP-AES first requires dissolving the material into solution. A variety of digestions are available commercially. The standard technique for difficult-to-dissolve minerals requires heating the pulverized sample with lithium metaborate until the solvent liquefies, and then dissolving the cooled and crushed solid into a weakly acidic solution. A less-intense (and cheaper) method is to dissolve the material into a mixture of four acids: nitric, hydrofluoric, hydrochloric, and perchloric. The lithium metaborate fusion method will cause almost any mineral to dissolve, but some elements can be volatized and the resulting solution is very Li-B-rich, which itself can potentially cause analytical problems.

My samples were analyzed by ICP-MS; some elements (e.g., Zr, REE, Sn) were analyzed from a subsample digested with lithium metaborate, while others (e.g., Ca, Al, Mg, P, and some trace elements) were analyzed from a subsample digested with the four-acid mix.

The commercial chemical analyses of the concentrates yielded a bimodal distribution of atomic (REE+Y+Th)/P (Fig. 4.3). The first population, plotting in the vicinity of the 1:1 line, represents analyses with atomic P approximately equal to (REE+Y+Th). This group exhibits a weak correlation between ppm Y and atomic (REE+Y+Th)/P.

The second grouping has atomic (REE+Y+Th)/P > 1, and shows a strong correlation between the ratio and ppm Y. All the samples from streams draining into the NNC are included in this group.

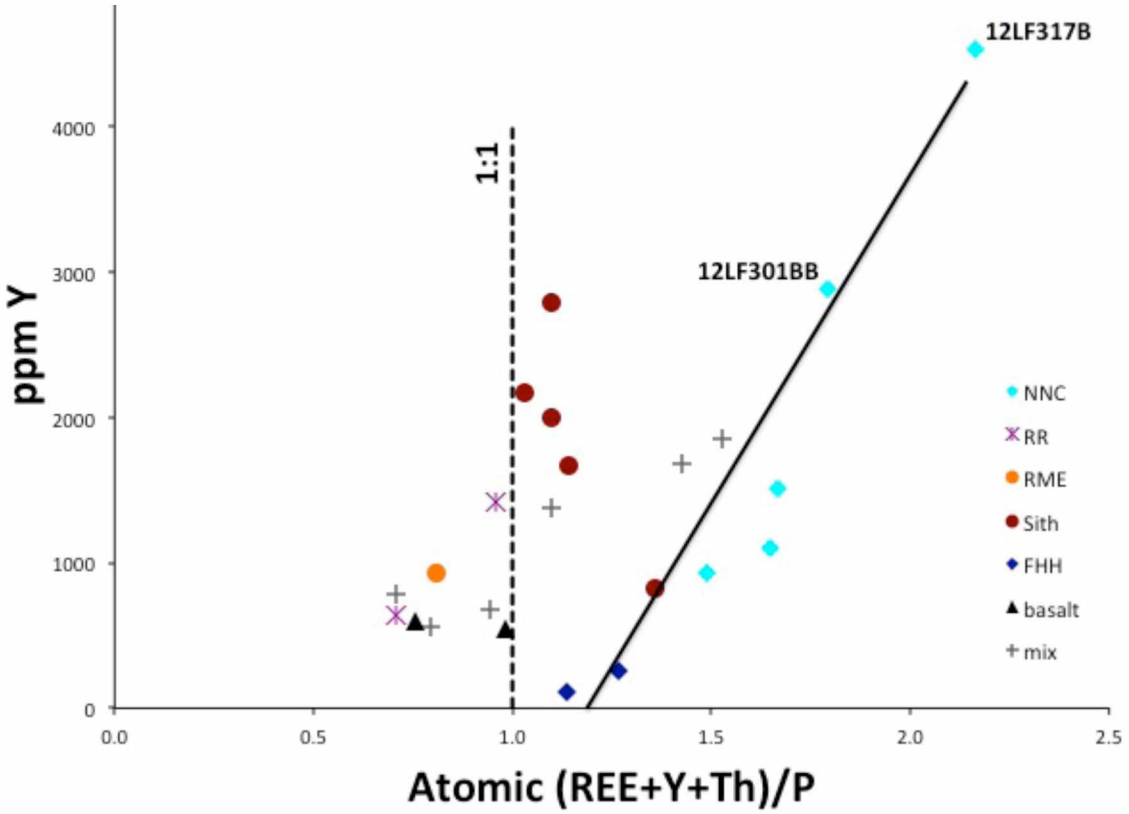

Figure 4.3. Concentration of Y vs. atomic (REE+Y+Th)/P for the lab concentrates from the study area. The dashed 1:1 line indicates samples for which atomic P approximately equals REE+Y+Th. The pluton or rock type from which the gravel sample was likely derived codes samples. "NNC" = No Name Creek, "RR" = Ray River, "RME" = Ray Mountains East, "Sith" = Sithylemenkat, "FHH" = Fort Hamlin Hills. "mix" indicates sample derived from a mixture of potential sources.

A ratio of atomic (REE+Y+Th)/P > 1 requires either the presence of a non-phosphate mineral as a carrier of REE and Y, and (or) a severe analytical problem. The fact that the ratio becomes increasingly large with the concentration of Y implies in particular that Y is associated with a non-phosphorous mineral (or an analytical issue); however, there are no common Y-rich minerals outside of xenotime (YPO_4).

In an effort to determine if additional Y-rich minerals were present, I created and examined grain mounts composed of material from lab concentrates 12LF301BB and 12LF317B (Table 4.2) from the NNC drainages. I chose these two samples as they contain the highest atomic (REE+Y+Th)/P ratios (Fig. 4.3).

Table 4.2. Mineral abundances (%) observed in two grain mounts of heavy-mineral concentrates associated with the No Name Creek pluton

Sample	Zircon	Mz	Xn	Ilm	Rutile	Cass	Wolf	Tour	*n*
12LF301BB	11	37	17	26	4	4	1	1	192
12LF317B	8	42	15	8	2	16	9		112

Notes: Mineral identification confirmed by EDS on the electron microprobe. Mineral abbreviations: "Mz" = monazite, "Xn" = xenotime, "Ilm" = ilmenite, "Cass" = cassiterite, "Wolf" = wolframite, "Tour" = tourmaline.

No REE minerals outside of monazite and xenotime were identified. The ratio of monazite to xenotime analyzed was ~2 to 3. Additionally, though neither sample was identified as Pb contaminated, no Pb-bearing minerals were identified in either grain mount. The various data indicate that the atomic (REE+Y+Th)/P ratio > 1 samples is a result of incomplete digestion of P-rich minerals in the four-acid digest, and is hence associated with the under-reporting of P in the analyses. Since P is under-reported, it is not possible to calculate mineral abundances (e.g., apatite vs. monazite vs. xenotime) from the compositional data. Partial digestion problems are likely not restricted to the REE phosphate minerals.

4.2.3 Assessment of Analytical Errors

Standard reference materials were sent to the commercial laboratories with each batch of samples. Many of the standards sent were granites with low trace-element abundance. In the case of heavy-mineral concentrates, these standards acted essentially as blanks. Though poor for ensuring accuracy, the "blank" nature of these standards offered value as detectors of contamination among samples. At the commercial laboratory, unless otherwise advised, barren material was run through the pulverizing equipment only between batches, not between samples.

One such standard, referred to as the Chena Hot Springs Road granite (CHSRg), was sent with several batches of the concentrates without issue. Two analyses of this standard, however, were erroneous in unusually similar ways. In September of 2012, and again in January of 2013, this standard was sent with field-concentrated, heavy-mineral samples (simply referred to as field concentrates), and the resulting analyses yielded anomalous concentrations of elements typically found in dense minerals (Table 4.3). Conversely, elements not typically associated with dense minerals were measured at expected concentrations.

Table 4.3. Commercial laboratory trace-element analyses of the Alaska DGGS standard, CHSRg, with the 15-year average analysis (and standard deviation) for CHSRg

Sample	Nb	Rb	Y	Zr	Sr	Th	U	Ce	W	Sn	Pb
45	11	144	30	146	356	19	4	68	<1	2	28
46	10	152	29	143	342	16	5	63	1	5	26
47	11	154	28	158	345	16	6	70	2	13	34
48	11	152	28	148	348	17	4	68	1	8	**36**
49	12	157	30	157	347	18	6	70	1	14	34
50	**21**	**166**	**92**	**341**	**368**	**73**	**10**	**257**	**29**	**63**	35
52	11	159	30	172	331	18	5	65	1	8	32
53	13	159	30	181	356	17	6	69	1	21	30

	Nb	Rb	Y	Zr	Sr	Th	U	Ce	W	Sn	Pb
Avg	11	136	34	148	351	19	5	69	2	2	31
StDev	1	7	5	6	10	6	1	8	1	1	3

Sample	TiO_2	Al_2O_3	Fe_2O_3(t)	MnO	MgO	CaO	Na_2O	K_2O	P_2O_5	BaO
45	0.17	12.5	2.6	0.05	0.27	2.8	2.7	3.2	0.04	0.18
46	0.17	11.9	2.4	0.05	0.23	2.6	2.5	3.5	0.04	0.21
47	0.17	12.2	2.5	0.05	0.25	2.7	2.7	3.7	0.04	0.17
48	0.18	12.3	2.8	0.05	0.27	2.5	2.7	**4.0**	0.04	0.21
49	0.18	12.6	2.9	0.05	0.27	2.5	2.5	3.9	0.04	**0.24**
50	**0.33**	**13.8**	**3.1**	**0.07**	**0.28**	**2.8**	2.7	3.9	**0.07**	0.19
52	0.18	11.8	2.7	0.05	0.25	2.5	2.6	3.8	0.04	0.19
53	0.20	12.8	2.8	0.06	0.27	2.7	**2.8**	3.8	0.04	0.17

	TiO_2	Al_2O_3	Fe_2O_3(t)	MnO	MgO	CaO	Na_2O	K_2O	P_2O_5	BaO
Avg	0.18	14.1	2.9	0.05	0.4	2.6	2.6	3.6	0.05	0.19
StDev	0.06	0.5	0.3	0.01	0.2	0.2	0.1	0.2	0.02	0.02

Notes: Highest commercial values are in bold font; lowest are underlined. "Avg" indicates the 15-year average analysis. Elements given in ppm; oxides in wt%.

Sample 50 (Table 4.3) clearly has elevated concentrations in a wide variety of elements relative to the 15-year average values. This is particularly clear for elements present in dense minerals, e.g., Sn, W, Th, Ti, Nb, and Zr. Plots of one enriched element vs. another (Fig. 4.4), however, suggest that *all* of the samples of CHSRg were variably contaminated by material with elevated concentrations in these elements. The easiest explanation is that the placer concentrates physically contaminated the CHSRg samples that were run within the same batch.

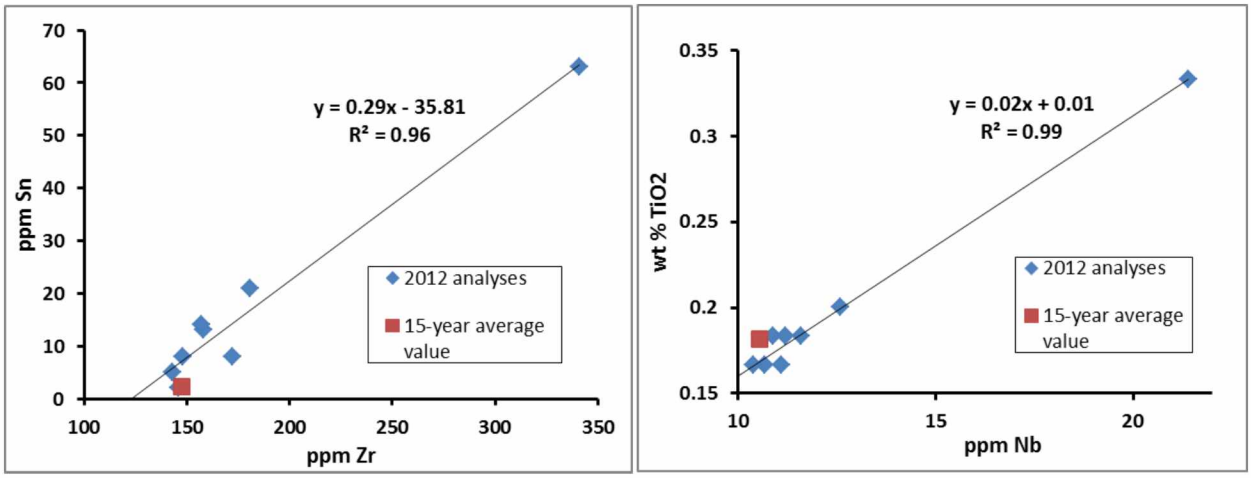

Figure 4.4. Concentration of Zr vs. Sn (left) and of Nb vs. TiO_2 (right) for samples of the DGGS CHSRg standard that was analyzed with the field concentrates. The approximately straight-line behavior for all of the 2012 CHSRg samples suggests that all have been contaminated by material with relatively high Sn, Zr, TiO_2, and Nb—e.g., typical heavy-mineral concentrate samples from the southern plutons.

Analysis of another standard yielded somewhat erroneous results. USGS standard reference material COQ-1, a pulverized carbonatite, was also included with the field concentrate samples. The concentrations provided in the USGS analytical certificate are typically higher—an average of 23% higher—than those analyses obtained by the commercial laboratory (Table 4.4). One of the worst offenders is Nb; the concentration reported by the commercial laboratory is 57% lower than that published by the USGS. For other elements (e.g., Ba, Ce, La, V, Y, and Zn), however, the elemental concentrations determined by the commercial laboratory are considerably higher than the published values.

Table 4.4. Commercial analysis for selected elements (in ppm unless indicated otherwise) of International Standard COQ-1 compared to official concentrations

Source	%CaO	%Fe_2O_3	%MgO	%TiO_2	% Ba	%Ce	%La	%Nb
Commercial	46.0	3.1	1.11	0.12	0.12	0.18	**0.091**	**0.17**
Published	**48.3**	2.9	1.25	0.15	0.10	0.17	**0.075**	**0.39**
±	0.4	0.1	0.03	.002	<.01	0.01	0.001	0.006

Source	Er	Gd	Th	Sc	U	V	Y	Zn	Zr	Ni
Commercial	**8.1**	**33**	**50**	1.0	12.2	**158**	**88**	95	51	**1**
Published	**7.0**	**50**	**10**	3.0	11.0	110	81	87	65	**13**
±	0.1	1	0.1	0.1	0.6	6	5	2	3	1

[1] Published values reported by USGS Certificate of Analysis with uncertainties as given. Values in bold display especially large deviations from one another. All values in ppm unless otherwise indicated.

Many of the chemical concentrations measured by the commercial laboratory were grossly different from the published values, e.g., 33 vs. 50 ppm Gd, 50 vs. 10 ppm Th, 0.17 vs. 0.39% Nb. I was concerned that the published values were wrong and (or) the material as supplied was not homogeneous. To test these hypotheses, I prepared two pressed pellets of COQ-1 and analyzed them for major elements by X-Ray fluorescence at the UAF Advanced Instrumentation Laboratory. My values of 0.35% Nb and 0.36% Nb are close to the published values and confirm that the commercial lab results were incorrect.

4.2.4 Use of Non-Magnetic Fraction of the Laboratory-Panned Concentrates

It has been common—especially in the U.S. Geological Survey—to prepare and analyze the non-magnetic fraction of a panned-concentrate sample. The intent is to heighten the sensitivity of the remaining concentrated elements found in the dense minerals. For the lab concentrates, the magnetic fraction was removed and the non-magnetic fraction was analyzed. The magnetic fraction constituted > 30% to < 1% of the concentrate, and removal has the potential to impact the final concentrations. I investigated this effect by measuring the magnetic susceptibilities and compositions of the magnetic fractions. I employed a portable XRF, which based on analyses of pressed pellet standards, yields at least semi-quantitative results. The results (Table 4.5) show that the magnetic fraction contains major-to-modest concentrations of Ti, Cr, and Mn, in addition to Fe and appreciable concentrations of Nb and Sn.

Table 4.5. Analytical data for the magnetic fractions of the lab concentrates

Sample	Source[1]	%Frac[2]	MS	%Cr	%Ti	%Fe	%Nb	%Mn	%P	%Sn	Zr (ppm)	Ti/Fe	Major Minerals
319C	Basalt	11	10	2.2	7	31	0.06	3.3	0.06	0.02	161	0.3	mt>ilm>chr
319D	Basalt	8	11	2.4	11	29	0.08	4.9	0.07	0.01	270	0.5	mt>ilm>chr
102A	FHH	3	0.1	0.03	22	18	0.15	1.8	<0.02	0.02	574	1.5	rutile+ilm
296B	Mix	8	1.2	0.39	17	31	0.10	3.6	0.15	0.13	253	0.7	mt>ilm
295B	Mix	2	8	0.10	12	41	0.09	2.7	0.18	0.02	303	0.3	Ti-mt>ilm
314B	Mix	11	3.2	0.70	16	24	0.18	6.0	0.25	0.03	181	0.8	ilm>mt
315B	Mix	30	**70**	2.7	7	35	0.08	7.0	0.06	0.02	101	0.2	**Ti-mt+chr**
316B	Mix	8	8.3	1.3	10	27	0.09	6.8	0.15	0.02	367	0.4	mt>ilm
318B	Mix	17	19	1.1	19	29	0.15	6.0	0.13	0.07	335	0.8	mt>ilm
340B	Mix	8	4.5	0.65	9	22	0.06	3.8	0.09	0.02	219	0.5	mt>ilm
253B	NNC	7	0.7	0.06	24	26	0.16	2.6	<0.02	0.05	612	1.1	ilm
301BA	NNC	4	0.5	0.03	17	20	0.15	2.0	0.08	0.04	410	1.0	ilm
301BB	NNC	8	1.0	0.03	30	29	0.33	4.0	<0.02	0.04	996	1.2	ilm
303B	NNC	1.4	0.8	0.04	24	27	0.26	3.2	<0.02	0.86	517	1.0	ilm
317B	NNC	24	5	0.04	29	31	0.38	4.4	0.12	0.30	231	1.1	ilm
240B	RME	9	13	0.06	16	31	0.11	2.6	0.18	0.02	330	0.6	ilm>mt
294B	RR	9	2	0.05	22	42	0.14	2.3	0.21	0.12	301	0.6	ilm>mt
237B	Sith	1.3	--	0.14	26	29	0.18	3.5	<0.02	0.06	682	1.0	ilm
238C	Sith	0.6	--	0.25	21	44	0.17	2.7	0.41	0.09	311	0.6	ilm>mt
285B	Sith	6	0.1	0.01	30	28	0.20	3.6	0.26	0.03	421	1.3	ilm
289B	Sith	17	1	0.03	25	30	0.18	3.6	0.25	0.12	372	1.0	ilm
290B	Sith	18	1.1	0.04	22	33	0.15	3.7	0.17	0.04	254	0.8	ilm

[1] "Source" indicates the most proximal, likely plutonic source for the dense minerals.
[2] "%Frac" indicates the proportion of the heavy-mineral separate that constituted the magnetic fraction.
Notes: "MS" = magnetic susceptibility (x 10^{-3} SI), "FHH" = Fort Hamlin Hills, "NNC" = No Name Creek, "RME" = Ray Mountains East, "Sith" = Sithylemenkat, "mt" = magnetite, "ilm" = ilmenite, "chr" = chromite.

Based on Ti:Fe ratios and magnetic susceptibilities, in about half of the cases, the majority mineral of the "magnetic" fraction was ilmenite. This was particularly true for concentrates derived from the NNC, Ray River, Sithylemenkat and Ray Mountains East plutons (Table 4.5). Based on a strong correlation ($R^2 = 0.83$) between Ti and Nb, it is likely that much of the Nb is in ilmenite, and thus the non-magnetic fraction is depleted in both Ti and Nb relative to the entire concentrate. If I take the Ti and Nb concentrations of the magnetic separate into account, as well as the relative size of the magnetic fraction, the original Ti and Nb concentrations rise by a factor of 1.5 to 4.8.

4.2.5 Sampling and Sample-Preparation Techniques

Sampling by several individuals introduces yet further variability among chemical analyses. To establish common panning techniques, seven field geologists panned samples from the same sample location at the same time. The chemical analyses presented in Table 4.6 show considerable variation: for most elements typically concentrated in dense minerals (e.g., Ti, Ta, Nb, all common in ilmenite; Zr in zircon; Cr in magnetite; Ce, Th in allanite), the concentrations in the sample taken by Geologist 1 are 2 to 3 times as great as those measured in the sample taken by Geologist 3. Based on the concentration of Y (again, a proxy for HREE + Y), Geologist 1 captured more than four times as much xenotime as did Geologist 3. Interestingly, both Geologists 1 and 3 were inexperienced at panning. The samples panned by the two experienced geologists contained concentrations intermediate between the two extremes.

Table 4.6. Concentrations of selected elements in panned concentrates for seven different samples taken at the same site by seven different geologists

Sample	%Al	%K	%Ca	%Fe	%Mn	%Ti	Ce	Y	Ba	Cr	Ta	Nb	Th	W	Zr
1*	**10**	0.7	1.5	**6.4**	**0.2**	**0.9**	**169**	**137**	**3700**	**200**	**1.9**	**19**	**22**	**16**	**355**
2*	8.6	0.7	1.2	4.7	0.16	0.7	132	90	1565	170	1.5	17	18	5	244
3*	6.4	**1.0**	1.0	3.8	0.14	0.4	53	28	1035	120	0.8	9	8	15	119
4*	9.0	0.7	1.4	4.6	0.18	0.5	113	54	1425	160	0.9	11	16	3	169
5+	9.1	0.8	**1.8**	4.9	0.18	0.5	103	62	1575	140	1.0	13	12	6	197
6+	7.5	0.9	1.0	4.7	0.17	0.4	95	47	1725	140	1.0	11	14	4	165
7*	8.4	0.9	1.7	4.6	0.15	0.5	73	38	1135	150	0.7	10	9	2	134

* indicates sample taken by geologist with beginner-level panning experience.
+ indicates sample taken by experienced geologist with proficient panning abilities.
Notes: All concentrations reported in ppm unless otherwise indicated. The highest concentration for a given element is shown in bold font; the lowest is underlined. Data compiled from Bachmann et al. (2013).

For some of the elements not concentrated into dense minerals (e.g., K in mica), Geologist 1's sample had the lowest or near-lowest concentrations, and Geologist 3's sample had the highest or near-highest concentrations. The only dense-mineral element for which Geologist 3 appeared to capture the near-highest concentration was W (Fig. 4.5, Table 4.6), likely present in scheelite. In all other respects, Geologist 3's panned concentrate simply appears less concentrated in dense minerals and richer in low-density minerals, specifically quartz and mica.

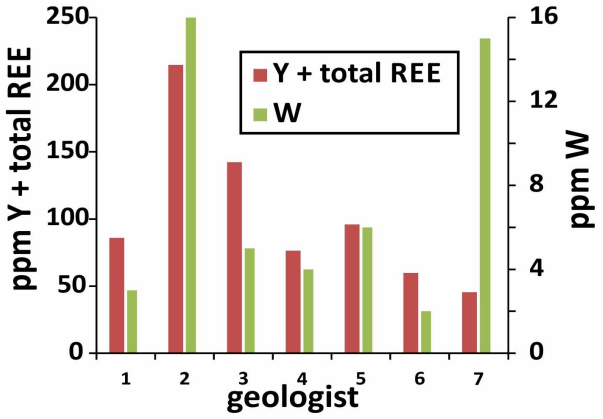

Figure 4.5. Elemental concentrations measured in heavy-mineral concentrates collected by seven different geologists.

Bulk sand-gravel samples (Appendix G) were taken in the field and processed for their dense minerals in Fairbanks. Some were treated with a sluice and then panned; some were strictly panned. Four cases are presented in Table 4.7, where samples taken from proximal sites are compared based on their processing techniques. The samples were collected between 0 and 160 m apart. In two cases, samples taken from essentially the same site were processed differently: one by sluicing and panning, the other strictly by panning. The other pairs represent sample pairs with the same processing technique applied.

For elements mostly present in low-density minerals (e.g., Ca, Mg, Rb, Ba, Sr), the sample pairs with contrasting processing techniques appear to have roughly similar concentrations. In contrast, for elements mostly present in minerals with moderate-to-high densities, the results vary.

The sample pair with the sluiced samples appears to have reproducible results, given the good correlations. On the other hand, the sample pair with the strictly panned samples has poor correlations, suggesting a lack of reproducibility. Similarly, the correlations between the two pairs of panned/sluiced samples fail to show similar results.

Furthermore, the nugget effect may also play a role. For the two panned/sluiced pairs, gold is better captured in the sluiced samples by a factor of 10 (Table 4.7). In the sample pair with the two sluiced samples, however, one sample has 11 times as much Au as the other.

There are two sources of variability with these samples: the intrinsic variability in heavy minerals within the streams, and the ability of the geologist to replicate her technique. These comparisons must be reviewed with caution, however, as the sample set is very small. A larger sample population would ensure statistical rigor.

Table 4.7. Ratio of concentrations in variably processed lab concentrates for closely spaced sample pairs and representative elements

Sample Pair	Concentration Technique	Low-Density Host					Moderate-to-High-Density Host									
		Ca	**Mg**	**Rb**	**Ba**	**Sr**	**Au**	**P**	**U**	**Th**	**Sn**	**Zr**	**W**	**Y**	**Ho**	**Ce**	**La**
1	**S-S**	1.2	1.6	1.0	1.0	1.3	11	1.1	1.1	0.8	5.3	1.4	2.7	1.1	1.1	0.7	0.7
2	**P-P**	1.1	**2.0**	0.6	**1.9**	1.0	**19**	**2.3**	**2.9**	**2.4**	**6.8**	1.1	**13**	**4.1**	**3.9**	2.0	2.1
3	**P-S**	1.0	1.1	**1.1**	1.2	1.2	0.1	1.9	1.9	2.1	2.0	**2.3**	2.4	1.9	1.9	**2.2**	**2.2**
4	**P-S**	1.1	1.5	1.1	1.0	1.0	0.1	1.0	1.0	1.0	0.8	1.0	0.5	1.2	1.3	0.9	0.9

Notes: Pair 1 refers to samples 319C/319D, taken 2 m apart; pair 2 refers to 317B/303B, taken 42 m apart; pair 3 refers to 301BB/301BA, taken from the same site; pair 4 refers to 238C/237B, taken 160 m apart. "S" = sluiced, "P" = panned. Highest ratio of concentration among sample sets is shown in bold; lowest is underlined. Data compiled from Appendix G.

In total, the data in Table 4.7 indicate that the manner in which a heavy-mineral concentrate is processed can considerably affect the elemental concentrations present. For the particular set-up employed, it is impossible to determine which method generated more reproducible results.

A final comparison lies between the field concentrates and the lab concentrates. There are numerous advantages to panning the sample in the field, but given weather conditions and time limitations, it may be preferable to simply collect a large sand-gravel sample in the field and transport it indoors for panning. All of the (24) lab concentrates processed at the lab were collected within 2 to 28 meters, with an average of 7 m, of a field-panned concentrate. A compositional comparison for the field vs. lab concentrates on an element-by-element basis (Table 4.8) yields correlation coefficients (R^2) of 0.94 (Sr) to 0.21 (Eu). (Due to the problems caused by analyzing the non-magnetic fractions of the lab concentrates, I have removed Fe, Ti, and Nb from consideration in this analysis. I removed Pb also, due to solder contamination (Figures 4.1, 4.2).)

Table 4.8. Comparison of concentrations for 24 sets of closely-spaced, field-panned and lab-panned heavy-mineral concentrates for representative elements

	Sr	**Na**	**Be**	**Co**	**Ca**	**Al**	**Rb**	**Ba**	**Mg**	**Y**	**P**	**Th**	**Ce**	**W**	**Sn**	**Zr**	**Eu**
R^2	0.94	0.91	0.86	0.84	0.81	0.77	0.67	0.65	0.64	0.57	0.53	0.50	0.48	0.30	0.27	0.25	0.21
Slope*	0.9	1.4	0.8	0.59	0.72	0.8	0.66	1.0	0.69	1.2	1.0	1.2	1.0	0.69	1.7	1.0	0.6

* indicates the slope is the average concentration in the lab-panned concentrates relative to the field-panned concentrate for that element.

For most elements present in low-density minerals (e.g., Sr, Na, Be, Ca, Al), the concentrations in field and lab concentrates agree very well, with high (> 0.75) R^2 values and slopes (representing the average concentration in the lab concentrate relative to the field concentrate) typically around 0.7 to 0.8. That is, the lab concentrates yield slightly lower concentrations.

For most elements in high-density minerals, the R^2 values are lower, but on average the ratio of concentrations in lab-to-field concentrates hover around 1 (Table 4.8). Figure 4.6 illustrates the typical patterns for two elements (Sn and Y), both of which yield poor R^2 values (0.57 and 0.25, respectively, Table 4.8) for the entire data set, but tremendously improved correlations if only one outlier is removed. For Sn, the outlier is a data point representing a lab concentrate with an anomalously high ratio. For Y, the outlier is a data point for which the lab concentrate has an unusually low ratio.

For the set of 39 elements and 24 comparison pairs, the average correlation coefficient is 0.53, and the average slope is 0.93. That is, on average, there is a fair correlation between elemental concentrations in the concentrates made in the field and in the lab. On average, the concentrations are similar and show similar trends (e.g., Fig. 4.8); however, within the set of 24 comparison pairs, there is commonly one sample that causes a poor correlation. In the case of the REE, it is the sample that also causes problems for the Y correlation (Fig. 4.6B).

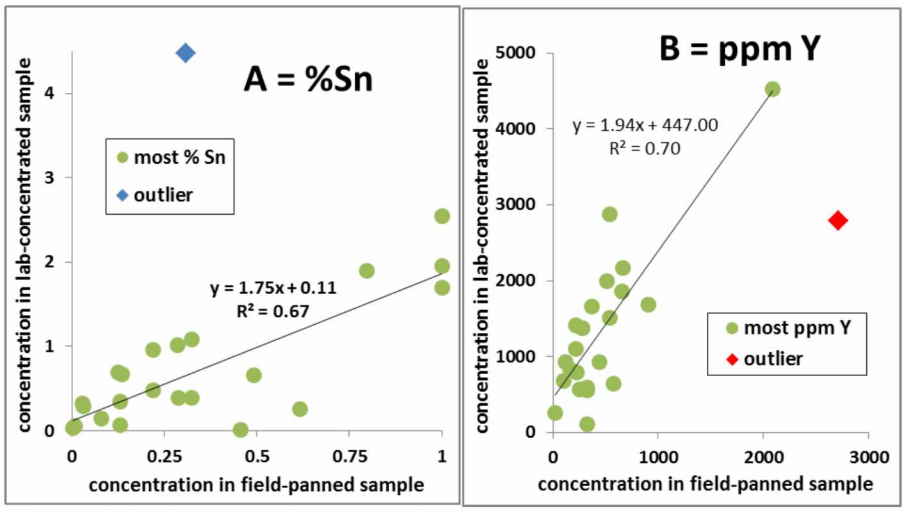

Figure 4.6. Representative plots showing elemental concentrations for field-panned samples vs. concentrations for lab-panned samples taken within 28 meters of one another. A) % Sn and B) ppm Y. In both cases, the overall correlation is considerably improved by removing only one outlier.

4.2.6 Summary of Issues Involving Drainage Samples, Especially Panned Concentrates

The problems I have encountered are mostly related to (a) the additional processing necessary for concentrated samples, (b) the high concentrations of many ore elements common in concentrated samples, and (c) the difficulty in dissolving many of the minerals characteristic of the dense-mineral fraction of a sediment. The additional processing can lead to contamination—both between samples and between processing material and samples. Given that the additional processing (panning) was performed by many geologists with variable levels of experience, the results must vary (e.g., Table 4.6). The high concentrations of elements also can lead to contamination, as traces of a sample with high elemental concentrations are transferred to other samples during crushing and other operations (e.g., Fig. 4.4). The high concentrations—combined with difficult-to-dissolve minerals—create situations that may lead to serious under-reporting of elemental concentrations (e.g., Table 4.4). Given these factors, caution is advised in examining the data sets.

4.3 Trace-Element Distribution in Stream and River Materials

4.3.1 Stream-Sediment Samples

As part of this study, approximately 400 stream-sediment samples (Fig. 4.7)—that is, samples of the fine-grained fraction of the active streambed—were collected and analyzed. At least 5 to 10 samples were taken in (or immediately downstream from) each of the major plutons in the study area (Fig. 4.7). I assigned a pluton to each analysis where such was unambiguous. Based on these assignments, I determined the average stream-sediment elemental concentrations for each pluton (Table 4.9) and arranged them by geography of the plutons (from northeast to southwest). I also included data for stream sediments draining the Melozitna pluton, 90 km southwest of the Ray Mountains West pluton (Freeman et al., 2012).

Most elements do not show much variation. For example, the highest average Ti (0.64%) is less than twice the lowest (0.35%). Elements generally enriched in mafic rocks, however, are present in highest concentrations in the stream sediments draining the northernmost Bonanza pluton; lowest concentrations are associated with the NNC and Ray Mountains East plutons. Although elements generally enriched in felsic rocks are typically at lowest concentrations in stream sediments associated with the Bonanza pluton, they are at highest concentrations in

stream sediments associated with the Sithylemenkat (and to a lesser extent, NNC) plutons. On the other hand, the felsic-associated elements Ta, Th, and U are lowest in stream sediments draining the Ray River pluton, and the lowest Rb is associated with the Fort Hamlin Hills pluton. Ironically, the highest average Zr concentrations are with plutons at the north and south ends of the data set (Table 4.9). For elements both representative to LREE (Ce) and HREE + Y (Y), the highest concentrations are in stream sediments associated with the Sithylemenkat pluton; the lowest are with the Ray River and Coal Creek plutons.

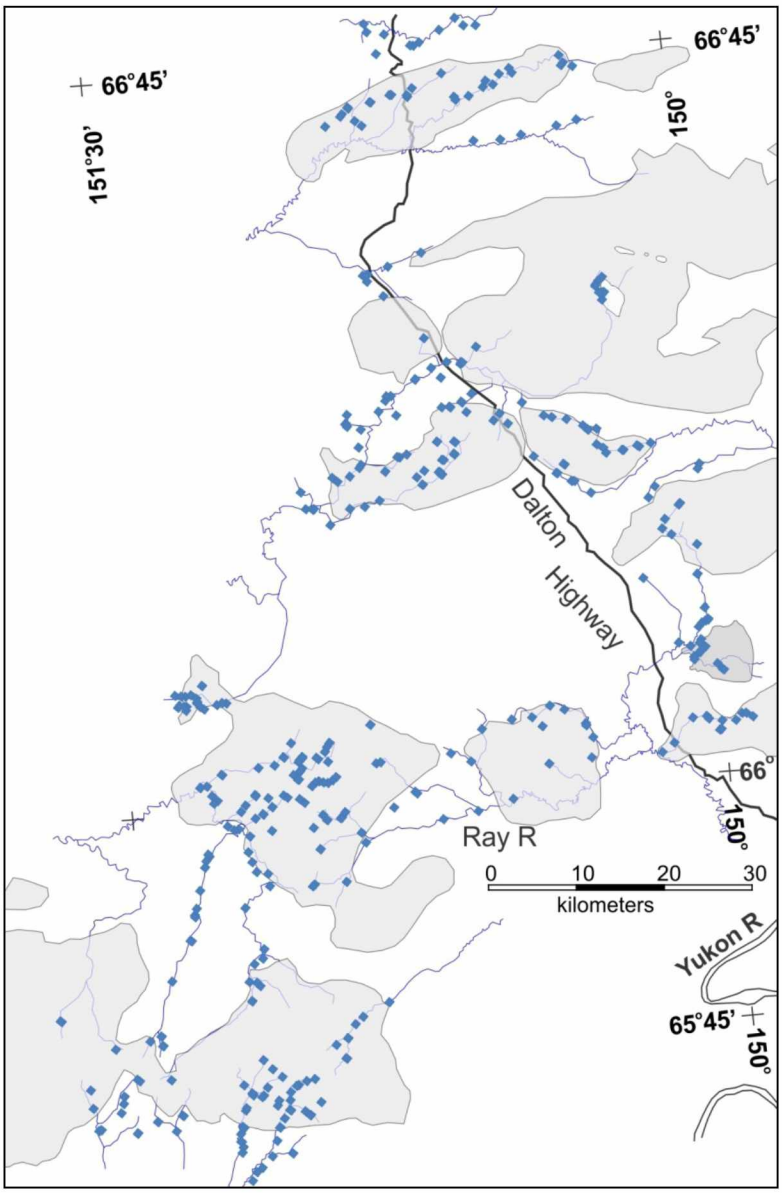

Figure 4.7. Map showing locations of stream-sediment samples (blue diamonds) taken as part of this study. Grey bodies are the major plutons of the central and southern Ruby batholith.

Table 4.9. Average stream-sediment compositions for representative elements associated with different plutons of the Ruby batholith, arranged north to south

Pluton	Mg%	Sr	V	Ti%	Be	Cs	Rb	Sn	Ta	U	W	Th	Zr	P	Eu	Ce	Y
Bon	**1.4**	**331**	**176**	**0.63**	2	5	82	3	1.9	12	2	26	**1254**	**1539**	**2.6**	132	55
Kanuti	1.0	281	127	0.56	3	12	125	4	1.8	14	17	40	489	911	1.7	159	51
HSE	0.93	255	118	**0.64**	3	7	103	4	3	15	15	50	668	**1163**	1.8	180	49
HSW	0.76	210	79	0.47	5	12	154	16	3	**33**	14	49	1038	742	1.3	141	59
Coal Creek	0.65	140	97	0.40	3	7	111	6	1.7	14	5	27	475	860	1.1	97	36
NNC	0.44	105	81	0.35	6	**41**	**393**	46	**5.2**	9	14	53	418	587	0.9	182	**92**
FHH	0.63	171	104	0.42	2	5	83	13	2.2	9	5	43	601	873	1.2	146	47
RR	0.78	155	133	0.41	2	6	91	12	1.3	7	8	20	336	754	1.3	96	43
Sith	0.44	120	76	0.40	**8**	16	248	**91**	**5.1**	**42**	**47**	**108**	837	730	1.1	**326**	**105**
RMW	0.56	149	81	0.36	5	12	258	52	4.3	15	28	59	507	941	1.3	209	60
RME	0.42	110	69	0.36	**8**	12	258	52	4.3	28	33	95	667	951	1.1	300	**99**
Melo	0.73	171	89	0.53	4	6	145	54	3.4	25	17	80	**1343**	957	1.4	276	63
Assoc*	M	M	M	M	F	F	F	F	F	F	F	F				F	F

* Assoc = Elemental association: The element is more concentrated in felsic (F) or mafic (M) rocks as taken from Faure (1998). Concentrations are in ppm unless otherwise indicated. Highest concentrations for each element are in bold font; lowest are underlined. Pluton abbreviations: "Bon" = Bonanza, "HSE" = Hot Springs East, "HSW" = Hot Springs West, "NNC" = No Name Creek, "FHH" = Fort Hamlin Hills, "RR" = Ray River, "Sith" = Sithylemenkat, "RMW" = Ray Mountains West, "RME" = Ray Mountains East, "Melo" = Melozitna. Data from Freeman et al. (2012) and Bachmann et al. (2013).

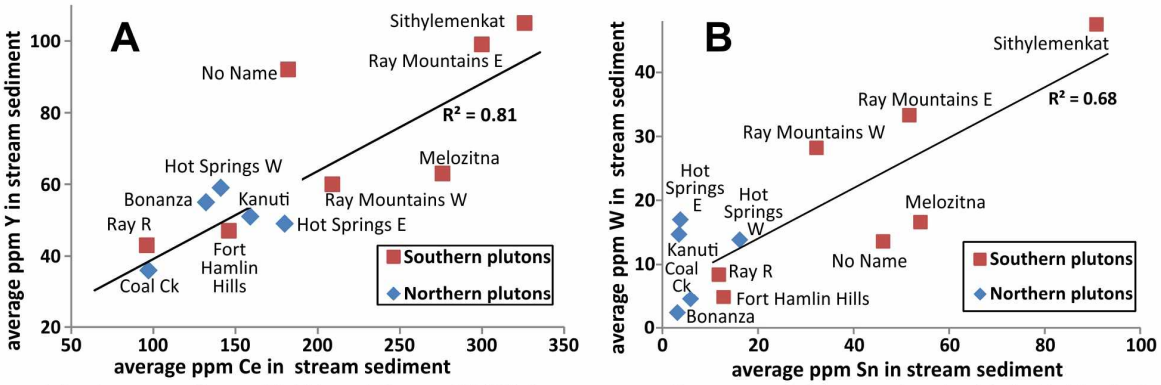

Figure 4.8. Average Ce vs. Y (A) and Sn vs. W (B) for stream-sediment samples associated with individual plutons of the Ruby batholith. Data taken from Table 4.10.

As shown on Figure 4.8, elemental concentrations in stream sediments tend to cluster into groups associated with northern and southern plutons, but only in a general sense. In particular, data for the Fort Hamlin Hills and Ray River plutons plot alongside the northern group. This contradicts the fact that both—in terms of rock trace-element concentrations (Chapter 3), and mineralization data (Table 2.7) for the Ray River pluton—clearly resemble the Sithylemenkat pluton.

For the average stream-sediment sample data, (HREE + Y) and LREE generally increase together, as indicated by Ce and Y concentrations (Fig. 4.8A). Stream sediments associated with the NNC pluton fall outside of the trend line defined by the others, but I have previously shown that the average rocks from the NNC pluton have an unusually low Ce/Y ratio (Fig. 3.19). Data for Melozitna-associated stream sediments seem low in Y relative to the other plutons, but rocks from the Melozitna pluton are low in Y (for a given TiO_2) relative to the other southern samples (Fig. 3.17A).

In a similar manner, average stream-sediment compositions from the various plutons show a rough proportionality between Sn and W (Fig. 4.8B), with sediments from the Ray Mountains plutons having higher W, and those from NNC and Melozitna plutons having lower W. Such is not borne out by the mineralized samples (Table 2.7), as altered rocks from the NNC pluton have higher W/Sn than the others.

Table 4.10. Correlation coefficients (R) for representative elements in the stream sediments

	Mg	**Ca**	**Be**	**K**	**Rb**	**Co**	**Sc**	**Hf**	**Sn**	**Ta**	**Nb**	**W**	**Th**	**La**	**Ce**
Ca	0.84														
Sr		0.78													
Rb			0.74	0.83											
Tl				0.81	**0.95**										
Mn						0.79									
Sc	0.84														
V	0.74						0.86								
Zr								**0.99**							
Nb										**0.91**					
W									0.77						
Th										0.83	0.85				
La									0.76	0.81	0.84	0.76	**0.95**		
Ce									0.78	0.81	0.84	0.75	**0.96**	**1.00**	
Y									0.75	0.86	0.84		0.87	0.88	0.89

Note: R-values < 0.74 have been omitted for clarity. Especially high R-values are shown in bold font.

Correlation coefficients for representative elements in the stream-sediment data set (Table 4.10) show patterns largely in agreement with rock patterns. For example, mafic-associated elements Sc-V-Mg show strong correlations, as do the felsic-associated elements K-Rb-Tl-Be. The strong Ta-Nb association reflects geochemical similarity; the strong Th-La-Ce

correlations presumably relate to co-occurrence in allanite and monazite. Sn correlates with Nb, Ta, REE, and Th, with the correlation likely related to co-occurrence with dense minerals.

4.3.2 Laboratory-Concentrated, Bulk Heavy-Mineral Samples

As previously discussed, the lab concentrates have analytical and sample preparation problems. Removing the magnetic portion also changed the concentrations of Ti, Nb, and possibly other components. Nevertheless, they represent the best characterization of the dense minerals in drainages from the various southern plutons. Average elemental concentrations for the lab concentrates associated with the various plutons are presented in Table 4.11.

Table 4.11. Average concentrations for selected elements from non-magnetic fractions of the laboratory concentrates draining the southern Ruby batholith plutons

Pluton	%Mg	Sr	V	Be	Cs	Rb	%Sn	Ta	U	W	%Th	%Zr	%P	Eu	%Ce	%Y	%tREE
NNC	0.11	31	35	**13**	**16**	275	1.4	**70**	97	959	0.05	0.31	0.10	2.5	0.16	**0.22**	0.44
FHH	0.05	27	25	3	6	184	0.02	14	18	38	0.01	0.24	0.02	1.0	0.03	0.02	0.08
RR	**0.19**	41	**69**	5	7	177	0.7	45	64	280	0.06	0.14	0.17	**4.0**	0.19	0.10	0.46
Sith	0.13	**52**	35	8	13	**280**	**1.7**	64	**199**	**1023**	**0.18**	**0.83**	**0.33**	3.2	**0.58**	0.19	**1.3**
Assoc*	M	M	M	F	F	F	F	F	F	F	F				F	F	

* Assoc = Elemental association: The element is more concentrated in felsic (F) or mafic (M) rocks as taken from Faure (1998). Concentrations are in ppm unless otherwise indicated. Highest concentrations for each element are in bold font; lowest are underlined. Pluton abbreviations: "NNC" = No Name Creek, "FHH" = Fort Hamlin Hills, "RR" = Ray River, "Sith" = Sithylemenkat. "tREE" = total REE. Data from this study (Appendix G).

Unlike the stream-sediment data, the heavy-mineral concentrates commonly exhibit concentration variations among source plutons of 5 to 20 times. For example, the average Sn concentration from the Sithylemenkat samples was 1.7%, 85 times that from the Fort Hamlin Hills pluton (0.02% Sn). Since lab concentrates were only taken from the southern plutons, one might expect similar heavy-mineral concentrations. In fact, the overwhelming pattern is that the samples draining the Fort Hamlin Hills pluton are low in practically all elements measured. The highest concentrations for most elements are observed in the Sithylemenkat and (or) NNC pluton samples (Table 4.11). Thus, it appears that the concentrates derived from the Fort Hamlin Hills pluton contain more quartz than the other samples. (I suspect the major dilutant is quartz because these samples also contain the lowest concentrations of Na, Al and Ca.)

The lab concentrates clearly show that the samples derived from the Sithylemenkat pluton contain the highest concentrations of total REE and (gauging from the %Ce) the highest

concentrations of LREE. In contrast, the samples draining from the NNC pluton contain the highest %Y and the highest %HREE.

4.3.3 Field-Concentrated, Heavy-Mineral Samples

Approximately 200 field concentrates were collected as part of this study. The number is smaller than that of the total stream-sediment samples because coarse (sand-size and larger) sediments were absent at many collection sites. In general, a sufficiently large number of sites per pluton adequately characterized the heavy-mineral suite for each of the major plutons. Only six samples, however, were taken from drainages in the Hot Springs East pluton, and two of these were highly enriched in a variety of metals. The data for this pluton are skewed relative to the others. Kanuti pluton samples were exclusively from the western portion. I also included data for heavy-mineral concentrates from the Melozitna pluton (Freeman et al., 2012).

The pluton-averaged data for the field concentrates (Table 4.12) are broadly similar to that of the stream-sediment data, but with more striking differences among the plutons. For most of the elements, a compositional distinction is present for the samples from the northern vs. southern plutons. For the mafic-associated elements, Mg, Sr, and V, the highest concentrations are present in concentrates taken near the Bonanza, Kanuti, Hot Springs East and Hot Springs West plutons. The lowest concentrations of these elements are in samples associated with the NNC, Fort Hamlin Hills, and Sithylemenkat plutons. The samples from the Coal Creek pluton do not appear very diagnostic, as they contain low concentrations of most elements analyzed. I suspect that the Coal Creek concentrates are simply not very concentrated. The Ti concentrations do not fit into the same patterns as the other mafic-associated elements. The highest- and lowest-average Ti concentrations are from the southern plutons. For these plutons, most of the Ti is likely present in ilmenite, and the panned concentrates reflect variable degrees of natural (within the stream) and human (panning technique) concentration of ilmenite.

Table 4.12. Average concentrations for select elements of the field-panned concentrates draining the southern plutons of the Ruby batholith, arranged from north to south

Pluton	%Mg	Sr	V	%Ti	Be	Cs	Rb	%Sn	Ta	Nb	U	W	Th	%Zr	%P^+	%Ce	%Y
Bon	**1.1**	215	**225**	1.2	2	3	60	0.01	7	68	22	16	49	0.25	0.09	0.03	0.02
Kanuti	0.91	**232**	143	1.2	3	4	83	0.004	7	49	15	30	72	0.10	0.06	0.03	0.01
HSW	0.87	**225**	120	1.5	3	7	137	0.05	11	61	17	114	52	0.13	0.03	0.02	0.01
HSE	**1.4**	204	187	4.1	2	3	75	0.04	54	273	51	351	338	**0.27**	0.13	0.14	0.04
Coal Ck	0.24	96	47	0.9	4	7	183	0.01	7	30	15	15	51	0.13	0.04	0.02	0.01
NNC	0.29	44	44	1.5	**21**	**16**	258	0.48	**86**	**324**	47	323	236	0.14	0.06	0.07	**0.10**
FHH	0.17	80	52	2.5	4	6	158	0.08	23	120	18	33	265	0.12	0.05	0.09	0.02
RR	0.37	54	87	**5.9**	4	6	169	0.16	23	110	23	121	193	0.07	0.09	0.07	0.04
Sith	0.18	73	45	1.3	6	9	**262**	**0.83**	37	180	**68**	**487**	**438**	0.21	0.13	0.18	0.06
RME	0.38	96	62	0.9	5	7	237	0.12	14	81	23	179	200	0.09	0.09	0.08	0.02
Melo	0.42	103	95	2.0	4	7	131	0.28	36	232	**92**	211	**651**	**0.36**	**0.16**	**0.27**	0.04
Assoc*	M	M	M	M	F	F	F	F	F	F	F	F	F			F	F

* Assoc = Elemental association: The element is more concentrated in felsic (F) or mafic (M) rocks as taken from Faure (1998). Concentrations are in ppm unless otherwise indicated. Highest concentrations for each element are in bold font; lowest are underlined. Pluton abbreviations: "Bon" = Bonanza, "HSW" = Hot Springs West, "HSE" = Hot Springs East, "Coal Ck" = Coal Creek, "NNC" = No Name Creek, "FHH" = Fort Hamlin Hills, "RR" = Ray River, "Sith" = Sithylemenkat, "RME" = Ray Mountains East, "Melo" = Melozitna. Data compiled from Lough et al. (2012) and Bachmann et al. (2013).

Felsic-associated elements (e.g., Be, Cs, Rb, Ta, Sn, U) are exclusively present in high concentrations in samples from the southern plutons, especially the NNC, Ray River, Sithylemenkat and Melozitna plutons (Table 4.12). Conversely, the lowest concentrations of these elements are restricted to field concentrates from the northern plutons. Ce (representing the LREE) and Y (representing the HREE + Y) are most concentrated in samples from the southern plutons (Melozitna and NNC, respectively). The REE are least concentrated in samples from the northern plutons, although samples from the Hot Springs East pluton contain higher-than-expected Ce and Y concentrations, as well as a wide range of felsic-associated elements (Table 4.12).

The REE patterns are illustrated for the complete set of concentrates, not just the averages (Fig. 4.9). Concentrates from most of the southern plutons have the highest REE concentrations. Although not shown by the average data (Table 4.12), there is a clear south-to-north decrease in maximum REE concentration in the panned concentrates, from (in this specific instance) Melozitna (farthest south) to Ray River (farthest north). Concentrates from the NNC pluton have generally higher HREE + Y and similar or lower LREE concentrations than those

from the other southern plutons. Data from the northern plutons plot together at low REE concentration—with one exception, the Hot Springs East pluton, from which two of the highest REE concentrates were derived (Fig. 4.9).

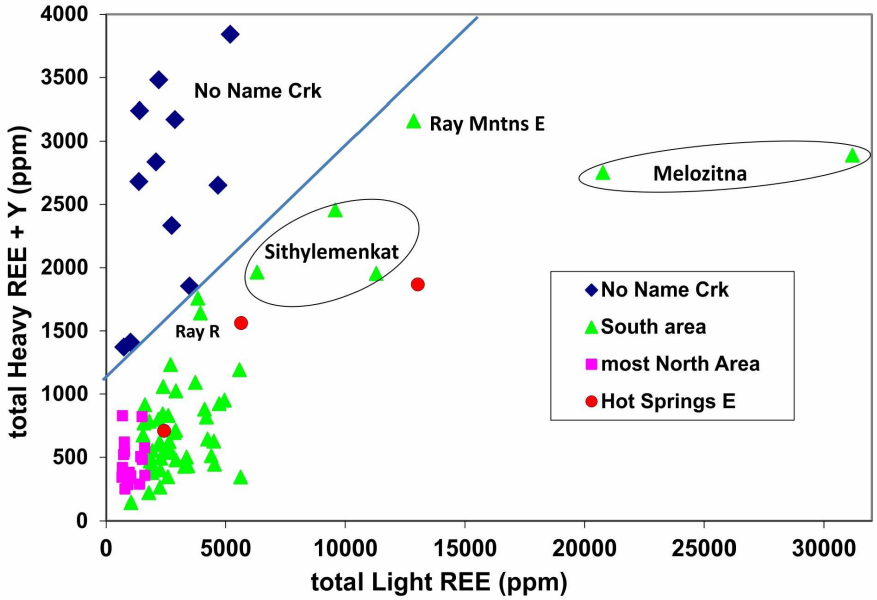

Figure 4.9. Total LREE vs. total (HREE + Y) concentrations for field concentrates from the central and southern Ruby batholith. Data from Freeman et al. (2012) and Bachman et al. (2013).

The spatial pattern of REE concentrations (Fig. 4.10) emphasizes the REE distinctions shown on Figure 4.9. Two of the field concentrates from the Hot Springs East pluton are truly anomalous in their REE content. All of the other high-REE field concentrates are derived from the southern plutons (Fig. 4.10A). Even the Fort Hamlin Hills pluton yields panned concentrates with higher REE concentrations than those of the northern plutons.

Although samples with low-total REE concentrations can have relatively high ratios of (HREE + Y)/LREE (Fig. 4.10B), among those samples with appreciable total REE concentrations, only samples from NNC really have high HREE + Y. The unique character of the NNC pluton and its associated REE patterns are striking.

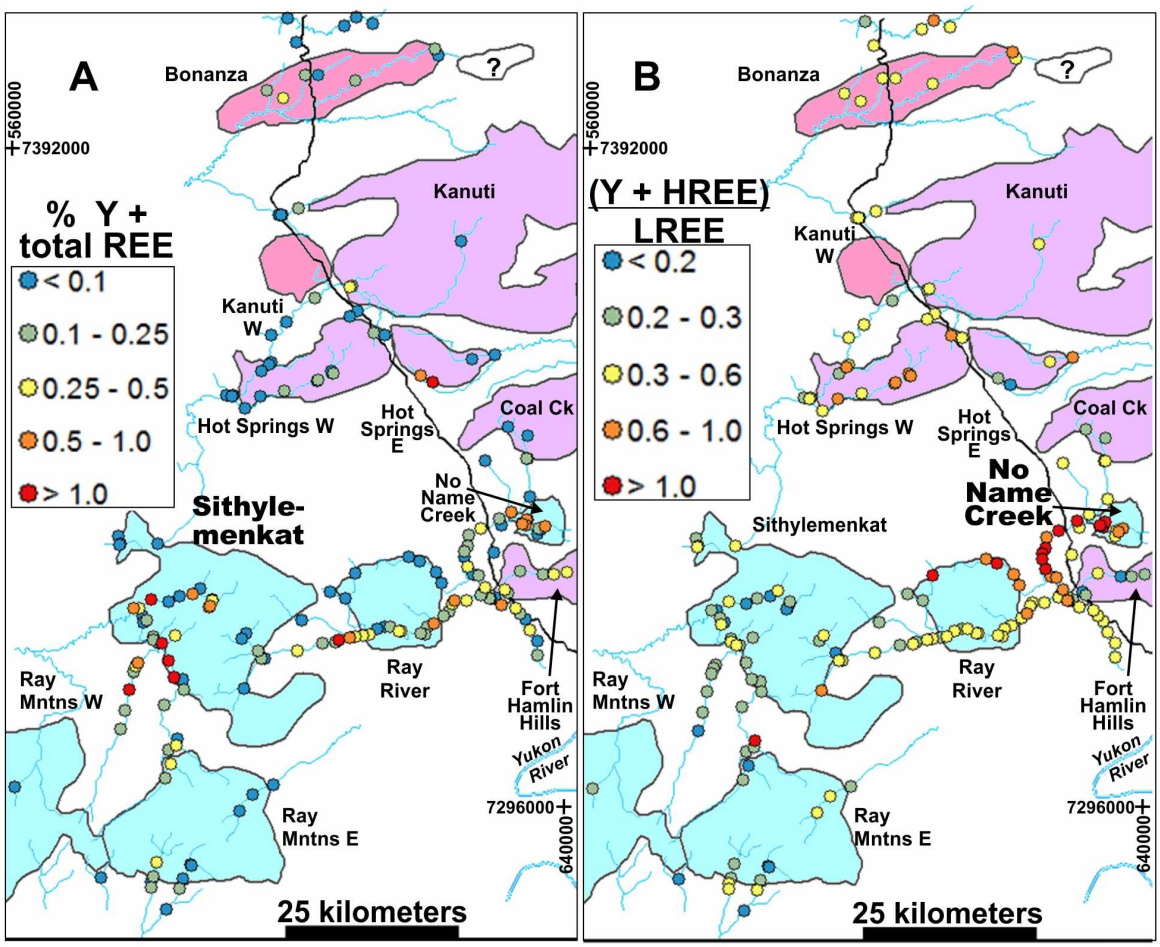

Figure 4.10. Distribution of % total (REE + Y) (A) and of (HREE + Y)/LREE (B) for field panned concentrate samples from the central and southern Ruby batholith. Plutons are labeled and shaded according to grouping: characteristically northern plutons are pink; transitional plutons are purple; southern plutons are blue. The highest total concentrations of REE in the map area are from samples draining the Sithylemenkat pluton, but also from the Hot Springs East pluton. The highest ratios of (HREE + Y)/LREE are almost entirely restricted to the NNC area. Data compiled from Bachmann et al. (2013).

The contrast in Sn and W data for the field concentrates relative to the stream sediments is also unusual. Figure 4.11A shows Sn vs. W for the field concentrates with patterns similar to those seen for the stream sediments, yet with completely different Sn:W average ratios. The field concentrate data also clearly shows that relative to the average trends, Hot Springs East is seriously depleted in Sn, and that relative to a "normal" northern pluton, the concentrates contain far too much W. Samples from the Hot Springs West pluton also appear to be slightly enriched in W relative to the other northern plutons. Furthermore, concentrates from the Ray Mountains East pluton are either depleted in Sn, enriched in W, or both relative to the other southern plutons.

The concentrations of Nb and Ta were too low in the stream sediments to show any contrast. The field concentrate data, however, shows a clear separation between the northern and southern plutons for all but the Hot Springs East pluton, which plots with the southern group. The strong Nb-Ta correlation is true both for pluton-averaged samples and also for individual samples (see ahead).

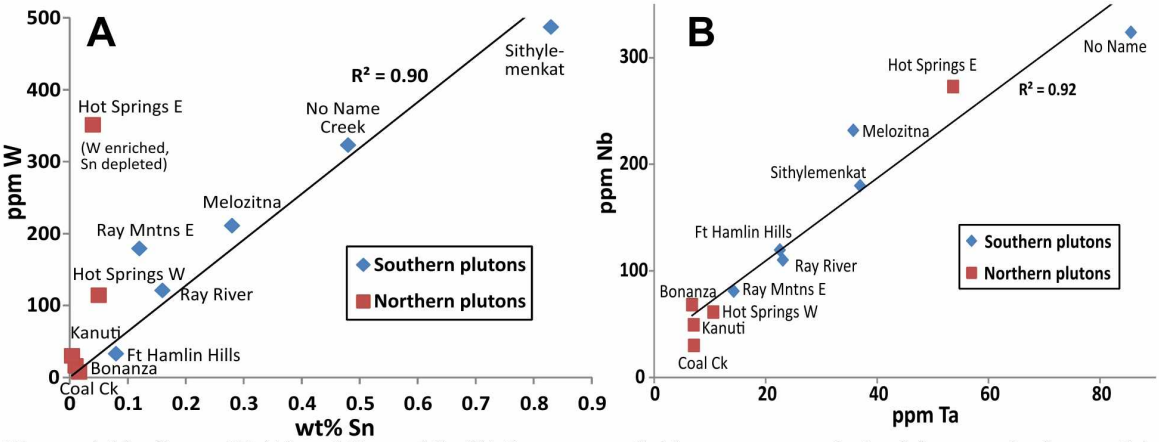

Figure 4.11. Sn vs. W (A) and Ta vs. Nb (B) for average field concentrates derived from each pluton of the central and southern Ruby batholith. Correlation line in A excludes data from the Hot Springs E pluton, but includes all others shown. The correlation is similar to that shown for stream sediment analyses (Fig. 4.7B), but for those the average Sn:W is approximately 2; for the panned concentrates, the average ratio is approximately 10.

The spatial pattern of Sn concentrations in field-concentrated samples (Fig. 4.12) for mostly southern plutons shows the difficulty in deciphering the source for a particular sample. Near-continuous samples taken along the Ray River, beginning in the Sithylemenkat pluton, show a near-abrupt drop in Sn concentration just after crossing into the Ray River pluton, and then rise again farther downstream. It seems unlikely that all the Sn in the lower Ray River is derived from the Sithylemenkat pluton, but it appears to be so.

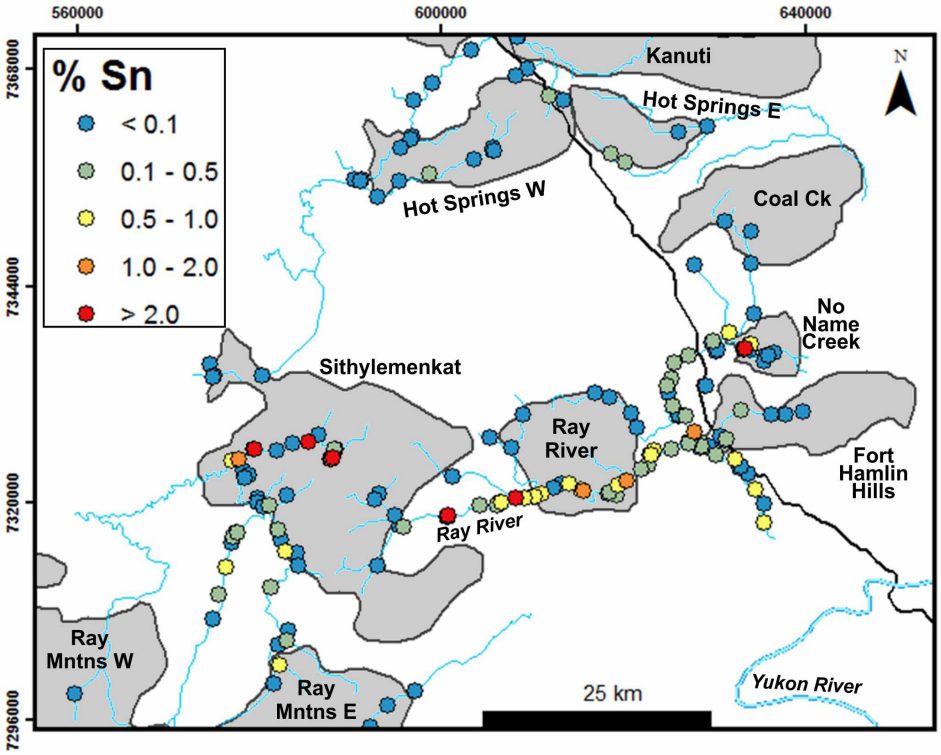

Figure 4.12. Distribution of Sn concentrations in field concentrates from the central and southern Ruby batholith area. Major plutons are in grey with names as indicated. Data compiled from Bachmann et al. (2013).

Correlation coefficients for representative elements in the field concentrates show both expected and unexpected values (Table 4.13). Among elements likely present in silicate minerals, notable are very strong correlations between K-Tl-Rb (which are all relatively large ions with a +1 charge), Ca-Mg-Sr (with a +2 charge), and Mn-Fe-Sc (elements that concentrate in mafic minerals). Strong correlations between Ti-Fe-Mn-Nb reflect their occurrence in ilmenite. Very strong Hf-Zr correlations reflect their near-identical geochemical behavior and their occurrence in zircon. Extremely strong (R = 0.98 to 1.0) correlations between Ce-La-Th reflect the co-occurrence of these three within allanite and monazite. Relatively strong correlations between Hf-Zr-P-U-Th-La-Ce-Y likely reflect occurrence of these elements in dense minerals, although not the same minerals. In particular, neither Sn nor W strongly correlate with one another, nor do they correlate with other elements in dense minerals. That is, intrinsic differences in how the elements occur in rocks must play a role in the eventual heavy-mineral concentrates. Sn, for example, mostly occurs in greisen-altered granite, which does not usually contain anomalous concentrations of REE-bearing minerals (Table 2.7).

Table 4.13. Correlation coefficients (R) for representative elements in the field concentrates

	Ca	Mg	K	Rb	Co	Fe	Mn	Ta	Nb	Hf	Zr	P	U	Th	La	Ce
Ca		0.84														
Sr	0.81															
Rb			0.82													
Tl			0.81	**0.98**												
Ni					0.83											
Sc						0.87										
Mn						0.79										
Ta							0.77									
Nb							0.79	**0.96**								
Ti						0.84	0.83	0.83	0.89							
Zr										**0.99**						
P										0.85	0.84					
U										0.78	0.76	0.80				
Th									0.78	0.81	0.78	0.93	0.84			
La										0.84	0.81	0.93	0.84	**0.98**		
Ce										0.86	0.82	0.93	0.85	**0.98**	**1.00**	
Y								0.80	0.87	0.77		0.82	0.80	0.87	0.85	0.86

Notes: R-values < 0.74 have been omitted for clarity; especially high R-values are shown in bold font. Data is from Bachman et al. (2013).

4.4 DISCUSSION

4.4.1 Contamination

Based on observation of spherical solder beads in all of the Pb-rich laboratory concentrates, I attribute the high-Pb content to solder contamination. Possible solder contamination of samples was discussed previously (Chapter 2) and is likely due to contamination from sampling equipment or other laboratory facilities.

It is conceivable that the solder was in the drainage prior to sampling due to past anthropogenic activities. If that were the case, however, then field-panned concentrates from nearby locations ought to have been enriched in Pb as well. Such samples were taken 2 to 5 m from those contaminated, and they all contained less than 40 ppb Pb. Further, the maximum Pb concentration in all of the field concentrates was 95 ppm, drastically lower than the 300-1250 ppm Pb in the solder-contaminated lab concentrates. I am forced to conclude that the solder contamination occurred after sample collection and during the sample-processing procedures.

I submit that the reason why Pb shows such a strong correlation with many dense-mineral elements (Table 4.1), including Zr, La, Th, P, and W, is that the solder was introduced into the samples prior to or during the concentration steps. I also suggest that the contaminated (but unprocessed) samples possessed similar monazite, zircon, and scheelite/wolframite contents. During the concentration process, all of the dense phases (minerals and solder alike) were sub-equally concentrated. This process would cause Pb to correlate with many dense-mineral elements.

Though the Pb-Sn solder alloy contributed to significant Pb contamination in few samples, the concentration of Sn due to contamination is sufficiently small relative to the concentration of Sn naturally occurring (via cassiterite) that the Sn contamination is negligible and does not affect the overall Sn concentrations. The lesson here is that increased handling of materials increases the likelihood for contamination.

4.4.2 Digestion Methods

The elemental concentrations reported for the REE, Y, and Th were generated by ICP-MS following lithium metaborate fusion digestion, which is said to provide "complete" digestion. P concentrations were instead generated from analytical techniques following four-acid digestion, which provides "near-complete" digestion. Both digestion methods were used on splits from the same sample, and both methods were attempting to digest the REE-phosphate minerals monazite and xenotime. Given the chemical analyses, it is apparent that the lithium metaborate fusion digestion was more efficient at digestion of the REE phosphates than was the four-acid digestion. This is not to imply that four-acid digestion is ineffective at digesting all phosphate phases; the common phosphate accessory mineral, apatite, can be efficiently digested via four-acid digest. A significant presence of apatite is necessarily responsible for those samples with atomic P > atomic (REE+Y+Th).

Furthermore, REE may be present in non-phosphate minerals, such as allanite, in cases where atomic (REE+Y+Th) > atomic P. Unfortunately, due to the partial digestion for P, quantifying either the amount of apatite or non-P REE minerals present in the samples is not possible. Considering all the NNC samples plot in the field of atomic (REE+Y+Th) > atomic P, and I never identified any allanite in the NNC samples, P deficiency due to partial analysis (and relatively abundant apatite) is at least sometimes the case.

I suspect that the inaccurate commercial analyses of USGS standard COQ-1 resulted from incomplete digestion as well. Though the standard did undergo lithium metaborate fusion digestion, it is possible that the very high concentration of "insoluble" minerals in that standard exceeded the capacity of the fusion process to solubilize them. Okina et al. (in press) determined that HF concentration—not the ratio of various acids—and the duration of the digestion process control the actual digestion of a rock.

4.4.3 Sampling and Sample-Preparation Techniques

As noted from the example of multiple geologists panning at the same site (Table 4.6), variability in panning technique is a significant factor for variability in the concentrates, and it needs to be taken into consideration. At best, panning concentrates minerals with greater mass, and mass is a function of both density and size. Fine-grained, dense minerals are more likely to be lost in panning than are coarser ones. Standard gravity separation theory dictates that a minimum grain size of 75 μm is required to efficiently separate a mineral with a density of 5 g/cm^3 (e.g., monazite, xenotime) from quartz (Gupta and Yan, 2016). Given that the xenotime I have observed is rarely larger than 20 μm in diameter, and only somewhat larger than monazite, one would expect that panning is not terribly efficient for these minerals.

If the data in Table 4.6 is representative, one could expect variations of at least ± 50% in elemental abundance for panned concentrates—depending on who did the panning. It is likely that for a large enough sample set, variations in panning ability would average out, but for plutons with less than a dozen heavy-mineral concentrates it is possible that the data is skewed.

Laboratory concentration of the bulk heavy-mineral samples did not tend to create better concentrates; the average of a given element in the lab-panned concentrate relative to the corresponding field-panned concentrate (Table 4.8) was close to 1, with much scatter in the data. Panning in the laboratory may be more efficient and less time restrictive, but it did not necessarily produce better results. Panning in the lab certainly does increase chances for sample contamination, however, as indicated by the solder issue.

I am unable to compare data for Fe, Ti, Nb or V due to the selective removal of these elements with the magnetic fraction (Table 4.5). In this situation, with limited magnetite present in most samples, it seems to have not improved the concentrate but makes direct comparison to

the field-panned samples more problematic. I recommend not removing the magnetic separate in future studies of this sort.

Of the four variably processed lab-concentrate pairs (Table 4.7)—given the limited data and the variable results—it is inconclusive which technique is superior. It may appear that sluicing leads to more reproducible results, possibly because a larger sample is likely more representative of the material. Also, Au might be better concentrated by sluicing rather than by strictly panning, but with only two comparison pairs, drawing a conclusion seems premature.

4.4.4 Stream-Sediment vs. Pan-Concentrate Sampling

Stream-sediment sampling targets the very fine-grained (clay-rich) material onto which cations and anions have adsorbed. Pan-concentrate sampling targets dense minerals in the sediment load. It takes much less time (< ¼) and expertise to collect a stream-sediment sample than a pan-concentrate sample. In the study area, it was not possible to collect a pan-concentrate sample in roughly one-half of the drainages, though it was almost always possible to collect stream sediments. (Furthermore, the work plan did not call for panned concentrates at all sample sites, only at major drainages and sites where there was identified alluvial volume.) Because they contain large concentrations of elements in difficult-to-dissolve minerals, panned concentrates are more expensive to analyze and may further require re-analysis for especially abundant elements. These factors make stream-sediment sampling much less expensive and easier; however, in this particular case, they appear to yield data of somewhat marginal utility.

Stream-sediment and field concentrate samples were successfully collected at essentially the same site in 132 cases. Table 4.14 gives correlation coefficients (R^2) between concentrations in the stream-sediment sample and the corresponding pan-concentrate sample for representative elements. The highest R^2 is 0.69 (Ca); the lowest is 0.19 (W). The average slope of the best-fit line—usually an approximation to the average concentration in the stream-sediment sample relative to the concentrated sample—was usually < 1, and commonly < 0.1 (Table 4.14). Cases where the concentration in the stream-sediment sample was higher are restricted to cases where more of the element was adsorbed onto fine-grained sediment surfaces than was present in dense minerals. In this setting, such was true for Cs, Co and Cu. Especially low-concentration ratios are caused by both the presence of the element in a high-density mineral(s), and a slight tendency to be adsorbed onto clay surfaces. Elements with high oxidation states, e.g., Ti, Nb, Ta, Sn, and

W, fit into this category. Their concentrations in a given pan-concentrate sample were typically 20 times greater than in the associated stream-sediment sample (Table 4.14). The concentrations of REE—not quite as extreme—are typically 10 times as great in the concentrated samples.

Table 4.14. Correlation coefficients (R^2) and best-fit slopes for the stream-sediment vs. pan-concentrate samples collected at the same site

	Avg	**Ca**	**Cs**	**Eu**	**Rb**	**Y**	**V**	**Th**	**Ce**	**P**	**Ti**	**Co**	**Nb**	**K**	**Zr**	**Sn**	**W**
R^2	0.37	0.69	0.61	0.50	0.48	0.43	0.42	0.40	0.39	0.35	0.32	0.32	0.29	0.28	0.27	0.24	0.19
Slope*	0.34	0.48	**1.4**	0.15	0.65	0.10	0.32	0.13	0.10	0.28	0.07	**1.4**	0.06	0.39	0.12	0.06	0.08

* Slope = best-fit average concentration in stream sediment relative to panned concentrate.
Notes: Avg = average R^2 for all 48 elements analyzed. Bold font indicates an especially high slope, whereas an underline denotes an especially low slope. Data from Bachmann et al. (2013).

Stream-sediment sample concentrations do not correlate very well with pan-concentrate sample concentrations for individual samples. How do the two different sampling media contrast in their ability to identify the elemental character of the various plutons? To address this question, I compared the average elemental concentrations of a dozen representative elements (Table 4.15) for stream-sediment samples (Table 4.9) and pan-concentrate samples (Table 4.12) associated with each pluton. I have arranged the elements in Table 4.15 according to decreasing R^2 in an effort to highlight the differences between different elements.

Table 4.15. Correlation coefficients (R^2) and best-fit lines for pluton-averaged elemental concentrations in stream-sediment vs. pan-concentrate samples

	Sn	**Sr**	**Cs**	**Rb**	**Zr**	**W**	**Ce**	**Nb**	**Th**	**Ta**	**Y**	**U**	**Be**	**P**	**Ti**
R^2	0.79	0.76	0.75	0.59	0.55	0.52	0.48	0.43	0.40	0.36	0.34	0.16	0.13	0.10	0.02
Slope*	0.01	0.89	**2.5**	1.0	0.28	0.06	0.07	0.05	0.10	0.03	0.05	0.18	0.14	0.20	0.01

* Slope = best-fit average concentration in stream sediment relative to panned concentrate.
Notes: Data from Table 4.10 and 4.13. Highest slope in bold font, lowest is underlined.

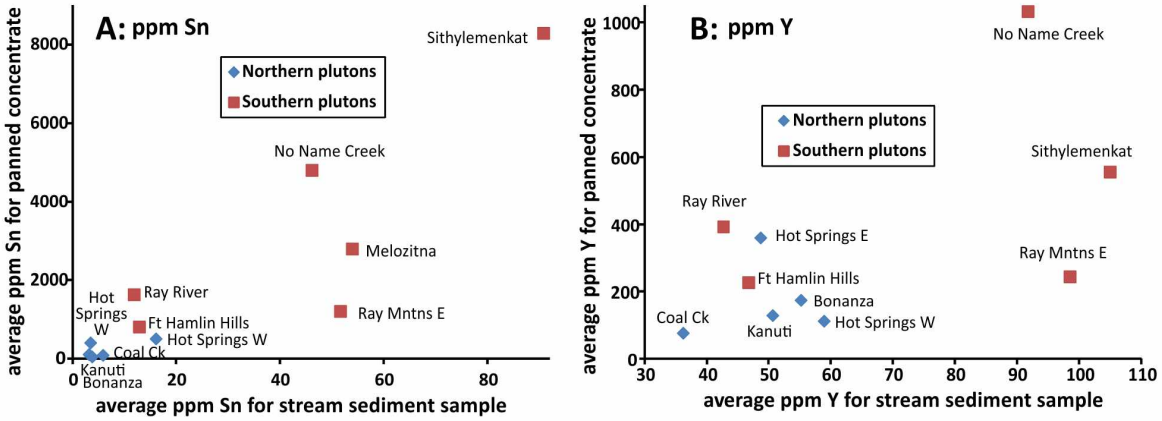

Figure 4.13. Comparison between pluton-averaged elemental concentrations for stream-sediment samples vs. field concentrate samples for plutons of the Ruby batholith. A) Sn, with high R^2 and modest correlation; B) Y, with lower R^2 and poor correlation.

Correlation coefficients (Table 4.15) range from a high of 0.79 (Sn), to a low of 0.02 (Ti), with an average of 0.40. Figure 4.13 illustrates how these R^2 values translate into inter-pluton correlations for two cases, high R^2 (Sn), and low R^2 (Y). For Sn (Fig. 4.13A), stream-sediment and pan-concentrate samples both identify the Sithylemenkat pluton as the highest-concentration source. This tallies with data from mineralized samples (Table 2.7), for which the highest Sn concentrations are from the Sithylemenkat pluton. Stream-sediment data, however, indicates the next three plutons are sub-equally favorable, with Melozitna > Ray Mountains East > NNC >> Ray River pluton. Pan-concentrate data shows a very different story, with NNC >> Melozitna > Ray River > Ray Mountains East. The pan-concentrate data clearly separate the higher-Sn southern plutons from the lower-Sn northern plutons. The stream-sediment data does not do this; and in fact, this data puts the Sn-absent Hot Springs West pluton ahead of the Sn-bearing Ray River and Fort Hamlin Hills plutons (Fig. 4.13A). In other words, the best case of agreement for pluton-averaged metal concentrations between the two media is not very good.

The correlation coefficient for Y (representing the HREE + Y) is on the lower end of the average (0.34 vs. the average of 0.40) and shows that—for this case—there is not much agreement (Fig. 4.13B). The order of enrichment from panned concentrates is NNC > Sithylemenkat > Ray River > Hot Springs East > Ray Mountains East > Fort Hamlin Hills > all northern plutons. The order from stream-sediment analysis is quite different: Sithylemenkat > Ray Mountains East > NNC > most northern plutons > Fort Hamlin Hills > Ray River pluton. This latter order fails to make sense in light of the abundant xenotime in the NNC and Ray River plutons, but the former order does appear to make more sense. The one possible exception is the

high-average concentration of Y in panned concentrates from the Hot Springs East pluton—from which I lack data. Only six panned concentrates were secured, two of which are highly concentrated in REE, and only a few rock samples were collected. (Recognition of the Hot Springs East pluton as a separate pluton was not made until well after the field season was complete.) I do know, however, that Hot Springs East drainages have the highest Y concentrations of the northern plutons—which is not what the stream-sediment data expresses (Fig. 4.13B).

In sum, stream sediments can yield extremely useful information about rocks and mineralization; however, in this particular study for the examination of Sn and REE resources, the time and effort required for heavy-mineral concentrates seemed to be worthwhile.

4.5 Relationship Between the Stream Materials and the Ruby Batholith

Systematic changes in the REE concentrations in the coarser stream sediments (sand and gravel) align with the variability I have documented in the central and southern Ruby batholith. In general, the northern and few transitional plutons—Bonanza, Kanuti, Hot Springs West, and Coal Creek—are associated with sand and gravel containing low-total REE concentrations. Hot Springs East stands out, however, as its drainages highlight high total REE concentrations. This corresponds to its anomalous character amongst the northern plutons. Unfortunately, insufficient information was obtained on the Hot Springs East pluton for further comment.

Sand and gravel in the southern area mimics the southern plutons, and contains the highest concentrations of REE. Materials draining the Sithylemenkat pluton—e.g., in the upper Ray River—have the highest concentrations of REE. There may be some geomorphic effects, as REE concentrations are not uniform in Ray River sediments (Fig. 4.10A). Furthermore, the (HREE + Y)/LREE concentrations increase from the Ray Mountains East and Sithylemenkat drainages, east toward the Ray River pluton, and into the Fort Hamlin Hills (Fig. 4.10B). Proceeding downstream along the Ray River, the concentrates suddenly posses higher (HREE + Y)/LREE ratios, marking where the Ray River pluton drains into the Ray River itself. NNC has the highest (HREE + Y)/LREE ratios, and the concentrates in the Ray River are also high in (HREE + Y)/LREE below the junction with the NNC. The ratios fall in the lower Ray River due to the influence of the sediments derived from the unfavorable Fort Hamlin Hills pluton. The NNC gravels—and the NNC pluton—have the highest (HREE + Y)/LREE ratios.

Additional chemical signatures are present that reflect variations within the plutons. P concentrations (that were measured following four-acid digest) in the stream sediments are highest in streams draining the Bonanza pluton, reflecting both high P_2O_5 in the Bonanza pluton and the fact that virtually all of the P is in the form of the more readily soluble mineral apatite. The Bonanza drainages also have relatively high Zr concentrations, both in the stream sediments and the panned concentrates. This likely reflects the higher average Zr concentrations in the less-evolved rocks of the Bonanza pluton (Chapter 3). Concentrations of the felsic-associated elements (Rb, Be, Cs) are generally higher in the more fractionated southern plutons as a whole, and are especially high in the NNC (Table 4.12). Rb and Cs are especially common elements in igneous muscovite; Rb and Cs concentrations are highest in streams draining the two-mica granites.

The proportion of Fe to Ti in the gravels can indicate specific iron-oxide mineralogy. High Ti relative to Fe implies the presence of ilmenite. The highest Ti concentrations are present in the Ray River, and are associated with both the Sithylemenkat and Ray River plutons (Table 4.12). High Ti in panned concentrates from the Melozitna pluton (Table 4.12) points to ilmenite being the dominant Fe-Ti mineral there as well. In contrast, V readily substitutes into magmatic magnetite, and high-V concentrations in panned concentrates are restricted to the northern plutons. V concentrations are especially high in sediments from the magnetite-rich (highest magnetic susceptibility, Table 2.1) Bonanza pluton (Table 4.12).

4.6 Economic Significance of the Gravels

Gravels near the Dalton Highway have been the focus of numerous investigations due to their "ease" of access. The most simplistic approach to an economic comparison is to determine the gross metal value (equaling the current price for a commodity multiplied by the average concentration of that commodity) for a prospect. The NNC and Hot Springs East plutons—having the highest gross REE-metal values (Fig. 4.14)—are indeed relatively close to the Dalton Highway. The Sithylemenkat pluton, also having a high gross REE-metal value, as well as the highest gross Sn-metal value, is far west of the highway, but travel along the Ray River is feasible.

Looking at Figure 4.14, which expresses the gross metal value of REE and Sn (using field panned concentrate data) in the plutons, the Hot Springs East pluton appears to have the

highest gross REE-metal value. It is worth reiterating that only six panned concentrate samples were taken from the Hot Springs East pluton, and two of those samples had anomalously high concentrations of most elements. These two samples may not be representative of the Hot Springs East as a whole. More sampling is necessary.

The gross REE-metal value is higher than the gross Sn-metal value for most plutons. Interestingly, the gross REE-metal values for sands and gravels associated with the Ray River and Sithylemenkat plutons are essentially equal to their respective gross Sn-metal values. The NNC, which sometimes follows the trends of the Ray River and Sithylemenkat plutons, differs in that its gross REE-metal value is twice that of its gross Sn-metal value.

Although the Sithylemenkat pluton is associated with the highest total REE concentrations (Fig. 4.10A), the high proportion of HREE + Y in the NNC (Fig. 4.10B) appears to outweigh its lesser total (Fig. 4.14).

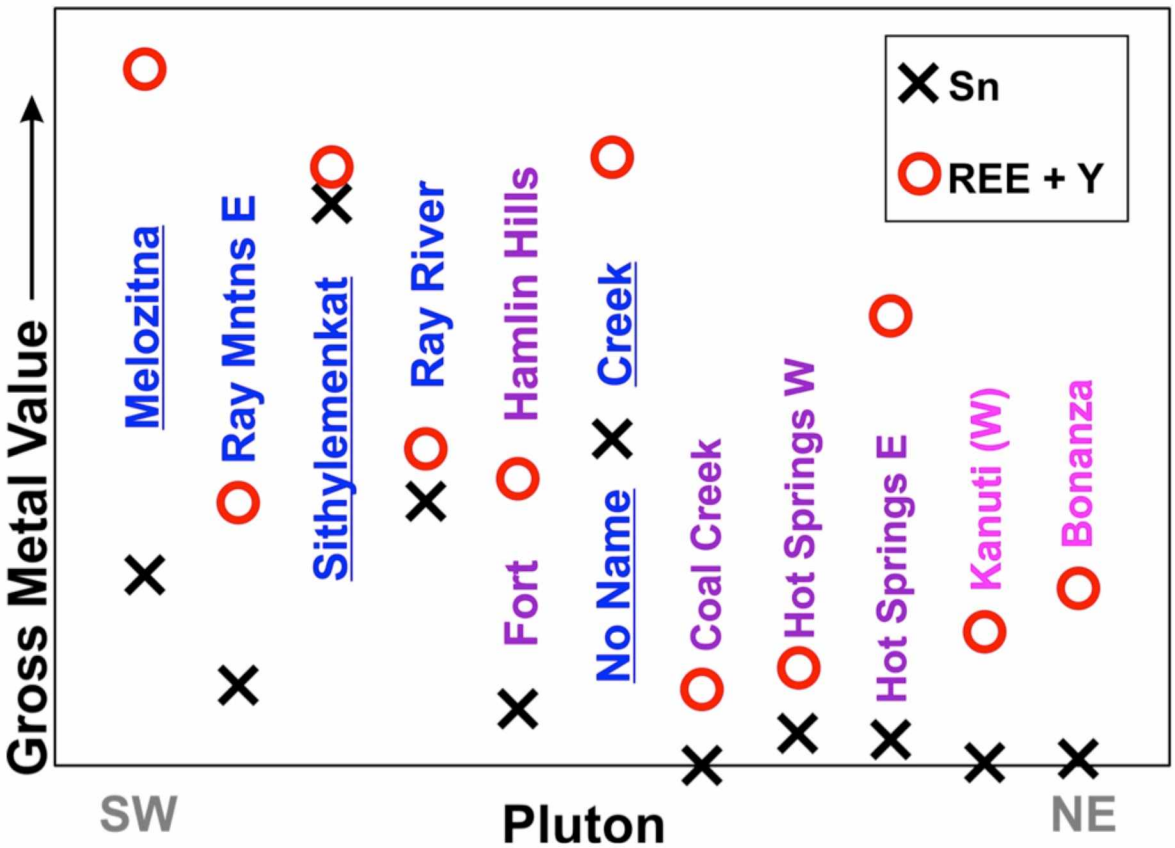

Figure 4.14. Relative gross metal values of total REE (red) and Sn (black). Pluton labels are color-coded according to association with northern (pink), transitional (purple), or southern (blue) characteristics. Data based on average elemental concentrations of field-panned concentrates (Table 4.13). Concentration factor is estimated ~30.

4.7 SUMMARY

In this chapter, I have identified several analytical issues with the sampling, preparation, and analysis of gravels in the Ray Mountains area. Additionally, I have shown that the highest concentrations of REE are measured in the southern drainages, with the highest totals associated with the Sithylemenkat pluton. The highest (HREE + Y)/LREE ratios, however, are associated with the NNC pluton, and these high ratios are what give the pluton's drainages the high gross REE-metal value.

5 SUMMARY AND CONCLUSIONS

5.1 CHARACTERISTICS OF RUBY BATHOLITH MAGMA SOURCES

Granitic magmas in continental environments are generally considered to have three broad origins: a) Fractionation (± crustal contamination) from an intermediate parent magma that is broadly subduction (arc) related; (b) melted lower crust caused by heating due to intrusion of voluminous mafic melts (bimodal magmatism); (c) melted crust related in some way to crustal collision (Frost et al., 2001). Pearce et al. (1984) proposed using certain trace-element combinations as a means to identify the origins of granitic bodies. Plotting Ruby batholith data on discriminant diagrams (Figure 5.1) yields mixed results. Rocks from some of the northern plutons plot in the volcanic arc field; rocks from most of the southern plutons plot in the syn-collisional field; rocks from several plutons plot in several fields. Because many trace elements show systematic changes in concentration with rock TiO_2 (indicative of degree of fractionation), I plotted the best estimated "primitive" melt composition on the same diagram (Figure 5.1c) with somewhat more consistent results. Northern plutons—with lower "primitive" Rb concentrations (Figure 3.13)—plot in the volcanic arc field, whereas the southern plutons plot in a region close to the empirical boundaries for all three.

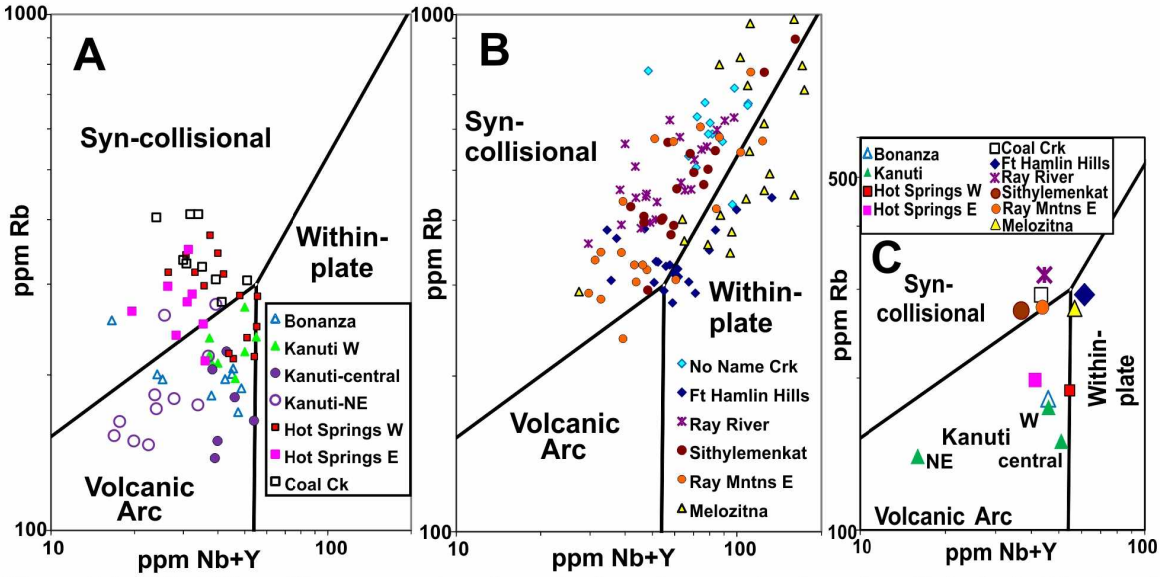

Figure 5.1. (Nb + Y) vs. Rb concentrations for rocks from the central and southern Ruby batholith plotted on the tectonic discriminant diagram of Pearce et al. (1984). A) Northern plutons, B) southern plutons, C) "best-estimated" primitive melt composition based on concentration vs. TiO_2 plots (Chapter 3).

An alternative interpretation of the Pearce et al. (1984) plots is that the diagrams mostly indicate differences in melt source(s) rather than melting environment. Frost et al. (2016), for example, note that rocks from the Bishop Tuff plot in the volcanic arc field of Pearce et al. (1984), despite the fact that this felsic body is clearly the product of bimodal (extensional) magmatism. Given the absence of any obvious subduction zone in the vicinity of the Ruby batholith in the mid-Cretaceous (thus ruling out an arc-related origin), and the absence of associated mafic magmatism (thus ruling out extensional, within-plate settings), the consensus over the decades is that the Ruby batholith represents a crustal melting episode most logically associated with a collisional event. Implicitly, the differences highlighted on Figure 5.1 point to two broadly different source materials, one that generated moderate Rb siliceous melts and one that generated high Rb siliceous melts (Figure 5.1c).

In Chapter 2, I showed evidence that the central and southern Ruby batholith does not represent a single magmatic event, but rather contains plutonic rocks with crystallization ages of approximately 113 to approximately 90 Ma. With the present state of knowledge, however, it is likely that the bulk of the batholith was intruded at 111 ± 2 Ma. Granites of likely collisional origins in the Himalayan suture zone yield U-Pb ages of 24 to 17 Ma (Le Fort, 1981; Harrison et al., 1999); so a spread between 113 Ma (Kanuti West) and 107 Ma (NNC) for most plutons of the batholith seems consistent with a general collisional origin. On the other hand, the Hot Springs West and Kanuti Northeast plutons are simply too young to have the same magmatic origin. Further radiometric dating can assess how many such younger plutons are present within the batholith. The origins and number of such younger bodies lie beyond the scope of this study. If the younger magmatism is also largely associated with crustal melting, then the nature of *what* melted is more important than *when* it melted. Based on the characteristic greenschist facies assemblages present in the metamorphic rocks in the study area, the rocks presently at the surface experienced temperatures too low for melting. Rather, melting took place far deeper in the crust, perhaps as much as 10 to 15 km below the current surface.

Despite the evidence for at least two different magmatic events (ca. 107 to 113 Ma and ca. 90 to 98 Ma), the central and southern Ruby batholith can be broadly divided into "northern", "southern", and—for those that do not fall neatly into either category—"transitional" plutons based on a variety of characteristics. These characteristics include (Table 5.1) minor and trace minerals (Table 2.6), initial $^{87}Sr/^{86}Sr$ isotopic ratios (Fig. 2.6), general range of bulk

compositions (Table 2.5, Figs. 2.8, 2.9), likely primitive trace-element concentrations (Figs. 3.13-3.18), and importantly, aluminum saturation (Fig. 2.11) and oxidation state (Table 2.1, Fig. 2.12). Aluminum saturation and oxidation state are particularly significant because (a) they provide information about the source materials that melted and (b) they have major implications with regard to mineralogy and trace-element fractionation.

Table 5.1. General characteristics of three major plutonic groups in the central and southern Ruby batholith

Characteristic	Northern Plutons	Transitional Plutons	Southern Plutons
Initial $^{87}Sr/^{86}Sr$ isotope ratio	< 0.714	~ 0.714	> 0.714
Rock types	Granite to tonalite	Granite to granodiorite	Monzogranite to syenogranite
Mineralogy	mt, hbl, ti, al	ilm, mz, mt, ti, al	mus, ilm, mz
Average ASI	1.0 to 1.05	1.04 to 1.1	1.06 to 1.14
Average MS	0.5 to 10	0.05 to 0.5	< 0.05
Primitive Rb	180 to 190 ppm	130 to 280 ppm	270 to 320 ppm
Primitive CaO	3 to 3.5 wt%	2 to 3 wt%	1.5 to 2.2 wt%
Primitive P_2O_5	0.25 to 0.35 wt%		0.1 to 0.2 wt%
Plutons	Bonanza, Kanuti West	Kanuti Northeast, Hot Springs East, Hot Springs West, Coal Creek, Fort Hamlin Hills	Sithylemenkat, Melozitna, Ray River, No Name Creek, Ray Mountains

Notes: "ASI" = aluminum saturation index; "MS" = magnetic susceptibility; "hbl" = hornblende, "mt" = magnetite, "ti" = titanite, "al" = allanite, "ilm" = ilmenite, "mz" = monazite, "mus" = "muscovite"

Based on the characteristics listed in Table 5.1, the southern plutons were almost certainly derived in large part from partially melted carbonaceous shale. Such rocks would be intrinsically rich in Al and K (and hence, Rb), and would create a low oxidation state given the presence of reduced carbon. In contrast, the two "end-member" northern plutons—Bonanza and Kanuti West—must have been derived from rocks with significant (but lower) Al and K (hence, Rb), and lacking an intrinsic reductant. The most obvious source rocks that would satisfy these requirements would be magnetite-bearing igneous rocks of any composition, from mafic to felsic. The transitional plutons have both variable degrees of aluminum saturation and oxidation state. For example, the Kanuti Northeast pluton is both peraluminous and relatively oxidized (Fig. 2.20), whereas the Fort Hamlin Hills pluton has a relatively low oxidation state but is weakly peraluminous. Implicitly then, additional components (e.g., non-carbonaceous shales

and magnetite-poor igneous rocks) are likely part of the "mixture" that melted to form the transitional plutons.

Projected "primitive" Rb concentrations (Table 5.1, Fig. 3.13) appear to be quite different for the northern, southern, and transitional pluton groups. This suggests two distinctly different sources (and likely a mixture of the two). The initial $^{87}Sr/^{86}Sr$ ratios, however, express a different story: Figure 5.2 shows the initial $^{87}Sr/^{86}Sr$ ratio (SIR) versus the average aluminum saturation index (ASI) for individual plutons (and lobes of plutons). In a very general way, increasing ASI is associated with increasing initial $^{87}Sr/^{86}Sr$. The "northern" and "southern" pluton groups are clearly distinguishable, but the transitional plutons fail to fall on a mixing line between the two end members. In particular, the northern plutons have relatively low SIR and low ASI. The transitional plutons have moderate-to-low SIR and moderate ASI. The southern plutons have high-to-very high SIR and moderate-to-high ASI.

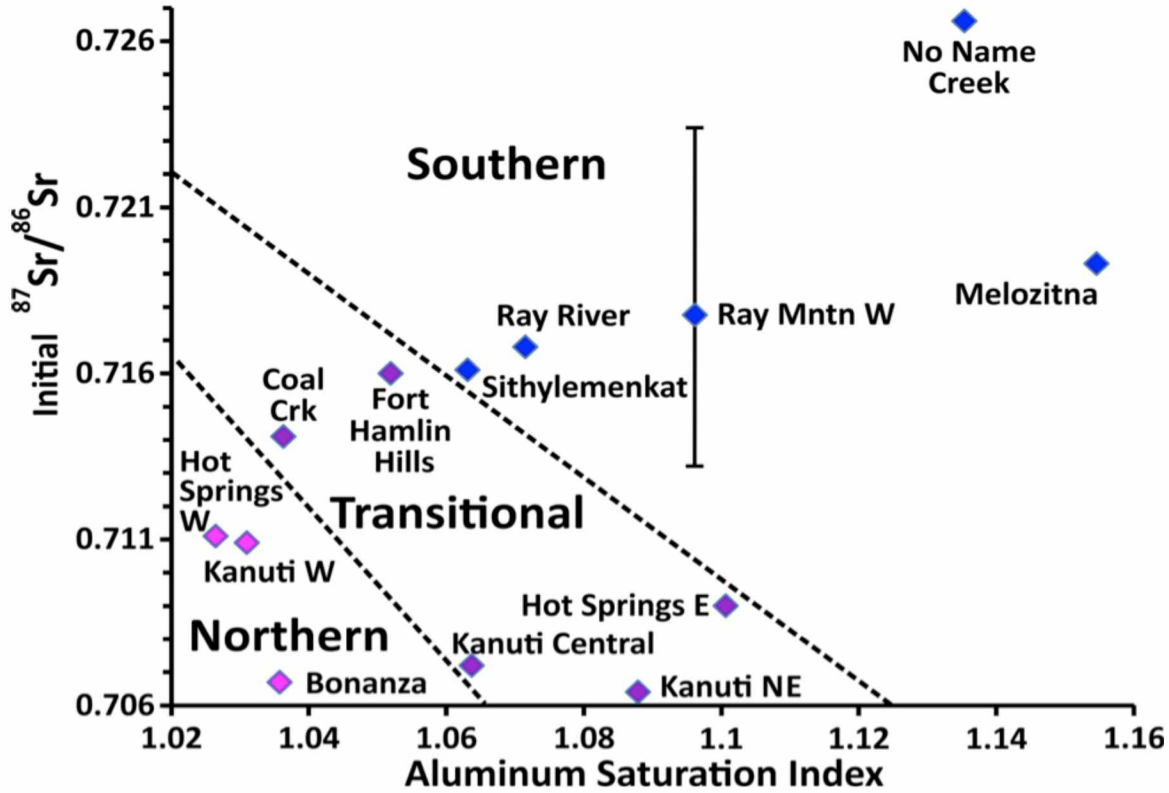

Figure 5.2. Aluminum saturation index (ASI = molecular $Al_2O_3/(CaO - 1.67P + Na_2O + K_2O)$) vs. initial $^{87}Sr/^{86}Sr$ ratio for plutons of the central and southern Ruby batholith. In a very general sense, higher SIR is associated with higher ASI.

Most importantly, Figure 5.2 shows that it is not possible to model the plutons as a two-component mixture. Although data for many of the plutons fall on or near a line connecting data for Hot Springs West and Kanuti West with the Melozitna-pluton data, much of the data also falls far off such a line. For many of the plutons, increasing SIR is associated with increasing ASI. For several plutons (Bonanza, Kanuti Central, Hot Springs East, and Kanuti Northeast), however, an increase in ASI is not associated with an increase in SIR. From this plot (Fig. 5.2), one might infer at least three major source components: (a) Al- and Rb-rich (yielding high SIR and ASI), (b) Al- and relatively Rb-poor (yielding moderately low SIR and low ASI), and (c) relatively Al-rich but Rb-poor (yielding low SIR but moderately high ASI).

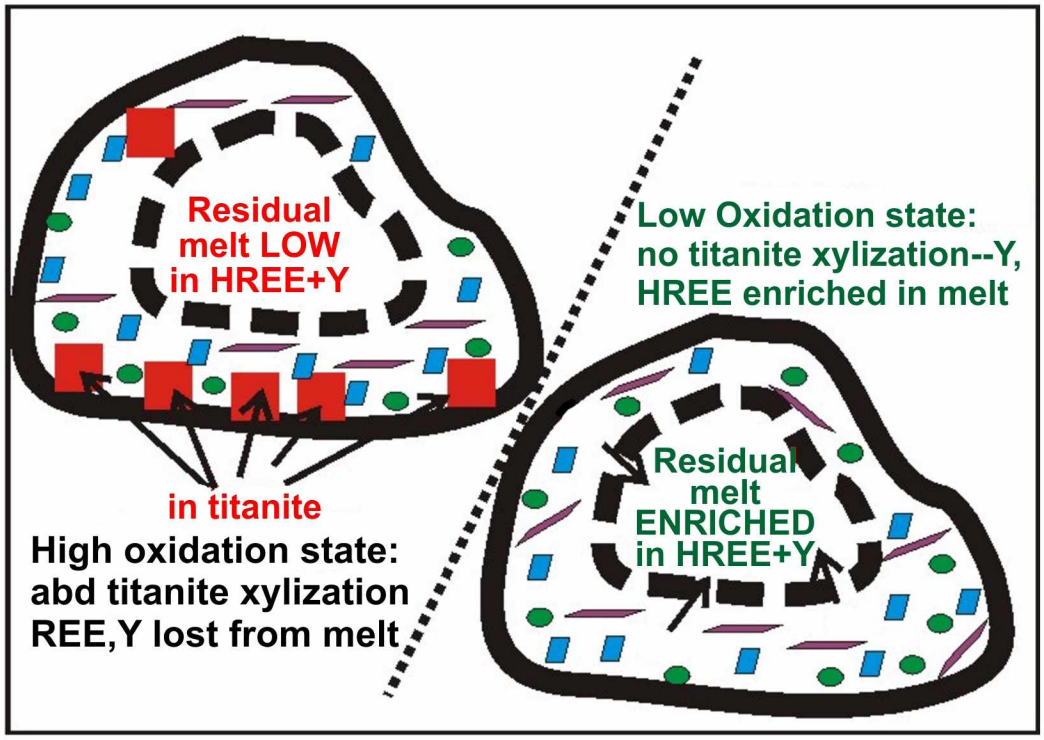

Figure 5.3. Schematics of (HREE + Y) partitioning in the magma chamber. In a high-oxidation environment (left), much of the HREE allowance is fractionated into titanite; hence, the residual melt is depleted in HREE + Y. This is the case for the northern and many of the transitional plutons. Conditions for titanite crystallization are not met in magma chambers with sufficiently low oxidation states (right), such as those melts generating the southern plutons. Consequently, though other minerals partitioning HREE + Y may crystallize, the overall HREE + Y budget remains high and the residual melt is enriched in HREE + Y.

Source materials are important not only with regard to the original melt compositions, but also with how the melts concentrated (or failed to concentrate) critical elements during fractional crystallization (Fig. 5.3). In particular, a high oxidation state (characteristic of northern and some transitional plutons) is responsible for crystallization of the assemblage magnetite + titanite; low oxidation state (southern and some transitional plutons) favors Ti and Fe crystallization in other minerals, e.g., biotite. I have shown, based on microprobe compositions (Tables 3.14, 3.15), that titanite from the northern plutons contains anomalous concentrations of Y, and by inference, REEs. Abundant crystallization of titanite, then, caused loss of REEs from the melt by crystallization of titanite (Fig. 5.3, left). Melts with little or no evidence for titanite crystallization (Fig. 5.3, right), in contrast, were able to concentrate Y and REEs until they reached saturation with REE-phosphate minerals.

5.2 NO NAME CREEK PLUTON

The No Name Creek pluton—beyond the north/south/transitional characteristics—is truly unique. At 107 Ma, the NNC pluton is distinctly younger than the majority of the Ruby batholith. Age alone, however, cannot explain its differences from the others, as the Hot Springs West pluton, and Kanuti Central and Kanuti Northeast lobes are yet younger.

The NNC pluton is the only truly peraluminous granite, as well as the only true S-type granite in the central Ruby batholith. Only the Melozitna pluton—at the far southwest end of the belt (and outside of the study area)—is comparably as peraluminous. The NNC pluton has by far the highest initial $^{87}Sr/^{86}Sr$ ratio, and even the least-fractionated rocks contain low TiO_2 and plot as syenogranite (modal) or alkali feldspar granite (normative).

I hypothesize that what we observe on the surface as the NNC pluton is rather the visible, hyper-fractionated, ascended core of a subsurface pluton (Fig. 5.3). I make this claim for a number of reasons:

1) Foremost, after extensive (and exhaustive) sampling efforts, I was unable to locate any sample containing more than 0.25 wt% TiO_2, or less than 425 ppm Rb. It is the only pluton in which I identified topaz, a high-F and -Al mineral. Based on limited XRF analyses, rocks from this pluton average ~0.2 wt% F, approximately twice as high as the other southern-group plutons.

2) For many trace elements (e.g., Rb, Y; Figs. 3.13, 3.17A), rocks from the NNC pluton plot at significantly higher concentrations than do any of the others at similar TiO_2. Conversely, NNC pluton rocks plot at significantly lower Ca concentrations (Fig. 3.16A), and lower Ce/Y (Fig. 3.19) and Eu/Eu* ratios (Fig. 3.14) relative to rocks from the other plutons in the study area.

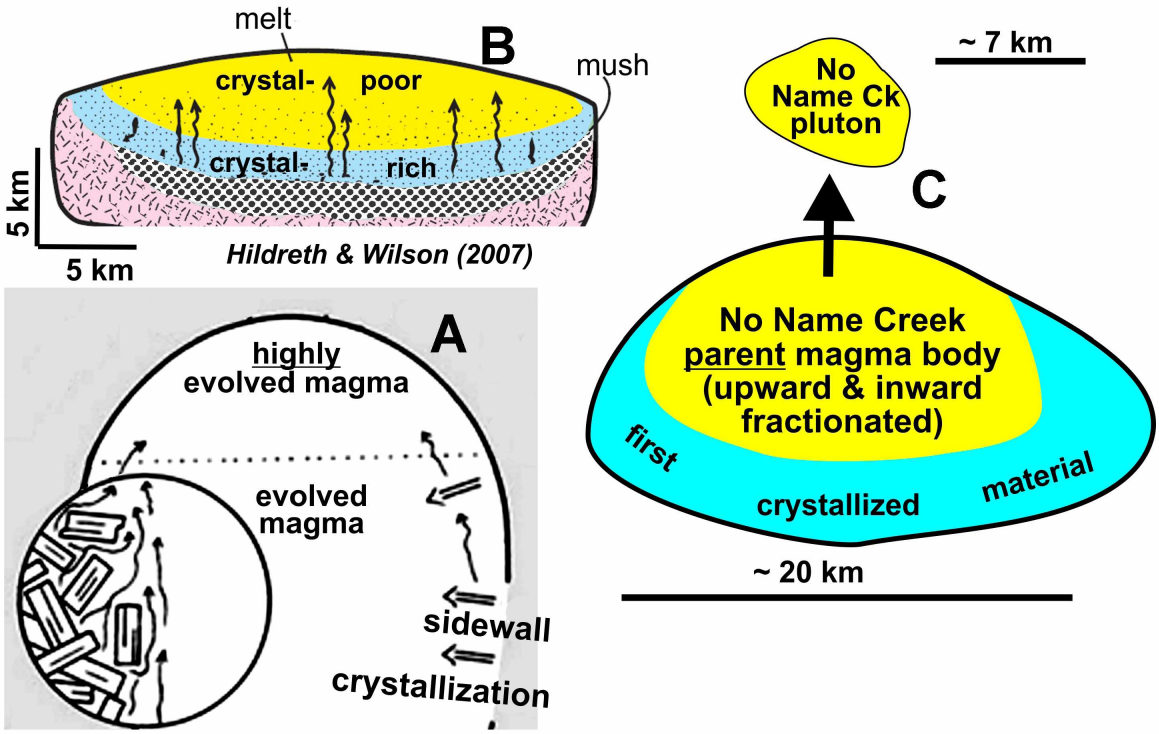

Figure 5.4. Schematic cartoons depicting possible mechanisms for ascension of the NNC pluton as a hyper-fractionated, buoyant core of a much larger subsurface magma chamber. A) The magma chamber experienced sidewall crystallization, with compatible elements partitioning into minerals, leaving the magma enriched in incompatible elements. Modified from Best and Christiansen (2001). B) Crystallization progressed from the bottom and sides of the magma chamber inward and upward. The base (in pink) is a crystallized "granitoid rind". The mush (in black) is dominantly crystallized, yet contains sufficient melt to allow magma mixing. Note that the crystal-poor melt extends to the roof of the magma chamber. Modified from Hildreth and Wilson (2007). C) A simplified hypothesis. The bottom and sides of the magma chamber crystallized first. The magma fractionated inward and upward. The core became sufficiently hyper-fractionated to completely detach and ascend, and the core is the surficial NNC pluton.

Furthermore, high-F (another incompatible element) concentrations (to a certain extent) can cause magma densities and viscosities to decrease (Dingwell et al., 1993; Lange, 1994). As these processes occurred, this may have allowed the still-molten core to ascend beyond the original extent of the subsurface body. Figure 5.4 illustrates the model of sidewall crystallization

and upward ascent of residual magma. Hildreth and Wilson (2007) proposed a similar model for the magma chamber, with the most-fractionated magma in the upper portion, producing the Bishop Tuff. It is obviously unclear if the NNC pluton expressed at the surface is completely detached from its original body.

5.3 EXTENSIONAL TECTONICS

Another peculiarity of the NNC pluton is that it is much smaller in surface area (Table 5.2) than any of the other plutons (or lobes of plutons) of the Ruby batholith. I propose that surface areas of these plutons represent (in part) depth of erosion into broadly teardrop-shaped (in cross-section, Fig. 5.4C) magmatic bodies. That is, the NNC pluton appears to be small because it is near the top of a larger body. Evidence for this geometry is in part derived from the nearby geology.

Table 5.2. Surface areas of plutonic bodies in the central and southern Ruby batholith

Pluton	Surface Area (km^2)
No Name Creek	38
Kanuti West	70
Hot Springs East	74
Fort Hamlin Hills	141
Ray River	160
Hot Springs West	167
Coal Creek	177
Bonanza	235
Ray Mountains East	354
Sithylemenkat	521
Ray Mountains West	863
Kanuti (composite)	1012

Tertiary (~30 Ma) basalts are exposed near the NNC pluton (Fig. 2.1B; Barker, 1991a,b). An oddity is that this basalt is present in a relatively small area, mostly in the immediate vicinity of the NNC pluton. Based on its trace-element characteristics (e.g., Pearce and Cann, 1973), it plots as a "within-plate" basalt, i.e., one generated through a non-subduction mechanism. In

continental environments, "within-plate" basalt is typically associated either with extension or with a hot spot. In this case, extension is a more likely cause, and I hypothesize that extensional faults acted both as feeders for the basalt and as a graben-bounding features that constrain present exposures of basalt. A nonconformity resulted as the basalt was covered with late Tertiary sediments; thus, the basalt was preserved within down-dropped structural blocks. Meanwhile, basalt that extruded onto what became horsts stayed at the surface and hence eroded long ago. In this scenario, it is plausible that the NNC pluton—spatially associated with mid-Tertiary basalt—was also present on a down-dropped block and was covered with sediments and preserved. Sediments (of mid-Tertiary to Quaternary age) cover much of the area and such extensional faults are strictly hypothetical. Such a scenario could however explain the small surface area of the NNC pluton relative to the other plutons of the Ruby batholith.

5.4 Potential Rare-Earth and Sn Resources

The highest concentrations of REE and Sn are measured in gravels originating from the southern plutons, particularly the Sithylemenkat, NNC and Melozitna plutons. The economic potential, however, is dependent upon current metal prices and beneficiation techniques. Monazite and xenotime are not refractory REE minerals and add solvent extraction of metals.

The Sithylemenkat and Melozitna plutons, and associated drainages, are relatively far from the Dalton Highway and would require relatively more infrastructure and expense to develop and operate an alluvial processing plant. Meanwhile, the NNC and Ray River plutons and associated drainages (and ancestral drainages) are proximal to the Dalton Highway. Sediments derived from the Fort Hamlin Hills pluton, however, dilute Lower Ray River sediments. An active and apparently economic placer gold mine in Prospect Creek, immediately north of the Bonanza pluton, indicates that extraction of alluvial metal resources can be feasible. Evaluation of the economic value of the alluvial REE resources and their extraction costs is beyond the scope of this thesis.

5.5 FUTURE WORK

Additional mapping is necessary to better define the physical extent of the plutons, and lobes within plutons, of the Ruby batholith. In particular, the Kanuti "pluton" has several lobes with variable characteristics, especially variable ages. It must be a composite body, intruded over a 20-Ma period. With future mapping and sampling, the body will likely be renamed the Kanuti "batholith". The eastern boundaries of the NNC and Fort Hamlin Hills plutons need to be more accurately located. Similarly, the southern boundary of the Ray River pluton and the eastern boundary of the Coal Creek pluton are currently poorly defined.

The newly segregated Hot Springs East and West plutons need to be further characterized. Only six panned concentrates were collected from drainages associated with the Hot Springs East pluton, yet two of them were anomalously high in trace elements.

Given that reliable ages for the plutons now span a 20-Ma period, it is no longer reasonable to assume that they all are the same age. Every undated pluton needs to be dated, and the larger bodies (e.g., Kanuti) need additional radiometric ages. U-Pb zircon ages are ideal, but given their cost, $^{40}Ar/^{39}Ar$ biotite and hornblende ages may be more practicable. For instance, the NNC pluton has an age of approximately 107 Ma. Do its neighbors, the Coal Creek and Fort Hamlin Hills plutons, have similar ages? Are they between 107 and 113 Ma? If so, this would augment the evidence that the NNC pluton is a result of the same magmatic event that produced many granites in the area. Additionally, the Kanuti pluton formed by at least two, and possibly three, magmatic events. Generating ages for all the lobes of the pluton may aid in defining physically separate plutons.

REFERENCES

Ackerson, M.R., 2011, Trace element partitioning between titanite and groundmass in silicic volcanic systems: The University of North Carolina, Chapel Hill, M.S. thesis, 76 p.

Arth, J.G., Zmuda, C.C., Foley, N.K., and Criss, R.E., 1989, Isotopic and trace element variations in the Ruby Batholith, Alaska, and the nature of the deep crust beneath the Ruby and Angayucham Terranes: Journal of Geophysical Research, v. 94, p. 15,941-15,955.

de Baar, H.J.W., Bacon, M.P., and Brewer, P.G., 1985, Rare earth elements in the Pacific and Atlantic Oceans: Geochimica et Cosmochimica Acta, v. 49, p. 1,943-1,959.

Bachmann, E.N., Blessington, M.J., Freeman, L.K., Newberry, R.J., Tuzzolino, A.L., Wright, T.C., and Wylie, W., 2013, Geochemical major-oxide, minor-oxide, trace-element, and rare-earth-element data from rocks and stream sediments collected in 2012 in the Ray Mountains area, Beaver, Bettles, Livengood, and Tanana quadrangles, Alaska: Alaska Division of Geological & Geophysical Surveys Raw Data File 2013-5, 4 p.

Barker, J.C., 1991a, Investigation of tin-rare earth element placers in the Ray River watershed: U.S. Bureau of Mines Open-File Report 34-91, 63 p., 1 sheet, scale 1:63,360.

Barker, J.C., 1991b, Tin placers associated with the downcutting of fissure basalts, Ray River drainage, Alaska, in Reger, R.D., ed., Short Notes on Alaskan Geology 1991: Alaska Division of Geological & Geophysical Surveys Professional Report 111A, p. 1-8.

Barker, J.C., and Foley, J.Y., 1986, Tin reconnaissance of the Kanuti and Hodzana Rivers uplands, central Alaska: U.S. Bureau of Mines Information Circular 9104, 27 p.

Bayliss, P., and Levinson, A.A., 1988, A system of nomenclature for rare-earth mineral species: Revision and extension: American Mineralogist, v. 73, p. 422-423.

Bea F., Pereira, M.D., and Stroh, A., 1994, Mineral/leucosome trace-element partitioning in a peraluminous migmatite (a laser ablation-ICP-MS study): Chemical Geology, v. 117, p. 291-312.

Bédard, J.H., 2003, Evidence for regional-scale, pluton-driven, high-grade metamorphism in the Archaean Minto Block, Northern Superior Province, Canada: Journal of Geology, v. 111, p. 183-205.

Best, M.G., and Christiansen, E.H., 2001, Igneous Petrology: Oxford, Blackwell Science, 480 p.

Blum, J.D., Blum, A.E., Davis, T.E., and Dillon, J.T., 1987, Petrology of cogenetic silica-saturated and -oversaturated plutonic rocks in the Ruby geanticline of north-central Alaska: Canadian Journal of Earth Sciences, v. 24, p. 159-169.

Bowie, S.H.U., and Horne, J.E.T., 1953, Cheralite, a new mineral of the monazite group: Mineralogical Magazine, v. 30, p. 93-99.

Britton, J., 2000, Alaska resource data file, Beaver Quadrangle: U.S. Geological Survey Open-File Report 2000-308, 10 p.

Britton, J., 2003, Alaska resource data file, Bettles Quadrangle, Alaska: U. S. Geological Survey Open-File Report 2003-52, 43 p.

Brosge, W.P., and Reiser, H.N., 1964, Geologic map and section of the Chandalar Quadrangle, Alaska: U.S. Geological Survey Miscellaneous Geologic Investigations Map 375, 1 sheet, scale 1:250,000.

Brosge, W.P., Reiser, H.N., and Yeend, W., 1973, Reconnaissance geologic map of the Beaver Quadrangle, Alaska: U.S. Geological Survey Miscellaneous Field Studies Map 525, 1 sheet, scale 1:250,000.

Broska, I., Petrík, I., and Williams, C.T., 2000, Coexisting monazite and allanite in peraluminous granitoids of the Tribeč Mountains, Western Carpathians: American Mineralogist, v. 85, p. 22-32.

Burt, D.M., 1989, Compositional and phase relations among rare earth element minerals: Reviews in Mineralogy and Geochemistry, v. 21, p. 259-308.

Chappell, B.W., and White, A.J.R., 1974, Two contrasting granite types: Pacific Geology, v. 8, p. 173–174.

Chappell, B.W., and White, A.J.R., 2001, Two contrasting granite types: 25 years later: Australian Journal of Earth Sciences v. 48, p. 489–499.

Cherniak, D.J., and Watson, E.B., 2001, Pb diffusion in zircon: Chemical Geology, v. 172, p. 5-24.

Chesner, C.A., and Ettlinger, A.D., 1989, Composition of volcanic allanite from the Toba Tuffs, Sumatra, Indonesia: American Mineralogist, v. 74, p. 750-758.

Clautice, K.H., 1983, Geological sampling and magnetic surveys of a tungsten occurrence, Bonanza Creek area, Hodzana highlands, Alaska: U.S. Bureau of Mines Open-File Report 80-83, 80 p., 4 sheets, scale 1:250,000.

Clautice, K.H., Burns, L.E., and Liss, S.A., 1993, Land selection units 30 and 31 (Bettles, Beaver, Wiseman, and Chandalar quadrangles) references, geochemical and major oxide data: Alaska Division of Geological & Geophysical Surveys Public Data File 93-30A, 21 p., 1 sheet, scale 1:250,000.

Cuney, M., and Friedrich, M., 1987, Physicochemical and crystal-chemical controls on accessory mineral paragenesis in granitoids: Implications for uranium metallogenesis: Bulletin de Minéralogie, v. 110, p. 235-247.

Dahl, P.S., 1996, The effects of composition on retentivity of argon and oxygen in hornblende and related amphiboles: A field-tested empirical model: Geochimica et Cosmochimica Acta, v. 60, p. 3,687-3,700.

DeCarlo, J.M., 2004, Early Cretaceous mafic magmatism in the southern Ruby Terrane, central Alaska: University of California, Davis, M.S. thesis, 142 p.

Decker, J.E., and Dillon, J.T., 1982, Aeromagnetic map of the Bettles quadrangle, Alaska: Alaska Division of Geological & Geophysical Surveys Open-File Report 179, 1 sheet, scale 1:250,000.

Deere, W.A., Howie, R.A., Zussman, J., 1986, Rock-forming minerals, v. 1B: Disilicates and ringsilicates (2nd edition): Bath, The Geological Society of London, 630 p.

Dillon, J.T., Patton, W.W., Jr., Mukasa, S.B., Tilton, G.R., Blum, J., and Moll, E.J., 1985, New radiometric evidence for the age and thermal history of the metamorphic rocks of the Ruby and Nixon Fork terranes, west-central Alaska, in Bartsch-Winkler, Susan, and Reed, K.M., eds., The United States Geological Survey in Alaska; accomplishments during 1983: U.S. Geological Survey Circular 945, p. 13-17.

Dingwell, D.B., Knoche, R., and Webb, S.L., 1993, The effect of F on the density of haplogranite melt: American Mineralogist, v. 78, p. 325-330.

Dini, A., Rocchi, S., and Westerman, D.S., 2004, Reaction microtextures of REE-Y-Th-U accessory minerals in the Monte Capanne pluton (Elba Island, Italy): a possible indicator of hybridization processes: Lithos, v. 78, p. 101-118.

Dodson, M.H., 1973, Closure temperature in cooling geochronological and petrological systems: Contributions to Mineralogy and Petrology, v. 40, p. 259-274.

Dollase, W.A., 1971, Refinement of the crystal structures of epidote, allanite and hancockite: American Mineralogist, v. 56, p. 447-464.

Donelick, R.A., O'Sullivan, P.B., and Ketcham, R.A., 2005, Apatite fission-track analysis: Reviews in Mineralogy and Geochemistry, v. 58, p. 49-94.

Drake, M.J., and Weill, D.F., 1972, New rare earth element standards for electron microprobe analysis: Chemical Geology, v. 10, p. 179-181.

El-Hinnawi, E., 2016, Evaluation of boundary lines in the total alkali-silica diagram for the discrimination between subalkali and alkali basalts, and a new method to distinguish transitional basalts: Periodico di Mineralogia, v. 85, p. 51-58.

Ewart, A. and Griffin, W.L., 1994, Application of proton-microprobe data to trace-element partitioning in volcanic rocks: Chemical Geology, v. 117, p. 251-284.

Faure, G., 1998, Principles and applications of geochemistry (2^{nd} ed.): University of California, Prentice Hall, 625 p.

Fletcher, W.K., 1997, Stream sediment geochemistry in today's exploration world, in: Gubins, A.G., ed., Proceedings of Exploration 97: Fourth Decennial International Conference on Mineral Exploration, p. 249-260.

Foley, J.Y., and McDermott, M.M., 1983, Podiform chromite occurrences in the Caribou Mountain and lower Kanuti River areas, central Alaska, part I: reconnaissance investigations: U.S. Bureau of Mines Information Circular 8915, 8 p., 1 sheet.

Förster, H.J., 1998a, The chemical composition of REE-Y-Th-U-rich accessory minerals in peraluminous granites of the Erzgebirge-Fichtelgebirge region, Germany, Part I: The monazite-(Ce)-brabantite solid solution series: American Mineralogist, v. 83, p. 259-272.

Förster, H.J., 1998b, The chemical composition of REE-Y-Th-U-rich accessory minerals in peraluminous granites of the Erzgebirge-Fichtelgebirge region, Germany, Part II: Xenotime: American Mineralogist, v. 83, p. 1302-1315.

Freeman, L.K., Szumigala, D.J., Blessington, M.J., and Werdon, M.B., 2012, Geochemical trace-element and rare-earth element data from stream-sediment and pan-concentrate samples collected in 2011 in the Melozitna mining district, Tanana and Melozitna quadrangles, interior Alaska: Alaska Division of Geological & Geophysical Surveys Raw Data File 2012-3, 3 p.

Frost, B.R., Barnes, C.G., Collins, W.J., Arculus, R.J., Ellis, D.J., and Frost, C.D., 2001, A geochemical classification for granitic rocks: Journal of Petrology, v. 42, p. 2,033-2,048.

Frost, C.D., Frost, B.R., and Beard, J.S., 2016, On silica-rich granitoids and their eruptive equivalents: American Mineralogist, v. 101, p. 1,268-1,284.

Gieré, R., Virgo, D., and Popp, R.K., 1999, Oxidation state of iron and incorporation of REE in igneous allanite: Journal of Conference Abstracts, v. 4, p 721.

Gieré, R., and Sorensen, S.S., 2004, Allanite and other REE-rich epidote-group minerals: Reviews in Mineralogy and Geochemistry, v. 56, p. 431-493.

Gromet, L.P., and Silver, L.T., 1983, Rare earth element distributions among minerals in a granodiorite and their petrogenetic implications: Geochimica et Cosmochimica Acta, v. 47, p. 925-939.

Gupta, A., and Yan, D.S., 2016, Mineral processing design and operations, 2nd Edition: Amsterdam, Elsevier, 882 p.

Harrison, T.M., 1982, Diffusion of ^{40}Ar in hornblende: Contributions to Mineralogy and Petrology, v. 78, p. 324-331.

Harrison, T.M., Duncan, I., and McDougall, I., 1985, Diffusion of ^{40}Ar in biotite: Temperature, pressure and compositional effects: Geochimica et Cosmochimica Acta, v. 49, p. 2,461-2,468.

Harrison, T.M., Grove, M., McKeegan, K.D., Coath, C.D., Lovera, O.M., and Le Fort, P., 1999, Origin and episodic emplacement of the Manaslu Intrusive Complex, Central Himalaya: Journal of Petrology, v. 40, p. 3-19.

Harrison, T.M., Célérier, J., Aikman, A.B., Hermann, J., and Heizler, M.T., 2009, Diffusion of ^{40}Ar in muscovite: Geochimica et Cosmochimica Act, v. 73, p. 1,039-1,051.

Hermann, J., 2002, Allanite: thorium and light rare earth element carrier in subducted crust: Chemical Geology, v. 192, p. 289-306.

Hildreth, W., and Wilson, C.J.N., 2007, Compositional zoning of the Bishop Tuff: Journal of Petrology, v. 48, p. 951-999.

Hodges, K.V., 1991, Pressure-temperature-time paths: Annual Review of Earth and Planetary Sciences, v. 19, p. 207-236.

Hurley, P.M., and Fairbairn, H.W., 1957, Abundance and distribution of uranium and thorium in zircon, sphene, apatite, epidote, and monazite in granitic rocks: American Geophysical Union, v. 38, p. 939-944.

Iimori, T., Yoshimora, J., and Hata, S., 1931, A new radioactive mineral found in Japan: Scientific Papers of the Institute of Physical and Chemical Research, Tokyo, v. 15, p. 83-88.

Imeokparia, E.G., 1981, Ba/Rb and Rb/Sr ratios as indicators of magmatic fractionation, postmagmatic alteration and mineralization—Afu Younger Granite Complex, Northern Nigeria: Geochemical Journal, v. 15, p. 209-219.

Lange, R.A., 1994, The effect of H_2O, CO_2 and F on the density and viscosity of silicate melts: Reviews in Mineralogy and Geochemistry, v. 30, p. 331-369.

Le Bas, M.J., and Streckeisen, A.L., 1991, The IUGS systematics of igneous rocks: Journal of the Geological Society, London, v. 148, p. 825-833.

Le Fort, P., 1981, Manaslu leucogranite: A collision signature of the Himalaya: A model for its genesis and emplacement: Journal of Geophysical Research, v. 86, p. 10,545-10,568.

Lehmann, B., 1982, Metallogeny of tin: magmatic differentiation versus geochemical heritage: Economic Geology, v. 77, p. 50-59.

Lough, T.A., Freeman, L.K., Elliott, B.A., Griesel, G.A., Newberry, R.J., and Szumigala, D.J., 2012, Geochemical, major-oxide, minor-oxide, trace-element, and carbon data from rocks collected in 2011 in the Moran area, Tanana and Melozitna quadrangles, Alaska: Alaska Division of Geological & Geophysical Surveys Raw Data File 2011-4 v. 2, 176 p.

Ludwig, K.R., 2008, User's manual for Isoplot version 3.7, A geochronological toolkit for Microsoft Excel: Berkeley Geochronology Center, Special Publication 4, 76 p.

Lyons, P.C., 1971, Staining of feldspars on rock-slab surfaces for modal analysis: Mineralogical Magazine, v. 38, p. 518-519.

Miller, T.P., 1989, Contrasting plutonic rock suites of the Yukon-Koyukuk Basin and the Ruby Geanticline, Alaska: Journal of Geophysical Research, v. 94, p. 15,969-15,987.

Neuendorf, K.K.E., Mehl, J.P., and Jackson, J.A., 2005, Glossary of geology: Alexandria, VA: American Geological Institute, 779 p.

Nieto, A., Guelly, K., and Kleit, A., 2013, Addressing criticality for rare earth elements in petroleum refining: The key supply factors approach: Resources Policy, v. 38, p. 496-503.

Okina, O., Lyapunov, S., Avdosyeva, M., Ermolaev, B., Golubchikov, V., Gorbunov, A., and Sheshukov, V., (*in press*), An investigation of the reliability of HF acid mixtures in the bomb digestion of silicate rocks for the determination of trace elements by ICP-MS: Geostandards and Geoanalytical Research.

Pabst, A., and Hutton, C.O., 1951, Huttonite, a new monoclinic thorium silicate: American Mineralogist, v. 36, p. 60-65.

Patton, W.W., Jr., and Miller, T.P., 1973, Bedrock geologic map of Bettles and southern part of Wiseman quadrangles, Alaska: U.S. Geological Survey Miscellaneous Field Studies Map 492, 1 sheet, scale 1:250,000.

Patton, W.W., Jr., Stern, T.W., Arth, J.G., and Carlson, C., 1987, New U/Pb ages from granite and granite gneiss in the Ruby Geanticline and southern Brooks Range, Alaska: Journal of Geology, v. 95, p. 118-126.

Patton, W.W., Jr., Wilson, F.H., Labay, K.A., Shew, N., 2009, Geologic map of the Yukon-Koyukuk Basin, Alaska: U.S. Geological Survey Scientific Investigations Map 2909, 2 sheets, scale 1:500,000.

Pearce, J.A., and Cann, J.R., 1973, Tectonic setting of basic volcanic rocks determined using trace element analyses: Earth and Planetary Science Letters, v. 19, p. 290-300.

Pearce, J.A. Harris, N.B.W., and Tindle, A.G., 1984, Trace element discrimination diagrams for the tectonic interpretation of granitic rocks: Journal of Petrology, v. 25, p. 956-983.

Poitrasson, F., 2002, The current state and future of accessory mineral research: Chemical Geology, v. 191, p. 3-24.

Puchner, C.C., 1984, Intrusive geology of the Ray Mountains Batholith: Geological Society of America, Abstracts with Programs, v. 16, p. 329.

Renne, P.R., Deino, A.L., Walter, R.C., Turrin, B.D., Swisher, C.C., Becker, T.A., Curtis, G.H., Sharp, W.D., and Jaouni, A.R., 1994, Intercalibration of astronomical and radioisotopic time: Geology, v. 22, p. 783-786.

Renne, P.R., Mundil, R., Balco, G., Min, K., and Ludwig, K.R., 2010, Joint determination of ^{40}K decay constants and $^{40}Ar^*/^{40}K$ for the Fish Canyon sanidine standard, and improved accuracy for $^{40}Ar/^{39}Ar$ geochronology: Geochimica et Cosmochimica Acta, v. 74, p. 5349-5367.

Samson, S.D., and Alexander, E.C., 1987, Calibration of the interlaboratory $^{40}Ar/^{39}Ar$ dating standard, MMhb-1: Chemical Geology, v. 66, p. 27-34.

Shand, S.J., 1943, Eruptive Rocks, 2nd Ed.: New York, John Wiley & Sons, 444 p.

Silberman, M.L., Moll, E.J., Chapman, R.M., Patton, W.W., Jr., and Connor, C.L., 1979, Potassium-argon age of granitic and volcanic rocks from the Ruby, Medfra, and adjacent quadrangles, west-central Alaska, in Johnson, K.M., and Williams, J.R., eds., The United States Geological Survey in Alaska; accomplishments during 1978: U.S. Geological Survey Circular 804-B, p. B63-B65.

Smith, S.M., 2006, National geochemical database - Reformatted data from the National Uranium Resource Evaluation (NURE) Hydrogeochemical and Stream Sediment Reconnaissance (HSSR) Program: U.S. Geological Survey Open-File Report 97-492 v. 1.40.

Solie, D.N., Wiltse, M.A., Harris, E.E., and Roe, J.T., 1993, Land selection unit 34, (Bettles and Tanana Quadrangles): References, DGGS sample location, geochemical and major oxide data: Alaska Division of Geological & Geophysical Surveys Public Data File 93-34, 42 p., 1 sheet, scale 1:250,000.

Stern, T.W., Bateman, P.C., Morgan, B.A., Newell, M.F., and Peck, D.L., 1981, Isotopic U-Pb ages of zircon from granitoids of the central Sierra Nevada, California: U.S. Geological Survey Professional Paper 1185, 17 p.

Streckeisen, A.L., and Le Maitre, R.W., 1979, A chemical approximation to the modal QAPF classification of the igneous rocks: Neues Jahrbuch für Mineralogie, Abhandlungen, v. 136, p. 169-206.

Swanson, S.E., Bond, J.F., and Newberry, R.J., 1988, Petrogenesis of the Ear Mountain Tin Granite, Seward Peninsula, Alaska: Economic Geology, v. 83, p. 46-61.

Szumigala, D.J., Graham, G.E., and Athey, J.E., 2004, Alaska resource data file, Tanana Quadrangle: U.S. Geological Survey Open-File Report 2004-1386, 309 p.

Taylor, S.R., 1965, The application of trace element data to problems in petrology: Physics and Chemistry of the Earth, v. 6, p. 133-213.

Till, A.B., Dumoulin, J.A., Phillips, J.D., Stanley, R.G., and Crews, Jesse, 2006, Preliminary integrated geologic map databases for the United States: digital data for the generalized bedrock geologic map, Yukon Flats region, east-central Alaska: U.S. Geological Survey Open-File Report 2006-1304.

Tuzzolino, A.L., Freeman, L.K., and Newberry, R.J., 2014a, Geochemical major-oxide, minor-oxide, trace-element, and rare-earth-element data from rock samples collected in 2013 in the Ray Mountains area, Bettles A-1 and A-6 quadrangles, Alaska: Alaska Division of Geological & Geophysical Surveys Raw Data File 2014-17, 3 p.

Tuzzolino, A.L., Newberry, R.J., Benowitz, J.A., Layer, P.W., and Freeman, L.K., 2014b, $^{40}Ar/^{39}Ar$ data, Ray Mountains area, Bettles Quadrangle, Alaska: Alaska Division of Geological & Geophysical Surveys Raw Data File 2014-19, 12 p.

Tuzzolino, A.L., O'Sullivan, P.B., Freeman, L.K., and Newberry, R.J., 2016, Zircon U-Pb age data, Ray Mountains area, Bettles Quadrangle, Alaska: Alaska Division of Geological & Geophysical Surveys Raw Data File 2016-7, 19 p.

U.S. Geological Survey, 1973, Aeromagnetic survey, western half of Beaver Quadrangle, northeast Alaska: U.S. Geological Survey Open-File Report 73-309, 1 sheet, scale 1:250,000.

van Emden, B., Thornber, M.R., Graham, J., and Lincoln, F.J., 1997, The incorporation of actinides in monazite and xenotime from placer deposits in western Australia: Canadian Mineralogist, v. 35, p. 95-104.

Wahrhaftig, C., 1965, Physiographic divisions of Alaska: U.S. Geological Survey Professional Paper 482, 52 p., 6 sheets, scale 1:2,500,000.

Weis, D., Kieffer, B., Maerschalk, C., Barling, J., de Jong, J., Williams, G.A., Hanano, D., Pretorius, W., Mattielli, N., Scoates, J., Goolaerts, A., Friedman, R.M., and Mahoney, J.B., 2006, High-precision isotopic characterization of USGS reference materials by TIMS and MC-ICP-MS: Geochemistry, Geophysics, Geosystems, v. 7, 30 p.

Wood, S.A., and Ricketts, A., 2000, Allanite-(Ce) from the Eocene Castro Granite, Idaho: Response to hydrothermal alteration: Canadian Mineralogist, v. 38, p. 81-100.

Zen, E., 1988, Phase relations of peraluminous granitic rocks and their petrogenetic implications: Annual Review of Earth and Planetary Sciences, v. 16, p. 21-51.

Appendix A. Modal Analyses

Table A-1. Modal analyses for rocks of the Ruby batholith

			Modal Percent			
Sample	**Pluton**	**Rock Type**	**K-Feldspar**	**Plagioclase**	**Quartz**	**Mafic**
12LF077A	Bonanza	mgr	34	30	25	11
12LF077A1	Bonanza	mgr	28	38	24	10
12LF080A	Bonanza	syg	47	22	20	11
12LF082A	Bonanza	gd	20	42	23	15
12RN135A	Bonanza	mgr	20	35	30	15
12RN138A	Bonanza	syg	43	16	31	10
12RN139A	Bonanza	qmz	20	35	5	40
12RN141A	Bonanza	gd	17	42	24	17
12RN142A	Bonanza	qmz	25	40	12	23
12RN142B	Bonanza	qmz	22	36	7	35
12RN143A	Bonanza	mgr	25	33	29	13
12RN143B	Bonanza	qmz	25	32	12	31
12RN144A	Bonanza	mgr	25	45	20	10
12RN147A	Bonanza	mgr	30	31	24	15
12RN373A	Bonanza	mgr	34	27	27	12
12RN374C	Bonanza	mgr	28	31	31	10
12RN375B	Bonanza	syg	45	22	25	8
12RN452A	Bonanza	mgr	37	28	27	8
12CW033A	Kanuti E	mgr	36	33	28	3
12LF115B	Kanuti E	mgr	31	36	29	4
12LF117A	Kanuti E	gd	17	47	34	3
12LF119A	Kanuti E	mgr	22	31	35	12
12RN184A	Kanuti E	mgr	26	32	36	6
12RN187A	Kanuti E	mgr	26	41	27	6
12LF243A	Kanuti N	gd	24	49	23	4
12LF243C	Kanuti N	mgr	41	34	24	0
12LF246A	Kanuti N	mgr	31	35	29	5
12LF247A	Kanuti N	mgr aplite	38	29	26	6
12LF250A	Kanuti N	mgr	22	34	42	2
12MJB098A	Kanuti N	mgr	20	30	39	10
12LF002A	Kanuti W	mgr	29	34	27	9
12RN372A	Kanuti W	gd	22	45	30	3
12LF057A	Hot Springs E	mgr	37	19	40	4
12LF059A	Hot Springs E	mgr	27	39	20	14
12LF062A	Hot Springs E	mgr	24	37	27	12
12LF062A	Hot Springs E	mgr	30	34	29	7
12LF064A	Hot Springs E	mgr	37	39	24	0.5
12LF323A	Hot Springs E	mgr	32	30	35	3

Table A-1 continued. Modal analyses for rocks of the Ruby batholith

			Modal Percent			
Sample	**Pluton**	**Rock Type**	**K-Feldspar**	**Plagioclase**	**Quartz**	**Mafic**
12LF328C	Hot Springs E	mgr	45	29	21	5
12LF332A	Hot Springs E	mgr	37	27	34	2
12RN121B	Hot Springs E	qmz	31	48	20	1
12RN123A	Hot Springs E	mgr	30	24	35	11
12RN127A	Hot Springs E	qmz	49	26	18	7
12RN127A2	Hot Springs E	mgr	23	36	25	15
12RN128B	Hot Springs E	gd	22	46	31	2
12RN129B	Hot Springs E	mgr	41	25	33	1
12RN130A	Hot Springs E	mgr	30	21	38	10
12RN132A	Hot Springs E	mgr	35	36	24	5
12RN476C	Hot Springs E	mgr	40	29	28	4
12RN480A	Hot Springs E	mgr	37	26	33	4
12RN483B	Hot Springs E	mgr	30	37	31	3
12RN484B	Hot Springs E	mgr	31	33	34	2
12LF046C	Hot Springs W	mgr	40	35	22	3
12LF054A	Hot Springs W	mgr	30	45	22	3
12RN078A	Hot Springs W	qmz	48	37	14	1
12RN093A	Hot Springs W	sgr	57	16	25	2
12RN096A	Hot Springs W	mgr	36	36	25	3
12RN098A	Hot Springs W	sgr	50	18	26	5
12RN100A	Hot Springs W	mgr	27	32	38	4
12RN101B	Hot Springs W	qs	56	26	13	5
12RN103A	Hot Springs W	mgr/gd	22	43	24	11
12RN104A	Hot Springs W	mgr	34	32	29	5
12RN107A	Hot Springs W	mgr	48	26	22	4
12RN109A	Hot Springs W	mgr	32	28	36	4
12RN113A	Hot Springs W	mgr	30	31	32	7
12RN114A	Hot Springs W	mgr	42	29	27	2
12RN117A	Hot Springs W	mgr	35	33	27	4
12RN118A	Hot Springs W	tn	4	50	24	22
12LF141A	Coal Creek	mgr	30	40	26	3
12LF144A	Coal Creek	mgr	36	22	35	6
12LF145A	Coal Creek	mgr	38	25	33	4
12LF149A	Coal Creek	mgr	26	35	32	6
12RN220A	Coal Creek	mgr	32	31	29	8
12RN226A	Coal Creek	mgr	28	30	36	7
12RN228A	Coal Creek	mgr	34	32	30	4
12LF227A	No Name	mgr	36	28	33	3
12LF304A	No Name	sgr por	42	13	42	2
13AT134A	No Name	sgr por	40	10	46	4
13AT135A	No Name	sgr por	32	14	46	7

Table A-1 continued. Modal analyses for rocks of the Ruby batholith

			Modal Percent			
Sample	**Pluton**	**Rock Type**	**K-Feldspar**	**Plagioclase**	**Quartz**	**Mafic**
13LF415A	No Name	sgr por	47	9	38	6
13LF416A	No Name	sgr por	38	11	48	3
12CW118A	FHH	mgr	38	24	36	2
12RN437A	FHH	mgr	32	29	37	2
12RN439A	FHH	mgr	28	31	39	2
12RN439C	FHH	sgr	41	20	36	3
12RN459A	FHH	mgr	31	35	30	4
12RN461C	FHH	mgr	24	34	41	2
12RN462A	FHH	mgr	29	25	40	6
12RN463A	FHH	mgr	35	23	32	9
12RN465A	FHH	mgr	33	24	38	5
12RN468A	FHH	mgr	33	24	35	8
12RN469A	FHH	mgr	37	27	32	4
12RN470A	FHH	mgr	36	25	35	4
12RN471A	FHH	mgr	38	27	28	7
12RN472A	FHH	mgr	37	30	24	9
12RN474A	FHH	mgr	32	28	28	12
12RN488A	FHH	mgr	36	30	32	1
12LF104A	Ray River	mgr	27	24	40	10
12LF108A	Ray River	mgr	36	26	36	2
12LF110A	Ray River	mgr	28	41	28	2
12LF111A	Ray River	mgr	25	36	36	3
12LF114A	Ray River	mgr	31	32	33	5
12LF258A	Ray River	mgr	19	36	34	11
12LF258B	Ray River	gd	17	36	39	8
12LF259A	Ray River	qmz por	39	39	20	2
12LF262A	Ray River	mgr	43	30	21	6
12RN353B1	Ray River	mgr	30	28	36	6
12RN353B2	Ray River	mgr	26	49	24	2
12RN380A	Ray River	sgr seriate	51	21	25	3
12RN382A	Ray River	mgr	24	37	33	6
12RN384A	Ray River	mgr	37	19	37	6
12RN386A	Ray River	mgr	29	32	34	6
12RN410C	Ray River	mgr	28	35	30	8
12RN415A	Ray River	mgr	31	30	28	10
12RN421A	Ray River	mgr	31	38	23	7
12RN426A	Ray River	mgr	35	35	25	6
12BW014A	Sithylemenkat	qmd por	17	66	16	1
12BW048A	Sithylemenkat	mgr	29	34	33	4
12CW004B	Sithylemenkat	mgr	25	39	30	7
12EB004A	Sithylemenkat	mgr	29	38	28	5

Table A-1 continued. Modal analyses for rocks of the Ruby batholith

			Modal Percent			
Sample	**Pluton**	**Rock Type**	**K-Feldspar**	**Plagioclase**	**Quartz**	**Mafic**
12EB004B	Sithylemenkat	mgr	36	30	31	3
12LF012B	Sithylemenkat	mgr	39	20	38	3
12LF015B1	Sithylemenkat	mgr	31	31	36	2
12LF015B2	Sithylemenkat	mgr	26	46	22	7
12LF019B	Sithylemenkat	mgr	24	34	32	10
12LF022A	Sithylemenkat	gd	15	47	34	4
12LF130A	Sithylemenkat	mgr	31	29	27	14
12LF150A	Sithylemenkat	mgr	32	27	36	4
12LF155C	Sithylemenkat	sgr	40	19	39	2
12LF156A	Sithylemenkat	mgr	35	29	30	6
12LF158A	Sithylemenkat	mgr	33	26	37	5
12LF161A	Sithylemenkat	mgr	39	26	33	2
12LF161A	Sithylemenkat	sgr	49	19	27	5
12LF270A	Sithylemenkat	mgr	33	34	28	5
12LF275A	Sithylemenkat	mgr	32	29	35	3
12LF276B	Sithylemenkat	mgr	25	37	33	4
12LF276B	Sithylemenkat	qmz	40	38	19	3
12LF277A	Sithylemenkat	mgr	43	25	29	3
12LF280A	Sithylemenkat	qmz	47	31	17	4
12LF280A	Sithylemenkat	mgr	29	37	26	8
12LF283A	Sithylemenkat	gd	21	45	27	8
12LF284A	Sithylemenkat	mgr	36	25	33	5
12LF284A	Sithylemenkat	mgr	39	26	33	2
12MJB004A	Sithylemenkat	mgr	38	29	30	3
12RN049B	Sithylemenkat	mgr	25	30	43	2
12RN065A1	Sithylemenkat	mgr	32	32	30	6
12RN065A2	Sithylemenkat	mgr	22	38	29	11
12RN066A	Sithylemenkat	sgr	45	21	32	2
12RN068C	Sithylemenkat	qmz	40	40	20	0
12RN196A	Sithylemenkat	mgr	42	30	23	4
12RN199B	Sithylemenkat	mgr	22	30	46	2
12RN202A	Sithylemenkat	mgr	43	25	23	9
12RN230A	Sithylemenkat	mgr	38	29	30	4
12RN235B	Sithylemenkat	mgr	28	26	40	6
12RN240C	Sithylemenkat	mgr	35	29	33	3
12RN240D	Sithylemenkat	mgr	36	31	31	1
12RN243A1	Sithylemenkat	mgr	28	30	31	11
12RN243A2	Sithylemenkat	mgr	33	32	31	5
12RN244A	Sithylemenkat	mgr	29	32	36	3
12RN246A	Sithylemenkat	mgr por	37	40	22	1
12RN256A	Sithylemenkat	mgr por	38	38	23	1

Table A-1 continued. Modal analyses for rocks of the Ruby batholith

			Modal Percent			
Sample	**Pluton**	**Rock Type**	**K-Feldspar**	**Plagioclase**	**Quartz**	**Mafic**
12RN391A	Sithylemenkat	mgr	37	24	31	9
12RN393A	Sithylemenkat	mgr	38	25	30	6
12RN397B	Sithylemenkat	mgr	31	35	28	7
12RN401A	Sithylemenkat	mgr	37	25	33	5
12RN405B	Sithylemenkat	mgr	41	26	30	4
12RN456A2	Sithylemenkat	mgr	20	38	36	5
12RN456B1	Sithylemenkat	mgr	45	28	21	5
12LF098A	Ray Mountains	mgr	47	36	29	16
12LF099A	Ray Mountains	mgr	26	36	36	3
12LF100B	Ray Mountains	mgr	36	32	31	1
12LF171A	Ray Mountains	qmz	44	36	14	7
12LF172A	Ray Mountains	mgr	30	38	25	7
12LF181A	Ray Mountains	mgr	38	29	29	4
12LF183A	Ray Mountains	mgr	36	25	32	7
12LF186A	Ray Mountains	mgr	27	37	30	6
12LF191B	Ray Mountains	mgr	28	32	35	6
12LF194A1	Ray Mountains	mgr	24	34	31	11
12LF194A2	Ray Mountains	mgr	28	32	32	8
12LF197B	Ray Mountains	mgr	20	35	41	4
12LF202A	Ray Mountains	qsy aplite	62	25	12	1
12LF203A	Ray Mountains	mgr	37	34	27	1
12LF207A	Ray Mountains	mgr	36	26	36	2
12LF208A	Ray Mountains	mgr	32	25	39	4
12LF211A	Ray Mountains	mgr	33	25	37	5
12LF211B	Ray Mountains	mgr	43	30	24	3
12LF212A	Ray Mountains	mgr	24	27	43	6
12LF344A	Ray Mountains	mgr	37	22	37	3
12RN266A	Ray Mountains	mgr	25	30	41	5
12RN267A	Ray Mountains	mgr	39	24	34	2
12RN273B	Ray Mountains	mgr	38	28	31	3
12RN277A	Ray Mountains	mgr	22	34	37	7
12RN280B	Ray Mountains	qmd	24	58	11	6
12RN284A	Ray Mountains	qgr	25	23	49	2
12RN289A	Ray Mountains	mgr	37	27	30	6
12RN290A	Ray Mountains	mgr	33	27	33	8
12RN292B	Ray Mountains	mgr	31	38	22	9
12RN294A	Ray Mountains	mgr	32	22	44	2
12RN304C	Ray Mountains	gd por	14	55	27	4
12RN314A	Ray Mountains	mgr	33	24	40	3

Notes: Rock type based off of modal analyses. "FHH" = Fort Hamlin Hills, "mgr" = monzogranite, "gd" = granodiorite, "qsy" = quartz syenite, "qmz" = quartz monzonite, "sgr" = syenogranite, "qmd" = quartz monzodiorite, "por" = porphyry, "tn" = tonalite, "qs" = quartz syenite. Refer to p. 13 for procedure.

Appendix B. Normative Analyses

Table B-1. Normative analyses for Bonanza-pluton samples

Sample	Analysis	Normative Mineral											
		Quartz	**Albite**	**Orthoclase**	**Anorthite**	**Corundum**	**Diopside**	**Hypersthene**	**Ilmenite**	**Magnetite**	**Apatite**	**An/(An+Or)**	**Q/(Q+F)**
12LF083B	Slab XRF	33.2	28.9	33.0	4.1	0	0.07	0.52	0.06	0.03	0.05	11	33
12RN147B	Slab XRF	32.0	38.2	27.6	1.1	0.3	0	0.63	0.06	0.04	0.14	4	32
12RN375A	Slab XRF	33.3	30.8	32.3	2.7	0	0.16	0.43	0.06	0.03	0.14	8	34
12RN452C	Slab XRF	35.6	24.7	34.0	3.6	0.44	0	1.36	0.15	0.12	0.09	10	36
12LF080A	Whole-Rock	13.3	28.8	31.9	13.9	0.09	0	9.62	1.14	0.65	0.65	30	15
12RN373A	Whole-Rock	15.7	28.4	29.2	14.4	0.32	0	9.42	1.27	0.67	0.63	33	18
12RN374C	Whole-Rock	16.1	28.9	30.0	13.2	0.87	0	8.55	1.16	0.61	0.58	30	18
12RN375B	Whole-Rock	21.4	27.3	29.6	11.4	0.54	0	7.59	1.06	0.55	0.58	28	24
12RN456A1	Whole-Rock	13.8	30.6	29.1	14.4	0.26	0	9.54	1.06	0.65	0.63	33	16
12RN456A2	Whole-Rock	14.1	31.1	28.0	14.7	0.24	0	9.54	1.14	0.65	0.63	34	16

Note: Refer to p. 13 for procedure.

Table B-2. Normative analyses for Kanuti-Northeast samples

Sample	Type	Normative Mineral											
		Quartz	Albite	Orthoclase	Anorthite	Corundum	Diopside	Hypersthene	Ilmenite	Magnetite	Apatite	An/(An+Or)	Q/(Q+F)
12AT041A	Whole-Rock	34.4	26.3	21.6	11.7	0.67	0	4.16	0.59	0.28	0.23	35	37
12AT042A	Whole-Rock	30.7	28.9	22.9	10.6	1.29	0	4.47	0.59	0.32	0.23	32	33
12EB103A	Whole-Rock	32.8	26.6	32.7	3.66	1.69	0	2.05	0.23	0.19	0.09	10	34
12LF246A	Whole-Rock	32.4	27.3	24.6	9.88	1.03	0	3.81	0.55	0.25	0.21	29	34
12LF247A	Whole-Rock	35.0	28.8	27.4	3.24	2.79	0	2.04	0.23	0.17	0.35	11	37
12MJB096A	Whole-Rock	29.2	31.6	17.2	13.4	1.72	0	5.67	0.66	0.35	0.25	44	32
12MJB097A	Whole-Rock	29.6	29.0	26.1	8.52	1.01	0	4.53	0.61	0.36	0.23	25	32
12MJB098A	Whole-Rock	33.0	27.0	26.7	7.8	0.69	0	3.88	0.46	0.29	0.21	23	35
12RN357A	Whole-Rock	29.4	31.7	15.7	15.5	1.15	0	5.25	0.68	0.35	0.25	50	32

Table B-3. Normative analyses for Kanuti-Center samples

Sample	Type	Normative Mineral											
		Quartz	Albite	Orthoclase	Anorthite	Corundum	Diopside	Hypersthene	Ilmenite	Magnetite	Apatite	An/(An+Or)	Q/(Q+F)
12CW033A	Whole-Rock	29.8	22.8	32.3	7.47	1.64	0	4.77	0.7	0.39	0.25	19	32
12RN450A	Slab XRF	38.6	27.3	28.1	3.51	1.07	0	1.08	0.11	0.09	0.16	11	40
12MJB039A	Whole-Rock	26.2	27.2	20.0	12.3	3.06	0	8.86	1.31	0.67	0.44	38	31

Table B-4. Normative analyses for Kanuti-West samples

Sample	Type	Normative Mineral											
		Quartz	Albite	Orthoclase	Anorthite	Corundum	Diopside	Hypersthene	Ilmenite	Magnetite	Apatite	An/(An+Or)	Q/(Q+F)
12LF002A	Whole-Rock	18.4	27.2	28.3	13.9	0.35	0	9.42	1.14	0.62	0.65	33	21
12RN367A	Whole-Rock	25.6	28.4	29.7	8.4	0.9	0	5.58	0.76	0.43	0.32	22	28
12RN369A	Whole-Rock	28.3	28.2	27.4	8.3	0.98	0	5.43	0.74	0.42	0.32	23	31
12RN370A	Whole-Rock	18.6	26.5	31.5	12.9	0.36	0	8.05	1.01	0.55	0.6	29	21
12RN372A	Whole-Rock	18.4	26.3	33.6	11.6	0.5	0	7.63	0.95	0.52	0.53	26	20

Table B-5. Normative analyses for Hot Springs East-pluton samples

Sample	Type	Normative Mineral											
		Quartz	Albite	Orthoclase	Anorthite	Corundum	Diopside	Hypersthene	Ilmenite	Magnetite	Apatite	An/(An+Or)	Q/(Q+F)
12LF059A	Whole-Rock	29.39	25.64	31.97	6.26	1.34	0	4.12	0.65	0.35	0.28	16	32
12RN484B1	Whole-Rock	34.04	27.16	29.02	5.02	0.88	0	3.15	0.32	0.26	0.14	15	36
12RN484B2	Whole-Rock	34.87	26.74	28.13	5.05	0.97	0	3.45	0.34	0.29	0.16	15	37
12LF323A	Whole-Rock	33.5	26.99	31.73	2.93	1.96	0	2.22	0.25	0.2	0.21	8	35

Table B-6. Normative analyses for Hot Springs West-pluton samples

Sample	Type	Normative Mineral											
		Quartz	Albite	Orthoclase	Anorthite	Corundum	Diopside	Hypersthene	Ilmenite	Magnetite	Apatite	An/(An+Or)	Q/(Q+F)
12LF039B	Slab XRF	40.43	28.69	27.83	1.92	0.56	0	0.36	0.15	0.03	0.02	6	41
12LF044A	Slab XRF	40.88	26.74	29.61	1.46	0.79	0	0.38	0.08	0.01	0.05	5	41
12LF046C	Slab XRF	33.42	29.62	32.03	3.21	0.11	0	1.21	0.21	0.1	0.09	9	34
12LF056A	Slab XRF	36.7	28.18	30.67	3.44	0.06	0	0.73	0.11	0.06	0.05	10	37
12RN099B	Slab XRF	39.49	28.69	26.71	3.52	0	0.03	1.2	0.21	0.12	0.02	12	40
12RN100B	Slab XRF	37.04	29.19	29.61	2.81	0	0.13	0.98	0.11	0.1	0.02	9	38
12RN103B	Slab XRF	38.8	25.98	30.14	2.68	0.3	0	1.63	0.23	0.16	0.07	8	40
12LF047A	Whole-Rock	37.43	26.49	31.85	1.52	1.37	0	1.08	0.13	0.1	0.02	5	38
12LF054A	Whole-Rock	29.3	27.42	31.85	4.93	0.91	0	4.37	0.65	0.41	0.19	13	31
12RN105B	Whole-Rock	27.69	28.69	33.33	3.5	1.1	0	4.86	0.27	0.39	0.19	10	30
12RN364A	Whole-Rock	26.08	29.7	25.77	10.46	0.88	0	5.57	0.82	0.41	0.3	29	28
12RN365A	Whole-Rock	27.62	30.29	23.28	10.74	0.73	0	5.73	0.85	0.43	0.32	32	30
12RN366A	Whole-Rock	27.01	30.29	26.53	9.17	0.49	0	5.03	0.78	0.41	0.3	26	29

Table B-7. Normative analyses for Fort Hamlin Hills-pluton samples

Sample	Type	Normative Mineral											
		Quartz	Albite	Orthoclase	Anorthite	Corundum	Diopside	Hypersthene	Ilmenite	Magnetite	Apatite	An/(An+Or)	Q/(Q+F)
12RN461B	Whole-Rock	31.08	17.94	46.8	0.95	0.59	0	2.13	0.25	0.2	0.07		
12CW118A1	Whole-Rock	27.9	24.71	34.22	6.33	0.59	0	4.81	0.74	0.45	0.25	16	30
12CW118A2	Whole-Rock	29.39	25.22	31.03	6.82	0.68	0	5.28	0.84	0.49	0.25	18	32
12LF343A	Whole-Rock	34.74	22.09	31.91	4.59	1.47	0	4.01	0.66	0.36	0.19	13	37
12RN439A	Whole-Rock	37.81	23.86	33.03	2.8	0.45	0	1.74	0.09	0.16	0.05	8	39
12RN439C	Whole-Rock	35.9	25.22	33.68	1.84	0.96	0	2.06	0.09	0.19	0.07	5	37
12RN441A	Whole-Rock	36.85	28.69	29.55	1.09	1.3	0	2.19	0.06	0.2	0.07	4	38
12RN443A	Whole-Rock	35.02	23.61	33.09	3.44	1.01	0	3.04	0.38	0.29	0.12	9	37
12RN460A1	Whole-Rock	28.77	24.12	34.39	5.75	0.78	0	4.8	0.72	0.45	0.23	14	31
12RN460A2	Whole-Rock	31.54	23.78	31.62	5.85	0.76	0	4.94	0.84	0.46	0.23	16	34
12RN461C1	Whole-Rock	30.73	24.2	31.97	5.99	0.69	0	4.99	0.74	0.46	0.23	16	33
12RN461C2	Whole-Rock	29.16	24.54	33.74	6.04	0.6	0	4.55	0.72	0.42	0.23	15	31
12RN464A1	Whole-Rock	35.29	17.77	40.84	1.41	1	0	3	0.32	0.28	0.12	3	37
12RN464A2	Whole-Rock	35.6	18.53	39.71	1.71	0.93	0	2.72	0.44	0.25	0.12	4	37
12RN464B	Whole-Rock	32.3	23.1	31.85	4.61	1.23	0	5.38	0.8	0.49	0.23	13	35
12RN464B1	Whole-Rock	28.47	24.12	31.2	5.73	1.23	0	7.13	1.14	0.65	0.32	16	32
12RN464B2	Whole-Rock	36.12	22	32.56	3.53	1.23	0	3.67	0.44	0.33	0.14	10	38
12RN474A1	Whole-Rock	28.97	23.78	33.39	6.33	0.76	0	5.19	0.84	0.48	0.25	16	31
12RN474A2	Whole-Rock	29.09	23.61	34.16	5.94	0.89	0	4.8	0.82	0.45	0.23	15	31

Table B-8. Normative analyses for No Name Creek-pluton samples

Sample	Type	Normative Mineral											
		Quartz	Albite	Orthoclase	Anorthite	Corundum	Diopside	Hypersthene	Ilmenite	Magnetite	Apatite	An/(An+Or)	Q/(Q+F)
12LF227A	Whole-Rock	38.6	25.2	30.1	1.38	1.65	0	2.48	0.27	0.23	0.09	4	41
12LF236A	Whole-Rock	36.5	31.0	29.8	0.66	0.81	0	0.99	0.13	0.09	0.05	2	37
12LF236B	Whole-Rock	38.8	28.1	30.2	0.58	0.93	0	1.18	0.06	0.1	0.02	2	40
12LF304A	Whole-Rock	38.2	24.7	31.1	0.78	1.88	0	2.61	0.32	0.25	0.16	2	40
12RN319A	Whole-Rock	40.9	21.3	29.8	1.99	1.46	0	3.66	0.38	0.36	0.14	6	44
12RN319B	Whole-Rock	33.9	20.7	41.5	0.85	0.76	0	1.71	0.21	0.16	0.14	2	35
12RN336A	Whole-Rock	35.4	28.3	29.0	0.63	3.35	0	2.55	0.23	0.23	0.39	2	38
12RN337A	Whole-Rock	31.6	34.7	29.7	0.72	1.21	0	1.63	0.06	0.14	0.25	2	33
13RN554A	Whole-Rock	39.8	23.8	27.7	3.1	1.21		3.52	0.46	0.32	0.19	10	42
13RN558A	Whole-Rock	38.8	23.2	30.4	1.89	1.75		3.17	0.38	0.29	0.14	6	40
13AT135A	Whole-Rock	39.9	24.7	27.9	1.99	1.35		3.35	0.36	0.32	0.14	7	42
13LF412A	Whole-Rock	43.2	23.7	26.4	0.8	1.93		3.23	0.32	0.3	0.14	3	45
13RN558B	Whole-Rock	46.6	20.7	25.9	1.11	2		2.99	0.32	0.28	0.12	4	48
13LF414A	Whole-Rock	46.6	20.9	26.7	1.19	1.33		2.68	0.28	0.25	0.07	4	48
13AT134A	Whole-Rock	43.5	23.4	27.1	1.09	1.64		2.76	0.25	0.25	0.07	4	45
13RN557A	Whole-Rock	42.8	25.0	26.6	1.24	1.76		2.23	0.19	0.22	0.07	4	44
13RN553A	Whole-Rock	37.4	27.1	30.4	1.08	1.4		2.17	0.17	0.2	0.16	3	38

Table B-9. Normative analyses for Ray River-pluton samples

Sample	Type	Normative Mineral											
		Quartz	Albite	Orthoclase	Anorthite	Corundum	Diopside	Hypersthene	Ilmenite	Magnetite	Apatite	An/(An+Or)	Q/(Q+F)
12LF108A	Whole-Rock	39.3	25.6	28.4	2.58	1.54	0	2.14	0.21	0.2	0.07	8	41
12LF259A	Whole-Rock	38.8	23.4	31.5	1.99	1.19	0	2.58	0.25	0.25	0.07	6	41
12RN350A	Whole-Rock	37.4	25.1	30.6	2.19	1.56	0	2.54	0.28	0.23	0.14	7	39
12RN352D	Whole-Rock	36.2	24.8	32.0	2.62	1.23	0	2.58	0.27	0.25	0.09	8	38
12RN383A	Whole-Rock	36.0	22.9	32.8	2.83	1.43	0	3.21	0.38	0.29	0.14	8	38
12RN390A	Whole-Rock	32.5	22.3	34.3	5	1.29	0	3.43	0.53	0.32	0.23	13	35
12RN412A1	Whole-Rock	37.1	26.4	31.2	2.71	0.54	0	1.77	0.06	0.17	0.02	8	38
12RN412A2	Whole-Rock	36.6	27.1	31.0	2.76	0.57	0	1.77	0.06	0.17	0.02	8	38
12RN418A1	Whole-Rock	34.4	21.8	33.3	4.31	1.06	0	3.98	0.55	0.38	0.16	11	37
12RN418A2	Whole-Rock	35.7	21.1	33.4	4.22	1.09	0	3.54	0.49	0.33	0.14	11	38
12RN424A1	Whole-Rock	36.7	27.7	29.7	2.7	0.72	0	2.13	0.11	0.22	0.05	8	38
12RN424A2	Whole-Rock	37.0	27.6	29.9	2.4	0.85	0	1.96	0.11	0.19	0.05	7	38
12RN424B	Whole-Rock	38.3	28.0	28.5	2.17	0.92	0	1.84	0.08	0.19	0.02	7	39
12RN424C	Whole-Rock	36.1	30.9	28.4	1.22	1.25	0	1.86	0.06	0.19	0.02	4	37
12RN429A1	Whole-Rock	32.8	21.9	33.5	5.18	1.06	0	4.36	0.65	0.39	0.19	13	35

Table B-10. Normative analyses for Sithylemenkat-pluton samples

Sample	Type	Normative Mineral											
		Quartz	Albite	Orthoclase	Anorthite	Corundum	Diopside	Hypersthene	Ilmenite	Magnetite	Apatite	An/(An+Or)	Q/(Q+F)
12BW048A	Whole-Rock	35.9	24.8	32.4	3.59	0.62	0	2.23	0.21	0.22	0.05	10	37
12LF015B	Whole-Rock	36.5	21.4	30.7	5.48	1.25	0	3.64	0.57	0.32	0.19	15	39
12LF150A	Whole-Rock	35.2	24.8	32.6	3.62	0.66	0	2.6	0.23	0.23	0.07	10	37
12LF158A	Whole-Rock	34.7	24.4	32.0	4.09	1.01	0	3.12	0.32	0.29	0.12	11	36
12LF270A	Whole-Rock	29.7	22.3	35.0	6.03	1.12	0	4.43	0.7	0.39	0.25	15	32
12LF280A	Whole-Rock	35.0	23.1	32.6	4.29	1.03	0	3.24	0.38	0.3	0.12	12	37
12LF283A	Whole-Rock	37.4	21.8	31.6	4.37	0.73	0	3.33	0.46	0.32	0.14	12	39
12LF284A	Whole-Rock	36.2	24.4	31.9	3.26	0.95	0	2.73	0.27	0.26	0.09	9	38
12MJB007B	Whole-Rock	32.7	21.1	33.7	5.94	0.8	0	4.46	0.72	0.38	0.23	15	35
12MJB070A	Whole-Rock	34.7	30.3	30.0	2.71	0.41	0	1.61	0.17	0.16	0.02	8	35
12RN070C	Whole-Rock	38.5	27.4	28.6	2.42	1.58	0	1.25	0.08	0.12	0.02	8	40
12RN342A	Whole-Rock	34.4	33.2	28.4	1.87	1.06	0	0.9	0.08	0.09	0.02	6	35
12RN344A	Whole-Rock	32.9	22.6	35.9	3.89	0.94	0	3.03	0.4	0.28	0.12	10	35
12RN398B	Whole-Rock	36.1	29.0	29.0	2.4	1.03	0	2.13	0.09	0.2	0.05	8	37
12RN399A1	Whole-Rock	33.3	25.6	32.1	4.02	1.05	0	3.18	0.34	0.29	0.14	11	35
12RN399A2	Whole-Rock	33.4	25.3	32.6	3.87	1.02	0	3.06	0.34	0.28	0.14	11	35
12RN406A	Whole-Rock	37.5	24.9	30.6	2.73	1.11	0	2.6	0.23	0.25	0.07	8	39

Table B-11. Normative analyses for Ray Mountains East-pluton samples

Sample	Type	Normative Mineral											
		Quartz	Albite	Orthoclase	Anorthite	Corundum	Diopside	Hypersthene	Ilmenite	Magnetite	Apatite	An/(An+Or)	Q/(Q+F)
12LF098A	Whole-Rock	32.2	26.2	35.8	2.0	0.78	0	2.53	0.11	0.25	0.02	5	33
12LF099A	Whole-Rock	39.4	27.3	27.1	1.9	1.48	0	2.38	0.15	0.23	0.09	6	41
12LF171A	Whole-Rock	31.0	24.5	32.4	4.9	1.66	0	4.21	0.74	0.38	0.35	13	33
12LF172A	Whole-Rock	25.3	25.9	27.0	13.4	0.25	0	6.64	0.82	0.49	0.3	33	28
12LF194A	Whole-Rock	30.0	23.9	33.1	5.0	1.93	0	4.59	0.76	0.39	0.42	13	33
12LF203A	Whole-Rock	38.9	28.0	27.2	0.1	2.83	0	2.6	0.15	0.26	0.07	0	41
12LF208A	Whole-Rock	35.8	26.0	31.4	2.0	1.75	0	2.33	0.25	0.22	0.25	6	38
12LF212A	Whole-Rock	36.8	22.9	31.6	3.1	1.24	0	3.38	0.47	0.32	0.16	9	39
12LF344A1	Whole-Rock	28.8	23.9	33.7	6.4	1.22	0	4.58	0.68	0.38	0.35	16	31
12LF344A2	Whole-Rock	29.7	23.9	32.6	6.5	1.13	0	4.87	0.7	0.39	0.35	17	32
12RN165A	Whole-Rock	28.7	23.8	30.9	8.3	0.11	0	6.12	1.29	0.58	0.25	21	31
12RN270A	Whole-Rock	35.1	22.8	33.8	4.1	1	0	2.7	0.25	0.22	0.09	11	37
12RN282C	Whole-Rock	35.4	25.4	30.9	1.6	3.34	0	2.5	0.28	0.22	0.39	5	38
12RN289A	Whole-Rock	35.9	26.9	29.1	1.8	2.83	0	2.57	0.28	0.23	0.37	6	38
12RN280C	Slab XRF	37.9	22.3	31.4	3.0	2.26	0	2.05	0.38	0.19	0.53	9	40
12LF186A	Slab XRF	35.9	24.4	29.1	5.1	1.07	0	3.11	0.65	0.28	0.51	15	38
12LF202A	Slab XRF	39.2	31.7	26.8	0.6	0.59	0	0.88	0.09	0.07	0.05	2	40
12RN315B	Slab XRF	34.3	27.9	34.5	2.1	0.48	0	0.53	0.02	0.03	0.07	6	35
12RN295E	Slab XRF	38.7	30.3	28.8	0.9	0.38	0	0.75	0.04	0.06	0.05	3	39
12LF100B	Slab XRF	38.1	28.3	28.1	3.7	0	0.32	1.3	0.08	0.13	0.02	12	39
12RN307A	Slab XRF	37.6	31.7	27.0	3.1	0	0.03	0.47	0.08	0.03	0.02	10	38

Appendix C. Magnetic Susceptibilities

Table C-1. Average magnetic susceptibilities for unaltered granites from the Bonanza pluton

Sample	Easting	Northing	Average MS
12LF077A	609990.25	7404526.5	11
12LF080A	609629.5	7404255.5	12
12LF082A	609361.81	7404107.5	6.6
12LF084A	609197.44	7403803.5	1.8
12LF086A	608961.75	7403489	12
12RN048A	600535.13	7406959.5	0.18
12RN135A	619045.94	7401658	0.13
12RN136B	618904.5	7402660.5	0.4
12RN138A	619226	7402129.5	0.04
12RN139A	619217.63	7402135	2.0
12RN141A	618995.19	7403373.5	0.25
12RN142A	618227.69	7406423	7.0
12RN142B	618133.94	7406423	0.7
12RN143A	619203.88	7404137.5	7.0
12RN143B	619197.63	7404172	2.0
12RN144A	618880.06	7405873.5	5.0
12RN145A	619179.69	7404358.5	1.0
12RN146A	619218.38	7404709.5	8.0
12RN147A	619209	7404697.5	5.0
12RN148A	619602.44	7405100	10
12RN148B	619597.75	7405111.5	6.0
12RN149A	619725.69	7405326.5	10
12RN373A	602035.75	7401928	8.5
12RN374A	602272.94	7400491.5	0.2
12RN374B	602310.94	7400469	32
12RN374C	602280.5	7400408	8.0
12RN375A	603016.69	7400679	0.015
12RN375B	603092.38	7400224	8.7
12RN452A	607539.44	7404310	7.5
12RN452C	607562.25	7404264.5	3.0
12RN453A	607459.75	7404299	1.5
12RN453B	607499.63	7404219	1.0
12RN455C	607539.44	7404253	0.01
12RN456A	607511	7404316	10
Average Magnetic Susceptibility of the Bonanza Pluton			**5.5**

Notes: "MS" = magnetic susceptibility (x 10^{-3} SI). Northing and easting reported for UTM Zone 5. Refer to p. 18 for procedure.

Table C-2. Average magnetic susceptibilities for unaltered granites from the Kanuti pluton

Sample	Easting	Northing	Average MS
12CW033A	624224.44	7380022	0.07
12EB103A	628549.44	7393450.5	0.2
12EB105A	628308.69	7393375	0.09
12LF003A	603430.38	7375650.5	3.4
12LF115B	624237.44	7381313.5	0.09
12LF117A	624263.13	7381307	0.02
12LF119A	624243.88	7381307	0.13
12LF243A	631690.63	7393173.5	0.08
12LF243B	631678.19	7393163	0.03
12LF247A	630072.25	7393069.5	0.04
12LF250A	629983.31	7392701.5	0.04
12LF251A	629969.94	7392698.5	0.07
12MJB039A	624018.25	7377124.5	0.08
12MJB040A	623978.06	7377001.5	0.13
12MJB044A	624265	7376940	0.01
12MJB097A	633456.81	7394687	2.0
12MJB098A	634008.44	7393376.5	1.1
12MJB098B	635094.81	7393582.5	0.5
12RN183A	623771.06	7377972	0.01
12RN184A	623743.81	7377972	0.07
12RN184B	623775.63	7377976.5	0.02
12RN185A	623775.63	7378004	0.01
12RN186B	623757.44	7377995	0.01
12RN187A	624044.88	7377341	0.08
12RN188B	624031.38	7377382	0.01
12RN356A	631719.44	7393101.5	0.07
12RN357A	632372.38	7393326	0.11
12RN366A	610113.5	7368785.5	1.0
12RN367A	604605.38	7373695.5	5.0
12RN368B	604076.13	7374843.5	0.1
12RN369A	603872	7376911.5	5.0
12RN370A	603086.63	7375629.5	6.2
12RN370B	603078.13	7375672	2.5
12RN372A	601002.5	7378655.5	9.0
12RN450A	624822.5	7396207	0.02
Average Magnetic Susceptibility of the Kanuti Pluton			**1.07**

Notes: "MS" = magnetic susceptibility (x 10^{-3} SI). Northing and easting reported for UTM Zone 5.

Table C-3. Average magnetic susceptibilities for unaltered granites from the Hot Springs East pluton

Sample	Easting	Northing	Average MS
12LF057A	623972.44	7359612	0.8
12LF058B	624991.25	7358177	0.11
12LF059A	624697.06	7358148	0.11
12LF060A	624643.13	7358142	0.11
12LF061B	625680.19	7359126	0.11
12LF063A	625680.19	7359114.5	0.11
12LF064A	625668.44	7359120.5	0.05
12LF066A	625574.63	7359236	0.05
12LF067A	625592.31	7359247.5	0.11
12LF070B	626861.88	7359176	0.87
12LF071A	627208.63	7360319.5	0.2
12LF320A	626687.94	7359049	0.66
12LF320B	626692.44	7359077.5	0.14
12LF327A	626331	7359518	0.14
12LF328C	626604.69	7359464.5	0.03
12LF331A	627126.25	7360737.5	0.4
12RN121B	619895.38	7363177	0.45
12RN121D	619789.75	7363206	9.0
12RN122A	619817.25	7362285	2.5
12RN123A	619825.13	7362269	3.0
12RN124A	620217.69	7361805	0.04
12RN125B	620195.75	7361805	2.0
12RN127A	620859.38	7361758	2.0
12RN128A	620897.88	7361789	0.02
12RN475A	619358.56	7362690.5	1.0
12RN476B	617233.44	7363268	0.2
12RN476C	617233.44	7363286	1.4
12RN477B	617233.44	7363292	2.0
12RN479A	617257.44	7363286	2.0
12RN480A	615154.56	7364337	0.8
12RN483A	614687.81	7363771	0.8
12RN483B	614716.31	7363671	2.0
12RN484A	614666.38	7363792.5	0.3
12RN484B	614666.38	7363742.5	0.4
Average Magnetic Susceptibility of the Hot Springs E Pluton			**1.0**

Notes: "MS" = magnetic susceptibility (x 10^{-3} SI). Northing and easting reported for UTM Zone 5.

Table C-4. Average magnetic susceptibilities for unaltered granites from the Hot Springs West pluton

Sample	Easting	Northing	Average MS
12LF026A	592204.75	7361273	0.04
12LF031A	592669.88	7359987	0.03
12LF033A	593980.81	7355293	0.05
12LF036A	593844.69	7355364.5	0.03
12LF039A	593833.88	7355391.5	0.03
12LF040A	593836.75	7355426	0.05
12LF041A	593149.38	7357477.5	0.05
12LF042A	594267.19	7356609.5	0.04
12LF045A	594317.19	7356702.5	0.02
12LF046C	594720.75	7357582	0.04
12LF048A	594671.5	7357593	0.03
12LF048C	594693.38	7357576.5	0.12
12LF051B	594709.81	7357593	0.04
12LF052A	594720.75	7357636.5	0.05
12LF053A	596419.19	7359561	0.06
12LF054A	596006.88	7357454.5	0.1
12LF055A	595922.19	7357566.5	0.11
12LF056A	594781.88	7360333	0.03
12RN078A	591789.81	7361700	1.04
12RN079A	593110.06	7359439	0.02
12RN085A	593180	7359027	0.03
12RN088A	593181.44	7359155.5	0.02
12RN089B	593194.25	7359122	0.02
12RN095A	603800	7363119	0.07
12RN097A	603358.38	7362650.5	0.3
12RN098A	603350.31	7362663	0.05
12RN099A	603750.94	7361848	0.05
12RN100A	603756.94	7361836	0.07
12RN101A	603821.44	7361521.5	0.3
12RN101B	603830.44	7361528.5	0.9
12RN102A	603696.38	7361141.5	0.33
12RN103A	604079.88	7360920	0.2
12RN104A	604048.94	7360920	0.4
12RN105A	604501.69	7362260.5	0.2
12RN105B	604446.75	7362212.5	0.17
12RN107A	609606.19	7366037	0.06
12RN108B	609602.88	7366010.5	0.06
12RN109A	609629.5	7366033.5	0.05
12RN111A	609334.56	7366424.5	0.05
12RN113A	609763.69	7365034.5	0.21
12RN114A	609741.38	7365034.5	0.2
12RN115A	609864.75	7364820	0.3

Table C-4 continued. Average magnetic susceptibilities for unaltered granites from the Hot Springs West pluton

Sample	Easting	Northing	Average MS
12RN117A	609464.06	7364606	0.55
12RN118A	609506.19	7364635.5	0.35
12RN364A	613461.63	7362575.5	0.3
12RN365A	611946.63	7364345.5	1.1
12RN365B	611916.75	7364309.5	0.34
Average Magnetic Susceptibility of the Hot Springs W Pluton			**0.18**

Notes: "MS" = magnetic susceptibility (x 10^{-3} SI). Northing and easting reported for UTM Zone 5.

Table C-5. Average magnetic susceptibilities for unaltered granites from the Coal Creek pluton

Sample	Easting	Northing	Average MS
12LF141A	627824	7352871.5	0.06
12LF143A	627200.44	7353076	0.1
12LF143A	626998	7353207	0.08
12LF144B	627185.06	7353122.5	0.4
12LF145B	628502.75	7352185	0.12
12LF145C	628441.13	7352220.5	0.39
12LF149A	628477.13	7352246.5	0.08
12RN220A	626743.81	7350062	0.05
12RN221A	626446.44	7350246.5	0.06
12RN221B	626417.13	7350246.5	0.09
12RN222A	626446.44	7350276	0.01
12RN224A	626654.13	7349533.5	0.04
12RN225A	626667.94	7349516	0.02
12RN226A	626647.19	7349516	0.06
12RN227A	626650.63	7349488.5	0.06
12RN228A	626654.13	7349534	0.07
Average Magnetic Susceptibility of the Coal Creek Pluton			**0.11**

Notes: "MS" = magnetic susceptibility (x 10^{-3} SI). Northing and easting reported for UTM Zone 5.

Table C-6. Average magnetic susceptibilities for unaltered granites from the No Name Creek pluton

Sample	Easting	Northing	Average MS
12LF227A	632741.81	7336306	0.06
12LF227B	632732.25	7336318	0.12
12LF228A	632763.31	7336280	0.1
12LF234A	632875.94	7336218.5	0.16
12LF236A	632661.63	7336362.5	0.13
12LF304A	632806.69	7336291.5	0.06
12RN318A	637649.5	7339672.5	0.02
12RN319A	637723.19	7341166.5	0.06
12RN319B	637773.75	7341175	0.03
12RN320A	637236.81	7340244	0.03
12RN326A	635166	7339728.5	0.03
12RN326B	635180.44	7339730	0.02
12RN326C	635183.31	7339731.5	0.03
12RN326D	635170.31	7339722.5	0.05
12RN336A	632099.94	7337435	0.04
12RN337A	631919.81	7337463.5	0.05
12RN337B	631907	7337447.5	0.05
13AT134A	632346.7642	7334665.478	0.01
13AT134B	632340.3887	7334660.011	0
13AT135A	633423.1991	7335025.274	0.04
13LF411A	633018.0463	7334691.138	0
13LF412A	633023.312	7334867.508	0.05
13LF412C	633023.5441	7334867.413	0
13LF413A	631826.5048	7337063.439	0.06
13LF414A	633398.3295	7336680.032	0.08
13LF415A	632036.4463	7337128.009	0.07
13RN553A	631846.6614	7336996.007	0.03
13RN554A	632173.4323	7336895.603	0.07
13RN555A	632274.0753	7336824.604	0.1
13RN555B	632298.1498	7336785.979	0.05
13RN556A	632363.6714	7336682.156	0.05
13RN557A	632421.3759	7336465.438	0.05
13RN558A	632520.0868	7336258.965	0.05
13RN558B	632520.0868	7336258.965	0.04
Average Magnetic Susceptibility of the No Name Creek Pluton			**0.05**

Notes: "MS" = magnetic susceptibility (x 10^{-3} SI). Northing and easting reported for UTM Zone 5.

Table C-7. Average magnetic susceptibilities for the Fort Hamlin Hills pluton

Sample	Easting	Northing	Average MS
12LF343A	628872.06	7328612.5	0.12
12RN437A	641171	7324830	0.04
12RN437B	641141	7324820	0.03
12RN439A	641164	7324830	0.02
12RN439B	641161	7324840	0.02
12RN439C	641161	7324830	0.02
12RN441A	640444	7324990	0.03
12RN442B	639237	7325830	0.03
12RN443A	639220	7325800	0.03
12RN459A	644507.56	7327271.5	0.04
12RN460A	644523.25	7327245.5	0.09
12RN461B	644450.19	7327292.5	0.03
12RN461C	644549.31	7327271.5	0.06
12RN462A	644523.25	7327266	0.08
12RN463A	644533.69	7327276.5	0.06
12RN464A	645209.5	7327858.5	0.06
12RN464B	645204.31	7327806.5	0.09
12RN465A	645285.19	7328451	0.09
12RN466A	645180.81	7328825	0.12
12RN467A	645163.63	7328821.5	0.095
12RN468A	644564.56	7329287	0.11
12RN469A	644542.94	7329265.5	0.1
12RN470A	644177.75	7329307	0.11
12RN471A	643733.19	7329696	0.1
12RN471B	643739.56	7329680	0.04
12RN472A	643104.94	7330770	0.12
12RN473A	642905	7330643.5	0.1
12RN474A	642342.13	7330714	0.11
12RN485A	641791.56	7330816	0.09
12RN486A	641116.69	7331449	0.09
12RN487A	640190.38	7331949.5	0.1
12RN488A	640180.31	7332080	0.07
12RN490A	638878.81	7331981	0.01
Average Magnetic Susceptibility of the Fort Hamlin Hills Pluton			**0.07**

Notes: "MS" = magnetic susceptibility (x 10^{-3} SI). Northing and easting reported for UTM Zone 5.

Table C-8. Average magnetic susceptibilities for average granites from the Ray River pluton

Sample	Easting	Northing	Average MS
12LF103A	616210.81	7323157	0.04
12LF104A	616214.81	7323109	0.09
12LF105B	616202.75	7323117	0.11
12LF107A	617141.88	7322487	0.07
12LF108A	617093.69	7322511	0.05
12LF109A	617096.88	7322252	0.05
12LF110A	617120.75	7322198	0.06
12LF111A	617335.44	7321719	0.12
12LF113A	617599.63	7321683	0.07
12LF114A	617599.63	7321674.5	0.07
12LF256A	615160.69	7328790.5	0.08
12LF258A	615239.31	7328985.5	0.08
12LF259A	614984.88	7329848	0.1
12LF261B	614933.75	7329824.5	0.07
12LF262A	615372.75	7329500.5	0.09
12RN176A	617975.38	7327349	0.01
12RN347A	614883.5	7330993	0.03
12RN348C	615094.38	7328551	0.02
12RN348D	615085.38	7328558	0.04
12RN349A	615227.88	7328911	0.03
12RN350A	615231.13	7328901.5	0.04
12RN352D	615224.63	7328917.5	0.05
12RN353B	615187.31	7329380	0.05
12RN377B	614398.13	7329091	0.04
12RN380A	614347	7327925.5	0.05
12RN381A	614315.13	7327900	0.03
12RN382A	613524.06	7327104	0.05
12RN382B	614479.56	7326269.5	0.03
12RN383A	614481.75	7326258.5	0.05
12RN384A	614263.94	7326139.5	0.05
12RN385A	613646.63	7325916.5	0.05
12RN386A	613992.25	7325513	0.05
12RN389A	614043.94	7323861.5	0.05
12RN390A	613854.19	7323052	0.05
12RN407A	611650.38	7327983.5	0.03
12RN407B	611589.06	7327929	0.04
12RN410B	611550.88	7326485.5	0.03
12RN410C	611615.38	7326505	0.04
12RN412A	609224.25	7328399.5	0.03
12RN412B	609208.69	7328244	0.02
12RN415A	612810.31	7328598	0.05
12RN415B	612824.44	7328590.5	0.15

Table C-8 continued. Average magnetic susceptibilities for average granites from the Ray River pluton

Sample	Easting	Northing	Average MS
12RN416A	613203.25	7327898.5	0.04
12RN418A	612905	7328582	0.05
12RN420A	610954.31	7325996	0.02
12RN421A	610953.38	7325778	0.03
12RN423A	609600.75	7326607	0.04
12RN424A	608597.56	7327527.5	0.04
12RN424B	608677.56	7327539.5	0.04
12RN424C	608717.63	7328521.5	0.03
12RN425A	608862.44	7327089	0.02
12RN426A	608898	7328710.5	0.05
12RN426B	608929.13	7328723	0.05
12RN427A	609243.75	7329121.5	0.05
12RN427B	609259.88	7329081	0.09
12RN428A	609273.94	7329494	0.03
12RN429A	609522.94	7329078	0.06
Average Magnetic Susceptibility of the Ray River Pluton			**0.05**

Notes: "MS" = magnetic susceptibility (x 10^{-3} SI). Northing and easting reported for UTM Zone 5.

Table C-9. Average magnetic susceptibility for unaltered granites from the Sithylemenkat pluton

Sample	Easting	Northing	Average MS
12CW004B	584057.81	7324272	0.05
12EB077A	585102.81	7323567	0.035
12EB078A	585115.75	7323573.5	0.07
12EB081A2	586909.63	7324936	0.045
12LF011C	583950	7325920	0.11
12LF012B	582321	7326770	0.09
12LF014B	577614.75	7336170.5	0.05
12LF015B	577622.13	7336163	0.11
12LF016A	577541.06	7336200	0.08
12LF017B	577504.19	7336170.5	0.09
12LF018B	578477.5	7335565.5	0.09
12LF019B	578224.94	7335962.5	0.07
12LF020A	578153.75	7334949.5	0.05
12LF022A	574835.44	7335637.5	0.07
12LF129A	591681.19	7328341.5	0.07
12LF130A	591699.81	7328335.5	0.09
12LF150A	587896.19	7328437.5	0.05
12LF151B	589930.5	7328958.5	0.08
12LF152B	587709.88	7327580.5	0.05
12LF153C	590107	7328995.5	0.04
12LF154B	587721.38	7327415.5	0.06
12LF155A	587691.25	7327602.5	0.03
12LF155C	587685.13	7327621	0.07
12LF155D	587706.63	7327605.5	0.06
12LF156A	587373.63	7327108	0.07
12LF157A	586695.44	7327535	0.06
12LF158A	586986.81	7327875.5	0.07
12LF270A	587441.81	7323335.5	0.1
12LF271A	587516.5	7322707	0.08
12LF275A	587440.56	7322955	0.07
12LF276A	588480.06	7322022.5	0.07
12LF277A	588031.63	7322601.5	0.08
12LF278B	588650.44	7322081.5	0.06
12LF279A	588616.06	7322116	0.08
12LF279B	588630.81	7322086.5	0.05
12LF280A	588898.63	7321804	0.06
12LF281A	588908.5	7321759.5	0.19
12LF283A	589616	7321290.5	0.09
12LF284A	595903.63	7329418	0.07
12LF287A	594570	7318435.5	0.07
12MJB004A	569254.63	7342376.5	0.13
12MJB005A	578414.19	7335475	0.08

Table C-9 continued. Average magnetic susceptibilities of unaltered granites from the Sithylemenkat pluton

Sample	Easting	Northing	Average MS
12MJB006C	583973.31	7323698	0.06
12MJB007B	583908.63	7323456.5	0.08
12MJB049B	590198.63	7330312	0.07
12RN049B	583860	7324220	0.07
12RN065A	577195.69	7337809	0.07
12RN066A	577413.88	7336438.5	0.05
12RN067B	577435.38	7336415	0.05
12RN068B	577423.63	7336442.5	0.02
12RN068C	577413.88	7336428.5	0.02
12RN070C	577280.19	7336118	0.04
12RN073A	576957.44	7336220.5	0.02
12RN073B	576966.56	7336228	0.06
12RN074A	576212.81	7335781	0.06
12RN196A	591663.06	7328015.5	0.03
12RN196B	591663.06	7328001.5	0.01
12RN197A	591700.19	7328034	0.03
12RN199B	591057.06	7327841	0.05
12RN200B	591061.69	7327781	0.02
12RN201C	591057.06	7327799.5	0.03
12RN202A	591126.69	7327785.5	0.05
12RN203A	591117.44	7327827.5	0.02
12RN208B	590864.94	7327203.5	0.02
12RN230A	585552.69	7323179.5	0.03
12RN232A	585551.25	7323165	0.02
12RN237A	585075.69	7324863.5	0.03
12RN240C	584955.19	7325473.5	0.07
12RN240D	585008.69	7325405.5	0.02
12RN241A	584955.19	7325464	0.05
12RN242A	584955.19	7325449	0.03
12RN243A	585028.81	7326241.5	0.02
12RN244A	584889	7326825	0.02
12RN245B	584055.56	7328404	0.01
12RN245C	584125.81	7328263.5	0.01
12RN246A	591593.75	7325357.5	0.04
12RN247A	591314.75	7325190.5	0.04
12RN250A	590933.88	7325298.5	0.02
12RN256A	590161.44	7326249	0.04
12RN341A	577094.5	7336692.5	0.06
12RN342A	576894.31	7336388.5	0.02
12RN344A	583933.5	7324132.5	0.05
12RN391A	593568.69	7326073	0.05
12RN393A	592907.13	7325661	0.05

Table C-9 continued. Average magnetic susceptibilities of unaltered granites from the Sithylemenkat pluton

Sample	Easting	Northing	Average MS
12RN395A	593373.06	7324851	0.03
12RN395B	593349.38	7324852.5	0.05
12RN397B	593743.25	7328373.5	0.05
12RN398B	593154.81	7325613	0.05
12RN399A	594187.5	7325230.5	0.06
12RN400A	595364	7325083.5	0.05
12RN401A	595490.25	7325159.5	0.05
12RN402A	596050.81	7324876.5	0.03
12RN403A	595598.31	7324774	0.05
12RN404B	596206.38	7324530.5	0.03
12RN404C	596219.25	7324525	0.05
12RN405B	596102.69	7324557	0.05
12RN406A	596162.94	7323481	0.06
Average Magnetic Susceptibility of the Sithylemenkat Pluton			**0.05**

Notes: "MS" = magnetic susceptibility (x 10^{-3} SI). Northing and easting reported for UTM Zone 5.

Table C-10. Average magnetic susceptibilities for unaltered granites from the Ray Mountains East pluton

Sample	Easting	Northing	Average MS
12LF098A	598269.25	7299768	0.09
12LF099A	589603.5	7290800	0.04
12LF208A	591959.31	7291146	0.09
12LF183A	567382.25	7291371	0.06
12LF186A	566799.94	7291858	0.1
12LF181B	567087.13	7291951	0.05
12LF191B	567270.44	7292008	0.05
12LF194A	566622.13	7292199	0.12
12LF197B	593601.25	7293971	0.04
12LF199C	592146.63	7294009.5	0.07
12LF097A	586308.31	7295984.5	0.035
12LF203A	594131	7297541	0.08
12LF212A	581131.5	7301653	0.08
12RN306C	585115	7302507	0.05
12LF211A	580625.25	7302566	0.08
12RN305A	584778.19	7303621	0.02
12RN268A	569265.38	7290058	0.02
12RN272A	569187.25	7290214.5	0.01
12RN283C	571345.13	7291106	0.03
12RN280C	571326	7291113.5	0.04
12RN281B	571333.63	7291121.5	0.02
12RN282C	571341.25	7291159.5	0.04
12RN278A	570940.06	7291196.5	0.02
12RN277B	570977.38	7291202.5	0.04
12RN277A	570865.5	7291221	0.05
12RN285B	572432.19	7291494	0.03
12RN284B	571954.75	7291803.5	0.03
12RN288B	571834.69	7292453	0.01
12RN289A	571624.75	7293218.5	0.05
12RN304B	588988.81	7293264.5	0.03
12LF202A	594577.19	7297257	0.04
12RN170D	584115.88	7289695	0.05
12RN267A	569310.56	7290005.5	0.05
12RN273B	569118.88	7290258	0.04
12RN276A	569156.19	7290301.5	0.07
12RN266A	568895.5	7290637.5	0.05
12RN166B	583409.56	7290761	0.06
12LF171A	566857.38	7292034.5	0.08
12RN288C	571839.19	7292444	0.03
12RN308B	591506.06	7292463	0.06
12RN286A	571785	7292466.5	0.05
12RN290A	568158.69	7292618.5	0.06
12RN294A	568022.88	7292694	0.07

Table C-10 continued. Average magnetic susceptibilities for unaltered granites from the Ray Mountains East pluton

Sample	Easting	Northing	Average MS
12RN291A	568019.13	7292720	0.06
12RN292B	568079.44	7292735.5	0.07
12RN304C	588988.81	7293276.5	0.04
12MJB038A	586124.63	7294226.5	0.03
12RN313B	583011.38	7303010	0.04
12RN314A	582975.75	7303090	0.04
12LF211B	580558.25	7302544	0.09
12EB053A	582790.13	7291198.5	1.2
Average Magnetic Susceptibility of the Ray Mountains E Pluton			**0.07**

Notes: "MS" = magnetic susceptibility (x 10^{-3} SI). Northing and easting reported for UTM Zone 5.

Appendix D. Chemical Analyses of Bulk-Granite Samples

Table D-1. Chemical analyses of bulk-granite samples from the Ruby batholith area

Sample			12LF304A	12LF305A	12RN348D	12RN343A	12RN341A	12CW118A	12LF344A	12RN344A
Pluton			NNC	Kanuti	RR	Sith	Sith	FHH	RME	Sith
Rock Type			Gr	Gr	Ms Greisen	Chl Greisen	Gr	Gr	Gr	Gr
Easting			632806.69	616652	615103	584025	577095	637279	558237	583934
Northing			7336291.5	7402200.5	7328587	7323960	7336693	7328675	7301337	7324133
Y	LiB	ppm	443	74.3	140.5	113.5	573	115	106	116.5
La	4AD	ppm	150	90	160	110	1370	290	340	420
La	LiB	ppm	172.5	90.8	169.5	189.5	1450	316	385	468
Ce	LiB	ppm	407	181.5	432	371	2930	611	776	932
Pr	LiB	ppm	45.8	19.2	54.4	40.1	328	63.1	80.9	99.4
Nd	LiB	ppm	162.5	67.8	207	137.5	1115	213	275	336
Sm	LiB	ppm	39.2	15.65	50.2	21.9	192	32.8	40.1	46.7
Eu	LiB	ppm	0.54	0.49	0.15	1.48	1.31	1.03	1.14	1.15
Gd	LiB	ppm	43	14	34.1	15.85	134	24.3	23.9	27.7
Dy	LiB	ppm	68.2	13	27.5	15.7	101	20.9	17.4	19.45
Ho	LiB	ppm	14.55	2.53	4.77	3.5	18.55	4.16	3.35	3.62
Er	LiB	ppm	49.4	7.06	13.9	12.3	55.9	12.8	10.7	11.65
Tm	LiB	ppm	8.24	1.05	2.2	2.25	8.98	1.91	1.77	1.98
Tb	LiB	ppm	9.54	2.22	5.09	2.58	19.2	3.78	3.35	3.69
Yb	LiB	ppm	53.3	7.01	15.35	17.65	61.8	12.7	12.95	14.65
Lu	LiB	ppm	7.63	1.03	2.11	2.91	9.28	1.9	2.13	2.48
P	4AD	ppm	730	570	280	770	2070	690	1120	1050
Th	4AD	ppm	130	70	160	150	680	140	190	210
Th	LiB	ppm	131	66.1	144.5	195.5	677	136	184.5	213
Au		ppb	10	6350	4	119	595	10	10	59
Ag	4AD	ppm	<0.5	<0.5	<0.5	69.6	<0.5	<0.5	<0.5	<0.5
Al	4AD	wt%	6.17	5.81	6.2	6.95	6.49	6.14	6.36	6.29
As	4AD	ppm	<5	136	<5	32	12	12	<5	7
Ba	4AD	ppm	70	330	20	360	270	320	280	270
Ba	LiB	ppm	79.7	327	17.4	383	289	341	297	294
Be	4AD	ppm	22.1	3.6	9.3	2.7	8.2	5.2	6.5	6.4
Bi	4AD	ppm	<2	4	16	57	3	2	<2	<2
Ca	4AD	wt%	0.38	0.54	0.19	3.21	1.12	1.19	1.29	1.27

Table D-1 cont. Chemical analyses of bulk granite samples from the Ruby batholith area.

Sample			12LF304A	12LF305A	12RN348D	12RN343A	12RN341A	12CW118A	12LF344A	12RN344A
Cd	4AD	ppm	<0.5	<0.5	<0.5	1.9	<0.5	<0.5	<0.5	<0.5
Fe	4AD	wt%	2.7	1.83	0.98	15.25	3.28	2.83	1.94	1.91
K	4AD	wt%	2.75	3.14	3.19	3.09	3.16	3.25	3.33	3.17
Mg	4AD	wt%	0.11	0.08	0.03	0.27	0.3	0.27	0.25	0.18
Na	4AD	wt%	2.05	1.75	2.52	0.26	2.08	1.92	2.01	2.01
S	4AD	wt%	0.03	0.03	0.01	0.05	0.07	0.02	0.02	0.01
Ti	4AD	wt%	0.1	0.05	0.04	0.43	0.77	0.43	0.26	0.26
Co	4AD	ppm	3	1	1	6	4	4	3	3
Cr	4AD	ppm	13	13	5	3	8	44	8	36
Cr	LiB	ppm	20	10	10	10	10	70	10	60
Cs	LiB	ppm	32.3	6.8	26.6	11.25	51.6	12.55	13.95	10.35
Cu	4AD	ppm	15	8	10	293	33	6	8	9
Ga	4AD	ppm	20	10	20	40	20	20	20	20
Ga	LiB	ppm	26.6	14.7	21	35.1	32.6	22	21.2	19.2
Hf	LiB	ppm	55.6	2.9	13.4	131.5	129.5	70	82.6	98.9
Mn	4AD	ppm	401	1910	326	7030	1060	538	463	468
Mo	4AD	ppm	2	1	1	117	1	4	1	3
Nb	LiB	ppm	61.7	14.2	35.4	85.4	86.3	38.2	29.6	30.7
Ni	4AD	ppm	2	1	2	<1	3	1	1	2
Pb	4AD	ppm	29	36	102	15050	62	35	48	59
Rb	LiB	ppm	424	188	492	329	354	262	277	250
Sb	4AD	ppm	<5	<5	<5	<5	<5	<5	<5	<5
Sc	4AD	ppm	7	3	3	4	7	7	4	3
Sr	4AD	ppm	32	64	14	55	114	100	144	147
Sr	LiB	ppm	31.6	59.6	10.7	51.3	88.6	98.8	139	143
Ta	LiB	ppm	21.7	2.5	8.4	11.5	14.9	5	3.5	3.9
Tl	LiB	ppm	1.7	1	2	2.5	1.9	1.2	1.1	0.9
U	4AD	ppm	<10	<10	<10	40	<10	20	<10	<10
U	LiB	ppm	37.3	11.75	25.3	73.5	88	45.7	24.4	28.3
V	4AD	ppm	10	3	2	19	16	28	20	16
V	LiB	ppm	16	<5	<5	28	24	37	26	21
W	4AD	ppm	310	<10	900	10	80	<10	140	90
Zn	4AD	ppm	34	36	27	1305	93	57	36	27

Notes: "4AD" = four-acid digestion, "LiB" = lithium borate fusion digestion, "Sith" = Sithylemenkat, "Gr" = granite, "Ms" = muscovite, "Chl" = chlorite. Northing and Easting reported for UTM Zone 5. Refer to p. 11-12 for procedure.

Appendix E. Chemical Compositions of Allanite

Table E-1. Chemical compositions of allanite from the Bonanza pluton

Grain 1	**Sample: 12RN375A**				Base: 10(1)	
Anhedral; 30 microns; no obvious zoning						
	No systematic point collection					
Points	1-3	StDev	4-6	StDev	7-9	StDev
MgO	--	--	--	--	--	--
Al_2O_3	17.3	0.3	15.4	0.2	15.63	0.08
SiO_2	32.7	0.1	32.0	0.2	30.5	0.3
CaO	14.5	0.1	12.1	0.3	11.4	0.2
TiO_2	2.2	0.3	0.9	0.1	1.63	0.07
MnO	0.77	0.05	1.1	0.1	1.1	0.1
Fe_2O_3	13.1	0.3	15.0	0.3	15.2	0.2
Y_2O_3	--	--	--	--	3.13	0.07
La_2O_3	2.66	0.05	4.4	0.3	3.0	0.2
Ce_2O_3	10.1	0.2	12	0.5	10.5	0.3
Pr_2O_3	1.9	0.1	1.9	0.1	1.9	0.2
Nd_2O_3	4.0	0.2	4.0	0.6	4.4	0.1
Sm_2O_3	0.52	0.08	0.48	0.03	--	--
ThO_2	0.33	0.02	0.54	0.07	1.2	0.1
Note: Refer to p. 14 for procedure.						

Table E-1 (continued). Chemical compositions of allanite from the Bonanza pluton

Grain 2	**Sample: 12RN375B**						Base: A1(1)	
Eu-to-subhedral; 500 microns; oscillatory zoning								
	Core		Core-Interior		Interior-Rim		Rim	
Points	2-4	StDev	5-7	StDev	8-10	StDev	11-13	StDev
MgO	--	--	--	--	--	--	--	--
Al_2O_3	16.8	2.8	19.3	2.8	15.8	2.7	18.0	2.8
SiO_2	24.8	1.1	25.3	0.6	26.1	1.1	26.0	1.2
P_2O_5	4.3	0.5	3.8	0.3	4.8	1.1	4.8	0.9
CaO	8.0	0.8	8.0	0.8	8.5	0.2	7.5	0.8
TiO_2	2.9	0.4	2.5	0.2	2.50	0.09	2.6	0.1
MnO	--	--	--	--	--	--	--	--
Fe_2O_3	16.2	1.6	15.4	1.2	14.9	0.8	17.1	0.2
La_2O_3	5.0	0.4	4.8	0.4	5.6	0.2	5.0	0.3
Ce_2O_3	11.8	0.9	10.9	1.0	12.3	0.5	10.4	0.9
Pr_2O_3	2.4	0.1	2.3	0.2	2.1	0.3	2.0	0.2
Nd_2O_3	2.8	0.3	2.3	0.3	2.4	0.2	1.8	0.2
Sm_2O_3	--	--	--	--	--	--	--	--
ThO_2	2.8	0.1	2.7	0.1	3.2	0.3	3.3	0.4

Table E-1 (continued). Chemical compositions of allanite from the Bonanza pluton						
Grain 3		**Sample: 12RN375B**			Base: A2(1)	
Euhedral; 350 microns; oscillatory zoning						
	Left Rim		Interior		Top Rim	
Points	1-3	StDev	4-6	StDev	7-9	StDev
MgO	--	--	--	--	--	--
Al_2O_3	16.9	2.6	14.8	0.2	16.3	0.7
SiO_2	21.9	0.3	24.2	1.0	22.8	0.7
P_2O_5	6.2	0.5	5.60	0.03	7.4	0.2
CaO	6.8	0.8	7.76	0.07	6.7	0.2
TiO_2	2.86	0.07	2.6	0.1	2.8	0.1
Fe_2O_3	21.2	0.7	18.6	0.6	23.2	1.2
La_2O_3	4.3	0.8	5.2	0.3	4.5	0.2
Ce_2O_3	9.9	1.1	12.1	0.2	8.7	0.4
Pr_2O_3	1.9	0.2	2.2	0.1	1.8	0.3
Nd_2O_3	2.3	0.1	2.38	0.08	1.7	0.3
Sm_2O_3	--	--	--	--	--	--
ThO_2	4.6	0.3	4.1	0.4	4.1	0.5

Table E-1 (continued). Chemical compositions of allanite from the Bonanza pluton								
Grain 4			**Sample: 12RN375B**				Base: A3(1)	
	Allanite 1 Euhedral; 300 microns; no obvious zoning		Allanite 2 Eu-to-subhedral; 500 microns; no obvious zoning				Allanite 3 Subhedral; 300 microns; no obvious zoning	
			Rim		Core			
Points	1-3	StDev	8-10	StDev	11-13	StDev	14-16	StDev
MgO	2.9	0.4	3.1	0.2	2.9	0.2	2.91	0.09
Al_2O_3	17.3	1.0	16.2	0.8	16.5	0.3	16.4	0.5
SiO_2	21.6	1.5	26.2	0.5	22.0	1.1	20.6	1.5
P_2O_5	5.6	0.5	3.1	0.3	5.6	0.7	6.2	0.6
CaO	6.1	0.4	7.0	0.2	6.0	0.6	5.1	0.3
TiO_2	2.0	0.2	2.33	0.02	2.5	0.3	2.5	0.2
Fe_2O_3	25.3	3.6	17.4	0.7	24.3	2.2	30.0	2.3
La_2O_3	4.2	0.3	5.2	0.4	4.0	0.4	2.6	0.5
Ce_2O_3	8.4	0.8	12.7	0.6	9.4	1.1	7.0	0.9
Pr_2O_3	1.6	0.3	2.3	0.1	1.7	0.3	1.4	0.3
Nd_2O_3	1.5	0.2	1.93	0.04	1.7	0.1	1.55	0.09
Sm_2O_3	--	--	0.3	0.1	0.16	0.06	--	--
ThO_2	3.5	0.5	2.3	0.2	3.3	0.3	3.8	0.4

Table E-2. Chemical compositions of allanite from the Kanuti pluton						
Grain 1			**Sample: 12LF002A**		Base: 2(1)	
Euhedral; 300 microns; oscillatory zoning						
	Left Rim		Core		Right Rim	
Points	2-4	StDev	5-7	StDev	8-10	StDev
MgO	1.13	0.03	1.1	0.2	1.2	0.2
Al_2O_3	10.8	0.1	15.8	0.3	15.91	0.09
SiO_2	26.9	0.2	32.7	0.3	32.9	0.5
CaO	16.9	0.1	9.0	0.1	9.3	0.3
TiO_2	4.52	0.06	2.5	0.2	2.4	0.2
Fe_2O_3	11.6	0.3	15.4	0.2	15.4	0.3
Y_2O_3	--	--	--	--	--	--
La_2O_3	3.6	0.2	5.2	1.1	5.4	0.6
Ce_2O_3	9.8	0.3	12.1	0.3	11.5	0.4
Pr_2O_3	4.7	0.2	1.3	0.4	1.0	0.3
Nd_2O_3	1.8	0.1	2.2	0.5	2.1	0.4
Sm_2O_3	0.93	0.05	0.17	0.06	--	--
ThO_2	1.4	0.1	2.6	0.2	2.77	0.09

Table E-2 (continued). Chemical compositions of allanite from the Kanuti pluton												
Grain 2			**Sample: 12LF002A**				Base: 5(2)					
Subhedral; fragmented; 150 microns; oscillatory zoning												
	Right Rim		Interior-Rim		Core		Core-Interior		Left Rim		Top Rim	
Points	1-3	StDev	4-6	StDev	7-9	StDev	10-12	StDev	16-18	StDev	13-15	StDev
MgO	0.8	0.1	0.82	0.02	1.03	0.2	0.98	0.02	0.5	0.1	0.55	0.01
Al_2O_3	15.8	0.2	15.1	0.2	15.41	0.3	14.5	0.1	15.96	0.03	15.06	0.09
SiO_2	34.7	0.6	33.4	0.1	33.62	0.3	35.6	0.5	33.5	0.3	35.2	0.5
CaO	9.80	0.06	9.59	0.02	9.59	0.1	8.9	0.1	10.2	0.2	9.8	0.1
TiO_2	4.4	0.6	2.1	0.2	2.23	0.2	2.0	0.2	1.6	0.1	3.5	0.5
Fe_2O_3	16.0	0.4	15.5	0.1	15.18	0.2	16.6	0.3	18.1	0.6	15.0	0.2
Y_2O_3	--	--	--	--	--	--	--	--	--	--	--	--
La_2O_3	4.4	0.4	5.7	0.5	5.36	0.5	4.6	0.6	5.7	0.2	5.9	0.5
Ce_2O_3	8.7	0.2	11.0	0.2	11.15	0.2	10.2	0.4	9.5	0.2	9.6	0.6
Pr_2O_3	0.92	0.07	1.19	0.09	1.10	0.08	1.1	0.2	0.9	0.1	0.9	0.1
Nd_2O_3	1.14	0.09	2.52	0.08	2.09	0.1	1.8	0.2	1.29	0.03	1.1	0.1
Sm_2O_3	--	--	--	--	--	--	--	--	--	--	--	--
ThO_2	3.4	0.2	2.94	0.03	3.21	0.3	3.5	0.2	2.8	0.1	3.4	0.1

Table E-2 continued. Chemical compositions of allanite from the Kanuti pluton								
Grains 3, 4, 5				**Sample: 12LF246A**				
Base	1(12)		1(9)		1(8)			
	Allanite 1 Euhedral; <10 microns		Allanite 2 Anhedral; 75 microns; fragmented; no obvious zoning		Allanite 3 Subhedral; 40 microns; no obvious zoning			
Points	1-3	StDev	1-3	StDev	1-3	StDev	4-6	StDev
MgO	--	--	1.5	0.2	1.06	0.09	0.6	0.1
Al_2O_3	17.2	0.2	12.70	0.03	14.2	0.1	14.4	0.1
SiO_2	38.8	1.2	30.6	0.9	34.5	0.4	32.2	0.3
CaO	10.2	0.5	10.5	0.1	11.2	0.2	10.8	0.2
TiO_2	2.40	0.06	2.0	0.2	1.5	0.2	1.79	0.03
MnO	--	--						
Fe_2O_3	13.0	0.8	16.3	0.2	14.3	0.2	14.7	0.4
Y_2O_3	--	--	--	--	--	--	3.7	0.2
La_2O_3	2.1	0.2	6.3	0.8	5.8	0.9	6.1	0.1
Ce_2O_3	9.8	0.9	12.9	0.4	11.8	0.4	10.0	0.5
Pr_2O_3	1.2	0.6	1.25	0.04	1.6	0.2	1.3	0.1
Nd_2O_3	3.3	0.7	2.5	0.6	2.8	0.2	1.7	0.1
Sm_2O_3	1.1	0.2	--	--	--	--	--	--
ThO_2	0.46	0.05	1.4	0.2	1.1	0.2	2.7	0.2

Table E-2 (continued). Chemical compositions of allanite from the Kanuti pluton								
Grain 6			**Sample: 12LF246A**				Base: 1(13)	
Euhedral; Plucked; 100 microns; oscillatory zoning								
	Rim		Interior-Rim		Core-Interior		Core	
Points	1-3	StDev	4-6	StDev	7-9	StDev	10-12	StDev
MgO	1.0	0.1	--	--	--	--	1.20	0.05
Al_2O_3	11.8	0.3	15.0	0.3	13.8	0.4	13.5	0.1
SiO_2	30.4	0.7	36.2	0.6	31.5	0.4	32.0	0.3
CaO	8.01	0.07	10.7	0.3	10.2	0.1	12.3	0.2
TiO_2	2.9	0.1	1.9	0.2	2.24	0.03	1.46	0.07
Fe_2O_3	14.3	0.2	13.8	0.5	14.5	0.4	15.3	0.3
Y2O3	7.3	0.2	--	--	4.1	0.5	--	--
La_2O_3	4.8	0.3	5.8	0.3	6.1	0.3	6.1	0.4
Ce_2O_3	8.8	0.5	9.9	0.7	10.1	0.8	12.6	0.2
Pr_2O_3	1.26	0.02	1.20	0.05	1.4	0.2	1.5	0.2
Nd_2O_3	1.7	0.2	1.59	0.09	1.6	0.2	2.8	0.1
Sm_2O_3	--	--	--	--	--	--	0.20	0.03
ThO_2	7.58	0.05	2.6	0.3	3.97	0.08	1.2	0.2

Table E-3. Chemical compositions of allanite from the Hot Springs West pluton										
Grain 1			**Sample: 12LF054A**				Base: 5(1)			
Euhedral; 600 microns; oscillatory zoning										
			Left Rim → Core							
Points	3-5	StDev	6-8	StDev	9-11	StDev	12-14	StDev	15-17	StDev
MgO	0.52	0.2	--	--	--	--	--	--	--	--
Al_2O_3	12.6	0.4	11.8	0.4	12.0	0.4	11.8	0.1	12.0	0.1
SiO_2	31.5	0.4	33.5	1.1	31.6	0.5	31.8	0.4	31.9	0.5
CaO	8.06	0.09	7.2	0.2	7.8	0.3	7.7	0.2	8.26	0.02
TiO_2	3.21	0.05	3.6	0.2	3.72	0.03	3.7	0.1	3.53	0.08
Fe_2O_3	15.9	0.3	16.4	0.6	16.0	0.3	16.7	0.2	16.8	0.1
Y_2O_3	--	--	--	--	--	--	--	--	--	--
La_2O_3	6.79	0.05	5.9	0.2	7.0	0.4	6.61	0.06	6.6	0.4
Ce_2O_3	12.8	0.3	12.0	1.3	13.1	0.7	12.7	0.6	12.1	0.4
Pr_2O_3	2.0	0.5	1.9	0.6	1.8	0.4	1.6	0.1	1.6	0.1
Nd_2O_3	3.6	0.4	3.46	0.07	3.2	0.1	3.24	0.03	3.7	0.2
Sm_2O_3	--	--	--	--	--	--	0.27	0.04	--	--
ThO_2	2.9	0.2	4.0	0.2	3.4	0.1	3.7	0.3	3.3	0.3

Table E-3 (continued). Chemical composition of allanite from the Hot Springs West pluton								
Grain 1 (continued)			**Sample: 12LF054A**				Base: 5(1)	
Euhedral; 600 microns; oscillatory zoning								
			Core → Right Rim					
Points	18-20	SD	21-23	SD	24-26	SD	27-29	SD
MgO	--	--	--	--	--	--	--	--
Al_2O_3	11.6	0.1	12.0	0.3	12.1	0.5	11.2	0.4
SiO_2	31.5	0.2	31.1	0.8	31.5	0.2	32.4	0.6
CaO	7.3	0.1	7.6	0.3	8.5	0.4	7.5	0.2
TiO_2	3.9	0.1	4.0	0.3	3.2	0.2	4.13	0.08
Fe_2O_3	16.8	0.4	16.7	0.5	16.6	0.4	18.1	0.3
Y_2O_3	--	--	--	--	--	--	--	--
La_2O_3	6.0	0.2	6.0	0.3	7.3	0.6	6.2	0.4
Ce_2O_3	12.0	0.4	12.8	1.1	12.6	0.9	10.9	0.4
Pr_2O_3	2.0	0.3	1.9	0.4	1.5	0.4	1.2	0.2
Nd_2O_3	3.7	0.1	3.6	0.1	3.5	0.1	3.3	0.1
Sm_2O_3	--	--	--	--	--	--	--	--
ThO_2	4.9	0.2	3.9	0.09	2.7	0.3	5.0	0.4

Table E-3 (continued). Chemical composition of allanite from the Hot Springs West pluton												
Grain 2			**Sample: 12LF054A**				Base: 8(1)					
Plucked; euhedral; 200 microns; oscillatory zoning												
	Right Rim →								Core →		Bottom Rim	
Points	7-9	StDev	10-12	StDev	13-15	StDev	16-18	StDev	19-21	StDev	22-24	StDev
MgO	--	--	--	--	0.41	0.04	--	--	--	--	--	--
Al_2O_3	12.0	0.07	12.9	0.2	12.7	0.4	12.4	0.1	12.2	0.2	11.2	0.4
SiO_2	30.8	0.2	33.3	1.4	33.3	0.5	32.6	0.5	33.4	0.2	30.2	0.8
CaO	8.5	0.2	9.5	0.3	8.6	0.3	7.8	0.2	8.8	0.2	8.3	0.4
TiO_2	3.8	0.3	2.9	0.2	3.1	0.1	3.8	0.3	3.4	0.2	3.8	0.2
Fe_2O_3	16.8	0.5	16.0	0.4	16.1	0.5	17.5	0.5	17.0	0.1	17.8	0.5
Y_2O_3	2.6	0.3	--	--	--	--	--	--	--	--	--	--
La_2O_3	4.9	0.6	6.1	0.2	5.6	0.5	5.0	0.6	5.5	0.4	5.3	0.8
Ce_2O_3	12.3	0.3	12.9	0.2	13.4	0.8	11.3	0.8	12.9	0.3	12.4	0.3
Pr_2O_3	1.2	0.3	0.9	0.2	1.4	0.6	1.4	0.5	1.2	0.2	1.73	0.08
Nd_2O_3	2.4	0.5	1.9	0.2	2.5	0.7	3.1	0.6	2.4	0.4	3.39	0.04
Sm_2O_3	--	--	--	--	0.15	0.05	0.31	0.04	0.39	0.07	--	--
ThO_2	4.3	0.2	2.32	0.08	2.9	0.2	4.98	0.08	2.9	0.2	4.5	0.1

Table 3 (continued). Chemical composition of allanite from the Hot Springs West pluton										
Grain 3			**Sample: 12LF364A**				Base: 2(1)			
Euhedral; zoned; 400 microns										
					Core → Right Rim					
Points	1-3	StDev	4-6	StDev	7-9	StDev	10-12	StDev	16-18	StDev
MgO	0.46	0.09	--	--	--	--	--	--	--	--
Al_2O_3	12.62	0.05	13.4	0.3	12.9	0.1	12.5	0.4	13.8	0.3
SiO_2	30.8	0.1	32.4	0.5	32.4	0.1	32.3	0.8	33.3	1.1
CaO	9.0	0.8	7.6	0.2	8.1	0.5	7.79	0.02	8.8	0.1
TiO_2	2.8	0.2	3.2	0.2	3.3	0.1	3.71	0.05	2.65	0.07
Fe_2O_3	17.7	0.5	15.76	0.09	16.6	0.1	16.30	0.01	15.7	0.5
Y_2O_3	3.8	0.5	2.7	0.2	2.7	0.1	--	--	--	--
La_2O_3	4.6	1.2	4.3	0.3	4.6	0.7	4.8	0.1	4.9	0.1
Ce_2O_3	10.4	0.4	11.4	0.7	10.7	0.2	9.8	0.3	9.4	0.4
Pr_2O_3	1.3	0.2	1.7	0.2	1.4	0.1	1.54	0.02	1.5	0.3
Nd_2O_3	2.75	0.08	2.64	0.05	2.6	0.1	2.7	0.1	2.8	0.2
Sm_2O_3	--	--	--	--	--	--	--	--	--	--
ThO_2	3.7	0.2	4.5	0.2	4.5	0.2	6.5	0.3	5.7	0.1

Table E-4. Chemical compositions of allanite from the Fort Hamlin Hills pluton						
Grain 1		**Sample: 12RN461B**			Base: 1(1)	
Subhedral; 250 microns; no obvious zoning						
	Right Interior		Left Interior		Top Rim	
Points	1-3	StDev	4-6	StDev	7-9	StDev
MgO	--	--	--	--	--	--
Al_2O_3	15.0	0.2	13.7	0.2	18.5	0.1
SiO_2	29.6	0.4	31.5	0.6	33.7	0.1
CaO	8.1	0.2	8.79	0.06	9.7	0.1
TiO_2	2.8	0.2	3.10	0.04	--	--
Fe_2O_3	16.8	0.5	16.4	0.2	13.9	0.1
Y_2O_3	3.7	0.4	--	--	--	--
La_2O_3	5.5	0.4	6.0	0.3	5.8	0.6
Ce_2O_3	11.4	0.5	13.8	0.2	12.6	0.3
Pr_2O_3	1.0	0.4	1.4	0.2	0.85	0.08
Nd_2O_3	2.3	0.7	2.7	0.2	3.1	0.4
Sm_2O_3	--	--	0.56	0.01	1.10	0.02
ThO_2	3.1	0.2	2.0	0.1	0.62	0.06

Table E-4 (continued). Chemical compositions of allanite from the Fort Hamlin Hills pluton						
Grain 2		**Sample: 12RN461B**			Base: 1(2)	
Subhedral; 350 microns; fragmented; weakly zoned						
	Top Rim		Top Rim		Core	
Points	10-12	StDev	1-3	StDev	4-6	StDev
MgO	--	--	--	--	--	--
Al_2O_3	16.2	0.1	16.2	0.1	16.6	0.3
SiO_2	31.0	0.1	29.8	0.1	30.8	0.3
CaO	8.3	0.1	7.8	0.2	8.0	0.1
TiO_2	0.44	0.03	2.6	0.1	0.51	0.04
MnO	1.34	0.02	--	--	1.54	0.07
Fe_2O_3	14.2	0.2	15.5	0.2	14.8	0.1
Y_2O_3	--	--	3.9	0.1	--	--
La_2O_3	5.49	0.06	5.1	0.5	5.4	0.1
Ce_2O_3	15.4	0.1	11.9	0.2	14.8	0.3
Pr_2O_3	1.89	0.03	1.49	0.01	1.6	0.2
Nd_2O_3	4.8	0.1	2.5	0.2	5.0	0.1
Sm_2O_3	0.19	0.06	0.54	0.07	0.5	0.2
ThO_2	0.77	0.09	2.7	0.2	0.66	0.08

Table E-4 (continued). Chemical compositions of allanite from the Fort Hamlin Hills pluton						
Grain 3		**Sample: 12RN461B**		Base: 1(3)		
Anhedral; 300 microns; fragmented; no obvious zoning						
	Core		Interior		Rim	
Points	1-3	StDev	4-6	StDev	7-9	StDev
MgO	--	--	--	--	--	--
Al_2O_3	14.3	0.2	16.9	0.5	17.9	0.2
SiO_2	29.8	0.4	30.0	0.4	32.0	0.2
CaO	8.5	0.2	8.8	0.2	9.5	0.1
TiO_2	2.7	0.2	0.97	0.08	0.65	0.03
MnO	--	--	--	--	--	--
Fe_2O_3	16.6	0.4	15.5	0.5	15.6	0.7
Y_2O_3	3.7	0.2	4.4	0.2	--	--
La_2O_3	5.5	0.5	4.8	0.7	4.9	0.3
Ce_2O_3	12.7	0.7	11.2	0.1	13.0	1.1
Pr_2O_3	1.2	0.3	1.3	0.2	1.2	0.3
Nd_2O_3	2.5	0.3	3.3	0.3	3.0	0.3
Sm_2O_3	0.4	0.1	0.79	0.04	0.86	0.06
ThO_2	2.18	0.08	1.78	0.05	1.4	0.3

Table E-5. Chemical composition of allanite from the Ray River pluton						
Pluton: Ray River		**Sample: 12RN429A**		Base: Base(2)		
Subhedral; 1 mm; no obvious zoning						
	Bottom Rim		Core		Top Rim	
Points	1-3	StDev	4-6	StDev	7-9	StDev
MgO	--	--	--	--	--	--
Al_2O_3	15.5	0.4	16.7	0.4	14.6	0.8
SiO_2	34.5	0.4	32.7	0.1	33.8	0.2
CaO	8.5	0.1	9.72	0.08	9.0	0.5
TiO_2	1.1	0.1	0.7	0.1	1.3	0.4
FeO	14.3	0.5	14.2	0.1	15.7	0.2
Y_2O_3	--	--	--	--	--	--
La_2O_3	5.2	0.6	6.00	0.03	5.1	0.4
Ce_2O_3	12.7	0.3	14.7	0.3	13.0	0.4
Pr_2O_3	1.15	0.08	0.9	0.1	1.0	0.1
Nd_2O_3	2.8	0.3	2.4	0.2	3.0	0.3
Sm_2O_3	0.7	0.1	0.8	0.2	0.7	0.1
ThO_2	3.5	0.3	1.15	0.02	2.7	0.3

Table E-6. Chemical compositions of allanite from the Sithylemenkat pluton								
Grain 1			**Sample: 12RN344A**				Base: Allanite1(1)	
Euhedral; fragmented; 1 mm; oscillatory zoning								
	Top Rim		Interior		Core		Bottom Rim	
Points	1-3	StDev	4-6	StDev	7-9	StDev	10-12	StDev
MgO	--	--	--	--	--	--	--	--
Al_2O_3	14.2	0.4	15.9	0.7	14.9	0.2	16.2	0.3
SiO_2	30.14	0.04	30.1	0.4	28.0	0.6	28.8	0.7
CaO	9.62	0.08	7.2	0.4	6.7	0.2	6.03	0.08
TiO_2	1.44	0.08	2.9	0.1	2.81	0.09	3.0	0.1
Fe_2O_3	15.8	0.3	16.9	0.1	21.2	0.9	18.0	0.6
Y_2O_3	--	--	--	--	--	--	--	--
La_2O_3	4.9	0.3	4.8	0.2	4.1	0.4	4.6	0.2
Ce_2O_3	13.6	0.1	12.0	0.9	12.3	0.8	12.6	0.2
Pr_2O_3	2.53	0.05	2.1	0.7	2.54	0.04	2.5	0.3
Nd_2O_3	5.6	0.2	3.4	0.2	3.7	0.1	3.1	0.3
Sm_2O_3	1.2	0.1	0.54	0.07	--	--	--	--
ThO_2	1.1	0.2	4.2	0.5	3.5	0.3	4.8	0.1

Table E-6 (continued). Chemical compositions of allanite from the Sithylemenkat pluton								
Grain 2			**Sample: 12RN344A**				Base: Allanite2(1)	
Subhedral; 500 microns; oscillatory zoning								
	Bottom Rim →				Core		Top Rim	
Points	4-6	StDev	10-12	StDev	1-3	StDev	13-15	StDev
MgO	--	--	--	--	--	--	--	--
Al_2O_3	17.5	0.7	15.4	0.4	14.5	0.3	14.9	0.7
SiO_2	29.9	0.8	29.5	0.7	30.2	0.9	29.5	0.9
CaO	6.2	0.3	7.0	0.3	8.8	0.2	7.3	0.1
TiO_2	3.9	0.3	3.0	0.2	1.66	0.08	2.1	0.2
Fe_2O_3	15.0	0.3	15.3	0.1	15.6	0.5	16.8	0.3
Y_2O_3	--	--	--	--	--	--	--	--
La_2O_3	3.8	0.4	5.4	0.2	5.5	0.3	5.9	0.3
Ce_2O_3	10.9	0.5	13.4	0.4	14.6	0.5	13.5	1.2
Pr_2O_3	2.1	0.4	2.7	0.4	2.4	0.3	2.6	0.3
Nd_2O_3	3.1	0.1	3.5	0.1	4.7	0.4	4.0	0.1
Sm_2O_3	0.4	0.1	0.5	0.2	0.7	0.2	--	--
ThO_2	7.1	0.2	4.3	0.2	1.3	0.2	3.1	0.4

Appendix F. Chemical Compositions of Monazite

Table F-1. Chemical compositions of monazite from the Fort Hamlin Hills pluton

	Sample 12RN439A											
	Grain 1						Grain 2					
Description	Subhedral; 50 microns; weakly zoned						Subhedral; 40 microns; no obvious zoning					
Location	Rim		Interior		Core		Left Rim		Core		Right Rim	
Point	1-3	StDev	7-9	StDev	4-6	StDev	7-9	StDev	1-3	StDev	4-6	StDev
SiO_2	1.24	0.05	1.6	0.2	4.26	0.09	3.2	0.1	3.47	0.09	1.3	0.1
P_2O_5	32.6	0.5	32.4	0.2	27.9	0.6	29.6	0.4	29.4	0.1	33.5	0.3
CaO	0.36	0.02	0.34	0.04	0.27	0.04	0.28	0.02	0.36	0.03	0.25	0.03
Y_2O_3	2.4	0.3	1.79	0.02	2.0	0.3	1.5	0.3	1.8	0.4	1.7	0.4
La_2O_3	9.4	0.2	9.1	0.4	7.7	0.3	8.9	0.2	9.2	0.2	10.0	0.2
Ce_2O_3	28.2	0.5	27.7	0.1	23.3	0.4	25.2	0.4	25.0	0.3	28.6	0.3
Pr_2O_3	2.8	0.3	3.0	0.2	2.7	0.3	2.8	0.3	2.49	0.03	2.7	0.5
Nd_2O_3	9.97	0.07	10.0	0.2	8.5	0.3	9.23	0.07	8.9	0.1	9.7	0.2
Sm_2O_3	2.08	0.04	2.0	0.2	1.58	0.03	1.3	0.1	1.58	0.08	2.3	0.2
Gd_2O_3	1.9	0.2	1.9	0.1	1.61	0.08	1.5	0.1	1.2	0.2	1.8	0.2
ThO_2	9.0	0.2	10.1	0.1	20.3	0.4	16.6	0.4	16.7	0.5	8.3	0.2

Note: Refer to p. 14 for procedure.

Table F-1 (continued). Chemical compositions of monazite from the Fort Hamlin Hills pluton

	Sample 12RN439A							
	Grain 3							
Description	Subhedral; fragmented; zoned							
Location	Top Rim		Interior		Core		Bottom Rim	
Point	1-3	StDev	7-9	StDev	4-6	StDev	10-12	StDev
SiO_2	2.5	0.09	4.0	0.1	2.7	0.1	3.4	0.2
P_2O_5	30.6	0.3	23.5	0.4	26.5	0.5	29.2	0.4
CaO	0.52	0.03	1.2	0.1	3.7	0.2	0.52	0.05
Y_2O_3	1.5	0.1	3.86	0.02	3.46	0.09	1.3	0.4
La_2O_3	8.5	0.2	8.1	0.4	7.6	0.3	8.5	0.4
Ce_2O_3	25.4	0.2	22.5	0.2	19.5	0.6	24.8	0.5
Pr_2O_3	3.2	0.1	2.8	0.3	2.7	0.1	2.9	0.2
Nd_2O_3	9.6	0.2	8.4	0.3	8.6	0.2	9.2	0.1
Sm_2O_3	2.0	0.2	1.5	0.2	1.3	0.1	1.38	0.07
Gd_2O_3	1.70	0.03	1.69	0.07	1.4	0.2	1.5	0.3
ThO_2	14.5	0.3	22.4	0.2	22.5	0.3	17.4	0.3

Table F-2. Chemical compositions of monazite from the Ray River pluton

	Sample 12RN424B		Sample 12RN429A							
Description	Grain 1 Anhedral; 50 microns; no obvious zoning		Grain 1 Anhedral; 30 microns; no obvious zoning							
Location			No systematic point collection							
Point	1-3	StDev	1-3	SD	4-6	SD	7-9	SD	10-12	SD
SiO_2	1.89	0.06	1.24	0.08	1.57	0.04	1.8	0.1	3.0	0.1
P_2O_5	34.0	1.1	32.2	0.5	30.7	0.3	31.0	0.4	21.8	2.4
CaO	--	--	0.36	0.02	0.36	0.01	0.41	0.01	0.35	0.06
Y_2O_3	--	--	2.7	0.4	2.27	0.10	1.69	0.07	--	--
La_2O_3	10.4	0.3	12.2	0.3	12.3	0.2	11.9	0.2	13.0	0.5
Ce_2O_3	31.2	0.4	28.4	0.2	28.7	0.2	28.2	0.1	30.4	0.9
Pr_2O_3	2.8	0.5	2.1	0.2	2.71	0.07	2.3	0.2	3.0	0.2
Nd_2O_3	7.915	0.005	9.2	0.1	9.1	0.1	8.4	0.2	9.4	0.3
Sm_2O_3	1.4	0.2	2.1	0.1	1.60	0.06	1.59	0.06	1.14	0.08
Gd_2O_3	0.77	0.09	1.2	0.1	0.99	0.09	1.3	0.3	1.1	0.1
ThO_2	9.3	1.1	8.30	0.07	9.7	0.2	11.35	0.08	16.1	0.3

Table F-2 (continued). Chemical compositions of monazite from the Ray River pluton

	Sample 12RN429A									
Description	Grain 2 Anhedral; fragmented, 40 microns; no obvious zoning				Grain 3 Subhedral; 40 microns; patchy zoning					
Location	Core		Rim		Core		Interior		Rim	
Point	1-3	SD	4-6	SD	1-3	SD	7-9	SD	4-6	SD
SiO_2	2.0	0.2	--	--	1.2	0.1	1.31	0.04	--	--
P_2O_5	30.6	0.7	34.5	0.7	31.5	0.2	31.6	0.5	34.3	0.7
CaO	0.13	0.03	0.25	0.03	0.46	0.04	0.56	0.07	0.6	0.1
Y_2O_3	--	--	1.0	0.3	3.7	0.2	3.3	0.4	--	--
La_2O_3	12.0	0.3	12.8	0.2	11.2	0.3	11.3	0.4	12.7	0.4
Ce_2O_3	29.3	0.3	33.9	0.3	27.10	0.03	28.0	0.2	33.5	0.3
Pr_2O_3	2.5	0.1	2.7	0.4	2.4	0.3	2.7	0.6	2.8	0.1
Nd_2O_3	9.3	0.2	9.2	0.2	9.6	0.2	9.4	0.4	10.2	0.2
Sm_2O_3	1.86	0.06	1.7	0.2	2.0	0.5	1.5	0.6	1.3	0.3
Gd_2O_3	0.8	0.2	0.5	0.1	1.64	0.03	1.7	0.2	0.9	0.3
ThO_2	11.2	0.1	2.7	0.4	9.2	0.1	8.6	0.2	2.55	0.08

Table F-3. Chemical compositions of monazite from the No Name Creek pluton

	Sample 12RN319A											
Description	Grain 1 Subhedral; 30 microns; weakly zoned						Grain 2 Anhedral; fragmented; 75 microns; no obvious zoning				Grain 3 Anhedral; fragmented; 75 microns; no obvious zoning	
Location	Core		Interior		Rim		Rim		Interior			
Point	1-3	StDev	4-6	StDev	8,9	StDev	1-3	StDev	4-6	StDev	1,3-6	StDev
SiO_2	2.14	0.02	2.1	0.2	1.87	0.01	1.3	0.1	0.93	0.03	3.2	1.1
P_2O_5	35.6	0.2	35.6	0.2	33.8	0.6	36.8	1.2	36.6	0.7	35.3	1.0
CaO	0.91	0.03	0.85	0.07	1.20	0.02	1.38	0.07	3.3	0.1	1.5	0.4
Y_2O_3	--	--	--	--	3.9	0.6	2.0	0.7	1.5	0.3	2.0	0.5
La_2O_3	11.1	0.1	11.0	0.4	10.5	1.0	9.1	0.6	6.2	0.2	9.3	1.4
Ce_2O_3	28.8	0.2	29.8	0.3	29.2	0.6	27.3	0.3	22.1	0.7	28.0	1.7
Pr_2O_3	2.86	0.01	2.7	0.3	3.8	0.4	2.2	0.5	2.1	0.4	2.7	0.8
Nd_2O_3	7.5	0.4	7.9	0.7	8.15	0.03	8.0	0.6	7.4	0.6	8.2	0.8
Sm_2O_3	0.74	0.04	0.8	0.2	--	--	1.5	0.1	1.7	0.2	1.0	0.1
Gd_2O_3	0.8	0.2	0.8	0.2	0.9	0.3	1.3	0.2	1.4	0.3	1.4	0.4
ThO_2	9.59	0.08	8.3	0.5	6.5	0.2	9.2	0.3	16.9	0.4	7.5	0.9

Table F-3 (continued). Chemical compositions of monazite from the No Name Creek pluton

	Sample 12LF304A			
Description	Grain 4 Subhedral; 75 microns; no obvious zoning		Grain 5 Subhedral; fragmented; 20 microns; weakly zoned	
Location				
Point	1-3	StDev	1-3	StDev
SiO_2	1.16	0.03	0.7	0.2
P_2O_5	34.1	0.3	33.2	0.2
CaO	0.29	0.07	0.61	0.02
Y_2O_3	2.6	0.2	2.1	0.3
La_2O_3	11.0	0.2	12.3	0.1
Ce_2O_3	31.5	0.1	31.8	0.3
Pr_2O_3	2.6	0.2	2.9	0.1
Nd_2O_3	8.7	0.1	7.9	0.4
Sm_2O_3	1.8	0.2	0.7	0.1
Gd_2O_3	1.3	0.2	0.6	0.2
ThO_2	4.95	0.07	7.2	0.2

Table F-4. Chemical compositions of monazite from the Sithylemenkat pluton

	Sample 12LF015B											
Description	Grain 1 Anhedral; 15 microns; no obvious zoning				Grain 2				Grain 3 Subhedral; 150 microns; no obvious zoning		Grain 4 Anhedral; 20 microns; no obvious zoning	
Location												
Point	1-3	StDev	4-6	StDev	7-9	StDev	10-12	StDev	1-3	StDev	1-3	StDev
SiO_2	3.3	0.2	2.1	0.2	1.2	0.5	2.5	0.4	1.6	0.2	1.1	0.1
P_2O_5	28.6	0.2	31.6	0.3	33.7	0.5	33.6	0.7	33.0	0.7	34.6	0.8
CaO	0.4	0.1	0.35	0.02	0.47	0.04	0.8	0.1	0.33	0.01	0.8	0.1
Y_2O_3	1.5	0.2	1.3	0.3	2.2	0.5	--	--	2.9	0.3	3.7	0.2
La_2O_3	10.6	0.5	11.4	0.3	12.9	0.5	11.3	0.4	12.0	0.4	10.9	0.3
Ce_2O_3	27.9	0.3	29.2	0.3	31.2	0.3	29.0	0.4	29.4	0.5	29.0	0.5
Pr_2O_3	2.9	0.1	2.40	0.05	2.39	0.05	2.1	0.6	2.1	0.3	2.0	0.7
Nd_2O_3	8.4	0.1	7.9	0.4	7.8	0.3	8.4	0.2	7.42	0.07	7.9	0.3
Sm_2O_3	0.80	0.08	1.0	0.3	1.17	0.08	1.05	0.08	1.4	0.3	1.6	0.1
Gd_2O_3	0.91	0.06	1.1	0.2	0.85	0.09	1.0	0.2	0.87	0.03	1.3	0.1
ThO_2	14.6	0.1	11.6	0.3	6.19	0.02	9.6	0.3	9.0	0.2	7.2	0.3

Table F-5. Chemical compositions of monazite from the Ray Mountains East pluton

	Sample 12LF212A												Sample 12LF194A	
Description	Grain 1 Subhedral; 40 microns; no obvious zoning		Grain 2 Anhedral; fragmented; 25 microns; no obvious zoning		Grain 3 Anhedral; fragmented; 40 microns; no obvious zoning		Grain 4 Subhedral; 15 microns; patchy zoning				Grain 5 Subhedral; 20 microns; no obvious zoning		Grain 1 Subhedral; 100 microns; no obvious zoning	
Point	Avg	StDev	Avg	StDev	Avg	StDev	1-3	StDev	4-6	StDev	Avg	StDev	Avg	StDev
SiO_2	1.3	0.2	1.42	0.20	1.41	0.12	1.87	0.08	1.9	0.4	0.90	0.03	1.2	0.2
P_2O_5	31.7	0.5	31.94	0.28	32.10	0.90	34.7	0.4	29.1	1.1	32.6	0.6	35.3	1.3
CaO	0.49	0.05	0.42	0.03	0.87	0.11	1.11	0.03	0.79	0.09	0.62	0.07	0.99	0.1
Y_2O_3	1.2	0.5	--	--	3.98	0.21	5.5	0.2	2.1	0.4	2.6	0.4	--	--
La_2O_3	13.6	0.1	13.65	0.17	9.60	0.35	10.5	0.1	12.8	0.5	11.7	0.1	12.4	0.7
Ce_2O_3	30.7	0.1	31.37	0.20	28.31	0.16	28.3	0.5	33.2	0.1	30.6	0.2	29.8	0.3
Pr_2O_3	2.7	0.3	2.86	0.06	2.71	0.52	2.4	0.2	3.4	0.5	3.0	0.3	3.4	0.8
Nd_2O_3	7.50	0.07	7.50	0.21	8.37	0.57	7.4	0.1	8.8	0.3	8.0	0.2	8.5	0.3
Sm_2O_3	0.86	0.04	--	--	1.55	0.23	--	--	--	--	0.78	0.09	1.0	0.2
Gd_2O_3	--	--	0.53	0.12	1.30	0.13	1.68	0.04	1.43	0.04	1.0	0.1	0.9	0.2
ThO_2	9.43	0.04	9.57	0.14	9.81	0.38	6.64	0.08	6.4	0.4	8.3	0.3	6.2	0.5

Appendix G. Laboratory-Concentrated, Bulk Heavy-Mineral Concentrates

Table G-1. Laboratory-concentrated, bulk-heavy mineral concentrates

ALS Minerals Method					ME-ICP61	ME-ICP61	ME-ICP61	ME-ICP61	ME-ICP61	ME-ICP61	ME-ICP61	ME-ICP61	Sn-XRF10	Th-XRF10
Digestion Technique					4AD	4AD	4AD	4AD	4AD	4AD	4AD	4AD		
	Easting	Northing	UTM Zone	Sluiced	Al	Ca	Fe	K	Mg	Mn	P	Na	Sn*	Th
					%	%	%	%	%	%	ppm	%	%	%
12LF237B	587316.9	7324476	5W	TRUE	6.2	0.49	2.39	2.77	0.12	783	3860	2.26	2.54	0.22
12LF238C	587439.7	7324578	5W	FALSE	6.9	0.52	2.23	2.51	0.18	677	3880	2.56	2.0	0.22
12LF240B	576867.3	7316454	5W	TRUE	5.35	1.8	3.91	1.91	0.32	1855	2500	1.19	0.662	0.0897
12LF289B	609609.2	7320035	5W	FALSE	3.61	1.04	3.51	1.55	0.16	2630	3780	0.76	1.9	0.19
12LF290B	606015.6	7319449	5W	FALSE	3.31	0.89	4.1	1.61	0.13	3030	3920	0.69	1.69	0.18
12LF294B	617904.7	7320305	5W	FALSE	4.1	0.91	4.24	1.8	0.18	2660	2080	0.7	1.08	0.0789
12LF295B	622547.9	7324504	5W	FALSE	3.7	0.62	3.49	1.74	0.19	1885	1240	0.63	0.255	0.0354
12LF296B	626864.8	7325810	5W	FALSE	4.24	0.86	2.29	1.9	0.33	926	1290	0.72	0.39	0.0325
12LF301BA	633592.6	7336556	5W	TRUE	6.39	0.21	2.61	2.48	0.11	1200	700	2.05	0.474	0.0334
12LF301BB	633592.6	7336556	5W	FALSE	6.05	0.21	2.51	2.46	0.12	1290	1310	1.82	1.0	0.0718
12LF314B	629495	7336885	5W	FALSE	4.45	1.78	3.97	1.02	0.44	3700	800	0.72	0.384	0.0235
12LF315B	624434.1	7332058	5W	FALSE	5.37	1.99	5.27	0.88	0.6	10400	710	0.73	1.0	0.01945
12LF316B	625665.4	7328798	5W	TRUE	4.59	1.09	2.59	1.51	0.32	1755	590	0.89	0.1	0.0152
12LF317B	632894.1	7336034	5W	FALSE	4.25	0.32	3.06	1.74	0.14	2060	1420	0.98	4.47	0.0821
12LF318B	628046.6	7325287	5W	FALSE	4.23	1.26	3.22	1.29	0.58	4590	1440	0.64	0.7	0.0561
12LF319C	627912.3	7325771	5W	TRUE	4.58	1.38	3.32	1.65	0.66	2000	910	0.86	0.3	0.0243
12LF319D	627914.2	7325771	5W	TRUE	4.23	1.18	2.64	1.62	0.42	1730	840	0.69	0.1	0.032
12LF340B	632339.5	7322970	5W	FALSE	4.09	0.93	2.83	1.93	0.43	1835	950	0.66	0.1	0.0314
12MJB101A	630744.1	7326023	5W	FALSE	2.99	0.04	1.02	3.07	0.04	398	150	0.16	0.0	0.0109
12MJB102A	628624.1	7331981	5W	FALSE	2.89	0.03	2.1	2.14	0.05	917	250	0.1	0.0	0.0111

Notes: "4AD" = four-acid digestion. Refer to p. 11-12 for procedure.

Table G-1 (continued). Laboratory-concentrated, bulk-heavy mineral concentrates

ALS Minerals Method	ME-ICP61	ME-ICP61	ME-MS81	Zr-XRF10	ME-MS81	ME-MS81	ME-ICP61	ME-MS81	ME-MS81	ME-MS81	ME-MS81	ME-MS81	ME-MS81	ME-MS81	ME-MS81	ME-MS81
Digestion Technique	4AD	4AD	LiB	LiB	LiB	LiB	LiB	LiB	LiB	LiB	LiB	LiB	LiB	LiB	LiB	LiB
	Ti	S	Y	Zr	Nb	La 1	La 2	Ce	Pr	Nd	Sm	Eu	Gd	Tb	Dy	Ho
	%	%	ppm	%	ppm	ppm	ppm	ppm	ppm	ppm	ppm	ppm	ppm	ppm	ppm	ppm
12LF237B	0.51	0.01	1665	1.01	160.5	3360	3000	7400	875	2960	585	2.68	341	50.3	268	53.3
12LF238C	0.45	-1	1990	1.05	127	2960	2560	6730	811	2770	584	2.71	366	58.1	315	68.1
12LF240B	1.12	-1	925	0.35	133	1600	1470	3340	373	1185	212	3.17	147	25.5	149	32.5
12LF289B	2.86	-1	2170	0.69	433	2790	2600	5950	686	2230	409	4.14	289	50.6	314	72.8
12LF290B	3.17	-1	2790	0.76	473	2950	2740	6260	723	2350	452	4.61	329	63.1	394	92.4
12LF294B	2.35	-1	1410	0.16	256	1300	1200	2720	311	1090	205	4.83	183.5	34.8	237	51.1
12LF295B	1.68	-1	637	0.13	167.5	558	500	1175	135	477	92.5	3.11	84.7	15.5	106	22.6
12LF296B	0.85	0.01	790	0.11	103	529	490	1105	126.5	451	89.2	4.14	91.6	17.75	125.5	27.3
12LF301BA	1.05	-1	1510	0.16	181.5	431	450	968	111.5	391	97	1.21	126	30	231	51.3
12LF301BB	1.21	-1	2880	0.35	271	943	920	2110	241	842	203	2.28	248	58.7	434	97.6
12LF314B	2.34	-1	1680	0.18	256	367	310	760	87.5	318	81.5	2.77	122.5	30.8	246	56.9
12LF315B	1.45	-1	1855	0.07	227	224	200	471	58.3	224	69.6	2.8	123.5	32.2	266	62.9
12LF316B	0.78	-1	674	0.14	86.1	237	210	495	57.9	212	48.9	1.75	59.5	13.4	103	23
12LF317B	1.46	-1	4520	0.27	455	954	870	2060	238	849	217	2.79	314	80.6	638	150.5
12LF318B	1.46	0.01	1370	0.23	172	922	810	1940	220	767	154	5.03	155	30.5	219	48.4
12LF319C	0.7	0.02	593	0.18	78.9	398	370	836	96.7	348	68.8	2.66	69.1	13.55	95.8	20.9
12LF319D	0.89	-1	550	0.13	85.2	550	500	1160	131	463	89.1	2.15	79.4	14.15	94.6	19.75
12LF340B	1.23	0.01	562	0.13	132	480	440	984	113	402	76.8	2.74	74	13.6	93.7	19.9
12MJB101A	0.74	-1	109.5	0.33	71.2	111	100	220	27.1	97	17.9	0.55	15.1	2.74	18.3	3.96
12MJB102A	1.17	-1	257	0.14	106.5	194.5	180	398	46.7	166	31.1	1.49	30.9	5.96	42	9.23

Notes: "4AD" = four-acid digestion; "LiB" = lithium borate (either metaborate or tetraborate)

Table G-1 (continued). Laboratory-concentrated, bulk-heavy mineral concentrates

ALS Minerals Method	ME-MS81	ME-MS81	ME-MS81	ME-MS81	ME-MS81	ME-ICP61	ME-MS81	ME-ICP61	ME-ICP61	ME-ICP61	PGM-ICP23	ME-MS81	ME-ICP61	ME-ICP61	ME-ICP61	ME-ICP61
Digestion Technique	LiB	LiB	LiB	LiB	LiB	4AD	LiB	4AD	4AD	4AD		LiB	4AD	4AD	4AD	4AD
	Er	Tm	Yb	Lu	Th 1	Th 2	U 1	U 2	Ag	As	Au 1	Ba 1	Ba 2	Be	Bi	Cd
	ppm	ppm	ppm	ppm	ppm	ppm	ppm	ppm	ppm	ppm	ppm	ppm	ppm	ppm	ppm	ppm
12LF237B	150.5	23.4	155	24.2	-2	2070	248	-1	0.5	31	0.174	155.5	150	10.5	65	-1
12LF238C	191	29.4	188	29	-2	2080	257	20	1	33	0.022	167	150	10.5	-1	-1
12LF240B	94.2	14.35	91	13.2	897	790	79.6	-1	-1	18	0.449	396	390	2.4	-1	-1
12LF289B	210	32.8	210	31		1620	190	-1	-1	16	0.598	158	160	6.1	-1	-1
12LF290B	277	42.3	272	39.7		1700	222	-1	-1	22	0.779	151.5	150	5.6	-1	-1
12LF294B	158	23.3	147	21.1	789	730	87.6	-1	-1	15	1.575	176	170	5.2	-1	0.6
12LF295B	68.5	10.15	63.9	9.03	354	330	39.5	-1	-1	5	0.855	190	180	5	-1	-1
12LF296B	84	12.25	77.1	10.8	325	310	40.9	-1	-1	-1	0.926	214	200	4.6	-1	-1
12LF301BA	166.5	26.2	176	25.4	334	340	67	-1	-1	6	0.563	114.5	130	14.9	-1	-1
12LF301BB	317	50.2	330	48.1	718	680	125.5	-1	-1	11	0.056	147	150	16.1	-1	-1
12LF314B	186.5	29.8	196.5	28.4	235	190	66.7	-1	-1	10	0.336	234	210	3.2	2	-1
12LF315B	211	32.9	215	31.6	194.5	160	68.7	-1	-1	23	5.65	190	180	3.4	6	-1
12LF316B	74.3	11.75	77.8	11.2	152	130	35.7	-1	-1	25	0.005	257	240	6.3	-1	-1
12LF317B	498	80	519	77.9	821	700	174.5	-1	-1	8	0.074	141	130	12.8	5	-1
12LF318B	152	23.3	150	21.5	561	490	68.8	-1	-1	7	0.368	220	200	4.1	-1	-1
12LF319C	65.3	9.97	64.6	9.26	243	230	34.7	20	-1	7	1.51	244	230	4	-1	-1
12LF319D	60.8	9.02	59.5	8.39	320	300	32.8	20	-1	15	0.14	227	220	4.5	-1	-1
12LF340B	61.5	9.19	58.8	8.37	314	300	35.6	20	-1	-1	1.735	246	230	4.4	2	-1
12MJB101A	12.8	2.1	14.9	2.46	109	100	20.1	10	-1	5	0.017	276	260	3.7	-1	-1
12MJB102A	28.4	4.25	27.4	3.94	111	110	16.55	10	0.7	-1	50.4	285	270	2.4	22	-1

Notes: "4AD" = four-acid digestion; "LiB" = lithium borate (either metaborate or tetraborate)

Table G-1 (continued). Laboratory-concentrated, bulk-heavy mineral concentrates

ALS Minerals Method	ME-ICP61	ME-MS81	ME-ICP61	ME-MS81	ME-ICP61	ME-MS81	ME-ICP61	ME-MS81	ME-ICP61	ME-ICP61	ME-ICP61	PGM-ICP23	PGM-ICP23	ME-MS81	ME-ICP61	ME-ICP61
Digestion Technique	4AD	LiB	4AD	LiB	4AD	LiB	4AD	LiB	4AD	4AD	4AD			LiB	4AD	4AD
	Co	Cr 1	Cr 2	Cs	Cu	Ga 1	Ga 2	Hf	Mo	Ni	Pb	Pd	Pt	Rb	Sb	Sc
	ppm	ppm	ppm	ppm	ppm	ppm	ppm	ppm	ppm	ppm	ppm	ppm	ppm	ppm	ppm	ppm
12LF237B	3	20	16	14.3	36	38.2	20	363	5	1	1220	-1	-1	366	-1	7
12LF238C	3	10	4	25.6	10	40.6	20	412	2	-1	81	-1	-1	399	-1	10
12LF240B	5	80	56	4.01	19	20.9	10	102.5	2	7	32	-1	-1	132	-1	17
12LF289B	4	50	31	7.36	6	28.2	10	205	3	5	49	-1	-1	167	-1	13
12LF290B	5	50	36	6.15	8	25.1	10	229	2	5	57	-1	-1	170.5	-1	13
12LF294B	4	80	52	6.7	6	19.3	10	53.9	-1	9	47	-1	-1	178.5	-1	11
12LF295B	3	90	54	6.24	7	14.3	10	37.9	-1	8	28	-1	-1	176	-1	8
12LF296B	4	170	103	6.09	5	15.1	10	34.8	-1	13	30	-1	-1	183	-1	8
12LF301BA	3	20	9	16.05	7	25.2	20	44.6	-1	4	326	0.001	-1	297	-1	8
12LF301BB	4	20	7	17.5	6	29.7	20	95.6	1	3	56	-1	-1	333	-1	10
12LF314B	6	500	331	3.84	8	17	10	52.5	1	16	25	-1	-1	84.3	-1	16
12LF315B	13	1080	826	3.19	12	18.7	10	23.5	1	30	32	-1	-1	69.1	-1	32
12LF316B	7	210	105	7.02	16	17.9	10	39.2	-1	14	28	-1	-1	141.5	-1	9
12LF317B	3	30	13	13.7	7	25.2	10	77.1	2	3	32	-1	-1	217	-1	11
12LF318B	7	570	397	4.58	8	18.8	10	67.5	1	25	38	-1	-1	122.5	-1	17
12LF319C	8	270	169	5.05	14	15.7	10	51.5	1	29	34	-1	-1	135	6	11
12LF319D	5	150	86	5.47	11	16.8	10	38.1	-1	14	36	-1	-1	134.5	7	10
12LF340B	5	140	87	5.71	7	15.3	10	39.6	1	17	28	-1	-1	167	-1	9
12MJB101A	1	10	5	6.74	3	9.1	10	97.3	-1	1	48	-1	-1	207	-1	4
12MJB102A	-1	40	27	5.61	8	9.1	10	43.1	-1	4	27	-1	-1	161.5	-1	6

Notes: "4AD" = four-acid digestion; "LiB" = lithium borate (either metaborate or tetraborate)

Table G-1 (continued). Laboratory-concentrated, bulk-heavy mineral concentrates

ALS Minerals Method	ME-MS81	ME-MS81	ME-ICP61	ME-MS81	ME-MS81	ME-ICP61	ME-MS81	ME-ICP61	ME-MS81	ME-ICP61	ME-ICP61	ME-MS81
Digestion Technique	LiB	LiB	4AD	LiB	LiB	4AD	LiB	4AD	LiB	4AD	4AD	LiB
	Sn	Sr 1	Sr 2	Ta	Tl 1	Tl 2	V 1	V 2	W 1	W 2	Zn	Zr
	ppm	ppm	ppm	ppm	ppm	ppm	ppm	ppm	ppm	ppm	ppm	ppm
12LF237B	-2	70.7	134	31.8	2.1	-1	17	11	2120	1800	64	10100
12LF238C	-2	70.3	128	24.5	2.2	-1	22	15	1050	830	63	10500
12LF240B	6620	181	204	28.8	0.8	-1	68	56	654	550	65	3540
12LF289B	-2	48	102	114	1	-1	55	41	857	690	73	6910
12LF290B	-2	40.6	98	129.5	1	-1	52	39	1010	820	81	7640
12LF294B	-2	41.4	65	60.2	1.1	-1	75	51	425	320	90	1630
12LF295B	2550	40.9	48	30.3	1.1	-1	63	42	135	100	69	1250
12LF296B	3900	53.8	61	25.2	1.1	-1	60	45	124	90	51	1120
12LF301BA	4740	28.3	39	54.6	1.6	-1	27	17	254	230	72	1550
12LF301BB	9610	33.2	52	86.1	1.9	-1	34	20	613	550	70	3520
12LF314B	3840	97.9	96	80.7	0.5	-1	97	74	142	100	78	1750
12LF315B	-2	97.7	98	95.8	-1	-1	87	87	160	100	93	670
12LF316B	530	80.6	77	23.9	0.8	-1	71	50	63	40	75	1350
12LF317B	-2	30.1	44	152.5	1.5	-1	45	23	3500	1880	57	2700
12LF318B	6870	76.3	86	51.2	0.8	-1	80	66	222	150	75	2270
12LF319C	3490	104.5	103	21.9	0.8	-1	78	60	118	80	64	1750
12LF319D	664	83.4	85	19.6	0.8	-1	74	56	44	30	63	1280
12LF340B	1440	59.3	64	29.2	1	-1	68	51	78	60	55	1340
12MJB101A	53	30.6	31	8.2	1.3	-1	14	12	12	10	105	3330
12MJB102A	323	24.1	26	20.5	1	10	35	27	63	50	28	1440

Notes: “4AD” = four-acid digestion; “LiB” = lithium borate (either metaborate or tetraborate)